Experimental study of radiative shocks in noble gases on the Orion laser and the MAGPIE pulsed-power facility

Thomas Clayson

Supervised by Dr. Francisco Suzuki-Vidal and Prof. Sergey V. Lebedev

Imperial College London

Department of Physics



June 23, 2018

Submitted in part fulfilment of the requirements for the degree of

Doctor of Philosophy in Physics of Imperial College London

and the Diploma of Imperial College London

Declaration of Originality

I hereby certify that the material in this thesis, which I submit for the degree of Doctor of Philosophy, is entirely original unless otherwise cited or acknowledged.

Thomas Albert Clayson June 23, 2018

Copyright Notice

The copyright of this thesis rests with the author and is made available under a Creative Commons Attribution Non-Commercial No Derivatives licence. Researchers are free to copy, distribute or transmit the thesis on the condition that they attribute it, that they do not use it for commercial purposes and that they do not alter, transform or build upon it. For any reuse or redistribution, researchers must make clear to others the licence terms of this work.

Abstract

This Thesis introduces two novel experimental configurations for studying radiative shocks with the aim of improving our understanding of the physics involved, which is relevant to laboratory astrophysics, inertial confinement fusion and for benchmarking numerical simulations.

Experiments on the Orion laser facility used lasers with an intensity of $\sim 5 \times 10^{14}$ W/cm^2 to drive counter-propagating shocks, with a velocity of $v_s \sim 60$ km/s, into a gas-fill (of Neon, Argon, Krypton or Xenon) with an initial mass density of $\rho_0 = 0.5 - 1.6$ mg/cm^3. These experiments simultaneously study both the post-shock material and radiative precursor for the first time, with a combination of X-ray backlighting, self-emission streaked imaging and laser interferometry. Experiments with Neon gas-fills allowed for post-shock compression measurements, $\Gamma \sim \times 23$, and the counter-propagating shock configuration allowed reverse shocks to be studied. In addition, large gas-cells allowed for shocks to evolve in three dimensions, resulting in the formation of post-shock instabilities which will be the subject of future work.

Experiments on the MAGPIE generator introduce the 'inverse liner z-pinch', building upon previous experiments on imploding liners where diagnostic access was limited and radiative effects occurred on spatial scales larger than the experiment. A $\sim$1 MA current pulse was passed through a liner embedded in a gas-fill (of Neon, Argon, Krypton or Xenon), with an initial mass density of $\rho_0 = 0.04$ mg/cm^3, and returned through a central post. This launched a cylindrically expanding radiative shock which propagated at $v_s \sim 10$ km/s. Experiments were diagnosed with a combination of self-emission imaging, laser interferometry and optical emission spectroscopy. Shocks were able to propagate for several centimetres, allowing the ionization in the radiative precursor to be measured, which was not possible in previous experiments. Future work will use this platform to study radiative shocks with perturbations by introducing well characterised grooves on the surface of the liner.

Acknowledgements

None of this work would have been possible without the guidance and tireless work of Francisco Suzuki-Vidal. Your constant support and strict corrections have taught me so much and made me a better person and scientist, for that I am truly grateful. I would like to thank Sergey Lebedev, whose wise words, insight and hilarious anecdotes never cease to amaze me. I would also like to thank the entire MAGPIE gang (+friends) for their assistance and teaching over the years, especially Simon Bland, George Swadling, Guy Burdiak, Jack Hare, Lee Suttle, Jack Halliday, Ellie Tubman, James Mc Donald and Daniel Russell. Thanks to my mother and father for providing constant encouragement, proof-reading services and a great place to stay for much of my writing up period. Thanks to my brother and sister for lively discussions. Thanks to Alan Finch and everyone in the workshop for carefully building accurate hardware only for me to blow it up. Finally, my greatest thanks goes to my wonderful wife Yu-Ting Cheng for keeping me happy, well balanced and supporting me as I pursue my interest. Thank you for putting up with me for all of these years.

謝謝羽婷。 你是我的世界和沒有你這個多不行。 我永遠愛你。 還是謝謝我的台灣的家人。 我很高興有很好的家人鼓勵我。

Contents

1 Introduction **14**
- 1.1 Overview of Thesis . . . 14
- 1.2 Background and motivation . . . 16
- 1.3 Author's contribution . . . 18
- 1.4 Plasma physics . . . 22
  - 1.4.1 Ionization . . . 23
  - 1.4.2 Quasi-neutrality . . . 26
  - 1.4.3 Mean free path . . . 28
  - 1.4.4 Emissivity and opacity in a plasma . . . 29
  - 1.4.5 Dimensionless scaling . . . 33
- 1.5 Shock waves . . . 36
  - 1.5.1 Rankine-Hugoniot relations . . . 37
  - 1.5.2 Strong shock limit . . . 42
  - 1.5.3 Rarefactions and blast waves . . . 44
- 1.6 Radiative shocks . . . 48
  - 1.6.1 Classification of radiative shocks by optical thickness . . . 49
  - 1.6.2 Radiative shock regimes . . . 51
  - 1.6.3 The radiative precursor . . . 53
  - 1.6.4 Radiative shock model . . . 55
- 1.7 HEDP research . . . 61
  - 1.7.1 Laser driven radiative shock experiments . . . 61
  - 1.7.2 Pulsed power driven radiative shock experiments . . . 70

2 Counter-propagating shock experiments **77**
- 2.1 Experimental setup . . . 78
  - 2.1.1 Overview of the Orion laser facility . . . 79
  - 2.1.2 Gas cell targets . . . 85
  - 2.1.3 Laser-piston interaction . . . 89
- 2.2 The Orion diagnostic suite . . . 93
  - 2.2.1 X-ray backlighting (XRBL) . . . 94
  - 2.2.2 Streaked self-emission . . . 102
  - 2.2.3 Laser interferometry . . . 104
- 2.3 Shock hydrodynamics . . . 113
  - 2.3.1 Shock velocity . . . 116
  - 2.3.2 Post-shock compression . . . 121
  - 2.3.3 The reverse shock . . . 128
  - 2.3.4 Experiments with Xenon gas-fills . . . 133
- 2.4 The radiative precursor . . . 138
  - 2.4.1 Precursor structure . . . 139

2.4.2 Evolution of the precursor . . . 144
2.4.3 Formation mechanism . . . 146
2.4.4 Precursor in Xenon gas-fills . . . 148
2.4.5 Variation with gas species . . . 152
2.5 Comparison to numerical simulations . . . 156
2.5.1 HELIOS 1-D simulations . . . 156
2.5.2 NYM - PETRA 2-D simulations . . . 161

3 Radially expanding shock experiments 169
3.1 Overview of the MAGPIE facility . . . 170
3.1.1 Marx banks . . . 171
3.1.2 Pulse forming lines . . . 174
3.1.3 Vertical transmission line . . . 177
3.2 Experimental setup . . . 179
3.2.1 Technical description . . . 181
3.2.2 Circuit model of the liner . . . 187
3.2.3 Current and magnetic skin depth . . . 193
3.3 MAGPIE diagnostic suite . . . 199
3.3.1 Current probes . . . 201
3.3.2 B-dot probes . . . 207
3.3.3 Multiframe optical self-emission camera . . . 210
3.3.4 Laser interferometry . . . 212
3.3.5 Optical spectroscopy . . . 214
3.4 Shock evolution . . . 217
3.4.1 Shock velocity . . . 219
3.4.2 Shock launch mechanism . . . 224
3.4.3 Magnetisation of the shocks . . . 228
3.4.4 Snowplough trajectories . . . 230
3.5 Shock structure . . . 233
3.5.1 Post-shock material . . . 237
3.5.2 The radiative precursor . . . 242
3.5.3 Edge shocks . . . 247
3.5.4 Variation with gas species . . . 252

4 Conclusions and future work 258
4.1 Summary . . . 258
4.1.1 Counter-propagating shock experiments . . . 258
4.1.2 Radially expanding shock experiments . . . 261
4.2 Future work . . . 264
4.2.1 Post-shock structure in laser driven experiments . . . 264
4.2.2 Magnetized radially expanding radiative shocks . . . 267
4.2.3 Seeding perturbation in radially expanding radiative shocks . . . 269

List of Figures

1.1 Examples of shocks observed in astrophysics. 16
1.2 Radiative shocks observed in ICF experiments. 18
1.3 Approximate conditions of different types of plasmas. 22
1.4 PrismSPECT calculations of ionization as a function of temperature. 25
1.5 Ionization energies for different noble gases, determined from [Kramida et al., 2015]. 26
1.6 Opacities for cold noble gases and ionized Xenon. 32
1.7 Diagram of a 1-D shock being driven by a rigid piston. 36
1.8 Ion and electron temperatures at the shock front. 37
1.9 A shock wave modelled as a discontinuity in density and temperature. 38
1.10 Evolution of an isothermal rarefaction and blast wave. 45
1.11 Diagram of a blast wave reflecting off a surface. 46
1.12 Diagram of a Mach stem forming between two shock waves. 46
1.13 1-D diagram of how temperature and mass density vary in a radiative shock. 49
1.14 Post-shock temperature as a function of shock velocity. 55
1.15 Post-shock temperature and ionization as a function of shock velocity. 59
1.16 Percentage of energy converted to radiation, ionization and heating. 60
1.17 The radiative shock experiment described in [Bozier et al., 1986]. 61
1.18 The radiative shock experiment described in [Keiter et al., 2002]. 62
1.19 The radiative shock experiment described in [Fleury et al., 2002]. 63
1.20 The radiative shock experiment described in [González et al., 2006]. 64
1.21 The radiative shock experiment described in [Koenig et al., 2006]. 65
1.22 The radiative shock experiment described in [Drake et al., 2011]. 66
1.23 The radiative shock experiment described in [Dizière et al., 2011]. 67
1.24 The radiative shock experiment described in [Falize et al., 2012]. 68
1.25 The radiative shock experiment described in [Singh et al., 2017]. 69
1.26 The conical wire array and radial foil experimental platforms. 70
1.27 Experimental setup used for converging radiative shock experiments. 73
1.28 Experimental data from converging shock experiments. 74
1.29 Self-emission streak images from experiments with different liner materials. . 75

2.1 Digram depicting experiments performed on the Orion laser facility. 79
2.2 Schematic of the Orion Laser Facility. 80
2.3 Schematic of the Orion beam lines 81
2.4 The Orion target chamber and position of beams and TIMs. 83
2.5 Details of the gas cell targets 86

2.6 Description of how the target pistons bulged under positive fill pressure. . . . 87
2.7 Gas cell piston expansion as a function of fill pressure. 88
2.8 The gas filling system used on the Orion facility. 89
2.9 Examples of how the drive beams were expected to overlap on the target pistons. 91
2.10 Total beam energy for each experiments performed on the Orion laser facility. 92
2.11 Schematic of laser driven ablation. 92
2.12 Schematic of diagnostics fielded on these experiments. 94
2.13 Emission spectrum from an Iron target after being exposed to a laser. 95
2.14 Simulated X-ray radiography images with different backlighter target materials. 98
2.15 X-ray backlighting setup used for these experiments. 99
2.16 XRBL image location with respect to the experimental hardware. 101
2.17 Description of how a streak camera operates. 103
2.18 Fringe pattern created by two interfering beams. 105
2.19 Schematic of a Mach-Zehnder laser interferometry setup. 107
2.20 Example interferometry image recorded with a GOI camera. 108
2.21 Steps involved in processing interferometry images to produce phase maps. . 109
2.22 Example streak interferometry image. 110
2.23 Diagram describing how Abel inverse transformations were performed numerically. 112
2.24 Test of the numerical Abel transform method. 113
2.25 Time sequence constructed from XRBL images from experiments with Neon gas-fills. 115
2.26 Position of the shock front as a function of time. 117
2.27 Shock velocity determined from self-emission streak image. 118
2.28 Self-emission streak images plotted against XRBL images 119
2.29 Shocks were wapproximated as semi-ellipsoids centred. 122
2.30 Shock front position as a function of time along radial lines. 123
2.32 Description of how X-rays propagate through the gas cell. 126
2.33 Calculated intensity plotted on top of profiles obtained from the XRBL images. 126
2.34 Self-emission streak images from experiments with a Neon gas-fill. 129
2.35 X-Ray transmission through the reverse shock region. 131
2.36 1-D diagram of the formation of a shock 132
2.37 Time sequence constructed from XRBL images from experiments with Xenon gas-fills. 134
2.38 Time sequence constructed from XRBL images from experiments with Xenon gas-fills. 135
2.39 Shock velocity measured from a self-emission streak images for a experiment with a Xenon gas-fill. 136
2.40 Profiles of X-ray normalized intensity through the shock front. a) Position of profiles. b) Profiles offset to the shocks frame. Calculated normalized intensities for different compressions are plotted on top. 137
2.41 GOI interferometry images from experiment #5286 with a Neon gas-fill at 0.59 bar. 140
2.42 Profiles of n_eL from GOI and streak interferometry diagnostics. 141
2.43 Radial variation of electron density in the radiative precursor. 142
2.44 Abel inversions of vertical profiles taken from the 2-D GOI map. 143

2.45 Evolution of the radiative precursor investigated with streak interferometry. . 145
2.46 Comparison between a self-emission streak image and interferometry streak map of n_eL from the same experiment. 146
2.47 GOI interferometry images of an experiment Xenon gas fill at 0.27 bar. . . . 150
2.48 Axial profiles from 2-D maps of integrated electron density shown in Fig 2.47.e-h. 151
2.49 Profiles were taken at 25° to the shock axis from maps of n_eL shown in Fig 2.47. a) Location of profiles. b) Profiles from all four GOI images shifted to intercept at $n_eL = 2 \times 10^{18}$ cm^{-3}. 151
2.50 Self-emission recorded from experiments with different gas species. 153
2.51 Maps of n_eL produced from interferometry streak images from experiments with different gas species by similar mass densities. 154
2.52 Horizontal profiles of n_eL taken at different times, location indicated with red dashed lines in Fig 2.51. 155
2.53 a) Vertical profiles of n_eL taken from the gas cell centre, location indicated with white dashed lines in Fig 2.51. b) Estimated radiative precursor widths as a function of atomic number. 155
2.54 Setup of 1-D HELIOS simulations. 156
2.55 Electron and ion densities and temperatures in the shock predicted by HELIOS. 157
2.56 Shock front position as a function of time in experiments and HELIOS simulations. 159
2.57 Output from HELIOS simulations of a Neon gas-fill. 160
2.58 Time sequence created from the output of NYM/PETRA simulations with a Xenon gas-fill. 163
2.59 XRBL images from experiments with a Xenon gas-fill compared against 2-D simulations. 164
2.60 Axial profiles of mass density and electron temperature from 2-D simulations. 166
2.61 Axial profiles of electron density and temperature offset to the reference frame of the shock. 167
2.62 Electron density profile from 2-D simulations of Xenon gas-fills. 167

3.1 Diagram of the MAGPIE pulsed power facility. 171
3.2 Circuit diagram of a bipolar Marx bank. 172
3.3 Cross section of one of the four MAGPIE line switches. 176
3.4 Cross section of the top of the MAGPIE VTL 177
3.5 3D diagram of the 'inverse liner z-pinch' experimental configuration. 180
3.6 Diagram showing the formation of the radiative shock. 181
3.7 Transmission in Argon as a function of photon energy. 182
3.8 Cutaway view of the liner. 182
3.9 Cutaway view of the 'inverse liner z-pinch' hardware. 183
3.10 CAD model and picture of the gas cell. 185
3.11 Diagram of the gas filling rig. 185
3.12 Pictures of liner clamping methods. 187
3.13 Circuit diagram of the liner and return post. 188
3.14 Toroidal magnetic field strength within the liner. 189
3.15 Description of assumptions used to derive Ohmic heating model. 197
3.16 Analytical solution for the magnetic field and current within the liner. 199

3.17 Diagnostic setup for experiments performed on the MAGPIE facility. 200
3.18 Location of the Rogowski MITL bdot probes. 202
3.19 Cutaway of the Rogowski probes used on the MAGPIE facility 202
3.20 Example results from Rogowski probes. 204
3.21 Example results from MITL current probes. 205
3.22 Time derivative of the current plotted against the voltage on the MITL probe. 206
3.23 The high precision counter-wound magnetic induction probes. 209
3.24 The bipolar magnetic induction probes. 209
3.25 Example optical self-emission images. 210
3.26 Preshot images of an M2 bolt in the focal plane of the multiframe camera. . 211
3.27 Example of the automated fringe tracing algorithm. 214
3.28 Locations of collection volumes for optical spectroscopy 216
3.29 Shape of the optical spectroscopy collection volumes. 216
3.30 Optical self-emission images from experiment s0623_16. 217
3.31 Optical self-emission images from experiment s01212_17 219
3.32 Horizontal profiles of self-emission intensity from experiment s1212_16. . . . 221
3.33 Shock front positions plotted as a function of time. 222
3.34 Shock front position as a function of pixels averaged over in analysis. 222
3.35 Shock velocity and launch time plotted against peak current. 225
3.36 Magnetic pressure experienced by the liner for nine similar experiments. . . . 226
3.37 Action integral for nine experiments with similar initial mass densities. . . . 227
3.38 Signals from bipolar magnetic induction and Rogowski current probes. . . . 229
3.39 Comparison between snow-plough models and measured shock trajectories. . 231
3.40 Interferometry image from experiment s1212_16 233
3.41 Horizontal profiles of integrated electron density at several heights. 234
3.42 Inverse Abel transformation showing electron density as a function of radius. 235
3.43 Comparison between electron density and optical self-emission intensity. . . . 236
3.44 Spectra recorded from experiment s0623_16. 238
3.45 Spectra calculated for a PrismSPECT simulation of an Argon plasma. 240
3.46 Ionization and temperature as a function of radius in the precursor region. . 243
3.47 Peak electron density and radiative precursor width plotted against time after current start. 246
3.48 Peak electron density and radiative precursor width plotted against peak MAGPIE current. 247
3.49 Multiframe camera images from, experiment s1212_16, showing the edge shocks. 248
3.50 Edge shock position as a function of time. 248
3.51 Horizontal profile through the edge shock from a self-emission image. 249
3.52 Interferometry image of the edge shock. 250
3.53 Profiles through the primary and edge shock. 251
3.54 Self-emission images from experiments with Neon, Argon, Krypton and Xenon gas-fills. 254
3.55 Interferometry images from experiments with Neon, Argon, Krypton and Xenon gas-fills. 256
3.56 Electron density and ionization from experiments with Neon, Argon, Krypton and Xenon gas-fills. 257

3.57 Radiative precursor width plotted against gas-fill atomic mass. 257

4.1 Comparison of ionization measured in this work and previous converging shock experiments. 265
4.2 XRBL images shown with 2-D simulation predicted densities. 266
4.3 Self-emission image showing electrical breakdown at the top of the liner. . . 267
4.4 Magnetic probe signals from an experiment with a metal and plastic gas cell lid. 268
4.5 Process to create perturbed shocks on the inverse liner Z-pinch platform. . . 269
4.6 Details of grooves cut onto the inside surface of the liner. 270
4.7 Optical self-emission images from a perturbed shock experiment. 271
4.8 Position of the shock front of the perturbed shock as a function of time. . . . 272
4.9 Picture of two liners before and after an experiment. 273
4.10 Interferometry images and profiles of modulated shocks. 273
4.11 Description of the Vishniac overstability in a blast wave. 275

List of Tables

1 Constants used in this Thesis. 13

1.1 First ionization energies for different noble gases, determined from [Kramida et al., 2015]. 26

2.1 Average laser power for experiments on the Orion facility with fours beams per piston. Calculated from 29 experiments. 90
2.2 Critical electron density beyond which the plasma is opaque to a laser. . . . 93
2.3 The four possible levels and their quantum numbers for the helium-like $1s2p$. The energy of a transition to the $1s^2$ state for an Iron ion is also shown. Energies from the NIST database [Kramida et al., 2015]. 96
2.4 He_α lines from various transition metals. All energies expressed in electron volts. Energies from the NIST database [Kramida et al., 2015]. 96
2.5 X-ray backlighter material choices for different gas-fills and pressures used in these experiments. 97
2.6 Electron density per fringe shift (phase change of 2π) for several common wavelengths. 107
2.7 Comparison of key parameters between experimental series performed with Neon and Xenon gas-fills. 138
2.8 Fill pressure required to reach a mass density of $\rho_0 \sim 0.5$ mg/cm^3 for different noble gases. 152
2.9 Comparison of key parameters between experiments and HELIOS 1-D simulations with different laser powers. 159
2.10 Comparison of key parameters between experiments and NYM/PETRA 2-D simulations. 168

3.1 Comparison between these experiments on radially expanding shocks and previous work. 187
3.2 Current parameters determined for experiment s1212_16. 207
3.3 Fill pressure required to reach a mass density of $\rho \sim 0.04$ mg/cm^3. 253

4.1 Comparison of shock parameters measured in these experiments and previous work. 263

List of Constants

A list of commonly used physical constants is presented in Table 1 using the International System of Units (SI).

k_B	1.3806×10^{-23} $\mathrm{m^2.kg.s^{-2}.K^{-1}}$	Boltzmann constant
ϵ_0	8.8542×10^{-12} $\mathrm{F.m^{-1}}$	Vacuum permittivity
μ_0	$4\pi \times 10^{-7}$ $\mathrm{H.m^{-1}}$	Vacuum permeability
m_p	1.6726×10^{-27} kg	Proton mass
m_e	9.1094×10^{-31} kg	Electron mass
c	2.9979×10^{8} $\mathrm{m.s^{-1}}$	Speed of light in a vacuum
q/e	1.6022×10^{-19} C	Elementary charge
h	6.626×10^{-34} J.s	Planck constant
σ_{SB}	5.6704×10^{-8} $\mathrm{W.m^{-2}.K^{-4}}$	Stefan-Boltzmann constant
b	2.8978×10^{-3} m.K	Wien displacement constant

Table 1: Constants used in this Thesis.

Although SI units are used for the majority of this Thesis, centimetres are frequently used for lengths and electron volts for temperature. Converting between electron volts and Kelvin can be achieved using:

$$T[eV] = \frac{k_B}{e} T[K] \tag{1}$$

Chapter 1

Introduction

1.1 Overview of Thesis

This Thesis details two novel experimental configurations used to produce radiative shocks in low density gas-fills. In both experiments multiple diagnostics are fielded, allowing both the post-shock material and radiative precursor to be studied. This experimental data is relevant for both inertial confinement fusion and astrophysical research, helps to characterise radiative shocks in Neon, Argon, Krypton and Xenon and allows for benchmarking of numerical simulations.

Chapter 1 describes plasmas and conditions in these experiments, the formation and evolution of shock waves and introduces the concept of a radiative shock. In addition, a review of similar experiments in the literature is provided.

Experiments described in Chapter 2 detail an experimental configuration which uses high powered lasers to drive counter-propagating radiative shocks. This work modifies previous experimental setups, which use lasers to drive planar quasi-one-dimensional radiative shocks in low density Xenon gas fills. A larger gas cell is utilized, which allows for the unimpeded three dimensional evolution of the shocks over $\sim$2 mm and $\sim$30 ns. In addition, a second (counter-propagating) shock is introduced, allowing the interaction of radiative shocks and

formation of reverse shocks to be studied. To achieve this, the Orion high powered laser facility, at AWE Aldermaston UK, was used to ablate plastic foils on either side of the gas cell and drive shocks, with a velocity of ∼60 km/s, into Neon, Krypton, Argon or Xenon gas-fills with an initial mass density of $0.5 - 1.6$ mg/cm^3. X-ray backlighting and optical self-emission streak imaging were employed to study the shock hydrodynamics while multi-frame and streak imaging interferometry were simultaneously used to study the radiative precursor. Hydrodynamics observed in these experiments show qualitative agreement with 1-D and 2-D simulations. However, simulations overestimate the size of the radiative precursor. This experimental platform opens the prospect of future work to study instabilities in the post-shock material and the 3-D evolution of radiative and reverse shocks.

Experiments described in Chapter 3 detail the 'inverse liner z-pinch' experimental configuration for producing a cylindrically expanding radiative shock. This configuration was demonstrated on the MAGPIE generator at Imperial College London, UK. This work modifies previous experiments which passed a current pulse through a gas filled, thin-walled, metal tube to drive cylindrically converging radiative shocks. In this new experimental configuration current is discharged through a thin-walled metal tube (a liner) embedded in a gas-fill (Neon, Argon, Krypon or Xenon with an initial mass density of 0.04 mg/cm^3) and returned through a central post. This resulted in cylindrically expanding radiative shock being launched into the gas-fill, propagating at ∼10 km/s. This experimental platform provides improved diagnostic access compared to previous experiments and allows shocks to propagate unimpeded for several centimetres and several microseconds. A combination of multi-frame optical self-emission imaging, laser interferometry and optical emission spectroscopy were employed to study both the shock hydrodynamics and the radiative precursor. This experimental platform opens the prospect of future work to study radiative shocks with controllable perturbations, by introducing well characterised grooves on the inside surface of the liner, and the study of magnetized radiative shocks.

Finally, Chapter 4 summarises the results from these experiments and compares them

against similar experiments performed in the literature. Future experiments to investigate remaining questions or extend these new experimental platforms are then proposed.

1.2 Background and motivation

Shocks are ubiquitous in astrophysics and high energy density physics (HEDP). They are observed as enormous bow-shocks created as starts are born [Reipurth et al., 1997, Hartigan, 2005] and as spectacular Supernoave remnants as stars die [Remington et al., 2006], examples of both of these are shown in Fig 1.1. However, astrophysical shocks exist in a very different parameter regime to those usually encountered on Earth, for example in supersonic aviation. Material travels at many hundreds of kilometres per second and is heated to thousands of degrees, becoming a plasma. Under such conditions, radiation emitted by hot post-shock material plays a significant role and can drastically change the structure of the shock. This modified shock is commonly referred to as a radiative shock. Despite their prevalence, radiative shocks are among the least well understood objects observed in astrophysics as the combination of shock hydrodynamics and radiation transport makes them very challenging to model. A better understanding of these dynamic events will allow for an improved understanding of many astrophysical systems.

Recent advances in high powered lasers and pulsed power generators make it now possible to reproduce similar conditions to those found in astrophysical phenomena in the laboratory. With these facilities energy can be compressed both temporally (to $\sim$ns) and spatially (to $\sim$mm) allowing velocities of $\sim$100 km/s and temperatures of $\sim$10 eV ($\sim$120000 K) to be achieved. This has resulted in a new field of study, known as laboratory astrophysics, which aims to create models of astrophysical objects on scale lengths and time scales many orders of magnitude smaller than those found in astrophysics ($\sim 10^{-3}$ m and $\sim 10^{-6}$ s as opposed to $\sim 10^{16}$ m and $\sim 10^{9}$ s for astrophysical events). These can then be compared to astrophysical objects through use of hydrodynamic scaling, such as Euler scaling [Ryutov

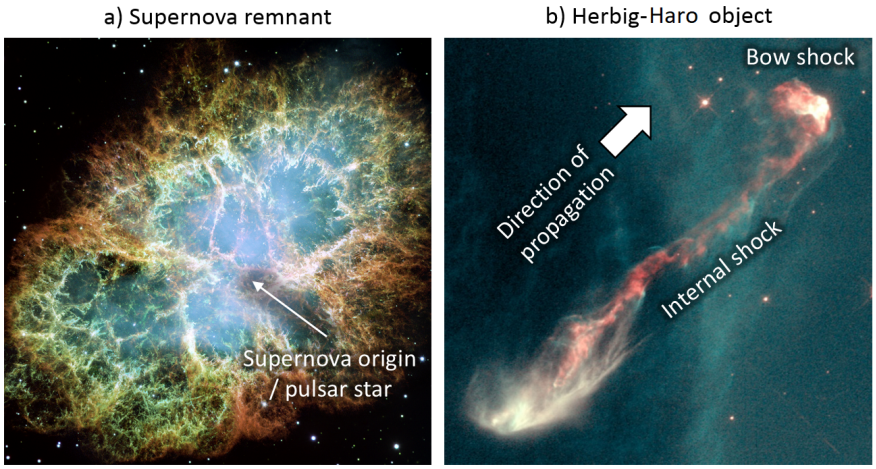


Figure 1.1: a) False colour image of the Crab Nebula, constructed from images taken by the Hubble telescope in 1999 and 2000 [NASA and ESA, 2005]. b) False colour image of the Herbig-Haro object HH47, taken with the Hubble Space Telescope in 1999 [J. Morse/STScI and ESA, 1995].

et al., 1999]. Laboratory astrophysics has already made significant contributions to our understanding of shocks in space [Hartigan, 2005] and is able to provide parameters such as spectral lines, excitation rates, recombination rates, opacity, temperature and pressure. Laboratory astrophysics allows experiments to be probed with local measurements, from multiple angles and across their entire evolution. In addition, by controlling initial conditions, the physics driving the systems may be better understood (e.g. by changing the gas species in order to understand the role of radiation transport).

These advances in high powered lasers have also enabled new methods of achieving conditions required for nuclear fusion, known as Inertial Confinement Fusion (ICF). This aims to achieve nuclear fusion by heating and compressing a fuel (a $50:50$ mixture of Deuterium Tritium) until ignition is achieved, whereby the energy released in fusion reactions results in a chain reaction which burns the remaining fuel. To achieve ignition, temperatures of $T_{ig} \sim 4$ keV are required and so an understanding of material at these extreme conditions is necessary. The most energetic laser facility at present, the National Ignition Facility (NIF) in the USA, uses 192 laser beams, with a total energy of 1.8 MJ, to irradiate the inside surface of a cylindrical gold tube known as a hohlraum, containing a small spherical fuel capsule,

as shown in Fig 1.2.a. X-rays produced by the hohlraum-laser interaction are absorption by the plastic outer layer of the fuel capsule resulting in a rapid expansion that causes the fuel mixture to compress, increasing in temperature and density until it reaches ignition conditions.

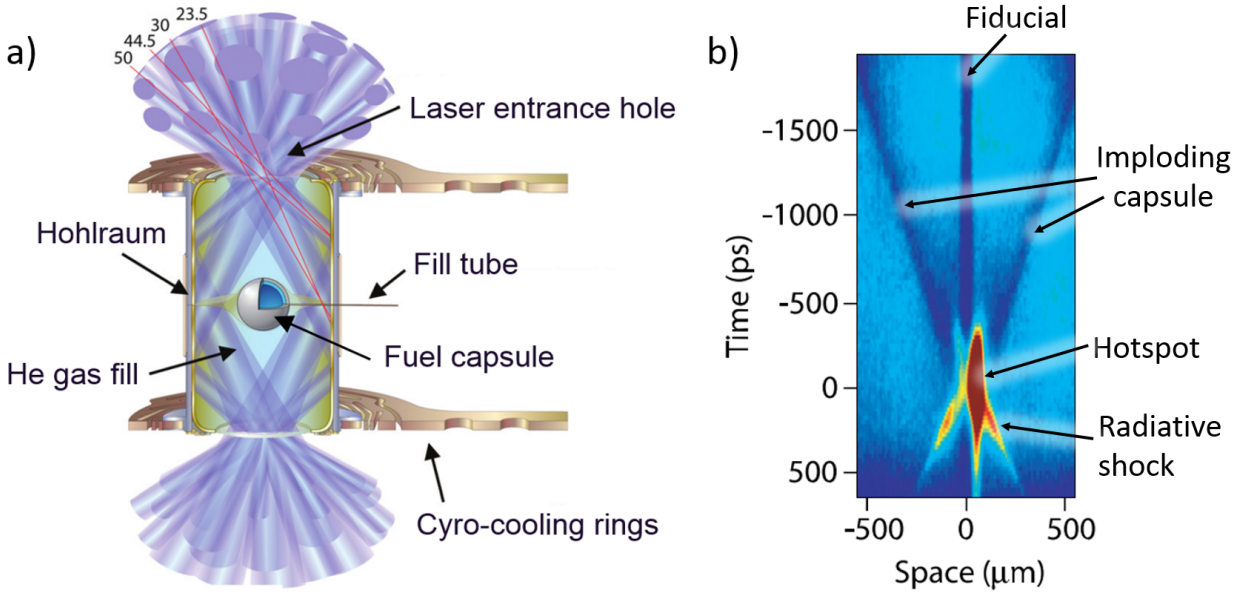


Figure 1.2: a) Indirect drive ICF setup showing a gold hohlraum surrounding the fuel capsule, reproduced from [Edwards et al., 2011]. b) Streaked X-ray emission image of a capsule implosion showing the formation of radiative shocks, reproduced from [Pak et al., 2013].

Experiments have not yet achieved ignition and so the HEDP community is attempting to better understand the conditions in such experiments. Streaked X-ray emission imaging has indicated the formation of radiative shocks, propagating at ∼350 km/s, ∼150 ps after peak compression [Pak et al., 2013]. As experiments take place within an optically opaque fuel capsule, experiments to understand these radiative shocks must be conducted on other facilities with improved diagnostic access.

1.3 Author's contribution

This Thesis details two novel experimental configurations used to produce radiative shocks in low density gas-fills. The author has played a key role in these experiments and analysing the

resulting data. This has yielded several publications and numerous presentations at internal conferences. In addition, the author has developed a numerical model for estimating the post-shock conditions in a radiative shock, presented in Section 1.6.4.

Experiments on the Orion laser facility

Experiments performed on the Orion laser facility, described in Chapter 2, were led by Francisco Suzuki-Vidal who acted as principal investigator (PI). Targets were manufactured by Chris Spindole [Spindloe et al., 2017] and operation of the Orion laser facility was performed by AWE staff. The author participated in all three weeks of the experimental campaign and was primarily responsible for preparing targets, recording data from X-ray backlighting diagnostics and assisting the PI in planning the shot schedule. After the campaign the author took a key role in analysing the experimental data, resulting in the following publications:

- **T. Clayson**, F. Suzuki-Vidal, S. V. Lebedev, G. F. Swadling, C. Stehl, G. C. Burdiak, J.M. Foster, J. Skidmore, P. Graham, E. Gumbrell, S. Patankar, C. Spindloe, U. Chaulagain, M. Kozlova J. Larour, R.L. Singh, R. Rodriguez, J. M. Gil, G. Espinosa, P. Velarde, C. Danson *'Counter-propagating radiative shock experiments on the Orion laser and the formation of radiative precursors'* High Energy Density Physics 23, 60-72 (2017)

- F. Suzuki-Vidal, **T. Clayson**, C. Stehl, G. F. Swadling, J.M. Foster, J. Skidmore, P. Graham, G. C. Burdiak, S. V. Lebedev, U. Chaulagain, R. L. Singh, E.T. Gumbrell, S. Patankar, C. Spindloe, J. Larour, M. Kozlova, R. Rodriguez, J. M. Gil, G. Espinosa, P. Velarde, C. Danson *'Counter-propagating radiative shock experiments on the Orion laser'* Physics Review Letters 119, 055001 (2017)

- C. Spindloe, D. Wyatt, S. Astbury, G. F. Swadling, **T. Clayson**, C. Stehl, J. M. Foster, E. Gumbrell, R. Charles, C. N. Danson, P. Brummitt, F. Suzuki-Vidal *'Design and fabrication of gas cell targets for laboratory astrophysics experiments on the Orion*

high-power laser facility' accepted for publication in High Power Laser Science and Engineering (2017)

In addition, this work has been presented by the author at numerous international conferences including:

- 6th International Conference on High Energy Density Physics 2017 in Shirahama, Japan (Oral presentation)
- 58th Annual Meeting of the APS Division of Plasma Physics 2016 in San Jose, USA (Oral presentation)
- Christmas Meeting of the High Powered Lasers Community 2016 in Abingdon, UK (Oral presentation)
- 11th Conference on High Energy Density Laboratory Astrophysics 2016 in Palo Alto, USA (Oral and poster presentation)
- Christmas Meeting of the High Powered Lasers Community 2015/2016 in Abingdon, UK (Poster presentation)

In addition, the author has been directly involved in planning future experiments which hope to be performed on the Sheng-Guan II laser facility at the Shanghai Institute of Optics and Fine Mechanics (SIOM). As part of this preparation, the author visited SIOM to discuss experiments and gave an invited seminar on the experiments performed on the Orion laser facility.

Experiments on the MAGPIE pulsed power facility

Experiments performed on the MAGPIE pulsed power facility, described in Chapter 3, were designed and led by the author with assistance from the MAGPIE team. Sergey Lebedev and Guy Burdiak assisted in designing the experimental configuration and the gas cell was

designed by John Skidmore [Skidmore, 2013]. The author was responsible for the analysis of all of the experimental data, resulting in a first author publication being submitted to the seventh Special Issue of IEEE Nuclear and Plasma Sciences Society and presentations at numerous conferences including:

- Stewardship Science Academic Programs Symposium 2018 in Washington DC, USA (Poster presentation)
- Matter in Extreme Conditions Winter School 2017 in Montgenèvre, France (Poster presentation)
- 10th International Conference on Dense Z-pinches 2017 in Lake Tahoe, USA (Oral presentation)
- 6th International Conference on High Energy Density Physics 2017 in Shirahama, Japan (Poster presentation)

The MAGPIE pulsed power facility is staffed by a team of post-graduate students and post-doctoral researchers, including the author. This team all participate in the maintenance and repair of the MAGPIE generator and assist in the majority of experiments. Therefore the author has also participated in a variety of experiments that have led to numerous publications in Physical Review Letters [Suttle et al., 2016, Hare et al., 2017b, Hare et al., 2018] and Physics of Plasma [Swadling et al., 2016, Burdiak et al., 2017, Hare et al., 2017a].

Experiments on the PALS facility

Although not summarised in this Thesis, the author also participated in experiments to produce counter-propagating radiative shocks on the Prague Asterix Laser System (PALS) facility, led by Chantal Stehle. The author participated in three out of five weeks of the experimental campaign. Analysis of the experimental data was primarily performed by Raj Singh, resulting in a publication in High Energy Density Physics [Singh et al., 2017].

1.4 Plasma physics

Plasma is the most abundant state of matter in the universe, forming the majority of stars, the interstellar medium and the intergalactic medium. Despite this, plasmas do not exist in a stable state on Earth and so must be artificially produced by heating matter to extreme temperatures, or by ionizing material with strong electric fields. This results in a quasi-neutral ionized gas comprised of electrons and ions that exhibit collective behaviour, by responding to and generating electric and magnetic fields. Plasmas cover a large range of conditions, from the low density and temperature of the interstellar medium (with temperatures $T \sim 1$ eV and particle densities of $n \sim 1$ cm^{-3}) to the high density and temperature of the solar core (with temperatures $T \sim 1000$ eV and particle densities of $n \sim 10^{26}$ cm^{-3}), as indicated in Fig 1.3.

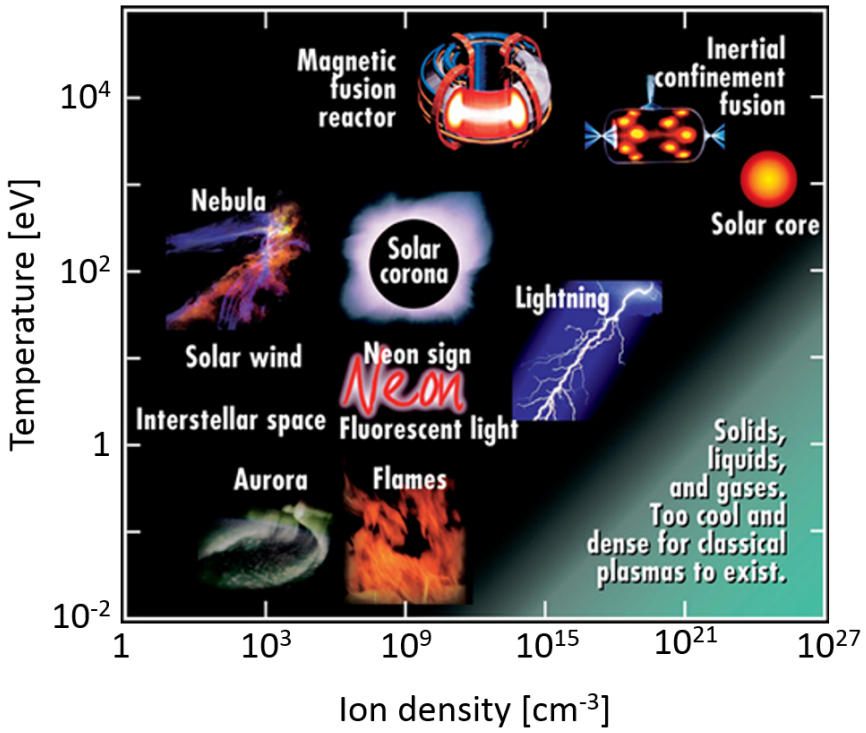


Figure 1.3: Approximate conditions of different types of plasmas found throughout the universe. Reproduced from [LLNL, 2010].

In this Thesis Neon, Argon, Krypton and Xenon plasmas are produced in the laboratory

with high powered lasers and pulsed power machines, achieving temperatures of $T \sim 1 - 100$ eV and particle densities of $n \sim 10^{17} - 10^{21}$ cm^{-3}. In this regime plasmas are partially ionized, with an average ionization of $Z < 5$, act quasi-neutrally and collisionally (with Debye lengths and particle mean free paths below the spatial scale lengths of the experiment) and quickly reach thermal equilibrium (with collision times below the temporal scale of the experiment).

1.4.1 Ionization

Plasmas reported in this Thesis exist as a mixture of free electrons and partially ionized ions. Collisions between particles in a hot plasma can result in ionization, a process known as collisional ionization [Drake, 2006]. Similarly, collisions between ions and electrons can result in recombination, a process known as collisional recombination. Both of these processes increase as the temperature of the plasma increases. If in thermal equilibrium, the effects of collisional ionization and collisional recombination are equal and the relative population of different ionization states is given by the Saha equation:

$$\frac{N_{\alpha+1}}{N_\alpha} n_e = \frac{2}{\lambda_B^3} \frac{g_{\alpha+1}}{g_\alpha} \left(\frac{k_B T}{\pi E_H} \right)^{3/2} exp \left[- \frac{\epsilon_{\alpha+1} - \epsilon_\alpha}{k_B T} \right] \tag{1.1}$$

where N_α is the density and g_α is the degeneracy of states of ions with an ionization of α. ϵ_α is the energy required to remove α electrons from a neutral atom, n_e is the electron density, k_B is the Boltzmann constant and T is the temperature. The thermal de Broglie wavelength, λ_B, of an electron is given by:

$$\lambda_B = \sqrt{\frac{h^2}{2\pi m_e k_B T}} \tag{1.2}$$

where m_e is the mass of the electron and h is the Planck constant. The energy required to remove α electrons may be approximated using the hydrogenic atom model so that:

$$\epsilon_{\alpha+1} - \epsilon_\alpha \approx (\alpha + 1)^2 E_H \tag{1.3}$$

where $E_H = 13.6$ eV is the energy required to ionize a Hydrogen atom. The average ionization, Z, may be estimated by assuming the ratio $N_Z/N_{Z-1} \approx 1$. Therefore, assuming the degeneracy ratio, $g_{\alpha+1}/g_\alpha \approx 1$, Eq. 1.1 may then be re-arranged to give:

$$Z^2 = \frac{k_B T}{2E_H} ln\left(\frac{2}{\lambda^3 n_e}\right) \tag{1.4}$$

This may then be approximated as:

$$Z \approx 20\sqrt{T_{keV}} \tag{1.5}$$

where T_{keV} is the temperature in keV. Thus for plasmas observed in this Thesis, where $T < 50$ eV, an average ionization $Z < 5$ is expected.

In reality, ionization is a complex function that is also dependant on the atomic species and plasma density. To more accurately determine how ionization varies with temperature, the atomic physics code PrismSPECT [MacFarlane et al., 2006] was used to simulate the expected ionization for a variety of plasma temperatures and densities.

PrismSPECT simulations were run for Neon, Argon, Krypton and Xenon plasmas with Detailed Configuration Accounting (DCA), which includes the fine splitting structure, and the Low Temperature Spectroscopy model, which only considers ionization energies < 100 eV. Fig 1.4 shows the resulting plots of average ionization as a function of temperature for several different mass densities. Higher temperatures result in a higher average ionization but increasing the mass density slightly decreases the average ionization. In addition the approximate ionization, calculated with Eq. 1.5, is shown with a dashed line. This approximation crudely follows the PrismSPECT ionizations for low atomic number materials, such as Neon, but significantly underestimates the ionization for higher atomic numbers such as Krypton and Xenon.

The absorption of high energy photons can also result in ionization, through a process known as photo-ionization. If a photon, with energy that exceeds the electron binding energy,

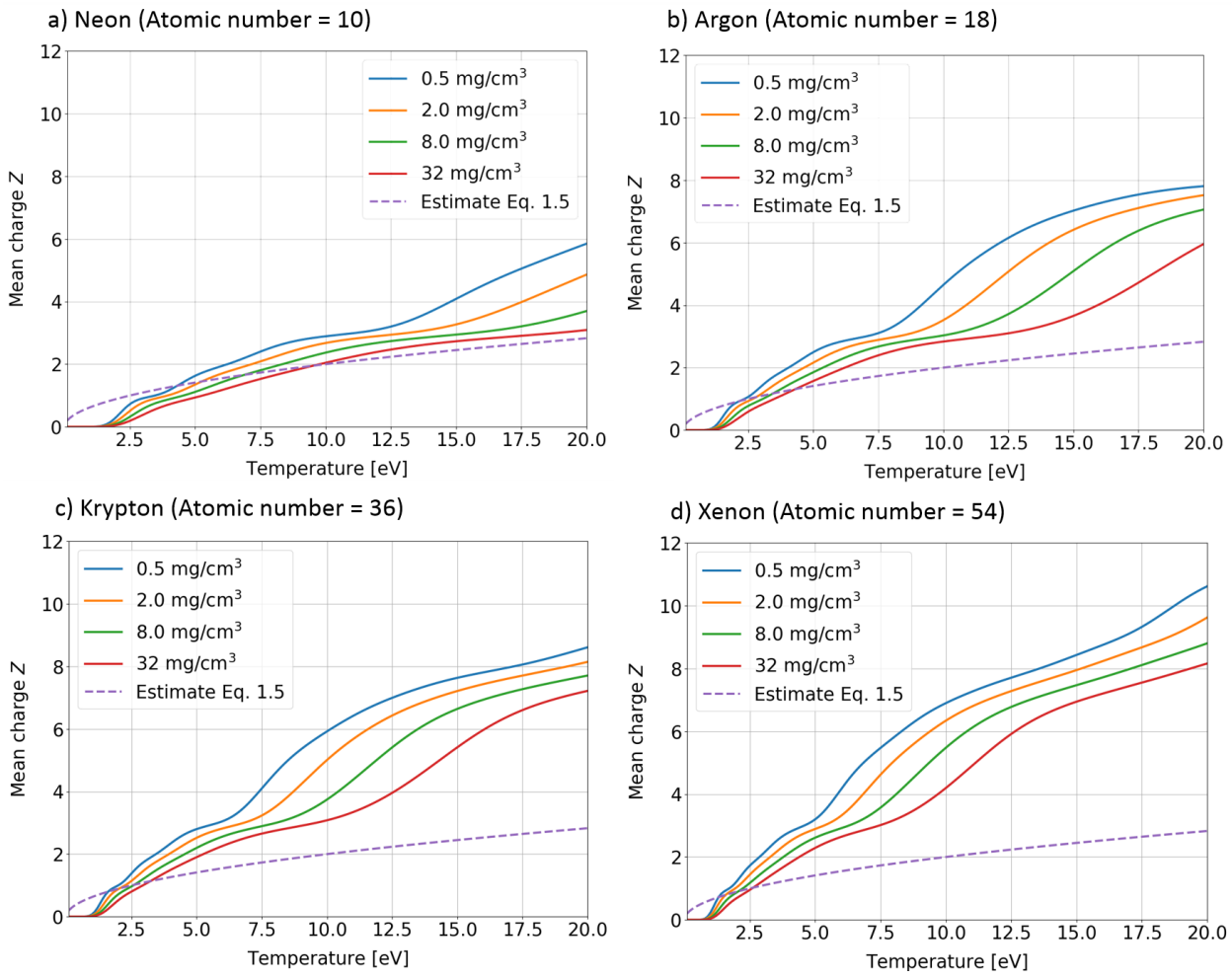


Figure 1.4: Output from PrismSPECT simulations showing ionization as a function of temperature for different gases: a) Neon, b) Argon, c) Krypton and d) Xenon. The dashed line is the approximate ionization calculated with Eq. 1.5

is absorbed by a bound electron it is able to liberate this electron, and the remaining energy is converted to kinetic energy of the electron. Helium has the highest binding energy of any neutral atom with the nuclear charge of heavier atoms being shielded by inner shell electrons. This makes ionization of heavier atoms more likely to occur. The binding energy also increases with the charge of the ion as the electron is further attracted to the nucleus. In this Thesis, ionization energies were taken from tabulated values available on the NIST Atomic Spectra Database [Kramida et al., 2015]. The binding / ionization energy for different noble gases used in this Thesis is plotted as a function of ionization stage in Fig 1.5 and the first ionization energies are listed in Table 1.1.

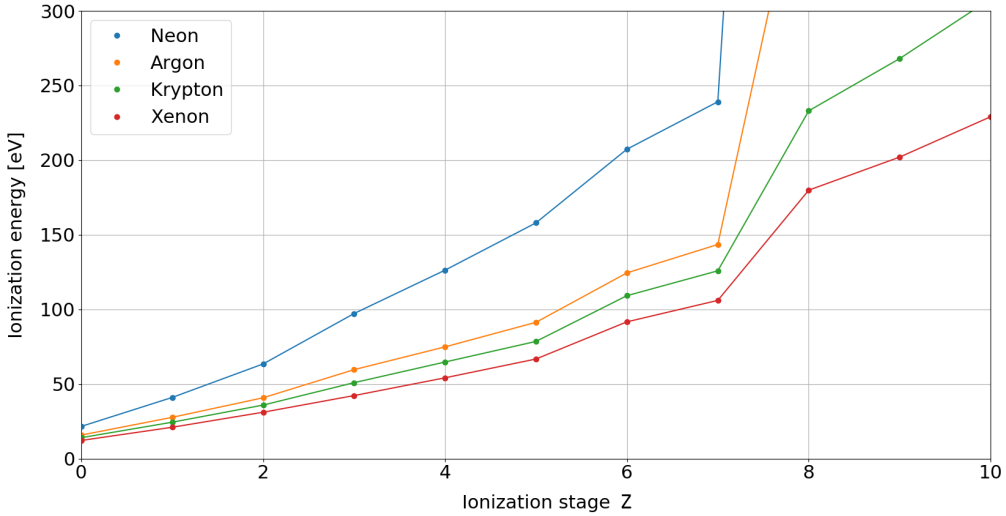


Figure 1.5: Ionization energies for different noble gases, determined from [Kramida et al., 2015].

Element	**First ionization [eV]**
Neon ($Z = 10$)	21.56
Argon ($Z = 18$)	15.76
Krypton ($Z = 36$)	14.00
Xenon ($Z = 54$)	12.13

Table 1.1: First ionization energies for different noble gases, determined from [Kramida et al., 2015].

1.4.2 Quasi-neutrality

Despite being charged, plasmas are typically assumed to be quasi-neutral [Drake, 2006]. The characteristic length of this shielding is known as the Debye length or Debye radius, λ_D, and in centimetre-gram-second (CGS) units is given by:

$$\lambda_D = \left[\frac{4\pi e^2}{k_B} \left(\frac{n_e}{T_e} + \sum_\alpha \frac{n_\alpha Z_\alpha}{T_\alpha} \right) \right]^{-1/2} \tag{1.6}$$

where e is the elementary charge and k_B is the Boltzmann constant. This is a sum with contributions from the electrons, with density n_e and temperature T_e, and each ion species α

with a density n_α, temperature T_α and ionization of Z_α. On fast time scales the ion species are unable to move and $\sum_\alpha n_\alpha Z_\alpha / T_\alpha \to 0$. Therefore Eq. 1.6 simplifies to:

$$\lambda_D = \sqrt{\frac{k_B T}{4\pi n_e e^2}} \tag{1.7}$$

However, this is not the case with experiments in this thesis which evolve on time-scales of hundreds of nanoseconds. Instead these experiments produce highly collisional plasmas with a single temperature, T. Therefore, Eq. 1.6 may be simplified to:

$$\lambda_D = \sqrt{\frac{k_B T}{4\pi n_e (1 + Z_{eff}) e^2}} \tag{1.8}$$

where Z_{eff} is the effective charge given by:

$$Z_{eff} = \frac{1}{n_e} \sum_\alpha n_\alpha Z_\alpha^2 \tag{1.9}$$

In SI units this is given as:

$$\lambda_D = \sqrt{\frac{\epsilon_0 k_B T}{n_e (1 + Z_{eff}) e^2}} \tag{1.10}$$

where ϵ_0 is the vacuum permittivity. The effective charge, Z_{eff}, may be approximated as the average ionization, Z. For plasma conditions encountered in this Thesis, with $n_e = 10^{17} - 10^{21}$ cm^{-3}, $T < 10^6$ K ($T < 100$ eV) and $Z < 5$, Debye lengths of $\lambda_D < 100$ nm are expected. This is far below the experimental scale, $\sim$mm, and thus these plasmas are expected to act quasi-neutrally.

The Coulomb logarithm, Λ, is a factor that frequently appears in plasma physics and helps to take account of electrostatic shielding effects in a plasma [Drake, 2006]. There are several definitions of the Coulomb logarithm in the literature, however this thesis adopts the approximation that it is the logarithium of the number of particles in the Debye sphere, i.e. a sphere with a radius of the Debye length. The Coulomb logarithm is therefore given as:

$$\Lambda \approx ln\left[n_e 4\pi\lambda_D^3\right] \tag{1.11}$$

Using Eq. 1.10 this may be written in SI units as:

$$\Lambda \approx ln\left[n_e 4\pi\left(\frac{\epsilon_0 k_B T}{n_e(1+Z_{eff})e^2}\right)^{3/2}\right] \tag{1.12}$$

For plasma conditions encountered in this Thesis the Coulomb logarithm is expected to be $\Lambda = 1-2$. This implies that the plasma is strongly coupled and collisions between particles are primarily binary in nature and frequently result in large angle deflections.

1.4.3 Mean free path

The mean free path of a particle, λ, is the average distance a particle travels before a collision. It is estimated as the collision time, τ, multiplied by the average particle velocity, estimated to be the thermal velocity, v_{th}. This is the velocity which yields a kinetic energy equal to the internal energy per particle and is given by:

$$\frac{3}{2}k_B T = \frac{1}{2}m v_{th}^2 \tag{1.13}$$

where k_B is Boltzmann's constant, T is the temperature and m is the particle mass. Note that the factor of 3/2 is sometimes omitted in the literature. This yields an electron/ion thermal velocity of:

$$v_{th(e/i)} = \sqrt{\frac{3T_{e/i}k_B}{m_{e/i}}} \tag{1.14}$$

The collision time, the average time between collisions, may be given for electrons and ions, τ_e and τ_i, as [Ryutov, 2015]:

$$\tau_e = \frac{3}{4\Lambda Z^2 e^4 n_i}\sqrt{\frac{m_e}{2\pi}}\,(T_e)^{3/2} \tag{1.15}$$

$$\tau_i = \frac{3}{4\Lambda Z^4 e^4 n_i}\sqrt{\frac{Am_p}{2\pi}}\left(T_i\right)^{3/2} \tag{1.16}$$

where m_e is the electron mass, T_e is the electron temperature, Z is the average charge per ion, e is the elementary charge, m_e is the electron mass, m_p is the proton mass, A is the atomic mass number, n_i is the ion density and Λ is the Coulomb logarithm. This yields electron and ion mean free path lengths, λ_e and λ_i, of:

$$\lambda_e = v_{th(e)}\tau_e = 2 \times 10^{19}\frac{\left[T_e(keV)\right]^2}{\Lambda Z n_e(cm^{-3})} \tag{1.17}$$

$$\lambda_i = v_{th(i)}\tau_i = 2 \times 10^{19}\frac{\left[T_i(keV)\right]^2}{\Lambda Z^3 n_e(cm^{-3})} \tag{1.18}$$

where $T_e, i(keV)$ are the electron and ion temperatures in keV, and Z is the average ionization, Λ is the Coulomb logarithm and $n_e(cm^{-3})$ is the electron density in cm^{-3}. For plasmas observed in this Thesis, electron and ion mean free paths $\lambda_{e/i} < 1$ μm are expected. This is far below the experimental scale and thus plasmas are expected to act collisionally and quickly reach thermal equilibrium.

1.4.4 Emissivity and opacity in a plasma

Emission from hot objects, such as plasmas, is frequently approximated to be a black-body. In this idealized system the body is in thermodynamic equilibrium and all emitted radiation is determined entirely by its temperature, T. Planck's law states that the total radiative power emitted, $F(\nu, T)$, per area of the black-body, per unit frequency, ν, is given as:

$$F(\nu, T) = \frac{2h\nu^3}{c^2}\left[exp\left(\frac{\nu h}{k_b T}\right) - 1\right]^{-1} \tag{1.19}$$

where h is the Planck constant, c is the speed of light and k_B is the Boltzmann constant. This spectrum peaks at a frequency/wavelength, $\nu_{max}(T)/\lambda_{max}(T)$ given by Wien's

displacement law:

$$\nu_{max}(T) = \frac{T}{2\pi cb} \qquad (1.20) \qquad\qquad \lambda_{max}(T) = \frac{b}{T} \qquad (1.21)$$

where b is the Wien displacement constant. The total power irradiated by the black-body may be found by integrating the radiative power emitted, $F(\nu, T)$, over all frequencies, which yields the Stefan-Boltzmann law:

$$\int_0^\infty F(\nu, T)d\nu = \sigma_{SB}T^4 \qquad (1.22)$$

where σ_{SB} is the Stefan-Boltzmann constant. The black-body approximation represents the maximum radiative power emitted for an opaque object in thermal equilibrium. The emissivity of an object, $\epsilon(\nu)$ is defined as the emitted radiative power divided by that of a black-body and takes a value of $0 - 1$ (so a black-body has $\epsilon(\nu) = 1$ at all frequencies). The emissivity of a body is equal to the opacity of the object, $\kappa(\nu)$, a measure of how radiation is absorbed by the material. Therefore a black-body is perfectly opaque with $\kappa(\nu) = 1$.

However for semi-transparent materials, such as plasmas, light of intensity $I(\nu)$, propagating a distance dl in a medium will be modified by:

$$dI = F(\nu, T)\epsilon(\nu)dl - \kappa(\nu)I(\nu)dl \qquad (1.23)$$

where $F(\nu, T)\epsilon(\nu)dl$ represents emission of radiation and $\kappa(\nu)Idl$ represents absorption of radiation. Given sufficient time the temperature of this system will increase or decrease, until $F(\nu, T) = I$, and the system will satisfy Kirchoff's law (that emission and absorption occur at the same rate), thus achieving thermodynamic equilibrium. Assuming a uniform, cold medium, so that $F(\nu, T) \approx 0$, and integrating over a length x yields the Beer-Lambert law:

$$I(\nu) = I_0(\nu)e^{-\kappa(\nu)x} = I_0(\nu)e^{-\sigma(\nu)\rho x} \qquad (1.24)$$

where $I_0(\nu)$ is the initial intensity, $\sigma(\nu)$ is the mass attenuation cross section and ρ is

the mass density. This may also be expressed in terms of the optical depth, $\tau(\nu) = \sigma(\nu)\rho x$, where objects with an optical depth $\tau(\nu) > 1$ are said to be optically thick (with radiation unable to propagate through them) and optically thin otherwise. This will be utilized when examining X-ray backlighting results from counter-propagating radiative shock experiments in Chapter 2.

Opacity, emissivity and optical depth are not trivial to calculate and depend on several processes by which radiation can be absorbed by a medium. The dominant process in low temperature plasmas, such as those reported in this Thesis with $T < 50$ eV, is due to atomic line transitions. Transitions of electrons from high energy levels to lower ones results in the emission of a photon, with an energy $h\nu$ equal to the energy difference between the two levels. Similarly, photons may be absorbed by an electron if their energy is equal to the energy difference between the two levels. The electron is bound to the atom at all times in these processes and so they are known as a bound-bound transitions.

As the energy levels within an atom are quantized, this leads to a series of absorption/emission lines and the emissivity/opacity, $\epsilon_{bb}(\nu)/\kappa_{bb}(\nu)$ are not continuous in frequency. However, these lines may be broadened by thermal Doppler effects where particles travelling towards, or away from, the detector will emit Doppler shifted photons. In high density plasmas these lines may also be broadened by 'pressure broadening' due to perturbations caused by close proximity to other particles.

In higher temperature plasmas, recombination / photo-ionization (bound-free) and Bremsstrahlung (free-free) processes may dominate. Recombination occurs when an electron is captured by an ion, resulting in the emission of a photon of the kinetic energy of the electron plus the binding energy. The opposite, photo-ionization, occurs when an electron absorbs a photon with energy greater than it's binding energy, allowing it to escape the ion. Bremsstrahlung occurs when electrons are deflected and decelerated by an ion, resulting in the emission of a photon with energy equal to the change in kinetic energy. Radiation may also be absorbed via the inverse process where electrons oscillating in the electric field of

the photon collide with ions and convert their oscillatory energy to random thermal energy. These processes are not expected to be significant in plasmas encountered in this Thesis.

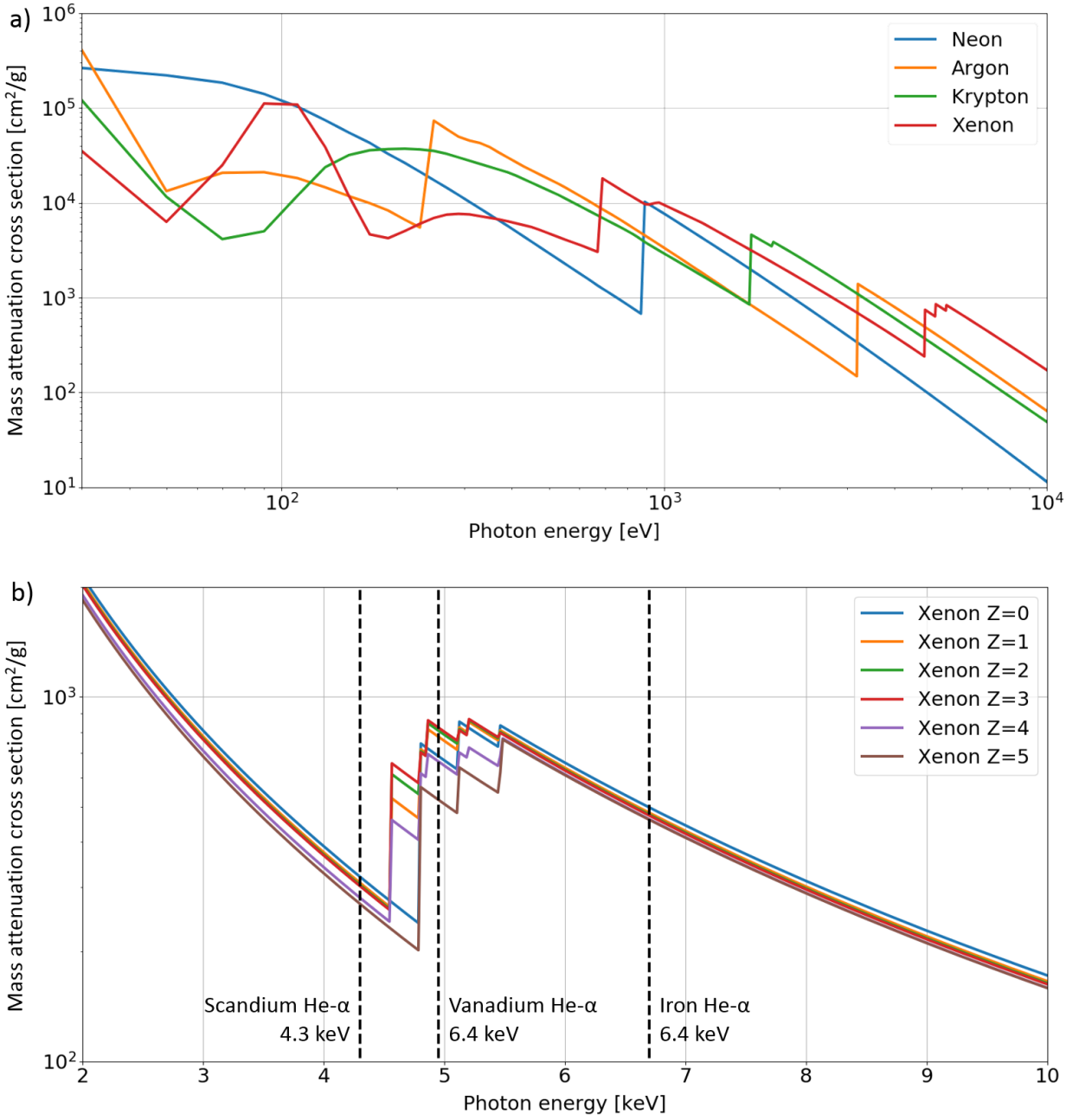


Figure 1.6: Opacities determined using online tools developed by Lawrence Berkeley National Laboratory [Henke et al., 1993]. a) Opacities for neutral Neon, Argon, Krypton and Xenon. b) Opacities for Xenon at different ionization stages, up to $Z = 5$.

In this Thesis tabulated values are used to calculate the opacity of a medium. These were obtained using online tools developed by Lawrence Berkeley National Laboratory [Henke

et al., 1993]. Opacities for cold Neon, Argon, Krypton and Xenon are plotted as a function of photon energy in Fig 1.6.a. These values were calculated from the transmission of photons through a 1 μm long sample of gas with a mass density of 1 g/cm^3. Using Eq. 1.24 the mass attenuation cross section, $\sigma(\nu)$ for a uniform sample can be shown to be:

$$\sigma(\nu) = -\frac{ln(T(\nu))}{\rho x} \tag{1.25}$$

where $T(\nu)$ is the transmission, ρ is the sample density and x is its thickness. These opacities vary with ionization due to changes in atomic transition energies. A plot of the mass attenuation cross section for Xenon gas at different ionizations is shown in Fig 1.6.b.

1.4.5 Dimensionless scaling

Laboratory Astrophysics is a relatively new field of study where astronomical events and conditions are modelled in the laboratory to understand the physics driving these systems. Although experiments occur on scale lengths and time scales many orders of magnitude smaller than astrophysical events ($\sim 10^{-3}$ m and $\sim 10^{-6}$ s as opposed to $\sim 10^{16}$ m and $\sim 10^{9}$ s for astrophysical events), hydrodynamic equations may be scaled through use of Euler scaling. An ideal gas (with zero viscosity and thermal conduction) may be described by the Euler equations, derived in Section 1.5.1. If a system is similar then these equations remain invariant under the transformation:

$$\mathbf{r} = a\mathbf{r}' \qquad \rho = b\rho' \qquad \mathbf{P} = c\mathbf{P}' \qquad t = dt' \qquad \mathbf{u} = e\mathbf{u}' \tag{1.26}$$

where $\mathbf{r}$ is the length scale, ρ is the density, $\mathbf{P}$ is the pressure, t is the time scale and $\mathbf{u}$ is the particle velocity. The primed variables are dimensionless parameters, with maximum magnitude of unity, and a, b, c, d, e are arbitrary positive constants. Substituting these variables into the Euler equation for momentum conservation:

$$\frac{\partial \rho \mathbf{u}}{\partial t} + \bigtriangledown.(\rho \mathbf{u}^2) = - \bigtriangledown P \tag{1.27}$$

yields:

$$\frac{be}{d}\frac{\partial \rho' \mathbf{u}'}{\partial t'} + \frac{be^2}{a} \bigtriangledown' .(\rho \mathbf{u}'^2) = -\frac{c}{a} \bigtriangledown' P' \tag{1.28}$$

For this equation to remain invariant under this transformation, the arbitrary constants must satisfy:

$$\frac{be}{d} = \frac{be^2}{a} = \frac{c}{a} \tag{1.29}$$

This therefore yields the following relationships:

$$d = a\sqrt{\frac{b}{c}} \qquad e = \sqrt{\frac{c}{b}} \tag{1.30}$$

which also hold for the other Euler equations, derived in Section 1.5.1. Therefore, two systems are similar if the dimensionless parameter:

$$Eu = v\sqrt{\frac{\rho}{P}} \tag{1.31}$$

is approximately constant [Ryutov et al., 1999] in both systems. This dimensionless parameter is known as the Euler number, or sometimes the Ryutov number [Drake, 2006]. Therefore, an experiment may be designed to simulate astrophysical phenomenon by matching the Euler number of both. For an ideal gas, where the sound speed is given by $c_s = \sqrt{\gamma P/\rho}$, the Euler number is very similar to the Mach number. However, to match two physical systems the same physical phenomenon must be present. This is quantified with additional dimensionless parameters such as the Reynolds number, magnetic Reynolds number and Peclet number.

The Reynolds number describes the important of viscosity in the fluid and is given by:

$$Re = \frac{vL}{D_{viscosity}} \tag{1.32}$$

where v is the velocity scale length, L is the length scale of the system and $D_{viscosity}$ is the viscosity of the fluid. If the Reynolds number $Re < 1$ then viscosity plays a significant role and flow is laminar. However, if the Reynolds number $Re > 1$ then viscosity is negligible and flow is turbulent.

The magnetic Reynolds number describes the important of magnetic diffusion in the fluid and is given by:

$$Re_M = \frac{vL}{D_{magnetism}} \tag{1.33}$$

where $D_{magnetism}$ is the magnetic diffusivity. If the magnetic Reynolds number $Re_M < 1$ then magnetic fields diffuse through the plasma. However, if the magnetic Reynolds number $Re_M > 1$ then magnetic fields are frozen into the plasma and thus changes in the plasma flow can modify magnetic fields and vice versa.

The Peclet number describes the important of thermal conduction in the fluid and is given by:

$$Pe = \frac{vL}{D_{thermal}} \tag{1.34}$$

where $D_{thermal}$ is the thermal diffusion. If the Peclet number $Pe > 1$ thermal conduction dominates and if the Peclet number $Pe < 1$ thermal convection dominates heat transport.

In astrophysics and ideal magnetohydrodynamics the Reynolds number, magnetic Reynolds number and Peclet number are all significantly higher than unity and so these plasmas have negligible viscosity, magnetic fields frozen into the plasma and thermal convection dominates over conduction. However, due to the limited scale size of laboratory experiments, these conditions are challenging to achieve in the laboratory. Many other dimensionless parameters exist, describing the importance of different physical phenomenon in a fluid.

1.5 Shock waves

Shock waves are abrupt changes in the properties of the medium which propagate faster than the speed of sound, i.e. supersonically. Typically, information within the medium is transmitted at the sound speed, so material in the upstream region (material ahead of the shock) has insufficient time to react, being limited to subsonic speeds. Therefore material piles up resulting in the formation of a shock front.

This concept is represented in one dimension in Fig 1.7, which shows a rigid piston moving to the right, compressing a medium initially composed of equally spaced spheres. Space is shown horizontally and time vertically. The piston moves at a constant velocity, v_p, and collides with the left most particle, accelerating it to the velocity of the piston. This first particle then collides with its neighbour causing that to also accelerate up to the piston velocity. This process continues, compressing additional material ahead of the piston and forming a shocked region. The leading edge of this is known as the shock front and moves with a shock velocity, v_s, faster than the piston velocity.

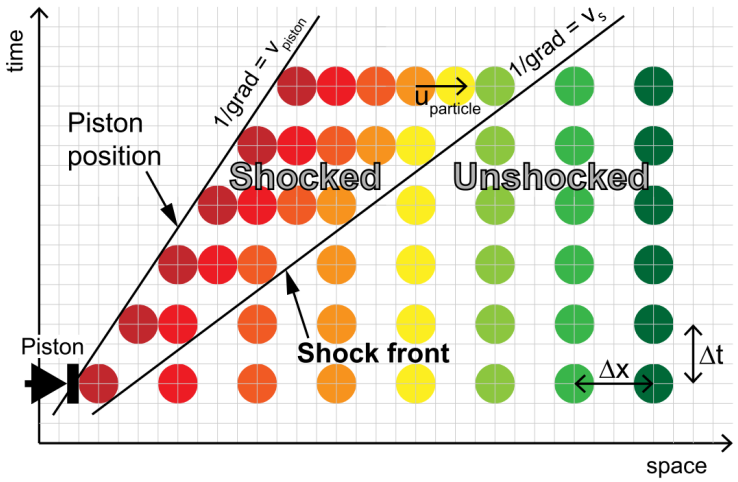


Figure 1.7: Diagram of a 1-D shock being driven by a rigid piston into a medium of evenly spaced spheres. Reproduced from [Burdiak, 2012]

The strength of a shock is represented by the dimensionless Mach number M:

$$M = \frac{v_s}{c_s} \tag{1.35}$$

where c_s is the sound speed in the unperturbed medium. While Mach numbers for supersonic aircraft are usually below $M < 5$, Mach numbers found in astrophysical shocks can exceed $M > 10$ [Remington et al., 2006].

Although frequently described as a discontinuity in density and temperature, a shock front does have a finite width. Schematic plots of the electron and ion temperatures in a shock front are shown in Fig 1.8, with the shock propagating to the right. Ions and electrons are heated over a spacial scale of several mean free path lengths [Zel'dovich and Raizer, 2002, Drake, 2005] (Eq. 1.17 and Eq. 1.18). As the ions have a significantly shorter mean free path, due to their increased mass, they are rapidly heated at the shock front to $T_i(max)$. The electrons and ions then reach equilibrium over several electron mean free paths, in a region know as the equilibrium zone, reaching a temperature of $T_e(eq) = T_i(eq)$. The ratio of peak ion temperature to equilibrium temperature $T_i(max)/T_i(eq) = (Z + 1)$, where Z is the average post-shock ionization state (assuming no energy losses via radiation).

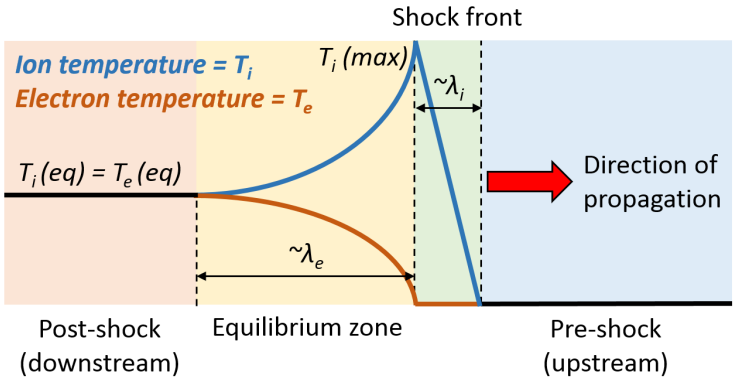


Figure 1.8: Ion and electron temperatures at the shock front. Not to scale.

1.5.1 Rankine-Hugoniot relations

The simplest model for a shock wave is to treat it as a 1-D discontinuity in density and temperature and neglect any radiative and magnetic effects. A 1-D model of this is shown

in Fig 1.9 with the pre-shock/upstream region to the right of the shock front and the post-shock/downstream region to the left of the shock front. In this model the pressure, P_i, mass density, ρ_i, temperature, T_i, and particle velocity, u_i, all take the form of a step function and are given the subscript 1 or 2 for the pre-shock or post-shock regions respectively. For simplicity, the following derivations will take place in the reference frame of the shock. The pre-shock and post-shock particle velocity in the reference frame of the shock (u_1 and u_2 respectively) can be found by subtracting the velocity of the shock in the lab frame, v_s, from the lab frame particle velocities, u_p for the post-shock region and typically negligible for the pre-shock region. Therefore $u_1 = -v_s$ and $u_2 = u_p - v_s$.

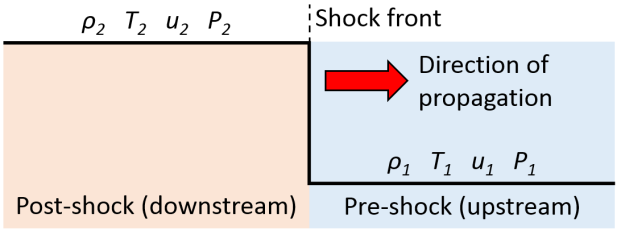


Figure 1.9: A shock wave modelled as a discontinuity in density and temperature.

Conservation laws can be used to relate properties on either side of the boundary in what are known as the Rankine-Hugoniot (RH) relations or shock jump conditions. These can be derived from Euler's equations which describe a adiabatic fluid with negligible viscosity. These take the general form of:

$$\frac{\partial \rho_i}{\partial t} + \bigtriangledown.\Gamma_i = S_i \tag{1.36}$$

Where i is the quantity of interest, S describes all sinks and sources, Γ is the flux of the conserved quantity and ρ is the density of the conserved quantity [Drake, 2006].

Mass Conservation

Mass is neither created nor destroyed, allowing $S_{mass} = 0$, and the mass flux can simply be expressed as the local density multiplied by the local velocity $\Gamma_{mass} = \rho u$. This yields:

$$\frac{\partial \rho}{\partial t} + \bigtriangledown.(\rho u) = 0 \tag{1.37}$$

For the 1D shock model currently being considered, this can be simplified to:

$$\frac{\partial \rho}{\partial t} = -\rho \frac{\partial u}{\partial x} \tag{1.38}$$

Integrating this equation across a small region straddling the discontinuity therefore yields:

$$\int_{x_1}^{x_2} \frac{\partial \rho}{\partial t} dx = \rho_2 u_2 - \rho_1 u_1 \tag{1.39}$$

where x_1 and x_2 are the on either side of the shock discontinuity. As the shock is a discontinuity the difference between x_1 and x_2 can be reduced to its infinitesimal limit where $x_2 - x_1 \to 0$. This results in the time dependant left hand side of the equation reduces to zero, allowing the two terms on the right hand side to be equated. This yields the Rankine-Hugoniot relation for mass conservation, also known as the continuity equation:

$$\rho_1 u_1 = \rho_2 u_2 \tag{1.40}$$

Momentum Conservation

The flux of the momentum can be expressed as the local momentum multiplied by the local velocity, yielding $\Gamma_{momentum} = \rho u^2$. In addition, the pressure gradient, $- \bigtriangledown P$, across the shock can be considered a source of momentum. The Euler equation for momentum therefore yields:

$$\frac{\partial \rho u}{\partial t} + \bigtriangledown.(\rho u^2) = - \bigtriangledown P \tag{1.41}$$

In 1D this can be simplified to:

$$\frac{\partial}{\partial t}(\rho u) = -\frac{\partial}{\partial x}\left(\rho u^2 + P\right) \tag{1.42}$$

Integrating this equation across a small region straddling the discontinuity yields:

$$\int_{x_1}^{x_2} \frac{\partial(\rho u)}{\partial t} dx = \rho_2 u_2 + P_2 - \rho_1 u_1 - P_1 \tag{1.43}$$

As before, the difference between x_1 and x_2 can be reduced to its infinitesimal limit yielding the Rankine-Hugoniot relation for momentum conservation:

$$\rho_1 u_1^2 + P_1 = \rho_2 u_2^2 + P_2 \tag{1.44}$$

Energy Conservation

The energy density is a sum of the kinetic energy density, $\rho u^2/2$, and the internal energy density, $\rho\epsilon$, where ϵ is the internal energy per unit mass. The energy flux is found by multiplying this expression by the local particle velocity, $\mathbf{u}$. While there are many different sources and sinks of energy which can occur in shocks, including ionization and radiation, this simple model only considers work done by compression. This allows the source term to be expressed as $\bigtriangledown.(P\mathbf{u})$, yielding:

$$\frac{\partial}{\partial t}\left(\frac{\rho u^2}{2} + \rho\epsilon\right) + \bigtriangledown.\left[\left(\frac{\rho u^2}{2} + \rho\epsilon\right)\mathbf{u}\right] = \bigtriangledown.(P\mathbf{u}) \tag{1.45}$$

For the 1D shock model currently being considered, this can be simplified to:

$$\frac{1}{2}\frac{\partial}{\partial t}\left(\frac{\rho u^2}{2} + \rho\epsilon\right) = -\frac{\partial}{\partial x}\left(\rho u\left(\epsilon + \frac{u^2}{2}\right) + Pu\right) \tag{1.46}$$

Integrating this equation across an infinitesimal region straddling the discontinuity again yields the Rankine-Hugoniot relation for energy conservation:

$$\rho_1 u_1 \left(\epsilon_1 + \frac{u_1^2}{2}\right) + P_1 u_1 = \rho_2 u_2 \left(\epsilon_2 + \frac{u_2^2}{2}\right) + P_2 u_2 + S \tag{1.47}$$

where the additional term, S, represents the flux across the shock front of all energy that is not convecting with the fluid, such as by radiation.

Equation of state

The Rankine-Hugoniot relations provide three equations with four unknown variables, ρ_2, u_2, p_2, ϵ_2. To close this set of equations a fourth equation is required, the Equation of State (EoS). For an ideal gas (a gas in which all collisions are elastic and there are negligible intermolecular forces) the EoS is given by:

$$\rho\epsilon = \frac{P}{\gamma - 1} \tag{1.48}$$

This assumes that the fluid is polytropic where $P \propto \rho^\gamma$, where γ is the adiabatic index. The adiabatic index is typically defined as the heat capacity at constant pressure, C_P, over the heat capacity at constant volume, C_V:

$$\gamma = \frac{C_P}{C_V} \tag{1.49}$$

For an ideal gas, this can be related to the number of degrees of freedom, n_d:

$$\gamma = \frac{n_d + 2}{n_d} \tag{1.50}$$

For a monatomic gas, such as Argon or Xenon, with 3 translational degrees of freedom, $n_d = 3$ yielding an adiabatic index of $\gamma = 5/3$. However, a diatomic molecule, such as Nitrogen, has 3 translational degrees and 2 rotational degrees of freedom, resulting in $n_d = 5$ and thus an adiabatic index of $\gamma = 7/5$. Meanwhile, photons have $n_d = 6$, resulting in a photon dominated gas having an adiabatic index of $\gamma = 4/3$. As the number of degrees of

freedom increases, due to processes such as ionization or energy being lost through radiation, the effective adiabatic index asymptotes towards 1. This means that higher mass densities are required to achieve the same pressure and so the post-shock compression in a radiative shock is expected to increase above that of a non-radiative shock. In general the adiabatic index varies across a shock front, but this effect is frequently assumed to be negligible in the literature.

1.5.2 Strong shock limit

In a strong shock (with Mach number $M \gg 1$), and neglecting radiation and ionization, there exists a maximum post-shock density, temperature and particle velocity. In this regime the pressure, P_1, and energy, ϵ_1, of the unshocked material are negligible. This allows Eq. 1.44 and Eq. 1.47 to be reduced to:

$$P_2 = \rho_1 u_1^2 - \rho_2 u_2^2 \tag{1.51}$$

$$\rho_1 u_1 \left(\frac{u_1^2}{2}\right) = \rho_2 u_2 \left(\epsilon_2 + \frac{u_2^2}{2}\right) + P_2 u_2 \tag{1.52}$$

Using the Rankine-Hugoniot relation for mass, shown in Eq. 1.40, allows Eq. 1.52 to be simplified to:

$$\frac{u_1^2}{2} = \epsilon_2 + \frac{u_2^2}{2} + \frac{P_2}{\rho_2} \tag{1.53}$$

By inserting the expression for the internal energy ϵ_i, shown in Eq. 1.48, this is further simplified to:

$$\frac{u_1^2}{2} = \frac{P_2}{\rho_2}\frac{1}{\gamma - 1} + \frac{u_2^2}{2} + \frac{P_2}{\rho_2} \tag{1.54}$$

By gathering together the terms of P_2/ρ_2 and the velocity terms, this can be simplified to:

$$(u_1 - u_2)(u_1 + u_2) = \frac{2\gamma}{\gamma - 1}\frac{P_2}{\rho_2} \tag{1.55}$$

An expression for $(u_1 - u_2)$ can be obtained by inserting Eq. 1.40 into Eq. 1.51:

$$u_1 - u_2 = \frac{P_2}{\rho_2 u_2} \tag{1.56}$$

Inserting this into Eq. 1.55 results in:

$$\frac{P_2}{\rho_2 u_2}(u_1 + u_2) = \frac{2\gamma}{\gamma - 1}\frac{P_2}{\rho_2} \tag{1.57}$$

This allows a ratio of the velocities on both sides of the shock to be expressed just in terms of the fundamental adiabatic index:

$$\frac{u_1}{u_2} = \frac{\rho_2}{\rho_1} = \Gamma = \frac{\gamma + 1}{\gamma - 1} \tag{1.58}$$

This represents the maximum post shock velocity and the maximum compression of a shock in the absense of radiative effects. For a monatomic gas, with an adiabatic index of $\gamma = 5/3$, the maximum shock compression is therefore limited to $\Gamma = \times 4$. However, as the shock speed and Mach number continue to increase, effects due to radiation and ionization become important resulting in higher shock compressions, as discussed in Section 1.6.

In the strong shock limit the post-shock temperature may also be determined from the Rankine-Hugoniot relation for momentum conservation, Eq. 1.51. Assuming an idea gas, the post-shock pressure, P_2, may be related to the post-shock temperature, T_2, by:

$$P_2 = n_2 k_B T_2 \tag{1.59}$$

where k_B is the Boltzmann constant and n_2 is the particle density in the post-shock region. The number of particles, a combination of ions and electrons may be approximated as:

$$n_2 = \frac{\rho_2}{Am_p}(Z+1) \tag{1.60}$$

where A is the atomic mass, m_p is the proton mass and Z is the average ionization per ion. Substituting these expressions into Eq. 1.51 therefore yields:

$$\rho_2 \frac{(Z+1)}{Am_p} k_B T_2 = \rho_1 u_1^2 - \rho_2 u_2^2 \tag{1.61}$$

Using Eq. 1.40 and Eq. 1.58 allows terms of ρ_2 and u_2 to be removed so that:

$$\rho_1 \frac{\gamma+1}{\gamma-1} \frac{(Z+1)}{Am_p} k_B T_2 = \rho_1 u_1^2 - \rho_1 u_1^2 \frac{\gamma-1}{\gamma+1} \tag{1.62}$$

This may be simplified to give an expression for the post-shock temperature dependent only on the atomic species, adiabatic index, ionization and shock velocity (as $u_1^2 = v_s^2$):

$$k_B T_2 = 2 \frac{Am_p}{(Z+1)} \frac{(\gamma-1)}{(\gamma+1)^2} v_s^2 \tag{1.63}$$

This expression will be used when estimating the post-shock temperature in experiments conducted on the MAGPIE facility in Section 3.5.1. However, this expression does not consider radiation and so is less valid in highly radiative shocks, introduced in Section 1.6.

1.5.3 Rarefactions and blast waves

Shocks are usually transient events where the pressure source only existing briefly, such as in a supernova or a nuclear explosions. In these scenarios a rarefaction wave is produced [Drake, 2006]. A rarefaction is a wave of decreasing pressure and density that can occur behind a shock wave when the pressure source ends or the shock enters a lower density medium, a process known as 'shock breakout'. In a plasma, unbound electrons are able to efficiently conduct heat to the expanding material resulting in an isothermal rarefaction. The mass density, $\rho(x,t)$, and particle velocity, $u(x,t)$, evolution for an isothermal rarefaction are shown

in Fig 1.10.a-c and given by:

$$\rho(x,t) = \rho_0 exp\left[-1 - \frac{x}{c_s t}\right] \tag{1.64}$$

$$u(x,t) = c_s + \frac{x}{t} \tag{1.65}$$

where ρ_0 is the initial mass density and c_s is the sound speed. The rarefaction wave is able to travel faster than the shock, eventually catching up and forming a thin shell of shocked material known as a blast wave. The formation of a blast wave is shown in Fig 1.10.d-f.

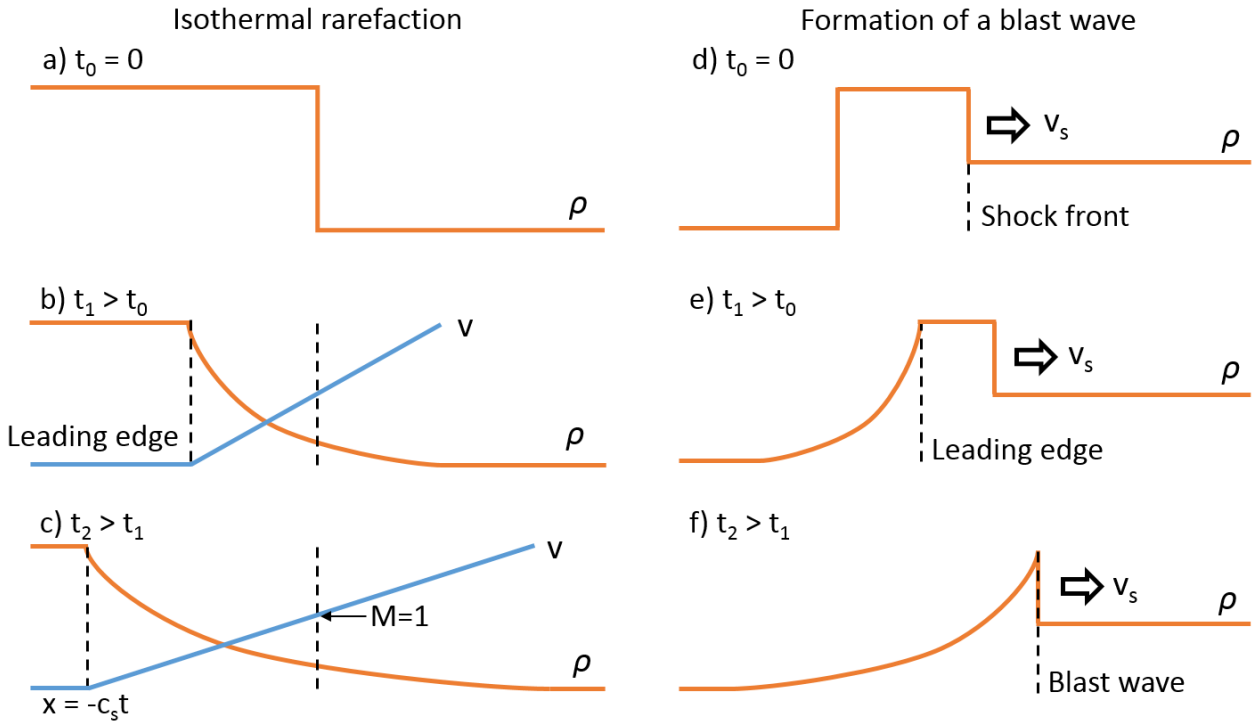


Figure 1.10: a-c) Mass density and particle velocity evolution for an isothermal rarefaction. d-f) Mass density in the formation of a blast wave.

Mach stems can form at the interaction of two blast waves. This effect has been observed in blast waves reflecting off surfaces, for instance in above ground nuclear weapon tests. This process is shown schematically in Fig 1.11. The initial blast wave collides with the ground resulting in a reflected blast wave. This reflected shock wave will travel at a higher velocity

through the super heated post-shock material. These two shock waves merge at a 'triple point', forming a Mach stem which extends to the ground.

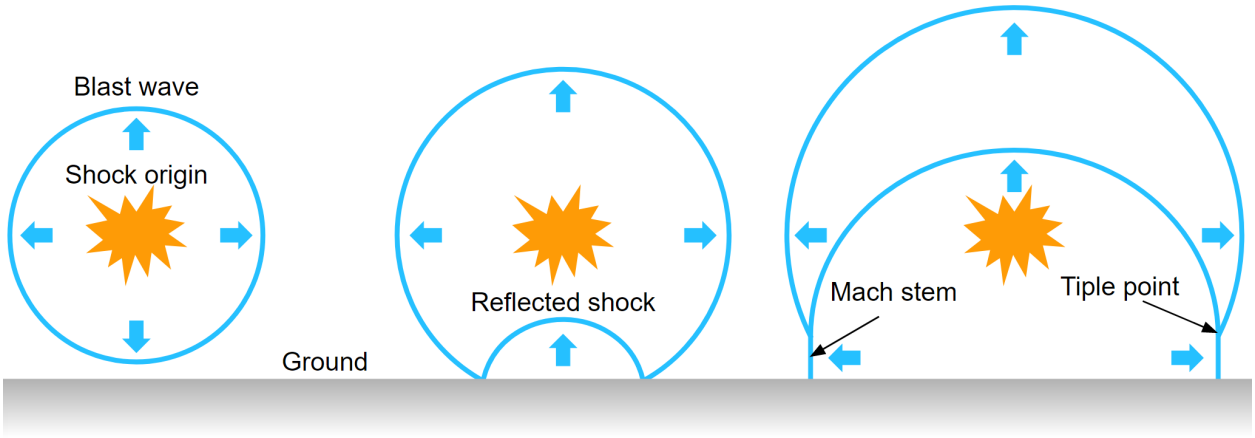


Figure 1.11: Diagram of a blast wave reflecting off a surface and forming a Mach stem in an above ground nuclear weapon test.

This effect is also predicted to occur in the interaction of two blast waves in an astrophysical or laboratory environment. When two blast waves intersect they reflect off one another, forming symmetric reflected oblique shocks [Hansen 2015]. Without a Mach stem, particles pass through both the initial shock and reflected shock so that the final direction of its velocity is unchanged. This scenario is depicted in Fig 1.12.a.

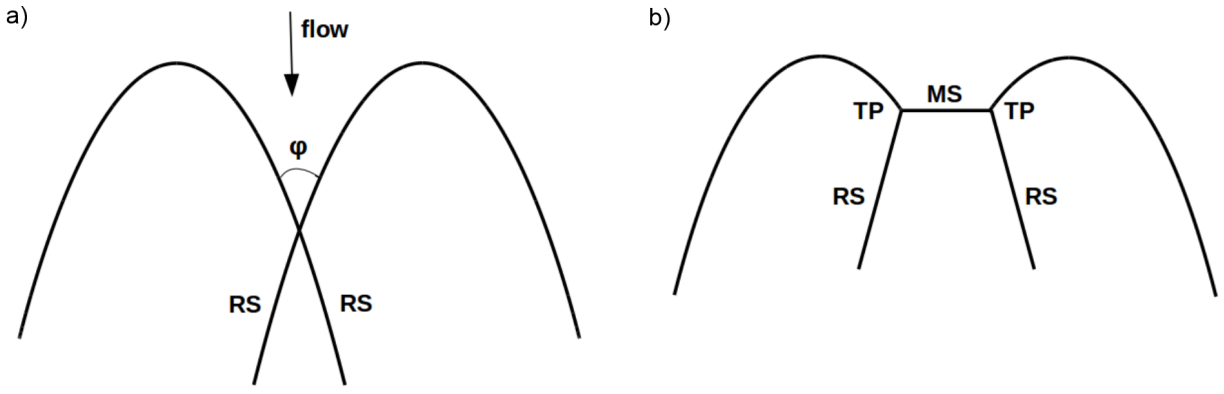


Figure 1.12: a) The collision of two blast waves at an angle ϕ, resulting in the formation of reverse shocks, labelled 'RS'. b)A Mach stem forming between two shock waves, MS = Mach stem and TP = triple point. Reproduced from [Hansen et al., 2014]

When the intersection of the shocks is above a critical angle, ϕ_c, particles may no longer

pass through the reflected shock and so piles up between the interacting blast waves forming a planar shock known as a Mach stem. This scenario is depicted in Fig 1.12.b. The point where the Mach stem meets the blast wave is known as the triple point.

For a strong shock (see Section 1.5.2), the critical angle, above which a Mach stem will form, may be approximated as a function of the adiabatic index so that:

$$\phi_c \approx 2\ sin^{-1}\left(\frac{1}{\gamma}\right) \tag{1.66}$$

For a monatomic gas with an adiabatic index of $\gamma = 5/3$ this yields a critical angle of $\phi_c \sim 74°$. As the adiabatic index decreases, for instance in a radiative shock, the critical angle increases. This will be utilized when investigating experiments performed on the MAGPIE facility, in Section 3.5.3.

As a blast wave expands, it sweeps up material in what is know as a 'snowplough' explosion. The equation of motion of a blast wave can therefore be given as:

$$F = ma + \frac{\partial m}{\partial t}v \tag{1.67}$$

where F is a driving force, m is the total mass swept up by the blast wave, a and v are the acceleration and velocity of the blast wave. The final term, due to accreted mass, may be rewritten using the relation: $\partial m/\partial t = \partial m/\partial r \times \partial r/\partial t$. Therefore for an undriven blast wave, with $F = 0$, Eq. 1.67 may be written as:

$$\frac{\partial m}{\partial r}\left(\frac{\partial r}{\partial t}\right)^2 = -m\frac{\partial^2 r}{\partial t^2} \tag{1.68}$$

where r is the radius of the blast wave. Assuming a uniform medium with a mass density of ρ_0, in cylindrical geometry the total mass, m, and its differential, $\partial m/\partial r$, may be given as:

$$m = \pi r^2 \rho_0 \qquad\qquad \frac{\partial m}{\partial r} = 2\pi r \rho_0 \tag{1.69}$$

Eq. 1.68 may be solved using the ansatz $r(t) = At^B$, with time differential of $\partial r/\partial t = ABt^{(B-1)}$ and double time differential of $\partial^2 r/\partial t^2 = AB(B-1)t^{(B-2)}$. Substituting this and Eq. 1.69 into Eq. 1.68 therefore yields:

$$2\pi At^B \rho_0 A^2 B^2 t^{(2B-2)} = -\pi A^2 t^{2B} \rho_0 AB(B-1)t^{(B-2)} \tag{1.70}$$

which simplifies to give $B = 1/3$. Therefore the radius of a cylindrically expanding blast wave will evolve as $r \sim t^{1/3}$. This will be utilized when considering cylindrically expanding blast waves produced in Chapter 3.

In spherical geometry the total mass, m, and its differential, $\partial m/\partial r$, may be given as:

$$m = \frac{4\pi}{3} r^3 \rho_0 \qquad\qquad \frac{\partial m}{\partial r} = 4\pi r^2 \rho_0 \tag{1.71}$$

Substituting this into Eq. 1.68 with a similar ansatz shows that the radius of the spherically expanding blast wave will evolve as $r \sim t^{1/4}$.

1.6 Radiative shocks

If the post-shock material is heated to sufficiently high temperatures it will begin to radiate energy. In hypersonic flows (with Mach number $\gg 1$) this radiative flux is non-negligible and plays an important role in the structure of the shock. This system is known as a radiative shock and is of interest to many areas of High Energy Density Physics (HEDP) and astrophysics [Zel'dovich and Raizer, 2002, Drake, 2006]. Radiative shocks are prevalent in astrophysics, and can be found in jets emitted from newly formed stars [Hartigan, 1989, Hartigan, 2005], in accretion shocks formed by material falling onto young stars [Orlando et al., 2013] and supernova remnants [Drake, 2006]. In addition, radiative shocks have been observed in inertial confinement fusion implosions [Pak et al., 2013].

The inclusion of radiation extends the model of a shock by introducing new regions either

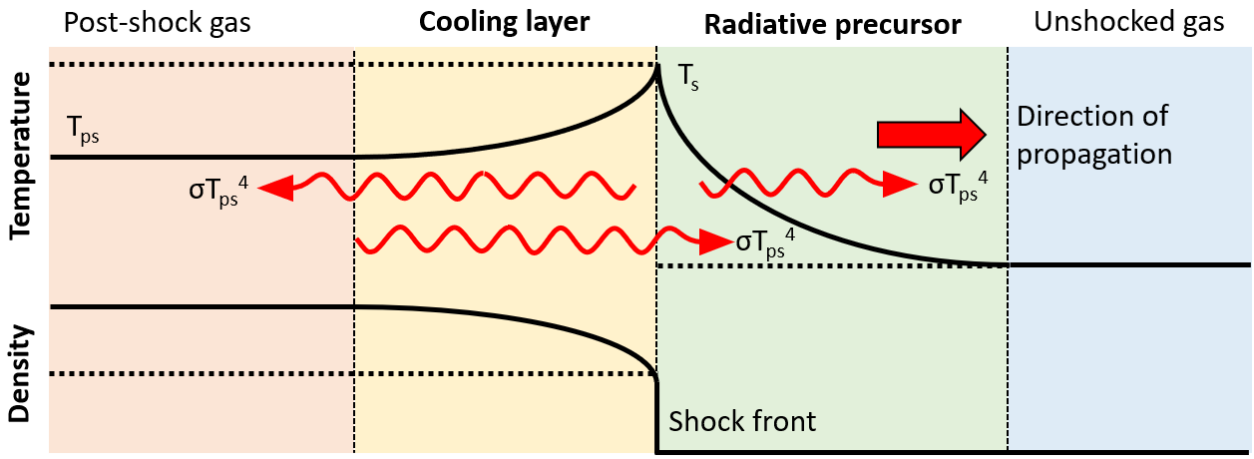


Figure 1.13: 1-D diagram of how temperature and mass density vary in a radiative shock.

side of the shock front, as shown in Fig 1.13. Temperature peaks at the shock front and is followed by a cooling layer. Photons are emitted from the post-shock plasma and carry energy with them, resulting in radiative cooling and a decrease in temperature. However, to maintain a constant pressure, the mass density further increases past the initial jump of $\times 4$ derived in Section 1.5.2.

In addition, photons which propagate upstream (into pre-shocked material) can heat and ionize material, resulting in the formation of a radiative precursor ahead of the shock [Drake, 2006], labelled in Fig 1.13. This has the effect of smoothing out the temperature gradient of the initially discontinuous shock front and is discussed further in Section 1.6.3. When the temperature of unshocked material just ahead of the shock front reaches a similar temperature to the post-shock material the shock is said to be supercritical, and subcritical if not.

1.6.1 Classification of radiative shocks by optical thickness

Radiative shocks are heavily dependant on the opacity (discussed in Section 1.4.4) of both the shocked and unshocked material. They may be grouped into four classes [Drake, 2005, Drake, 2006]:

Thick-thick regime

This class of radiative shock exists when both the shocked and unshocked material are optically thick, $\tau > 1$. Radiation emitted from the hot shocked material is able to heat the cooler unshocked material. This leads to ionization and a temperature increasing ahead of the shock front and the formation of a radiative precursor. The extension of the precursor depends upon the strength of the shock, with stronger shocks able to emit more radiation and sustain a more extreme radiative precursor. However, the shock cannot loose energy radiatively as radiation cannot escape the optically thick medium. This limits the shock compression to the same as a non-radiative shocks. This class of radiative shocks is commonly found in dense plasmas such as stellar interiors. Due to their high opacity they are difficult to detect and probe.

Thick-thin regime

This class of radiative shock exists when the shocked material is optically thick while the unshocked material is optically thin, $\tau < 1$. This allows radiation from the shocked region to escape downstream, resulting in a cooling layer forming behind the shock front. As the unshocked material does not absorb this radiation, no radiative precursor is formed. Radiative shocks found in accretion in young stars are of this class.

Thin-thin regime

This class of radiative shock exists when the shocked and unshocked material are optically thin. Radiation is allowed to escape, leading to large amounts of radiative cooling. As radiation is not absorbed by the unshocked material, a radiative precursor will not be formed. This class of radiative shocks is the most commonly observed in astrophysics, for example in supernova remnants.

Thin-thick regime

This class of radiative shock exists when the shocked material is optically thin while the unshocked material is optically thick. This is difficult to produce, as it typically requires the unshocked material to be of lower density than the shocked material, and thus is not found in astrophysics. However, if such a shock could be produced, it would have a very dense shock front and energy would be radiated away behind the shock, resulting in radiative cooling.

Radiative shocks examined in this Thesis most closely match the thick-thin class. However, this classification is insufficient and instead the unshocked medium is optically semi-thin and is able to reabsorb part of the radiation. Directly behind the shock front, in the cooling layer, the plasma is also expected to be optically semi-thin, allowing radiation to escape upstream as seen in Fig 1.13. The shocked material will cool from a peak temperature of T_s at the shock front, resulting in a rapid increase density. Eventually the mass density reaches the point that the shocked material is optically thick, marking the end of the cooling layer and resulting in a significantly reduced rate of cooling. In this post-shock material the plasma temperature is $\sim T_{ps}$.

As the cooling layer is optically semi-thin, the radiative flux will be less than that given by the Stefan-Boltzmann law, Eq. 1.22. However, radiation emitted from this region will propagate isotropically into both the post-shock and unshocked regions. In equilibrium the radiative flux absorbed by the post-shock region is remitted upstream [Drake et al., 2011], as shown in Fig 1.13. Assuming most of this radiation is able to propagate through the semi-thin cooling layer, the total emission from post-shock material may be given as of $F_r = 2\sigma T_{ps}^4$.

1.6.2 Radiative shock regimes

The definition of a radiative shock varies slightly across the literature but generally requires that radiation be non-negligible, leading to modifications to the shock structure. This results

in two major regimes: one in which the radiative energy flux dominates the system, and where the radiative pressure dominates the system [Drake, 2005, Drake, 2006].

Energy flux dominated regime

The least stringent definition for a radiative shock requires that the radiative energy flux emitted upstream exceeds the energy flux from particles in the upstream material. This regime is commonly reproduced in the laboratory and found in a the convection zone of stars. The radiation flux, F_r, emitted upstream is given by the Stefan-Boltzmann law, Eq. 1.22. The energy flux from upstream particles, F_m, is a combination of the kinetic energy of the incoming particles, in the reference frame of the shock wave, and their internal energy:

$$F_m = \frac{1}{2}\rho_0 v_s^3 + \rho_0 C_v T_{ps} v_s \tag{1.72}$$

where ρ_0 is the initial unshocked mass density, C_v is the specific heat capacity at a constant volume and v_s is the shock velocity. This approximation assumes the shock to be supercritical, and therefore the pre-shock temperature is approximately equal to the post-shock temperature. The literature frequently ignores the expression for the thermal energy of the particles, second term on the right hand side of Eq. 1.72, as this is expected to be smaller than the particles kinetic energy. As the post-shock temperature approximately scales with the shock velocity squared (shown in Eq. 1.63), both of these expressions increase at higher shock velocities, with the radiative flux increasing at a faster rate. Requiring $F_m < F_m$ and using Eq. 1.63 to approximate the post-shock temperature, T_{ps}, therefore yields:

$$v_e^5 > \frac{\rho_0}{32\sigma}\left(\frac{(Z+1)k_B(\gamma+1)^8}{Am_p(\gamma-1)^4}\right)^4 \tag{1.73}$$

Pressure dominated regime

The more stringent definition requires the radiation pressure, P_r, exceed the ram pressure of the oncoming material, P_m [Drake, 2005]. These may be given as:

$$P_m = \frac{1}{2}\rho_0 v_s^2 \qquad (1.74) \qquad\qquad P_r = \frac{2\sigma_{SB}}{c} T_{ps}^4 \qquad (1.75)$$

where ρ_0 is the unshocked mass density, v_s is the shock velocity, σ_{SB} is the Stefan-Boltzmann constant, T_s is the post-shock temperature and c is the speed of light. Typically this regime requires significantly higher shock velocities and so is very rarely reproduced in the laboratory (with the exception of [Dizière et al., 2011]) but is common in supernova explosions and very large stars. Requiring $P_m < P_r$ and using Eq. 1.63 to approximate the post-shock temperature, T_{ps}, yields:

$$v_p^6 > \frac{\rho_0 c}{64\sigma}\left(\frac{(Z+1)k_B(\gamma+1)^8}{Am_p(\gamma-1)}\right)^4 \qquad (1.76)$$

It can therefore be shown that the shock velocity required to reach the radiative pressure dominated regime, v_p, is proportional to the shock velocity required to reach the energy flux dominated regime, v_e, to the power of 5/6:

$$v_p^6 = \frac{c}{2} v_e^5 \qquad (1.77)$$

In high atomic number materials, such as Xenon, the plasma will not be highly ionized and $A > Z + 1$. Therefore the shock velocities required to reach both the radiative energy dominated and pressure dominated regimes is significantly reduced. For this reason, radiative shock experiments are typically conducted in Xenon, as can be seen in discussions of previous experiments in Section 1.7.1.

1.6.3 The radiative precursor

With an optically semi-thin or thick pre-shock medium, part of the radiation emitted by the shock front can be reabsorbed by the unshocked material. This results in a layer of heated and ionized material extending ahead of the shock front known as a radiative precursor, as shown in Fig 1.13. This acts to smooth out the temperature discontinuity of the shock front and can result in the formation of instabilities, such as the thermal cooling instabilities [Meerson, 1996, Hohenberger et al., 2010]. Note that the mass density in the precursor region is unchanged from the cold, unshocked gas as this material does not have sufficient time to expand after being heated.

A radiative precursor will be formed ahead of the shock front when a sufficient number of ionizing photons are emitted by the post shock material. This can be estimated to occur when the flux of photons travelling upstream exceed the flux of unshocked particles encountered by the shock wave [Keiter et al., 2002, Drake, 2005]. The photons flux can be approximated as the energy flux from a blackbody, given by the Stefan-Boltzmann law Eq. 1.22, divided by the energy of photons of the peak wavelength, given by the Wien displacement law:

$$\sigma_{SB} T_{ps}^4 \left(\frac{hb}{cT_{ps}} \right)^{-1} = \frac{\sigma_{SB} b}{hc} T_{ps}^3 \tag{1.78}$$

where σ_{SB} is the Stefan-Boltzmann constant, h is the Planck constant, b is the Wien displacement constant, c is the speed of light and T_{ps} is the post-shock temperature. The particle flux can given by the mass flux, $\rho_0 v_s$, divided by the particle mass Am_p, where ρ_0 is the unshocked mass density, v_s is the shock velocity, A is the atomic mass number and m_p is the proton mass. Therefore:

$$\frac{\sigma_{SB} b}{hc} \epsilon_1 \epsilon_2 \eta T_{ps}^3 = \frac{\rho_0 v_s}{A m_p} \tag{1.79}$$

where η is the proportion of ionizing photons, ϵ_1 is the emissivity of the unshocked material (which determines the proportion of photons which are absorbed) and ϵ_2 is the emissivity of

the shocked material (which determines the amount of blackbody photons absorbed). Using the strong-shock estimate for post-shock temperature, Eq. 1.63, the shock velocity required for a radiative precursor may be shown to be:

$$v_s > 35A^{-4/5}\left(\frac{\rho_0}{\eta\epsilon_1\epsilon_2}\right)^{1/5}\left(\frac{(Z+1)(\gamma+1)^2}{\gamma-1}\right)^{3/5}\ km/s \tag{1.80}$$

For an optically thick post-shock system $\epsilon_1 \approx 1$, and for a medium significantly longer than the photon mean free path $\epsilon_0 \approx 1$. In addition, at shock velocities $v_s > 50$ km/s nearly all photons are ionizing and therefore $\eta \approx 1$. This will be used when investigating radiative precursors observed in these experiments, in Section 2.4.3.

1.6.4 Radiative shock model

To estimate post-shock conditions in a radiative shock, a numerical model has been developed by the author based on energy balance arguments. A rough estimate for the post shock temperature can obtained by equating the radiative loss flux, F_R, to the kinetic energy flux of incoming particles, F_{KE}. As described in Section 1.6.1, the radiative flux, F_R for a post-shock region in thermal equilibrium can be approximated as twice the blackbody emission. The kinetic energy flux of incoming particles, F_{KE}, can then be approximated as half the product of the unshocked mass density ρ_0 and the shock velocity cubed, v_s^3. Therefore:

$$F_R = 2\sigma_{SB}T_{ps}^4 \tag{1.81}$$

$$F_{KE} = \frac{1}{2}\rho_0 v_s^3 \tag{1.82}$$

where σ_{SB} is Stefan-Boltzmann constant and T is the temperature. Equating these two expressions allows an expression for the post-shock temperature in terms of the shock velocity:

$$T_{ps} \approx \left[\frac{\rho_0 v_s^3}{4\sigma_{SB}}\right]^{1/4} \tag{1.83}$$

The post-shock temperature is plotted as a function of temperature for several initial mass densities in Fig 1.14.

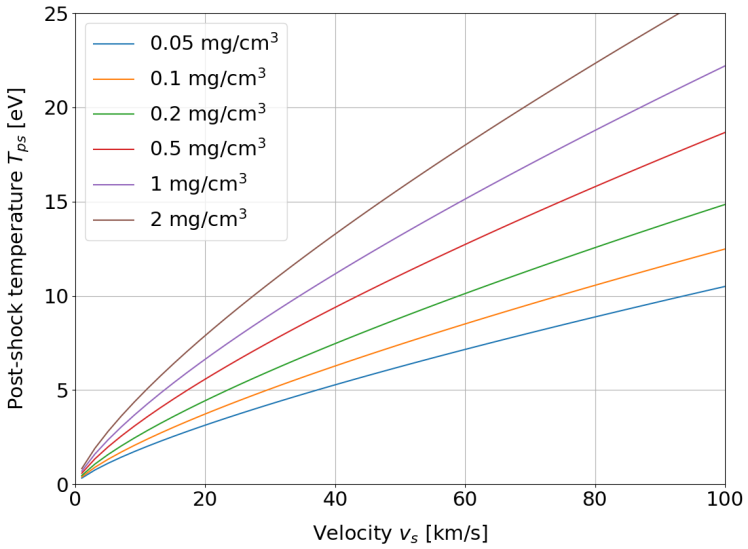


Figure 1.14: Post-shock temperature as a function of shock velocity.

At high shock velocities, where the radiative flux dominates, this model is expected to be reasonably accurate. However, this simple model does not account for losses to ionizing, F_I, and heating, F_{TH}, the incoming flux of particles and thus overestimates the post-shock temperature for lower shock velocities. The model may be improved by balancing the incoming kinetic energy flux against the losses to radiation, ionization and heating. Therefore:

$$F_{KE} = F_R(T_{ps}) + F_I(Z_{ps}) + F_{TH}(T_{ps}, Z_{ps}) \tag{1.84}$$

All of the terms are functions of the post-shock temperature, T_{ps} or post-shock ionization Z_{ps} which in turn is dependant on the post-shock temperature and mass density. By solving this equation the post-shock temperature may be deduced. The loss to ionizing the incoming flux of particles, F_I, can be approximated as the incoming flux of particles, $n = \rho_a v_s / A m_p$, where A is the atomic mass and m_P is the proton mass, multiplied by the average ionization potential for the post-shock ionization, $E(Z_{ps})$. So that:

$$F_I(Z_{ps}) \approx \rho_0 v_s / A m_p \times E(Z_{ps}) \tag{1.85}$$

The average ionization potential per ion was determined by linearly interpolating between ionization potentials for two integer ionization states. Ionization potentials were taken from tabulated values available on the NIST Atomic Spectra Database [Kramida et al., 2015]. The loss to heating the incoming particle flux, $F_{TH}(T_{ps})$ was approximated as the incoming flux of particles multiplied by the internal energy of an ideal gas. Thus:

$$F_{TH}(T_{ps}) = \frac{3}{2} n(1 + Z_{ps}) k_B T_{ps} \tag{1.86}$$

where the factor of $(1 + Z_{ps})$ accounts for heating of electrons, assuming the electrons and ions are thermalised in the post-shock region. The average post-shock ionization, Z_{ps}, was determined using tabulated data from PrismSPECT simulations, shown in Section 1.4.1, and depends on both the post-shock temperature, T_{ps} and post-shock mass density, ρ_{ps}. An estimate of the post-shock density, ρ_{ps}, can be made by considering the pressure in the post-shock region. This can be approximated as the pressure, P, of an idea gas of ions and electrons, given by:

$$P = \frac{\rho_{ps}(1 + Z_{ps})}{A m_p} k_B T_{ps} \tag{1.87}$$

where A is the atomic mass number, m_p is the proton mass and k_B is the Boltzmann constant. This may be equated to the ram pressure of the unshocked gas, given by:

$$P = \frac{\rho_0 v_s^2}{2} \tag{1.88}$$

Therefore the post-shock mass density may be estimated as:

$$\rho_{ps} = \frac{\rho_0 v_s^2 A m_p}{2 k_B T_{ps}(1 + Z_{ps})} \tag{1.89}$$

Eq. 1.84, Eq.1.85 and Eq.1.86 were solved numerically using a Python script. The total flux expended, right hand side of Eq. 1.84, was compared to the total kinetic energy flux, as

this is constant for a given shock velocity and initial mass density. If the total flux expended was lower, or higher, then the post-shock temperature could then be increased, or decreased. Post-shock variables, ρ_{ps} and Z_{ps}, could then be recalculated for this new temperature. The script iterated through this loop a thousand times until both the right and left hand side of Eq. 1.84 converged.

The resulting post-shock temperature and ionization estimates are shown as a function of initial shock velocity for a variety of gas-fills in Fig 1.15. Both increase at higher shock velocity and heavier atomic species achieve significantly higher post-shock ionizations (e.g. when $v_s = 100$ km/s $Z_{ps} = 5$ for Neon and $Z_{ps} = 10$ for Xenon) and slightly higher post-shock temperatures. Post-shock temperature is found to increase smoothly and undulations in the post-shock ionization approximately match those seen in simulations in Fig 1.4. Increasing the mass density of the initial gas fill results in significantly increased post-shock ionizations and temperatures for all species. In addition, estimates from the radiative only model, Eq. 1.83, are plotted with dotted lines. Reasonable agreement is found between the two models for high atomic mass numbers at high shock velocities and for low atomic mass numbers at low shock velocities. However, variations in post-shock temperature due to atomic species are not captured by the radiative only model.

The percentage of oncoming kinetic energy converted to radiation, ionization and thermal heating is plotted in Fig 1.16. In all gas species, all of the incoming kinetic energy is used to heat atoms at a low shock velocity and the majority is converted to radiation at high shock velocities. Due to higher post-shock temperatures, heavier gas species transition to a system dominated by radiative flux at a lower shock velocity. However, increasing the mass density of the initial gas fill was found to have the inverse effect, despite higher post-shock temperatures, with more energy being required to ionize and thermally heat the oncoming particles.

Predictions from this model are compared against experiments presented in this Thesis in Section 2.3.2 and Section 3.5.1. To further improve this model a more accurate treatment of

radiation is required.

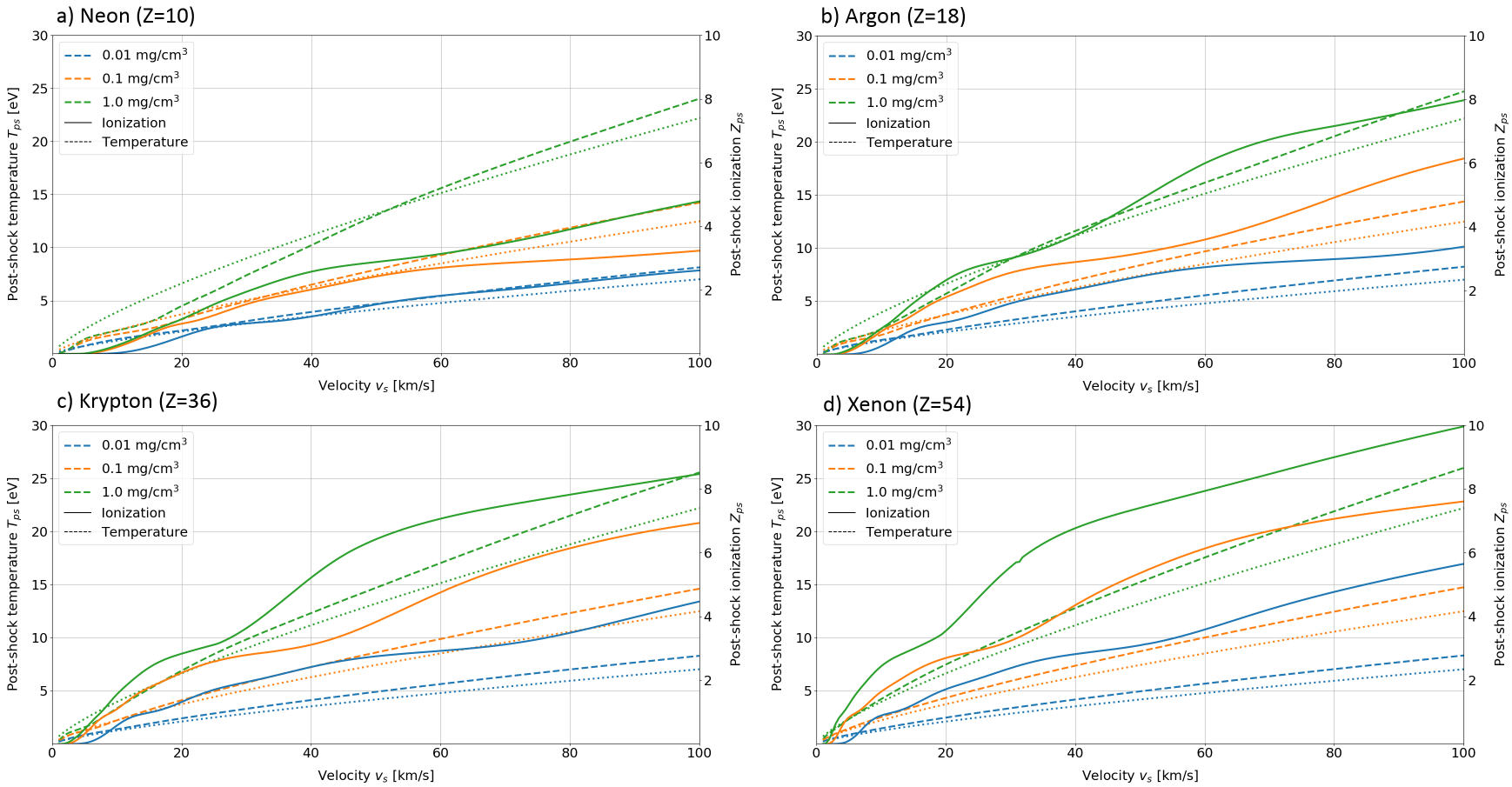


Figure 1.15: Post-shock temperature and ionization as a function of shock velocity. Calculated with the radiative shock model derived in this Section.

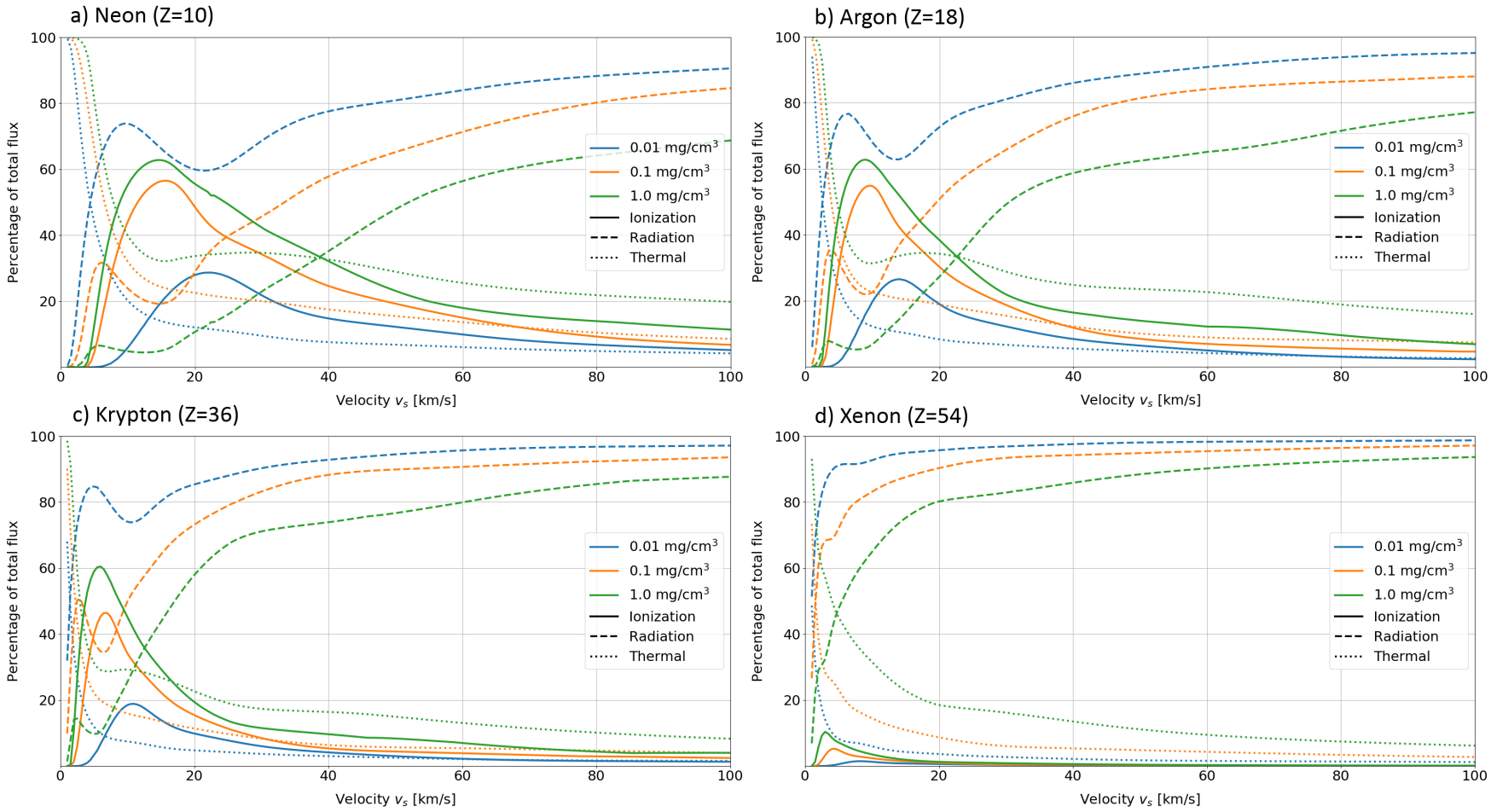


Figure 1.16: Percentage of kinetic energy converted to radiation, ionization and thermal heating. Calculated with the radiative shock model derived in this Section.

1.7 HEDP research

1.7.1 Laser driven radiative shock experiments

High powered lasers allow energy to be compressed both temporally, to ∼ns, and spatially, to ∼mm, allowing for the production of radiative shocks in the laboratory. In previous work, radiative shocks have primarily been driven in low pressure noble gases or low density foams, where the radiative regimes are accessible. A selection of notable previous experiments on radiative and reverse shocks is listed below, which experiments in Chapter 2 build on:

First observations of a radiative shocks in the laboratory

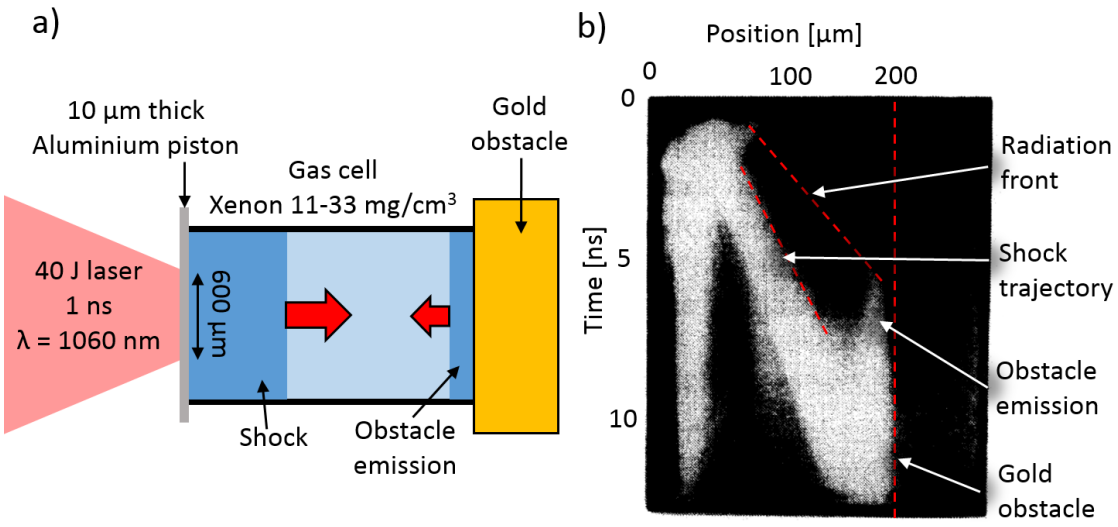


Figure 1.17: a) Experimental setup described in [Bozier et al., 1986]. b) Self-emission streak camera image from a radiative shock driven into a Xenon gas cell with an initial mass density of $\rho_0 = 11$ mg/cm^3. Reproduced from [Bozier et al., 1986].

Bozier et al. [Bozier et al., 1986] provided the first evidence of a radiative precursor propagating ahead of a laser driven shock. Experiments were performed at the CEA Limeil Laser Facility, where a 40 J laser (with a wavelength of 1060 nm and pulse duration of 1 ns) was focused onto a 10 μm thick aluminium foil. The foil served as a wall of a gas cell, filled with Xenon at $2-6$ bar ($\rho_0 = 11-33$ mg/cm^3). Laser ablation of the foil caused it to

act as a piston and drive a strong shock into the gas-fill, as described in Fig 1.17.a. This experimental configuration has been further developed by many groups studying radiative shocks, including experiments performed in this Thesis, described in Chapter 2. A streak camera was used to record self-emission and measured the shock velocity to be $v_s = 50 - 80$ km/s, as seen in Fig 1.17.b. A gold obstacle was placed ahead of the shock and emission observed prior to the collision. This indicated that radiation, emitted by the hot post-shock material, was preheating the obstacle.

First radiative shocks in aerogel and temperature measurements

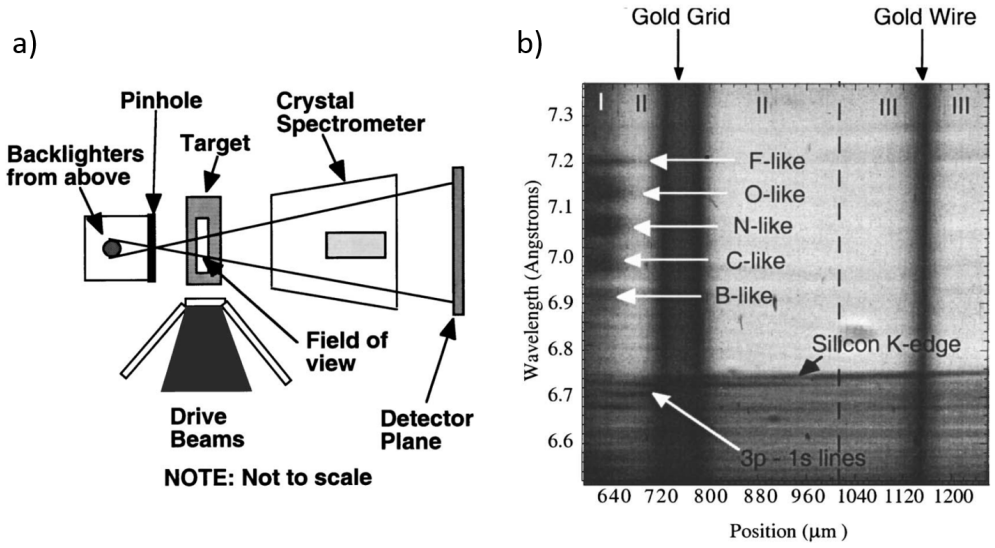


Figure 1.18: a) Experimental setup described in [Keiter et al., 2002]. b) X-ray absorption spectroscopy, reproduced from [Keiter et al., 2002].

Keiter et al. [Keiter et al., 2002] were the first to determine the temperature in a radiative shock experiment with spectroscopy, using the experimental setup described in Fig 1.18.a. A similar experimental platform to that used by Bozier et al. was used, however a SiO_2 aerogel foam was used in place of a gas-fill (with a mass density of $\rho_0 = 5 - 15$ mg/cm^3). Experiments were performed at the OMEGA laser facility, where ten separate beams (with a total energy of ~ 4 kJ, a wavelength of 351 nm and pulse duration of 1 ns) were focused onto a 60 μm thick plastic foil piston. This drove a radiative shock into the aerogel foam, propagating at

$v_s \sim 100$ km/s. X-ray absorption spectroscopy, shown in Fig 1.18.b, was used to measure the shock temperature to be $T \sim 30$ eV. This was significantly lower than predictions from 1D Hyades simulations, attributed to the 3D nature of the shock, as opposed to the 1D model.

First measurements of radiative precursor electron density

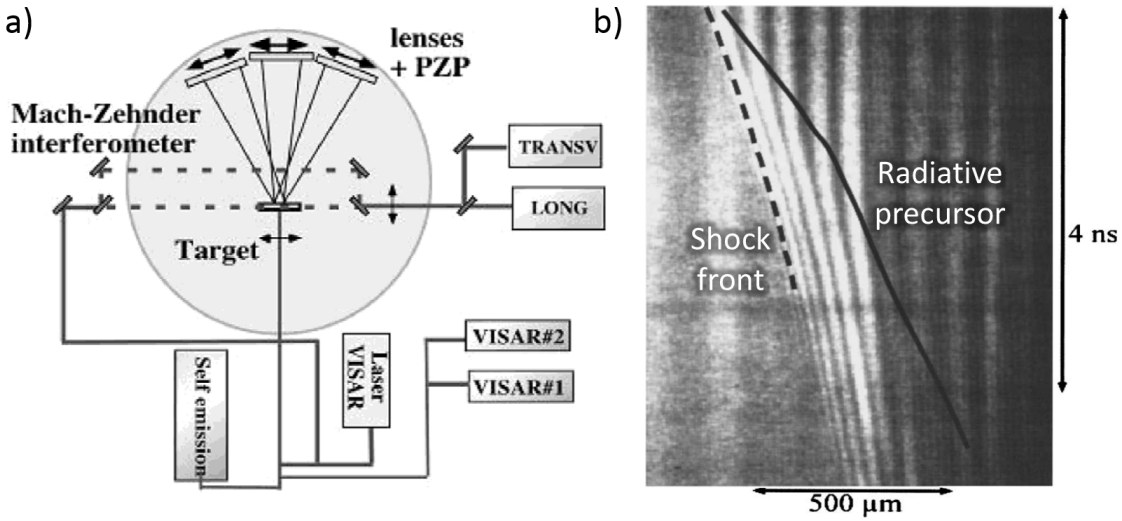


Figure 1.19: a) Experimental setup described in [Fleury et al., 2002]. b) Streak interferometry image reproduced from [Bouquet et al., 2004].

Both Fleury et al. and Bouquet et al. [Fleury et al., 2002, Bouquet et al., 2004] used the Laboratoire d'Utilisation des Lasers Intenses (LULI) facility to repeat experiments performed by Bozier et al., but with a more complete set of diagnostics, as shown in Fig 1.19.a. A 60 J laser (with pulse duration of 0.5 ns) was focused to a 600 μm spot on a composite foil piston on the side of a gas cell filled with Xenon, with an initial mass density of $\rho_0 = 1$ mg/cm^3. The piston consisted of a 2 μm thick layer of polystrene, acting as an ablator, a 3 μm thick layer of titanium, acting as an X-ray shield to prevent pre-ionization of the gas fill, and a 25 μm thick layer of polyethylene, acting as an accelerator. VISAR and Mach-Zehnder interferometry were used to measure shock velocity and free electron density within the precursor, shown in Fig 1.19.b. Results were compared with the 1D simulations MULTI and FCI, which confirmed the experimental shock velocity results but predicted higher precursor velocities.

Evolution of the radiative precursor

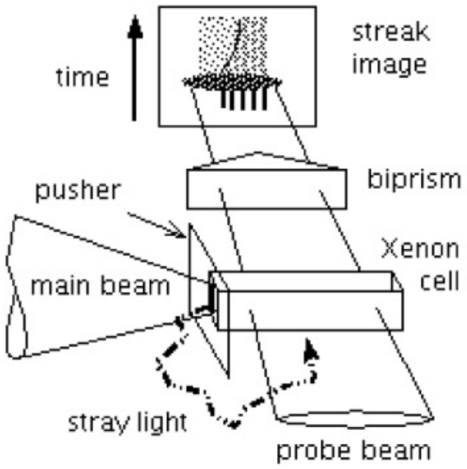


Figure 1.20: Experimental setup described in [González et al., 2006].

Gonzalez et al. [González et al., 2006] aimed to study the radiative shocks over a longer period of time, ∼40 ns using the experimental setup described in Fig 1.20. Experiments were performed at the Prague Asterix Laser System (PALS) facility with Xenon filled gas cells, with an initial mass density of $\rho_0 = 1$ mg/cm^3. A 700 J laser beam (with a wavelength of 438 nm and pulse duration of 0.35 ns) was focused to a 600 μm spot on a piston composed of a polystyrene ablator and gold x-ray shield. A shock velocity of $v_s \sim 60$ km/s was measured. Shadowgraphy and a visible streak camera were used to follow the dynamics of the precursor. The velocity of the radiative precursor was found to decrease in the early evolution of the radiative shock, before stabilizing at the shock velocity. To help understand this, 3D numerical simulations were performed using HERACLES which predicted a post-shock temperature of 15 eV. These simulations calculated radiation loss through the shock tube walls and discovered that this effect plays a major role in defining the length of the radiative precursor in this experiment.

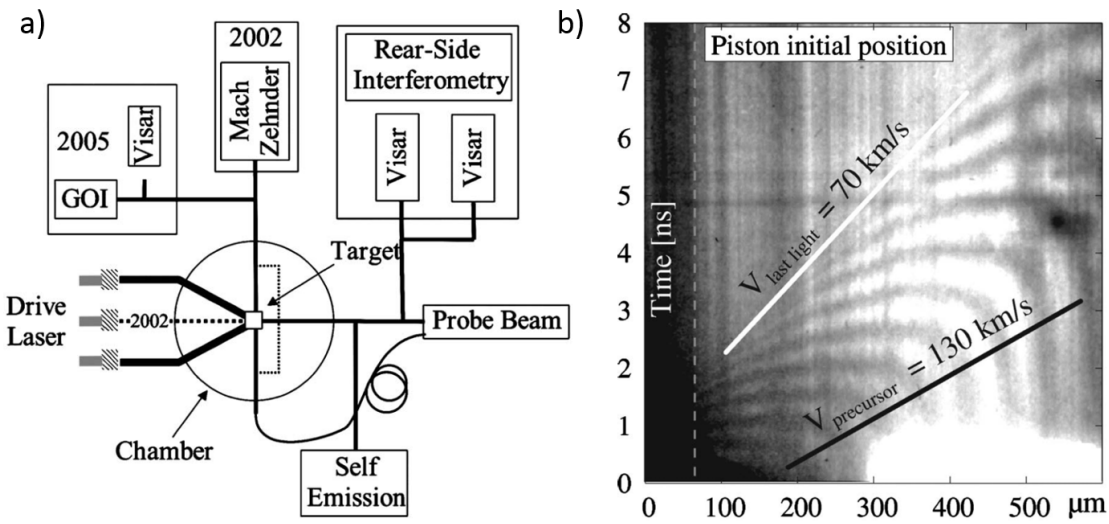


Figure 1.21: a) Experimental setup described in [Koenig et al., 2006]. b) Streak interferometry image. Reproduced from [Koenig et al., 2006].

Simultaneous measurements of the electron density and temperature

Koenig et al. [Koenig et al., 2006, Michaut et al., 2007] performed the first simultaneous measurements of electron density and temperature in a radiative shock using the experimental setup described in Fig 1.21.a. Experiments were performed at the LULI Facility with Xenon filled gas cells, with an initial mass density of $\rho_0 = 0.5 - 1.6$ mg/cm^3. Three lasers (with a total energy of 100 J, wavelength of 532 nm and pulse duration of 600 ps) were focused to a 300 μm diameter spot on a composite piston, with a 2 μm thick CH plastic ablator and a 3 μm thick Titanium X-ray shield. This drove radiative shocks with a velocity of $v_s \sim 70$ km/s, while a radiative precursor velocity of $\sim$ 130 km/s was observed. A significantly larger diameter gas cell was used, allowing the shock to also expand radially. Experiments were primarily diagnosed with self-emission and interferometry streak imaging, shown in Fig 1.21.b. In addition, self-emission gated optical intensifier (GOI) cameras recorded time-gated 2D images of the shock, allowing the radial expansion of the shocks to be studied. The post-shock temperature was determined to be $T \sim 16$ eV from the self-emission intensity while a similar temperature of $T \sim 15$ eV was determined for the radiative precursor region with shadowgraphy. These experiments were later repeated on the upgraded LULI2000

facility with increased laser energy of 1 kJ (delivered by two beams with pulse duration $1-5$ ns).

Quasi-planar radiative shocks in Xenon

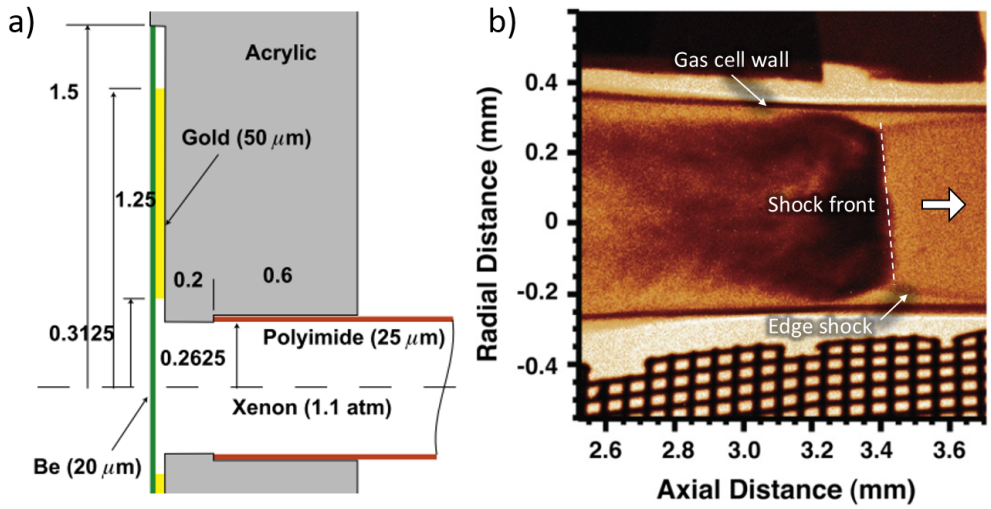


Figure 1.22: a) Experimental setup for producing quasi-planar radiative shocks in Xenon. b) X-ray backlighting showing transmission through the gas cell and shock. Darker regions indicate less transmission and thus higher mass densities. Reproduced from [Drake et al., 2011].

An extensive series of experiments to study radiative shocks have been performed at the OMEGA laser facility with a narrow shock tube filled with Xenon, with an initial mass density of 6 mg/cm^3, [Reighard et al., 2006, Doss et al., 2010, Drake et al., 2011] as described in Fig 1.22.a. Ten separate beams (with a total energy of ~ 4 kJ, a wavelength of 351 nm and pulse duration of 1 ns) were focused onto a 50 μm thick polyimide piston. The piston was coated with $20-40$ μm of polyvinyl or beryllium to absorb X-rays produced in the piston-laser interaction and thus prevent pre-ionization of the gas-fill. Laser ablation of the piston drove radiative shocks into the gas-fill, with a velocity of $v_s \sim 140$ km/s, at 8 ns, slowing to $v_s \sim 110$ km/s by 14 ns. The narrow shock tube resulted in quasi-planar shocks, but radiation from the post-shock material irradiated the gas cell walls. This resulted in plasma being ablated from the walls, forming transverse 'wall shocks' that disrupted the

primary shock. These experiments were diagnosed with X-ray backlighting which allowed the post-shock structure to be studied, as seen in Fig 1.22.b.

Shocks with non-negligible radiative pressure

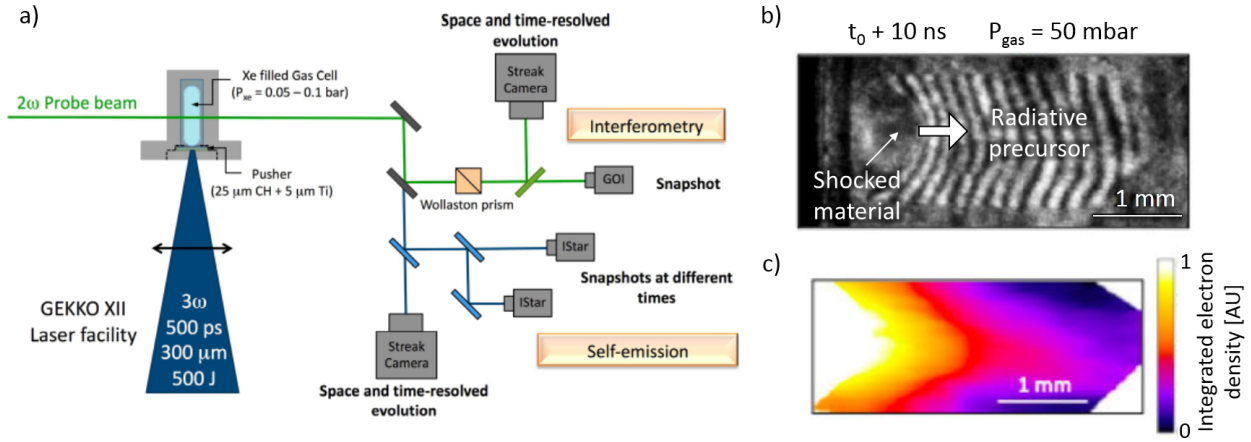


Figure 1.23: a) Experimental setup described in [Dizière et al., 2011]. b) Laser interferometry image of the radiative precursor. c) Map of line integrated electron density produced from laser interferometry images. Reproduced from [Dizière et al., 2011].

Dizière et al. [Dizière et al., 2011] produced radiative shocks with extremely high velocities, $v_s \sim 225$ km/s, resulting in non-negligible radiative pressure and thus accessing a new radiative shock regime, which is more representative of astrophysical phenomenon. Experiments were performed at the GEKKO-XII laser facility with the experimental setup described in Fig 1.23.a. Shocks were driven in Xenon filled gas cells, with an initial mass density of $\rho_0 = 0.2 - 0.6$ mg/cm^3, based on the design used by Koenig et al. Nine laser beams (with a wavelength of 351 nm and pulse duration of 0.5 ns) delivered a total of 1250 J to a 350 μm diameter spot on a composite piston, consisting of a 25 μm thick ablator layer of CH and 5 μm thick layer of Titanium which acted as an X-ray shield. These experiments were diagnosed with a combination of self-emission imaging and interferometry, shown in Fig 1.23.b. Interferometry allowed measurements of ionization in the radiative precursor to be made and showed a large, collimated radiative precursor, seen in Fig 1.23.c.

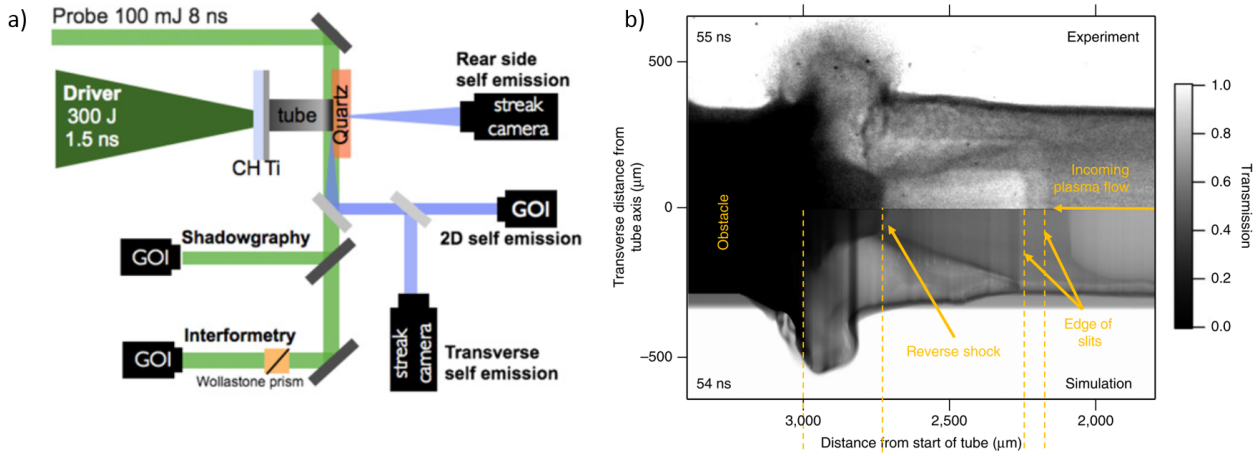


Figure 1.24: a) Experimental setup reproduced from [Falize et al., 2012]. b) X-ray backlighting showing transmission through the gas cell and shock, top shows experimental results and bottom shows synthetic images from 2-D simulations, reproduced from [Cross et al., 2016].

Falize et al. [Falize et al., 2012] attempted to model the reverse shock formed in highly magnetized cataclysmic variables using the experimental setup described in Fig 1.24.a. Experiments were performed at the LULI2000 laser facility where a 300 J laser beam (with a wavelength of 527 nm and pulse duration of 1.5 ns) was focused onto a foil, made of a 9 μm thick layer of plastic (CH) followed by a 5 μm thick layer of titanium. Ablation of the foil produced a plasma flow, propagating at $v_s \sim 80$ km/s, which was collimated using a PMMA plastic tube. A quartz obstacle was placed 2 mm away so that after the primary shock collided with it, a reverse shock was established. This expanded at $v_{rs} = 5 - 40$ km/s, increasing in velocity as it propagated through the decreasing density of the oncoming plasma flow. This experiment was diagnosed with self-emission streak imaging, shadowgraphy and interferometry. These experiments were found to closely agree with 2-D numerical simulations produced with the laser radiation hydrodynamic code. Cross et al. [Cross et al., 2016] further developed this experimental setup, using the Orion laser facility to deliver a total of 2 kJ to a 50 μm thick composite gold-plastic foil, resulting in plasma flow velocities of $v_s \sim 80$ km/s. This experiment was diagnosed with X-ray backlighting and optical self-emission streak

imaging, and showed excellent agreement with 2-D numerical simulations performed with the NYM Lagrangian radiative hydrodynamic code, shown in Fig 1.24.b. This simulation code is also used to model counter-propagatng radiative shock experiments performed in this Thesis, detailed in Section 2.5.

Asymmetric counter-propagating radiative shock experiments

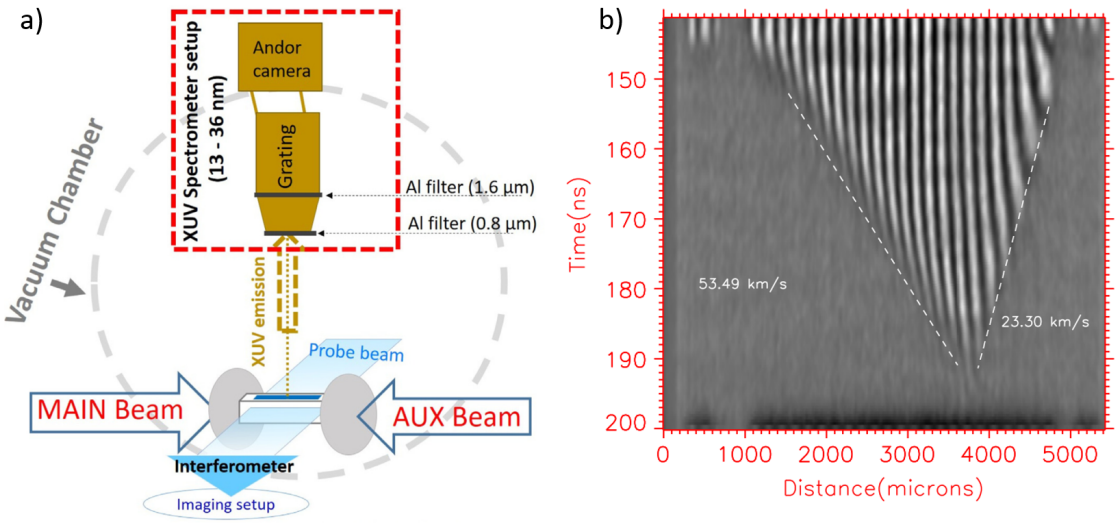


Figure 1.25: a) Experimental setup described in [Singh et al., 2017]. b) Streaked laser interferometry image of the radiative precursor. Reproduced from [Singh et al., 2017].

Singh et al. [Singh et al., 2017], including the author, performed a similar series of experiments to those described in Chapter 2. These experiments also drove two counter-propagating radiative shocks, albeit with lower energy, a different set of diagnostics and a narrow gas-cell resulting in quasi-planar shock evolution. The experimental setup is described in Fig 1.25.a. Experiments were performed on the PALS laser facility with Xenon filled gas cells, with an initial mass density of $0.5 - 3.3$ mg/cm^3. A 120 J laser beam (with a wavelength of 438 nm) was focused to a 550 μm diameter spot on to a piston (11 μm thick ablator of Parylene-N with a 0.6 μm thick gold X-ray shield) on one side of the gas cell. A second 60 J laser beam (with a wavelength of 1315 nm) was focused to a 300 μm diameter spot on a similar piston on the opposite side of the gas cell. This asymmetry in drive beams resulted in

asymmetric radiative shocks propagating with velocities of $v_s \sim 40$ km/s and $v_s \sim 20$ km/s (in experiments with an initial gas fill mass density of $\rho_0 \sim 1$ mg/cm^3). This experiment was diagnosed with streaked interferometry, shown in Fig 1.25.b, and XUV spectroscopy which indicated a post-shock temperature up to $T_{ps} \sim 15$ eV. After colliding, a reverse shock formed near the centre of the gas-cell with a temperature of $T_{rs} \sim 30$ eV.

1.7.2 Pulsed power driven radiative shock experiments

Pulsed power facilities also allow energy to be compressed both temporally, to ~ 100 ns, and spatially, to $\sim$mm. Several experiments studying plasma jets and radiative shocks have therefore been performed at the Mega Ampere Generator for Plasma Implosion Experiments (MAGPIE) facility, capable of providing a current pulse with a peak of up to 1.4 MA and 200 ns rise time [Mitchell et al., 1996]. This facility is also used for experiments performed in this Thesis and is described in detail in Section 3.1. A selection of notable previous experiments on plasma jets and radiative shocks are listed below:

Conical wire arrays

Lebedev et al. [Lebedev et al., 2005] produced supersonic plasma jets to model those emitted from young stellar objects. The MAGPIE current was passed through a conical array of 18 μm diameter Tungsten wires to produce a plasma jet which propagated along the axis at $v \sim 250$ km/s, as described in Fig 1.26.a-b. Experiments were expanded to model the effects of a cross wind, an angled plastic foil was placed above the wire array. This was irradiated by XUVs and soft X-rays emitted from the wire array which resulted in a constant stream of plasma being ablated from the foil, with an electron density of order $n \sim 10^{18}$ cm^{-3} and particle velocity of $20 - 40$ km/s.

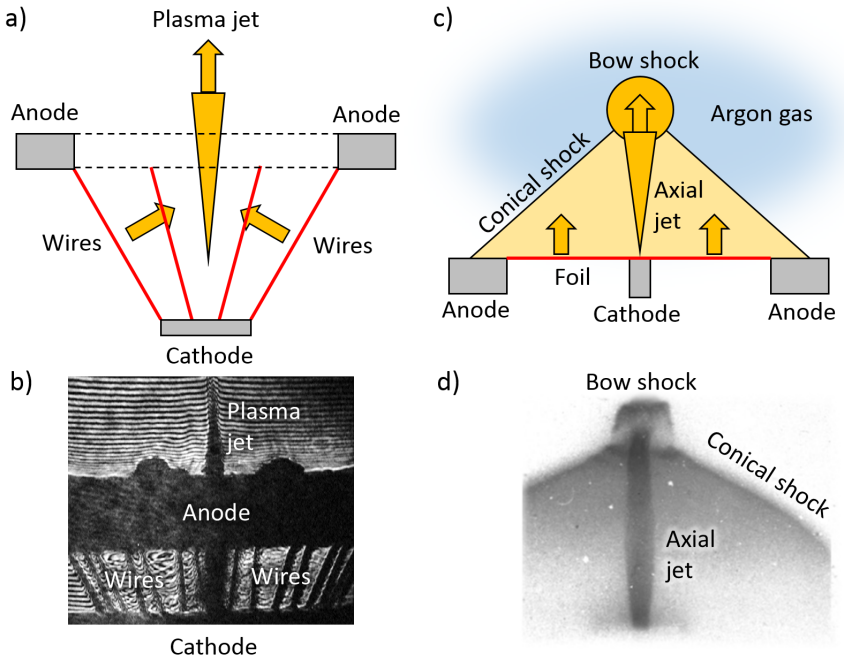


Figure 1.26: Experimental platforms used at the MAGPIE facility to study radiative shocks. a) Schematic of the conical wire array experimental platform. b) Interferometry image taken of a conical wire array experiment, reproduced from [Lebedev et al., 2005]. c) Schematic of the radial foil experimental platform. d) XUV self-emission image taken during a radial foil experiment with an ambient Argon gas, reproduced from [Suzuki-Vidal et al., 2012].

Radial foils

Lebedev et al. and Suzuki-Vidal et al. [Lebedev et al., 2005, Suzuki-Vidal, 2009, Suzuki-Vidal et al., 2010] further developed the radial foil platform for producing plasma jets. A 6 μm thick disk of aluminium foil was placed between two concentric electrodes with a radius of 55 mm and 3.1 mm as described in Fig 1.26.c. The MAGPIE current flowed radially through the foil causing it to Ohmically heat and generate a toroidal magnetic field. This resulted in plasma being ablated and accelerated upwards by the Lorentz force ($\mathbf{F} = \mathbf{j} \times \mathbf{B}$), and forming a cavity on the axis where there was no ablation. Plasma infilling this cavity and stagnating on the axis was redirected upwards forming an axial plasma jet as shown in Fig 1.26.c. Magnetic field diffusing through the foil resulted in episodic pinching of the plasma jet accompanied by the formation of expanding magnetic bubbles.

Suzuki-Vidal et al. [Suzuki-Vidal, 2009, Suzuki-Vidal et al., 2012] further modified the

radial foil experimental platform to produce collimated plasma jets and investigated their interaction with an ambient gas. A thicker radial foil, 15 μm, prevented the episodic formation of magnetic bubbles and instead resulted in a magnetically collimated plasma jet with an opening angle of $2-5^{\circ}$, particle velocity of 100 km/s and ion density of $n_i \sim 10^{18}$ cm^{-3}. A fast gas nozzle was used to create an ambient Argon gas medium above the radial foil, with a mass density of $\rho_0 \sim 0.004$ mg/cm^3. As the jet interacted with the argon gas-fill, a radiatively cooled spherical bow shock was formed at the jet axis, with a conical shock formed off-axis, shown in Fig 1.26.d. Experiments were also conducted using a gas cell, which allowed for a controlled and uniform ambient medium, yielding similar results.

Plastic formers

Skidmore et al. [Skidmore, 2013] expanded these experiments by introducing a larger gas cell and using plastic 'formers' coated with $\sim$1 μm of Aluminium, which allowed for higher fill pressures and arbitrary surface geometries. This new gas cell is also used for experiment performed in this Thesis on the MAGPIE facility, detailed in Chapter 3. Strong radiative shocks were produced, with a constant velocity of $v_s = 24-32$ km/s, showing similar results to Suzuki-Vidal et al. in an Argon gas fill.

Experiments were expanded to include other noble gas fills (Neon, Argon, Krypton and Xenon) while maintaining a constant mass density of $\rho_0 \sim 0.008$ mg/cm^3 in order to achieve similar shock hydrodynamics, such as the shock velocity. Experiments were primarily diagnosed with laser interferometry and showed higher peak electron densities in the shock front for higher atomic number (heavier) gas-fills, such Xenon and Krypton. In addition, heavier gas-fills exhibited significant ionization ahead of the shock front, indicating the presence of a radiative precursor and thus increased radiative effects with higher atomic number. Despite this, lower post-shock compressions were estimated for heavier gas-fills, in contradiction with predictions from 1-D HELIOS simulations.

Evidence of a thermal cooling instability was observed with shadowgraphy images of

shocks in Krypton and Xenon gas fills. The development of instabilities was suggested as a mechanism for limiting compression in heavier gases, increasing the effectively adiabatic index in these systems. Attempts were made to observe periodic oscillation of the shock front due to the thermal cooling instability, such as that observed by Hohenberger et al. [Hohenberger et al., 2010]. Self-emission images from experiments with a Krypton gas-fill indicated a period of ∼9 ns but were unable to confirm the existence of this phenomena.

Radially converging shocks

The concept of MagLIF [Slutz et al., 2010, Gomez et al., 2014] inspired experiments conducted on the MAGPIE and COBRA generators to study converging radiative shocks. These are detailed in several papers by G. C. Burdiak [Burdiak et al., 2013, Burdiak et al., 2014, Burdiak et al., 2015] as well as his award winning thesis [Burdiak, 2012]. Experiments performed in Chapter 3 of this Thesis build upon these experiments.

Cylindrically converging radiative shock were launched into noble gases with an initial mass density of $\rho_0 = 0.01$ mg/cm^3. This was achieved by discharging ∼1 MA of current through a 16 mm long Aluminium (Al 6061) liner with a wall thickness of 90 μm and outer diameter of 6 mm. The experimental setup is shown in Fig 1.27. However, unlike liner implosions in MagLif, the drive current in these experiments was insufficient to cause the liner material to move significantly. Instead, self-emission streak images in these experiments observed multiple converging shocks launched from the inner surface of the liner, seen in Fig 1.28.

The first shock was launched > 150 ns after current start and was observed to have a constant velocity of $v_s \sim 20$ km/s. This shock is believed to be launched mechanically (i.e. by material spalling off the inner surface) due to the magnetic pressure exceeding the material yield strength of the liner [Burdiak et al., 2015]. This occurred ∼90 ns after current start, shortly before this shock was launched. This would be ejected at $v_{pison} \sim 10$ km/s (double the sound speed in the Aluminium liner), resulting in shock velocities, $v_s = v_{piston}\Gamma/(\Gamma - 1)$

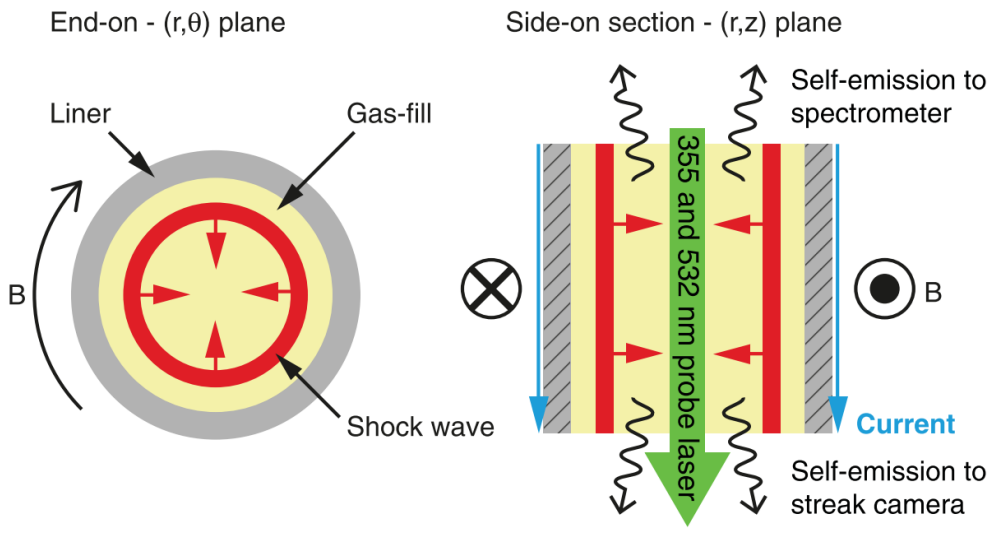


Figure 1.27: Experimental setup used for studying converging radiative shocks on the MAGPIE and COBRA generators. A fast rising current of ∼1 MA is passed through a thin walled liner, generating a strong toroidal magnetic field. The $J \times B$ force magnetically pinches the liner. However, the liner does not move on the time scale of the experiment and instead a radially converging shock, shown in red, is launched into a gas-fill. Reproduced from [Burdiak et al., 2015].

where Γ is the shock compression, found to be ∼5/3. This yields a velocity of ∼25 km/s, very similar to the experimentally measured shock velocity, $v_s \sim 20$ km/s.

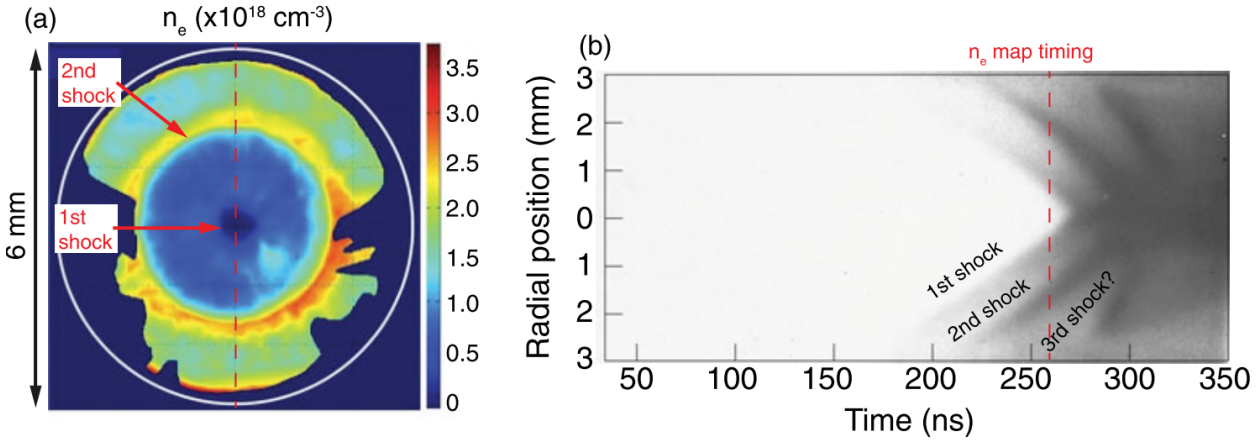


Figure 1.28: Experimental data from radially converging shocks experiments, reproduced from [Burdiak et al., 2015]. a) Map of the electron density looking down the axis of the liner, produced using laser interferometry. b) Streak image recording self-emission. Multiple converging shocks are observed and labelled in both images.

The second shock, labelled in Fig 1.28, has a curved trajectory indicating acceleration from

~20 km/s to ~50 km/s and so is believed to be magnetically driven. A strong correlation was found between the second shock launch time, ~240 ns and the time at which the liner melted. This was calculated by computing the energy deposited in the liner, finding good agreement with the energy required to take room temperature Aluminium to melting point. Melting of the liner results in a rapid increase in the resistivity, allowing the magnetic field to diffuse through the liner and for part of the current to switch to the gas adjacent to the liner. This formed a layer of plasma on the inside surface of the liner which could then be accelerated by the Lorentz force. As the shock converges, it accelerates as the magnetic pressure, $P_B \propto r^{-2}$, increases with lower radii. A magnetically driven shock, launched at a similar time, was reproduced in simulations run with the GORGON resistive MHD code [Weinwurm et al., 2013].

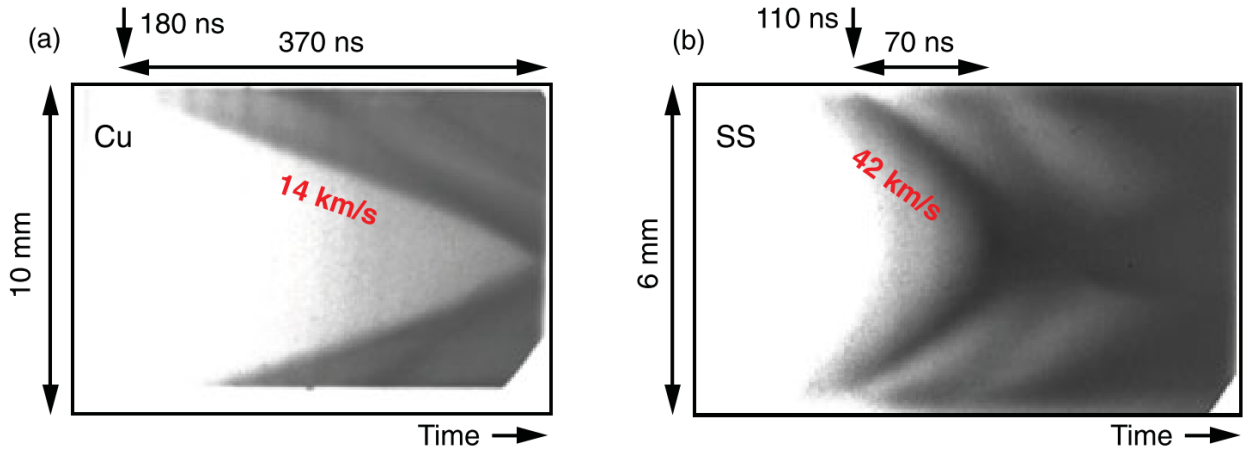


Figure 1.29: Self-emission streak images from radially converging shock experiments with different liner materials. a) Copper liners showing a single non-accelerating, mechanically driven, shock. b) Stainless steel liner showing an accelerating, magnetically driven, shock.

Experiments on liners with different materials offered further insight into shock launch mechanics [Burdiak et al., 2015]. Experiments using Copper liners (with a 10 mm diameter and 200 μm wall thickness) produced a single non-accelerating shock, as seen in Fig 1.29.a. This shock propagates at $v_s \sim 14$ km/s and was launched ~160 ns after current start, coincidental with when the magnetic pressure is expected to exceed the material strength. Therefore this shock is mechanically driven, like the first shock observed with Aluminium

liners. The high conductivity of the liner is expected to impede magnetic diffusion, resulting in lower magnetic/current skin depths. In addition, the large liner mass prevented bulk melting which would otherwise increase the resistance. Therefore no magnetically driven shocks were observed.

However, experiments using stainless steel liners (with a 6 mm outer diameter and 150 μm wall thickness) observed a single accelerating shock, as seen in Fig 1.29.b. This shock is launched early in time, $\sim$110 ns after current start, and propagates at an average of $v_s \sim 40$ km/s. This shock is magnetically driven as the higher liner resistivity results in current quickly switching to flow through gas adjacent to the liner, which is then accelerated by the Lorentz force. The higher material strength of steel resulted in no mechanically driven shock being launched in this experiment.

As all dynamics were located within an opaque metal liner and so the only method of probing the experiment was axially, as shown in the interferometry shown in Fig 1.28.a. This had the advantage that, assuming symmetry along the axis, any information integrated along probing lines (such as phase change in an interferometer setup) was constant allowing a local value to be determined simply by dividing by the length of the liner. However, the small diameter of the liners constricted the system to develop over a small region, where the converging shocks would not be able to propagate far before interacting. Radiation emitted by the post-shock material was able to propagate across the entire diameter of the liner. This resulted in the radiative precursors interacting at all times and no region of zero electron density. Therefore no region of zero phase change could be measured by the interferometry diagnostics and thus the absolute electron density could not be determined. In addition, as experiments took place within the liner, electrical and magnetic probes were difficult to field. Larger diameter liners may be able to mitigate these problems, but this would necessitate a thicker wall and significantly decreased the current density.

Chapter 2

Counter-propagating shock experiments

This Chapter describes counter-propagating radiative shock experiments, performed on the Orion laser facility at AWE Aldermaston, UK. These experiments simultaneously studied both the post-shock material and radiative precursor for the first time, with a combination of X-ray backlighting, self-emission streaked imaging and laser interferometry. The counter-propagating shock configuration allowed reverse shocks to be studied. In addition, large gas-cells allowed for shocks to evolve in three dimensions, resulting in the formation of post-shock instabilities which will be the subject of future work. These experiments have resulted in three publications in: 'High Energy Density Physics' [Clayson et al., 2017], 'Physical Review Letters' [Suzuki-Vidal et al., 2017] and 'High Power Laser Science and Engineering' [Spindloe et al., 2017].

Section 2.1 describes the Orion laser facility and experimental setup. Section 2.2 describes the diagnostic suite used to simultaneously study both the shock front and the radiative precursor. Section 2.3 investigates the evolution of the shocks, finding a shock velocity of $v_s \sim 60$ km/s and post-shock compressions of $\sim\times 23$, indicating strong radiative cooling. Section 2.4 investigates the radiative precursor observed ahead of the shock front and measures

it to be ∼200 μm wide in Neon and ∼500 μm wide in Xenon. Finally, Section 2.5 compares experimental results to those from radiative hydrodynamical 1-D and 2-D simulations, which were found to significantly overestimate the size of the radiative precursor.

2.1 Experimental setup

The experiments detailed in this Chapter introduce modifications which expand on previous experiments to study radiative shocks. Previous experiments have been performed in gas cells, usually filled with low density Xenon [Doss et al., 2010, Drake et al., 2011] or low density foams [Keiter et al., 2002, Foster et al., 2005]. High-powered lasers are focused onto a plastic foil on the side of the gas cell causing it to ablate. The expanding plastic plasma acts as a piston and drives a strong shock, propagating at velocities up to ∼100 km/s, as depicted in Fig 2.1.a-b. Many of these experiments focused on studying the radiative precursor [Bozier et al., 1986, Bouquet et al., 2004, Reighard et al., 2006, Koenig et al., 2006, Stehlé et al., 2010, Dizière et al., 2011, Chaulagain et al., 2015] while modifications to this experimental configuration have allowed for the study of more complex phenomena, such as the formation of reverse radiative shocks [Falize et al., 2012, Krauland et al., 2013, Cross et al., 2016] or collisions with obstacles [Hansen et al., 2007, Rosen et al., 2009]. In these experiments a significantly more complex system with two similar counter-propagating, collisional radiative shocks is introduced. This was achieved by focusing the Orion facility's 'long-pulse' beams onto plastic pistons on either side of a gas cell, as depicted in Fig 2.1.c. Ablation of these pistons drove two similar counter-propagating shocks towards the centre of the gas cell where they would collide and form a reverse shock.

The interaction of two identical radiative shocks, as presented in these experiments, is a model for the reflection of both hydrodynamics and radiation off of a perfectly reflective surface. Thus these experiments provide a unique platform for numerical validation and laboratory astrophysical models. While the collision of two independent shocks is a rare

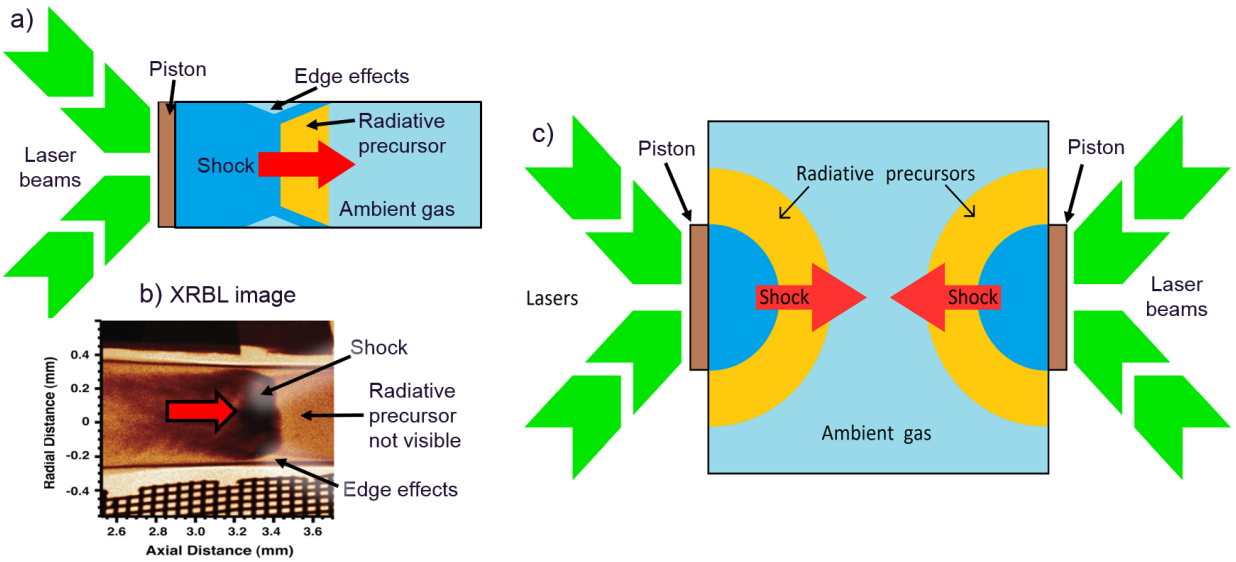


Figure 2.1: a) Diagram depicting how previous experiments have used high power lasers to drive radiative shocks. b) Example XRBL image showing a quasi-one dimensional radiative shock, reproduced from [Drake et al., 2011]. c) Diagram depicting these experiments.

astrophysical event, the formation of reverse shocks, which bear many similarities with the experiments presented here, are common place. These can occur, for instance, when supernovae remnants interact with dense molecular clouds [McKee, 1974], within the bow shock of jets launched from young stars [Hartigan, 2005] and as accretion shocks formed by material falling onto either young stars [Orlando et al., 2013] or dense objects in cataclysmic variable systems [Warner, 1995].

In addition, these experiments also introduce a new gas cell design with a large transverse width. This allowed shocks to expand freely into a large 3-D volume of gas without being confined by the side walls and thus preventing the formation of 'wall shock', found at shock velocities > 60 km/s [Doss et al., 2010, Drake et al., 2011]. In the future this platform may therefore be used to study 3-D effects, which may give rise to perturbations not found in 1-D and 2-D simulations. In principle, this could also lead to a more direct comparison to astrophysical phenomena.

2.1.1 Overview of the Orion laser facility

The Orion laser facility at AWE Aldermaston, UK, was used to perform counter-propagating radiative shock experiments and is described in detail by N. Hopps et al. [Hopps et al., 2015]. This facility hosts a 4 kJ neodymium glass laser and was designed to study high energy density relating to nuclear weapon development. The majority of experimental time on the Orion laser is dedicated to AWE, but a portion of the laser time is dedicated to academic research for furthering understanding of the conditions in astrophysics and inertial fusion.

A schematic of the Orion laser facility is shown in Fig 2.2. Orion is capable of producing ten 'long pulse' beams with a pulse duration of 1 ns, wavelength of 351 nm and up to 500 J of energy per beam (although ∼380 J is typically delivered by each beam). These are frequently separated into two groups of five beams, the 'Odd' and 'Even' beams. Each group enters the target chamber from different sides and can be seeded with a different pulse shape. In addition, Orion is capable of producing two 'short pulse' beams with a pulse duration of 0.5 ps, wavelength of 1054 nm and up to 500 J of energy per beam (although ∼230 J is typically delivered by each beam). These two beams may also be used as 'backlighter' beams, as was done for experiments in this thesis, in which case they are uncompressed and frequency tripled to 351 nm.

The long pulse beam lines are shown in the schematic in Fig 2.3.a. These are initially seeded with a 3 W continuous wave, fibre based commercial laser, labelled as 'CW osc.' in Fig 2.3.a. This sets the systems fundamental wavelength to be 1053 nm. Pulses are extracted from this and processed to achieve the desired pulse shape, typically a flat-top 1 ns pulse with a power of ∼50 mW.

This pulse is then transported via fibre to the pre-amplifier modules (PAM) in the laser hall, labelled as 'PAM01/PAM02' in Fig 2.3.a. This stage increases the beam power to a few millijoules using a regenerative Nd:YLF amplifier. The beam is then expanded to a beam diameter of 20.6 mm and a serrated aperture is used to produce a super-Gaussian beam

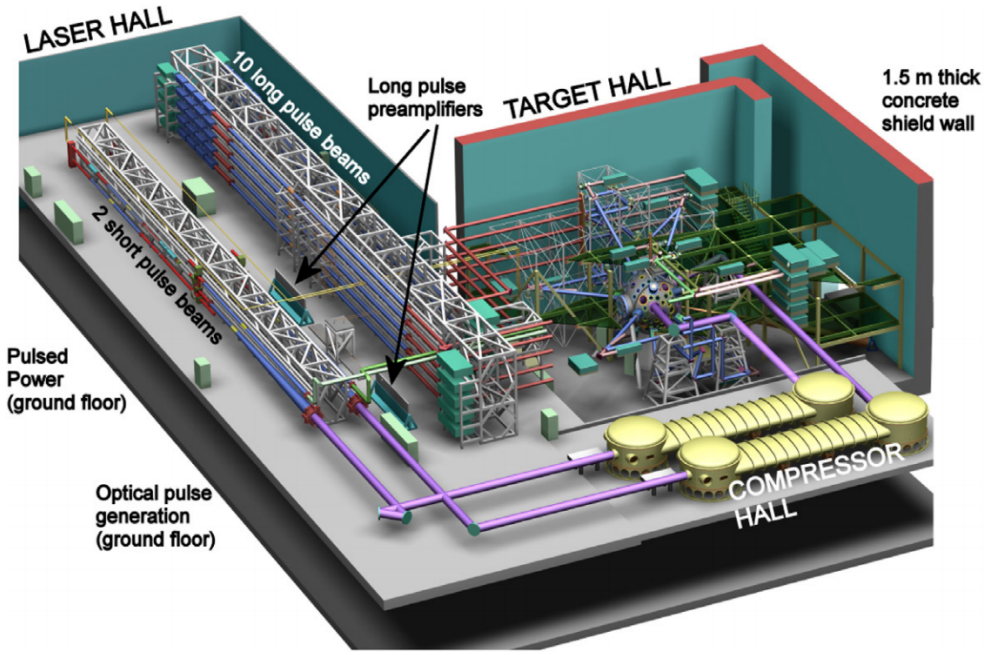


Figure 2.2: Schematic of the Orion Laser Facility, showing the laser hall, compressor hall and target hall. Reproduced from [Hopps et al., 2015].

profile. This is then further amplified using 32 mm diameter, flashlamp pumped, Nd:glass rod amplifiers. Each pass through this amplifier achieves a gain of $\times 10$ and four passes are achieved by polarisation switching, yielding a beam with $\sim$400 mJ of energy.

The output of the pre-amplifier is then split into ten beams using a cascaded series of half-wave plates and polarisers. The main amplification is performed on each beam separately with a series of four amplifiers, labelled as '200mm amps.' in Fig 2.3.a. Each amplifier has a gain of $\sim\times 2$ so that a double pass through all four achieves an amplification of $\sim\times 250$. The beams make four passes through these amplifiers achieving a total gain of $\sim\times 65000$ (with a Pockels cell gate isolating the first and second double pass to prevent self-lasing), amplifying the initial $\sim$15 mJ of each beam to $\sim$750 J.

The long pulse beams are passed to the target hall, using free space optics, where they are frequency tripled using a pair of 322 mm aperture KDP crystals, labelled as 'Frequency conversion' in Fig 2.3.a. Prior to entering the chamber dichroic mirrors, with a 351 nm reflective coating, allow the majority of the first and second harmonic to be excluded with a

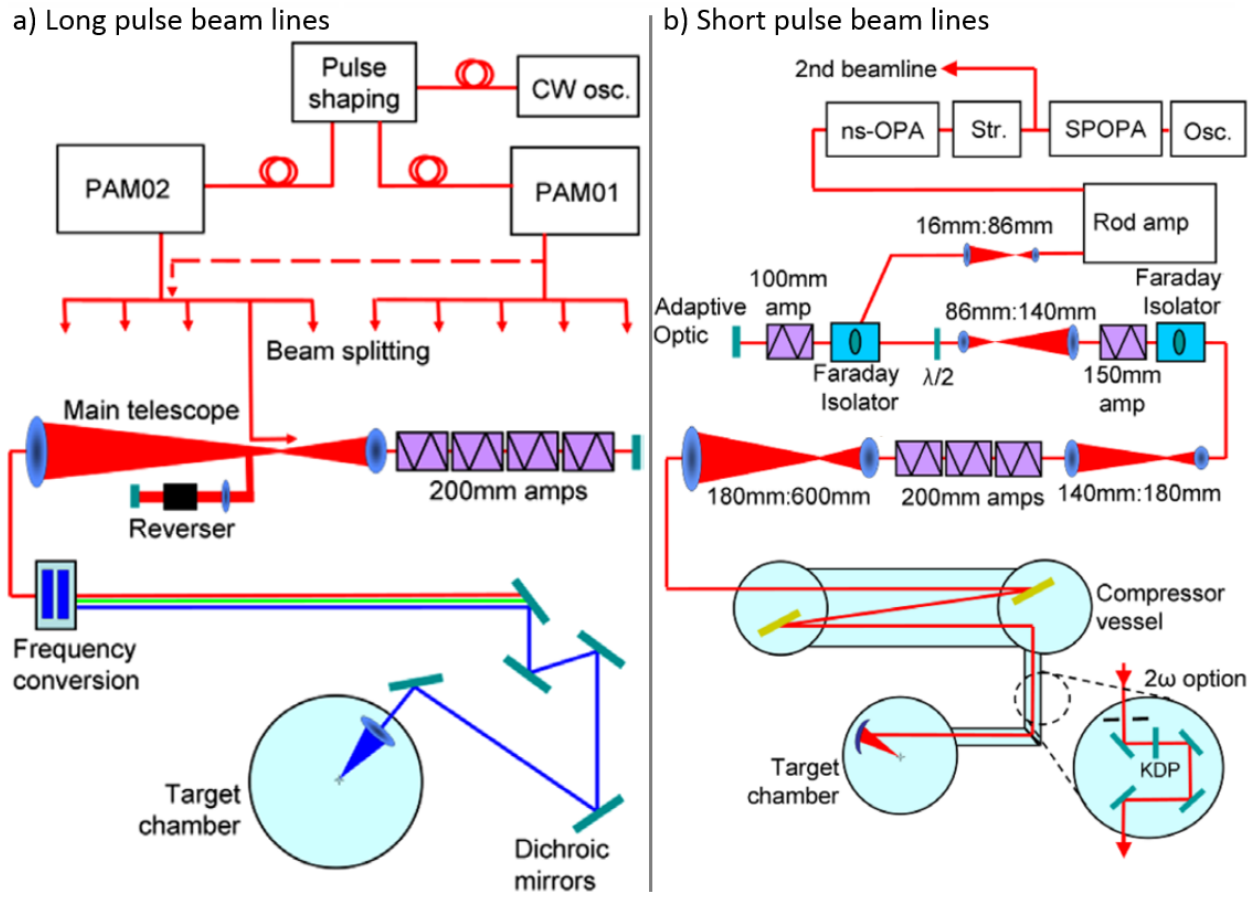


Figure 2.3: Schematic of the Orion beam lines. a) Long pulse beam lines. b) Short pulse beam lines. Reproduced from [Hopps et al., 2015].

discrimination of $\sim 10^{10}$.

The long pulse beams are focused into the chamber using $f/4$ aspheric focusing lenses with a focal length of 1200 mm. Beams are grouped into two groups, named 'odd' and 'even'. Each group converges on the target chamber centre (TCC) from opposite sides, forming two inverted cones sharing the same axis, depicted in Fig 2.4.b. The beams are evenly distributed and make an angle of 50° with the cone axis. Phase plates result in an eighth-power super-Gaussian circular profile with a minimum diameter focal spot of 290 μm. To measure beam quality on the final target and ensure beams arrive simultaneously, two gated X-ray detectors (GXD) diagnostics record X-ray emission on up to 12 images, each separated by 70 ps.

The short pulse beam lines are shown in the schematic in Fig 2.3.b. These are initially

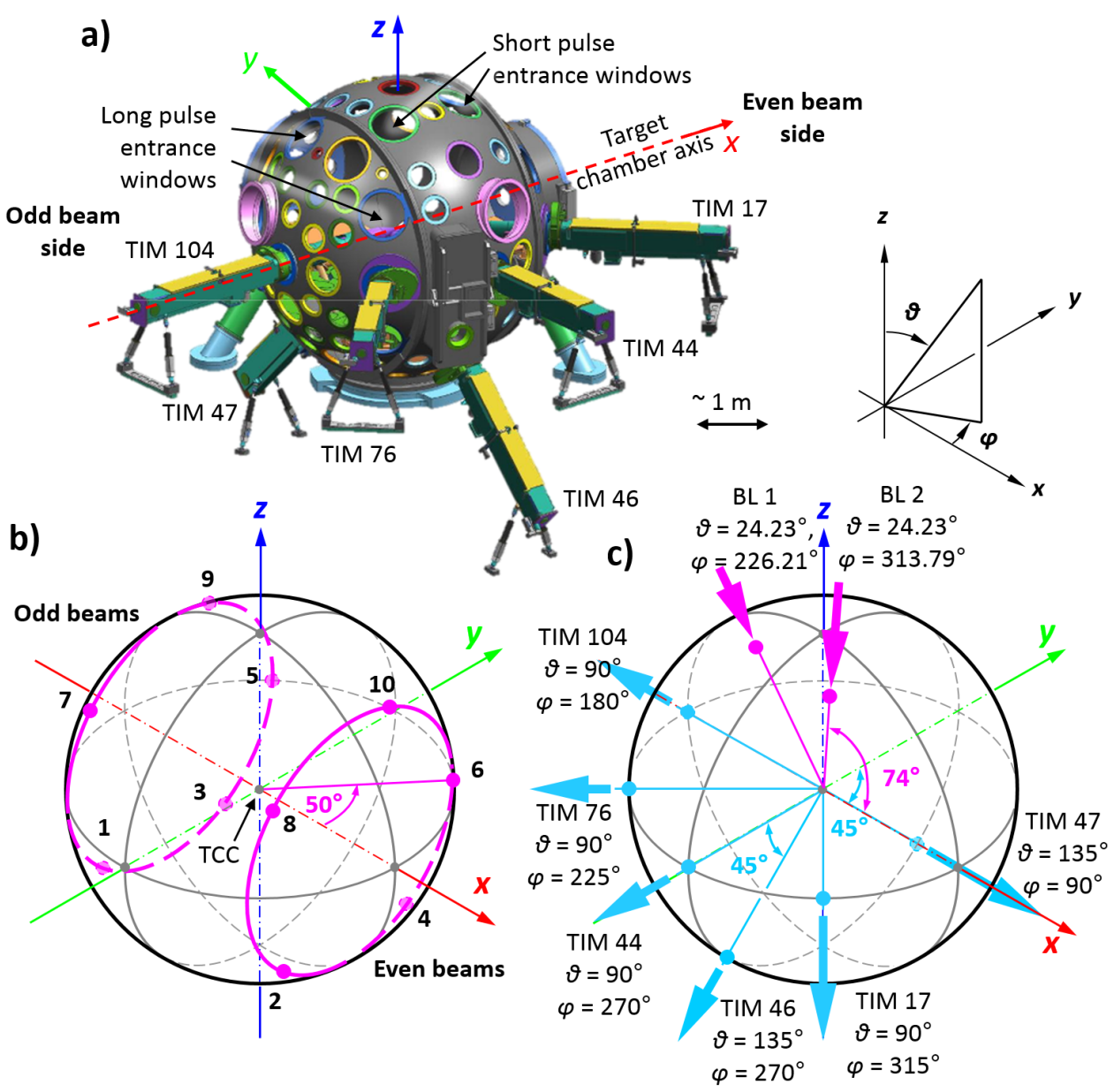


Figure 2.4: a) 3D CAD model of the Orion target chamber, reproduced from [Hopps et al., 2015]. b) Position of drive beams on the Orion chamber. c) Position of backlighter beams, labelled 'BL', and TIMs on the Orion chamber. [Hopps et al., 2015]

seeded with a mode-locked commercial laser, labelled as 'Osc.' in Fig 2.3.b, which produces 150 fs pulses with a wavelength of 1054 nm. Pulses are stretched to ∼1 ps and amplified to 40 μJ, in the component labelled as 'SPOPA' in Fig 2.3, before being divided.

After division to form two separate beams, pulses are then stretched to ∼1 ns to be amplified by a multi-stage optical parametric amplifier (OPA), labelled as 'Str.' and 'ns-OPA'

in Fig 2.3.b. To reduce jitter the OPAs for both beam lines are pumped by the same laser. This yields 1 ns long square function pulses with a total energy of 150 mJ. The short beam pulses are expanded to a diameter of 16 mm and relayed into the laser hall for the main amplification, labelled as 'Rod amp' in Fig 2.3.b. In a similar design to that found in the long pulse beams, PAMs are used to achieve four passes through 32 mm aperture Nd:glass rod amplifiers, amplifying the beam energy to ∼2 J. However, when firing in backlighter mode, as was done for experiments in this thesis, part of the output of the long pulses' PAMs are instead passed into the 32 mm aperture Nd:glass rod amplifier of the short pulse beam line.

The beams are further expanded to 86 mm and undergo a double-pass through a disk-amplifier, labelled as '100mm amp' in Fig 2.3.b, with an adaptive mirror allowing for minor corrections. This enhanced the energy of the beam to ∼50 J. The beams are further expanded to 140 mm and passed through another disk-amplifier, labelled as '150mm amp' in Fig 2.3.b, taking the beam energy to ∼150 J. Finally the beam is expanded to 140 mm and a series of three amplifiers, labelled as '200mm amps' in Fig 2.3.b, are used to raise its energy to ∼650 J.

If firing with short pulse beams, the beams are expanded to a large diameter of 600 mm prior to being passed into the compressor in order to prevent damage to downstream optics. Two compressors, labelled as 'Compressor vessel' in Fig 2.3.b, are held under vacuum and compress the ∼1 ns beams to ∼0.5 ps using a pair of gold coated diffraction gratings, with 1480 lines/mm, at 47.9°. The high power short pulse beams (∼1 PW) must now carried under vacuum to the target chamber.

However, when firing in backlighter mode, as was done for experiments in this thesis, the beams are left uncompressed, at $0.5 - 1$ ns, and are instead passed directly to the target hall. Both beams are frequency tripled to 351 nm using a pair of 322 mm aperture KDP crystals, achieving similar properties to the long pulse beams with a pulse duration of 0.5 ns and energy of ∼400 J. These are focused into the target chamber, entering at an angle of 74° to the long pulses cones axis shown in Fig 2.4.c.

The target hall (shown in Fig 2.2) is built around a large spherical target chamber with a diameter of 4.2 m, a 3D CAD model of which is shown in Fig 2.4.a This target chamber has been designed so that targets and diagnostics can be inserted through airlocks and remotely aligned. This allows the target chamber to maintain its vacuum for an entire experimental campaign and thus decreases the time between experiments.

Targets are inserted via an airlock on the top on the chamber and placed on a kinetic mount, known as the target positioning system, which is remotely driven to the centre of the chamber. The target positioning system has four degrees of freedom (three axes of movement and rotation about the vertical) which can be manipulated remotely to align the target anywhere within a $20 \times 20 \times 20$ mm cube to a high accuracy of 1 μm, with an accuracy of 0.01° in the rotational axis.

To position diagnostics closer to the target, diagnostics are mounted on a device known as a ten inch manipulator (TIM), with their position shown in Fig 2.4.c. These are based on a similar system used at the OMEGA laser facility at the University Laboratory For Laser Energetics in Rochester, USA. Each TIM contains a payload carrier and an airlock. Diagnostics or targets are mounted on the payload carrier and evacuated before being inserted in to the target chamber. Optical encoders on the payload carrier allow diagnostics to be automatically positioned to within 10 μm. In addition, the whole TIM is mounted on a 2-axis gimbal, allowing the diagnostic to move within the chamber to align the diagnostic.

2.1.2 Gas cell targets

The gas cell targets used in these experiments are shown in Fig 2.5. These targets were octagonal gas cells (8 mm across with a depth of 4 mm) manufactured by RAL/SciTech [Spindloe et al., 2017]. The targets were micro-machined from a single piece of aluminium and a 5 mm diameter hole was drilled through the centre of the octagonal faces. This large gas-cell diameter, relative to the small focal spot of 600 μm, was selected so that the shocks were able to expand freely into a large volume, avoiding interaction with the gas cell walls.

In addition, it offered diagnostic access from multiple angles.

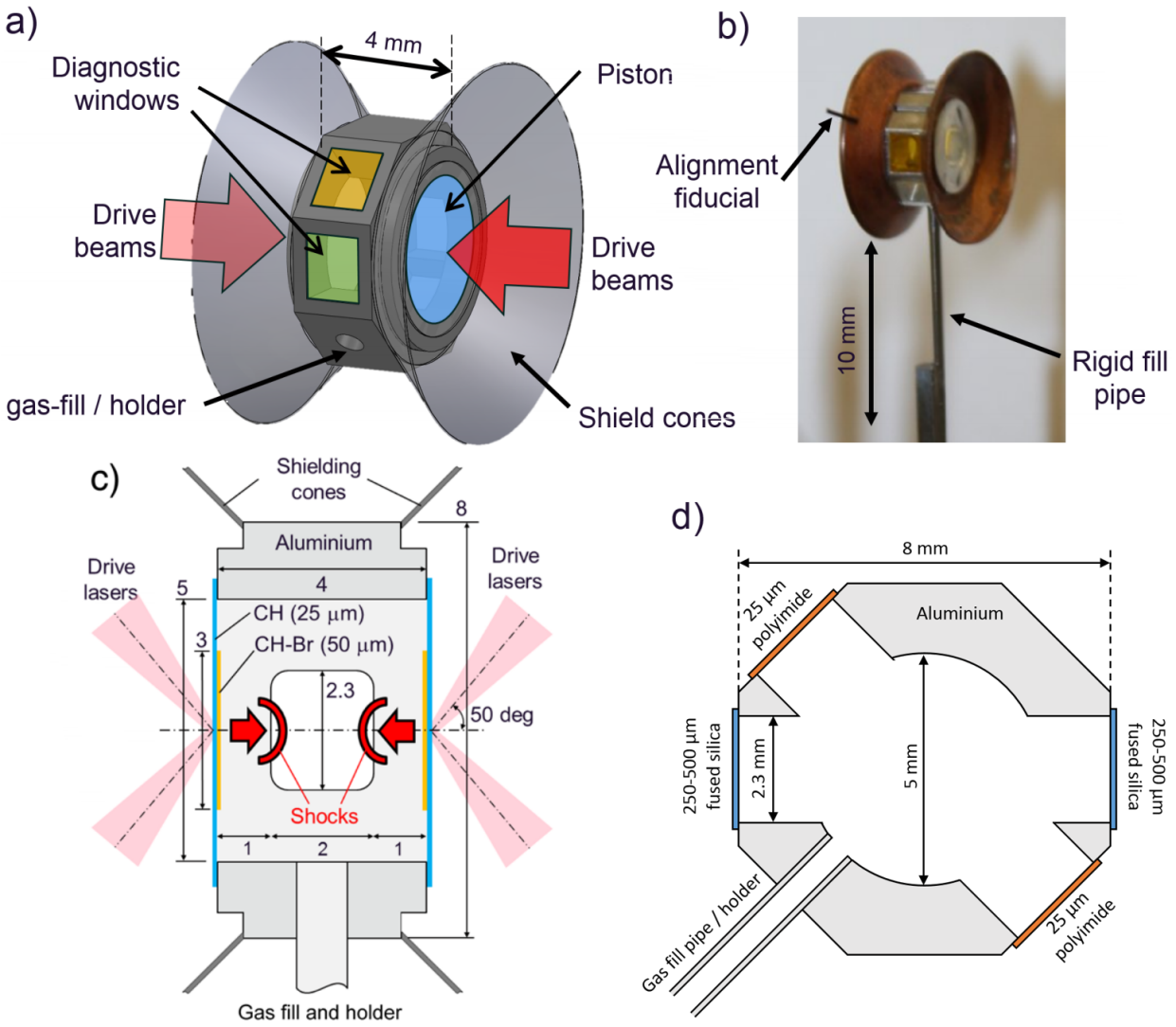


Figure 2.5: Details of the gas cell targets: a) 3-D CAD model. b) Photo. c) Side-on technical diagram. d) Face-on technical diagram. (all dimensions in mm)

Four diagnostic windows, with a width of 2 mm and height of 2.3 mm, were milled onto the rectangular faces, shown in yellow and green in Fig 2.5.a. These windows offered a view of the region where the two counter-propagating shocks interacted. However, a 1 mm wide region directly ahead of each of the pistons was obscured by the body of the gas cell. The windows were sealed with gas tight filters, allowing for transmission of X-rays or visible light for different diagnostics. Two filters, located on opposite faces, were made of 25 μm thick polyimide, for X-ray diagnostics, while the other two filters were made of fused silica for

optical diagnostics, with a thickness of either 250 μm or 500 μm. These were coated with an anti-reflection coating that matched the wavelength of the probe laser, 532 nm.

Copper shielding cones, shown in Fig 2.5.a-b, shielded diagnostics from X-rays produced at the laser focal spot. In addition a 100 μm wire, seen in Fig 2.5.b, was attached to these cones to act as a positioning fiducial for alignment when in the Orion vacuum chamber.

The gas cell was sealed with two circular, plastic pistons located on the two octagonal faces 4 mm apart, shown in blue in Fig 2.5.a. Ablation of these pistons by the Orion lasers drove the counter-propagating radiative shock into the gas fill, as described in Section 2.1.3. The structure of the pistons is shown in Fig 2.6. Pistons were made of polypropylene (CH) disks with a diameter of 5 mm, a thickness of 25 μm and a density of $\rho_{CH} \sim 0.9$ g/cm^3.

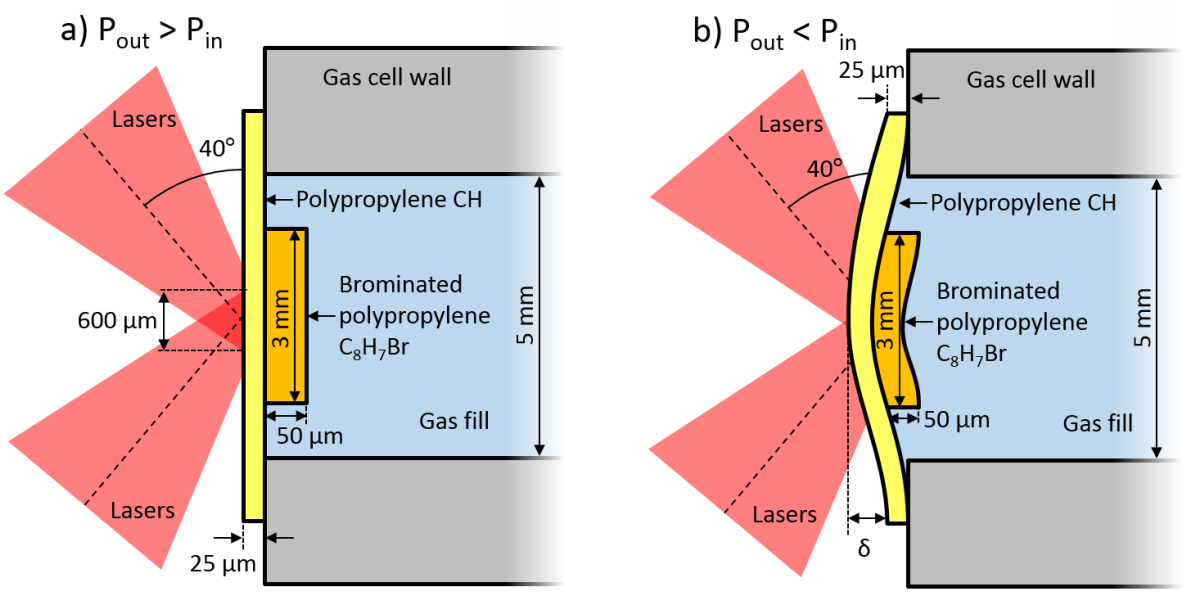


Figure 2.6: Schematic of the target piston for experiments at the Orion Laser Facility. a) When the exterior pressure, P_{out}, is greater than the pressure of the gas-fill, P_{in}. b) When the exterior pressure, P_{out}, is less than the pressure of the gas-fill, P_{in}, the piston bulges by δ. (not to scale)

Laser ablation of the pistons can result in a significant emission of X-rays and fast electrons which could preheat the gas-fill before the shock is launched, thus making it challenging to isolate the effects of a radiative precursor. Therefore, a layer of brominated polypropylene (C_8H_7Br), with a diameter of 3 mm, thickness of 50 μm and density of $\rho_{CHBr} \sim 1.53$ g/cm^3,

was attached to the piston on the inside surface of the gas cell with several spots of glue. This prevented gas from filling the gap between the polypropylene and brominated polypropylene that could result in perturbations being seeded into the resulting shocks.

As a result of pressuring the gas cells under vacuum, the pistons were found to budge slightly as indicated in Fig 2.6. Pistons were found to bulge by up to $\delta = 250$ μm with a fill pressure over 0.7 bar, shown in Fig 2.7. Analysis of experimental results therefore assumes an expansion of $\sim$200 μm, for a gas fill at 0.5 bar, so that the pistons are located at $\pm$2.2 mm relative to the centre of the gas cell. This was also taken into account for alignment of the drive beam lasers to ensure that the focal spot diameter remained at $\sim$600 μm during all experiments.

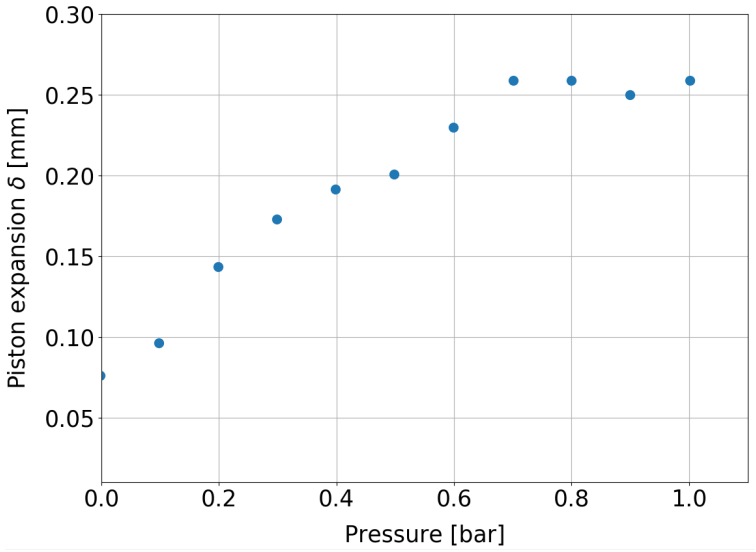


Figure 2.7: Gas cell piston expansion plotted as a function of fill pressure. Reproduced from [Spindloe et al., 2017].

The gas cells were held in position by a rigid metal gas fill pipe, shown in Fig 2.5.b. Prior to the experiment, gas cells were filled with noble gases (Neon, Argon, Krypton or Xenon) between 0.1 and 1.0 bar, whilst inside a separate vacuum vessel, shown in Fig 2.8. Gas cells were filled while under vacuum so that expansion of pistons and windows would not contribute to a reduction in gas-fill pressure when inside the Orion vacuum chamber. After filling, the gas cells were then removed from the vacuum vessel of the gas filling rig and

exposed to atmosphere pressures while being transferred to the Orion target chamber. The filters and pistons on the gas cells were therefore designed to hold both positive and negative pressures of up to ∼1 bar.

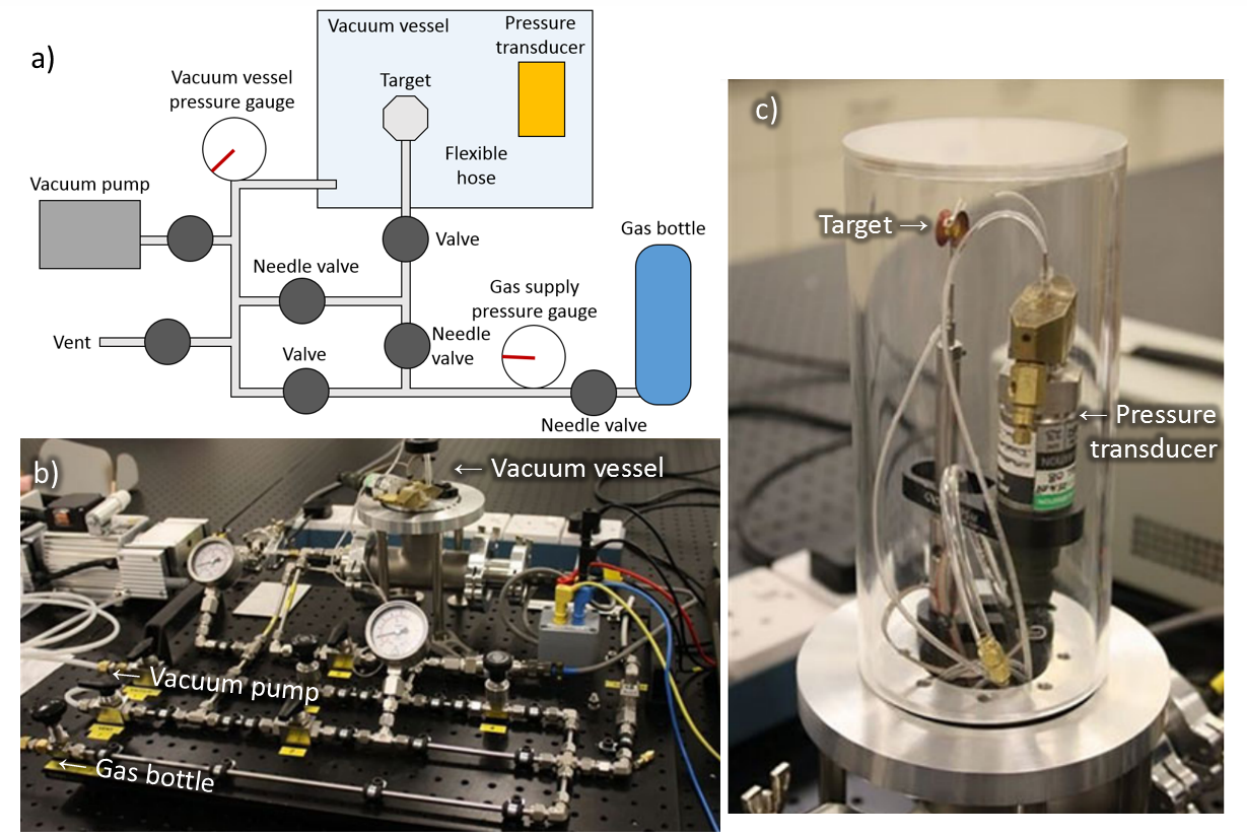


Figure 2.8: a) Diagram of the gas filling system used on the Orion facility. b) Picture of the gas filling system used to fill targets prior to the experiment. c) Picture of a gas-cell target under vacuum in the testing chamber. Reproduced from [Spindloe et al., 2017].

While inside the Orion target chamber a pressure transducer was connected to the fill pipe, allowing the gas pressure to be monitored until less than a minute before firing. Gas cell targets were aligned under vacuum inside the Orion target chamber and so had to maintain fill pressure for up to an hour prior to firing. Thus the gas cells were overfilled so that the fill pressure would have dropped to the desired value once ready for firing.

2.1.3 Laser-piston interaction

To drive the counter-propagating radiative shocks, four of the Orion facility's long-pulse beams were simultaneously focused to a ∼600 μm diameter spot on each of the plastic pistons. Ablation of the pistons then resulted in a strong shock being driven into the gas-fill. While it is possible to focus five beams onto each piston, a fault in one of the beam lines during the experimental campaign meant that the majority of experiments were performed with just four beams per piston, ensuring a consistent drive power.

Each beam is angled by 50° relative to the normal of the piston resulting in elliptical focal spots ∼600 μm by ∼900 μm. These were overlapped as shown in Fig 2.9.a to ensure the majority of the energy was deposited in a ∼600 μm focal spot. In the optimal case this resulted in 67% of the energy being deposited in a uniform ∼600 μm diameter focal spot. However, due to the slight expansion of the piston under different gas filling pressures (up to ∼250 μm with pressures over 0.7 bar) the focal spots would move radially outwards by up to ∼300 μm, as shown in Fig 2.9.b. To compensate for this effect, expansion of the pistons as a function of filling pressure was measured prior to the experiment, shown in Fig 2.7 and the laser focus offset accordingly. Beam focus was monitored with two Gated X-ray Detectors (GXD) cameras, one focused on each piston. Example GXD images of well focused drive beams and target misalignment are shown Fig 2.9.c-d.

Fig 2.10 shows the beam energy for all experiments performed on the Orion laser facility. The average laser power for the odd and even long pulse beam groups and backlighter short pulse groups (labelled as 'XRBL' and detailed in Section 2.2.1) are shown in Table 2.1, excluding experiments 5037, 5038 and 5040 (where all ten beams were used to perform high powered tests) and experiments 5285 (where timings of the streak cameras were recorded).

In 29 experiments an average energy of 1528 ± 126 J was delivered to the target, approximately 67% of which was focused to the ∼600 μm diameter spot on each of the plastic pistons achieving an intensity of $3.6 \pm 0.3 \times 10^{14}$ W/cm^2 and total energy of ∼1000 J in the focal

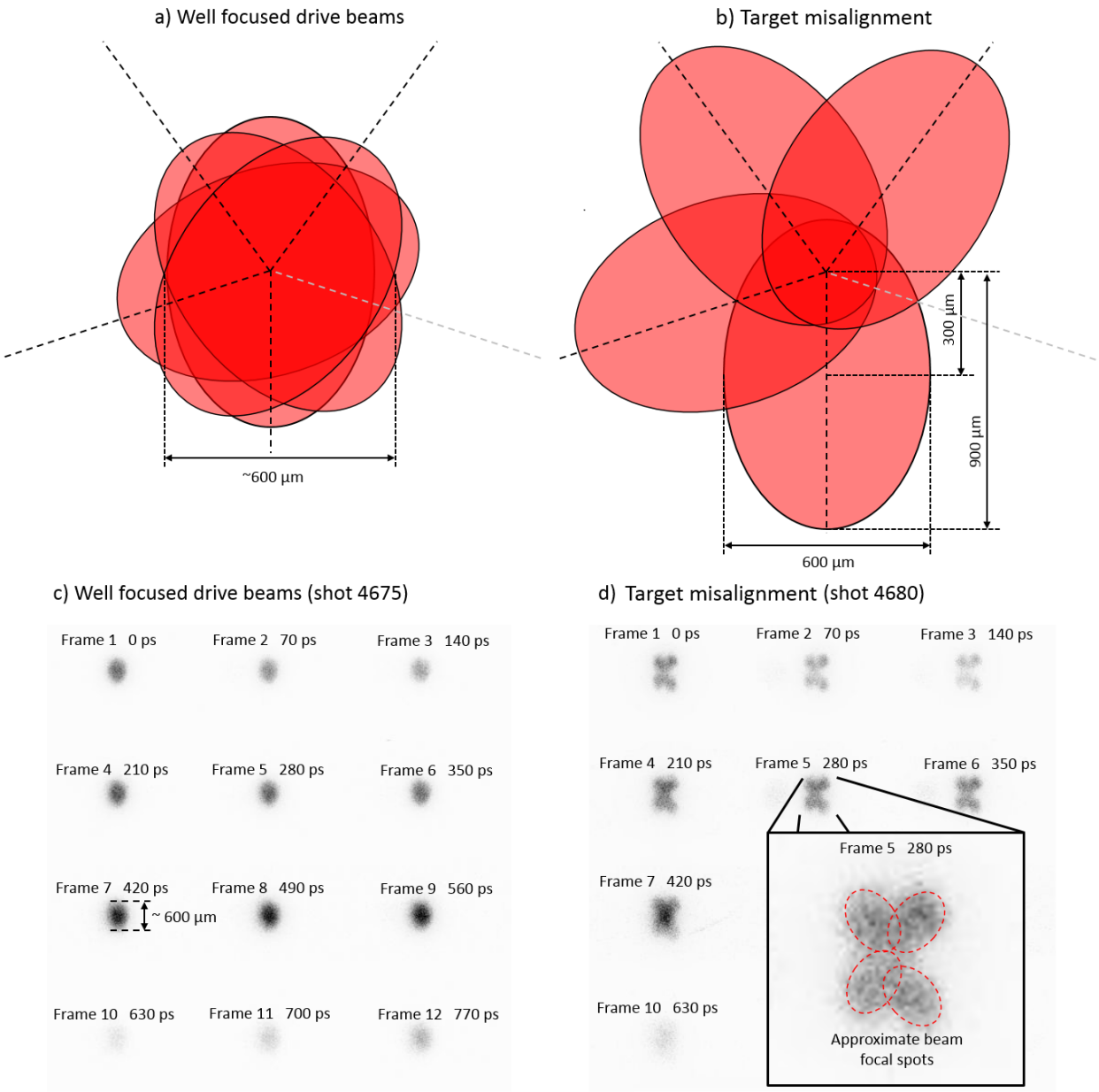


Figure 2.9: Examples of how the drive beams were expected to overlap on the target pistons. a) Well focused drive beams. b) Target misalignment resulting in drive beams focal spots being offset by 300 μm. c) GXD images of well focused drive beams. d) GXD images of focal spots on a misaligned target.

spot. The long-pulse beams, used for ablating the pistons, are consistent with a standard deviation of $< 7\%$. This consistency allows for comparisons to be drawn between different experiments as shocks are expected to propagate at similar velocities.

Pulsed lasers allow large amounts of energy to be compressed to small temporal and

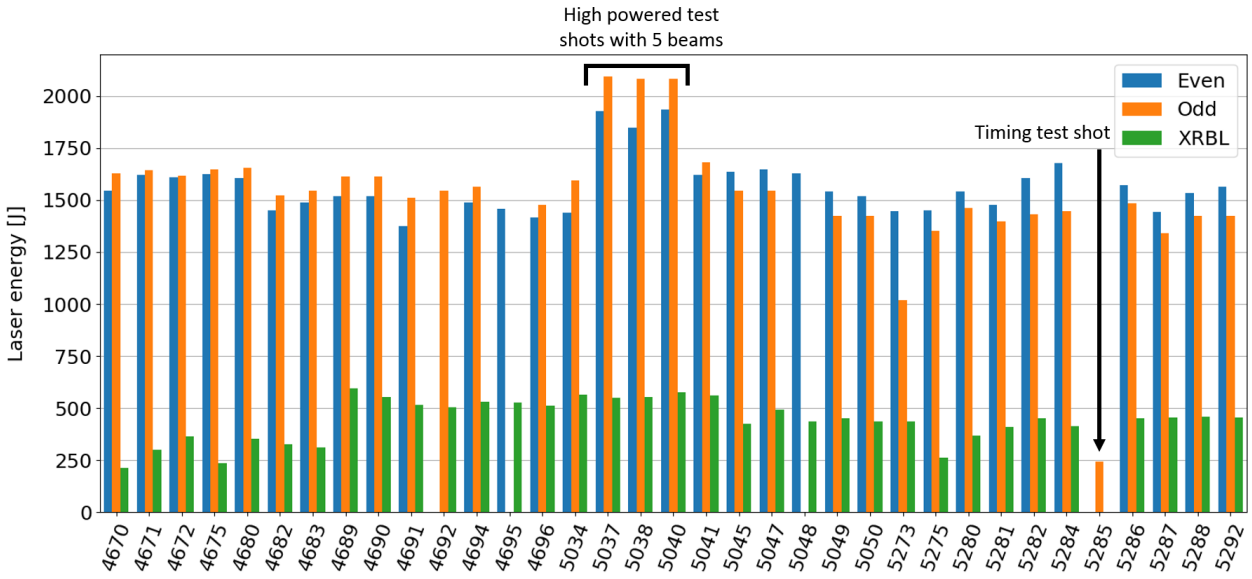


Figure 2.10: Total beam energy for each experiments performed on the Orion laser facility.

Beam group	Average energy
Even beams	1520 ± 97 J
Odd beams	1535 ± 80 J
Backlighter beams	442 ± 101 J

Table 2.1: Average laser power for experiments on the Orion facility with fours beams per piston. Calculated from 29 experiments.

spatial scales. Therefore focusing a high powered laser beam onto the surface of a material can result in ablation and can drive a shock into the material, as shown in Fig 2.11.

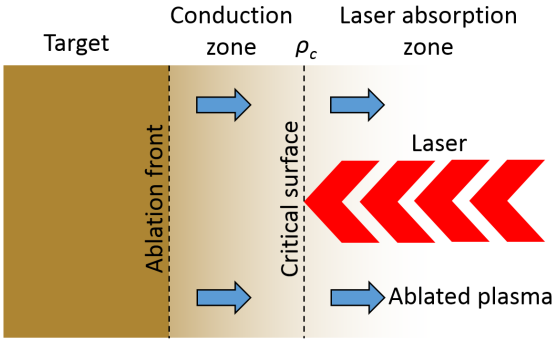


Figure 2.11: Schematic of laser driven ablation. The laser is incident from the right hand side and a shock is driven to the left while material is ablated to the right.

Material is ablated from the ablation front and forms a layer of expanding plasma. As the

Wavelength λ [nm]	Critical density n_c [cm^{-3}]
1064	9.85×10^{20}
532	3.94×10^{21}
355	8.85×10^{21}
351	9.05×10^{21}

Table 2.2: Critical electron density beyond which the plasma is opaque to a laser.

laser approaches the material it is absorbed by this plasma through inverse bremsstrahlung (described in Section 1.4.4). This is preferentially performed by the electrons, due to their low mass, and scales strongly with the electron density. Therefore, the laser is primarily absorbed at the critical surface, where the electron density reaches the critical density, n_c, and the laser frequency is similar to the plasma frequency and the laser is unable to penetrate further. The critical electron density is dependent on the laser wavelength, λ, and is given by:

$$n_c = \frac{4\pi^2 \epsilon_0 m_e c^2}{e^2 \lambda^2} \tag{2.1}$$

where ϵ_0 is the vacuum permittivity, m_e is the electron mass, c is the speed of light in a vacuum and e is the elementary charge. The critical density for several commonly used laser wavelengths is given in Table 2.2. When approaching at an oblique angle of θ, the laser is primarily absorbed when the electron density $n_e = n_c cos^2(\theta)$.

For a plasma with an average ionization of $< Z >$ and atomic mass A, the mass density at the critical surface, ρ_c can be determined as:

$$\rho_c = \frac{m_p A}{< Z >} n_c = \frac{m_p A}{< Z >} \frac{\pi m_e c^2}{e^2 \lambda^2} \tag{2.2}$$

where m_p is the mass of a proton. For experiments described in this part of this thesis a laser with a wavelength of $\lambda = 351$ nm was used, resulting in a critical electron density is $n_c = 9.05 \times 10^{25}$ cm^{-3}. Lasers were focused onto a polypropylene piston at an angle of 50° and so were absorbed at an electron density of $n_e = 3.74 \times 10^{21}$ cm^{-3}. Modelling the piston this as fully ionized carbon, with $A = 12$ and $< Z >= 6$, results in a mass density

at the critical surface of $\rho_c = 0.125$ mg/cm^3. This is significantly lower than the initial polypropylene density of $\rho_{CH} \sim 900$ mg/cm^3.

2.2 The Orion diagnostic suite

The octagonal targets used in counter-propagating radiative shock experiments provided access for multiple diagnostics and a view of the shock interaction region, as shown in Fig 2.12. X-ray Backlighting (XRBL), described in Section 2.2.1, captured a single 2-D image of X-ray transmission per experiment. This allowed the post-shock material to be studied. Optical self-emission of the shocks was recorded from a 1-D lineout along the centre of the gas cell by a streak camera, described in Section 2.2.2, in order to study the shock evolution over time. Laser interferometry, described in Section 2.2.3, was simultaneously performed in order to study the pre-shock precursor region and measure the electron density ahead of the shock front. Four 2-D images of laser interferometry were captured with gated optical intensifier (GOI) cameras and a 1-D lineout, along the centre of the gas cell, was recorded with a streak camera. In addition, a pressure transducer recorded the gas pressure immediately before firing and two gated X-ray detectors (GXD) recorded X-rays emission from the laser piston interaction, as shown in Fig 2.9.c-d.

2.2.1 X-ray backlighting (XRBL)

X-ray backlighting (also known as X-ray radiography) is a widely used diagnostic for imaging mass densities in plasma physics experiments [Matthews et al., 1983, Workman and Kyrala, 2001, Sinars et al., 2003, Park et al., 2006]. X-rays passing through dense materials will be attenuated more than those passing through less dense materials. Therefore, by placing an X-ray source on one side of the plasma and an X-ray detector on the other side, the path integrated density of the plasma can be spatially and temporally resolved.

X-rays with energies $E > 1$ keV can be generated by focusing lasers onto high atomic

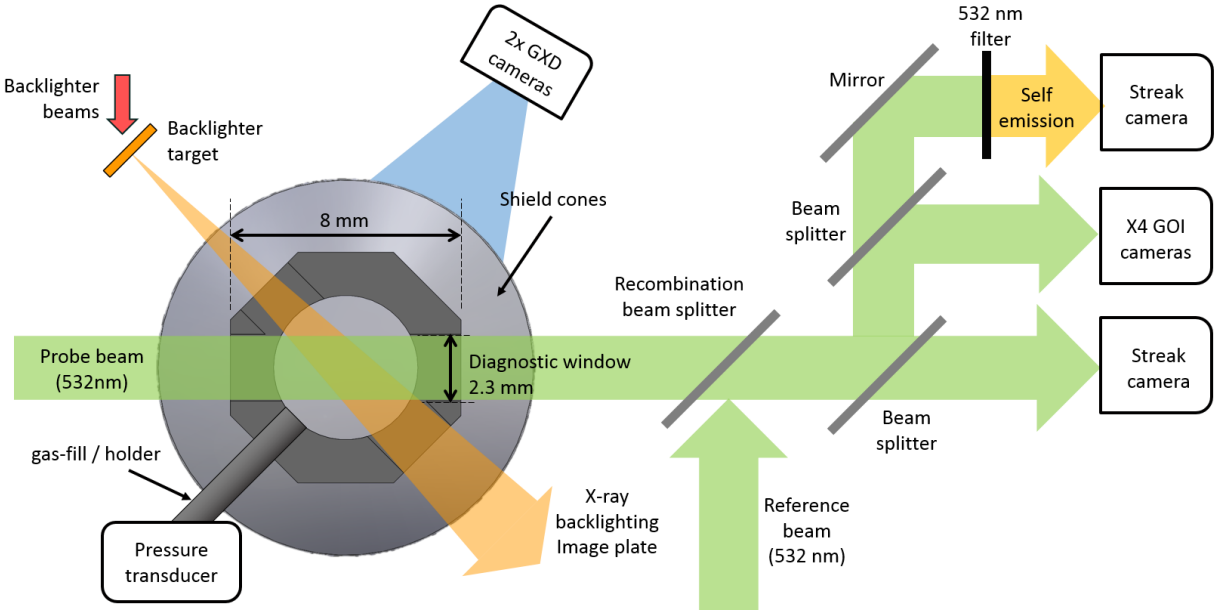


Figure 2.12: Cross section of the gas cell and schematic of diagnostics fielded on these experiments.

number materials, such as Iron, known as a backlighter target. This creates a hot plasma which emits high energy X-rays from electron transitions [Matthews et al., 1983, Phillion and Hailey, 1986].

Emission from plasmas, formed by lasers with intensities between $\sim 4 \times 10^{14}$ and $\sim 2 \times 10^{16}$, is dominated by the narrow band Helium-like transition $1s2p \rightarrow 1s^2$ [Workman and Kyrala, 2001], for instance at 6.7 keV in Iron, as shown in Fig 2.13. This is the transition from the L-shell ($2p$) to the K-shell ($1s$) in an ion with just two electrons and is known as He_α emission.

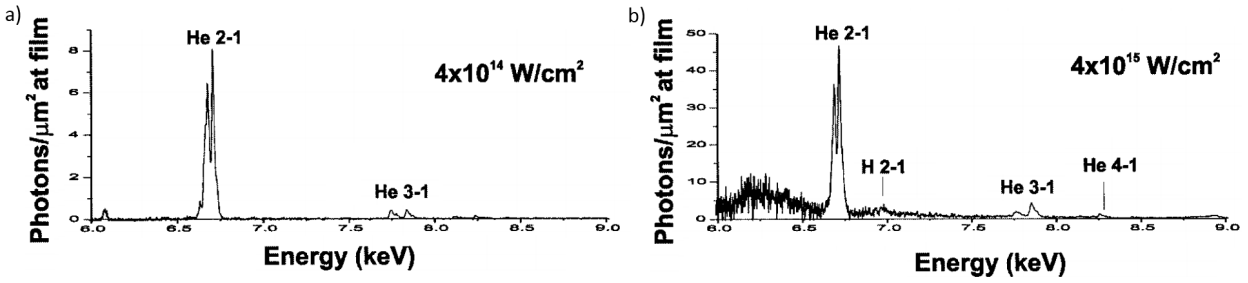


Figure 2.13: Emission spectrum from an Iron target after being exposed to a laser with an intensity of a) 4×10^{14} W/cm^2 b) 4×10^{15} W/cm^2. Reproduced from [Workman and Kyrala, 2001].

This transition is split into four due to the fine structure of the Helium-like $1s2p$ excited state. These states can be represented in spectroscopic notation labelled with the quantum numbers L (the total orbital angular momentum), S (the total spin), J (the total angular momentum):

$$^{2S+1}L_J^{\Pi}$$

where Π indicates the parity, the sum of the angular moment of all electrons in the atom. If the parity is odd $\Pi = o$ and if even this is blank. In this notation $L = 0$ is written as S, $L = 1$ is written as P and $L = 2$ is written as D. With two electrons, of spin $-1/2$ or $+1/2$, there exists two possible values for the total spin, $S = 0$ and $S = 1$. As the total angular moment J can take any integer value between $|L - S|$ and $L + S$, the $S = 1$ case is further split into three separate levels, as shown in Table 2.3.

Level	$\boldsymbol{L}$	$\boldsymbol{S}$	$\boldsymbol{J}$	**Fe $\boldsymbol{He_\alpha}$ transition**
$1s2p\ ^1P_1^o$	1	0	1	6700 eV
$1s2p\ ^3P_2^o$	1	1	2	6682 eV
$1s2p\ ^3P_1^o$	1	1	1	6668 eV
$1s2p\ ^3P_0^o$	1	1	0	forbidden

Table 2.3: The four possible levels and their quantum numbers for the helium-like $1s2p$. The energy of a transition to the $1s^2$ state for an Iron ion is also shown. Energies from the NIST database [Kramida et al., 2015].

Selection rules for transitions forbid any transition where the change in total angular momentum $\Delta J = 0$. In the $1s^2$ state the electrons must have opposite spin, so the total $S = 0$, resulting in $J = 0$. Hence the transition from $1s2p\ ^3P_0^o$ to $1s^2\ ^1S_0$ is not possible as this would leave J unchanged. As a result, the He_α line is split into a triplet. He_α emission photon energies for several transition metals are listed in Table 2.4.

However, when laser intensities on the target exceed $I > 10^{17}$ W/cm^2, K_α emission dominates the spectrum [Park et al., 2006]. In this process the laser quickly ionizes outer shell electrons to form hot electrons with energies as high as ~ 100 MeV [Key et al., 1998]. As these hot electrons move through the material they can ionize other atoms through

Material	Z	He_α from $^1P_1^o$	$He_{\alpha 1}$ from $^3P_2^o$	$He_{\alpha 2}$ from $^3P_1^o$
Scandium	21	4315	4300	4295
Titanium	22	4749	4734	4727
Vanadium	23	5205	5189	5180
Chromium	24	5682	5665	5655
Manganese	25	6180	6163	6151
Iron	26	6700	6682	6668
Cobalt	27	7242	7223	7207
Nickel	28	7805	7786	7766
Copper	29	8391	8371	8347

Table 2.4: He_α lines from various transition metals. All energies expressed in electron volts. Energies from the NIST database [Kramida et al., 2015].

electron-electron scattering. In some cases, inner-most shell electrons, in the K-shell, are ionized leaving a vacant energy level close to the nucleus. This vacancy is quickly filled by electrons from the L-shell or M-shell resulting in emission of X-rays at the K_α energy [Park et al., 2006].

In plasmas, the X-ray transmission, vary with ionization as demonstrated in plots of mass attenuation cross section shown in Fig 1.6.b. This is problematic for measuring mass density, as a change in ionisation cannot be distinguished from a change in mass density. To avoid this problem, X-ray photon energy was selected so that the transmission is similar at all expected ionisations. For example, for experiments with Xenon gas-fills an Iron backlighter target was used to produce a quasi-monochromatic source with a photon energy of 6.7 keV, where the transmission is similar for an expected ionization $Z < 5$. Using the Beer-Lambert law, Eq. 1.24, it can be shown that for an approximately monochromatic X-ray pulse, of initial intensity I_0 and frequency ν, the line integrated mass density is given by:

$$\int_L^0 \rho(z)dz = \frac{1}{\sigma(\nu)} ln\left[\frac{I(\nu)}{I_0(\nu)}\right] \tag{2.3}$$

where I is the recorded intensity and L is the path length. Target foils were also selected for optimal image contrast. To determine the optimal target material, simulated radiography images were produced from 2-D radiative hydrodynamic simulations (detailed in Section

2.5) for a variety of XRBL targets, as shown in Fig 2.14. These images were generated by integrating mass density through the gas cell, assuming cylindrical symmetry. By visually inspecting these simulated images for optimal contrast the foil material could be selected. Optimal XRBL target materials for different gas-fills and initial densities are summarised in Table 2.5.

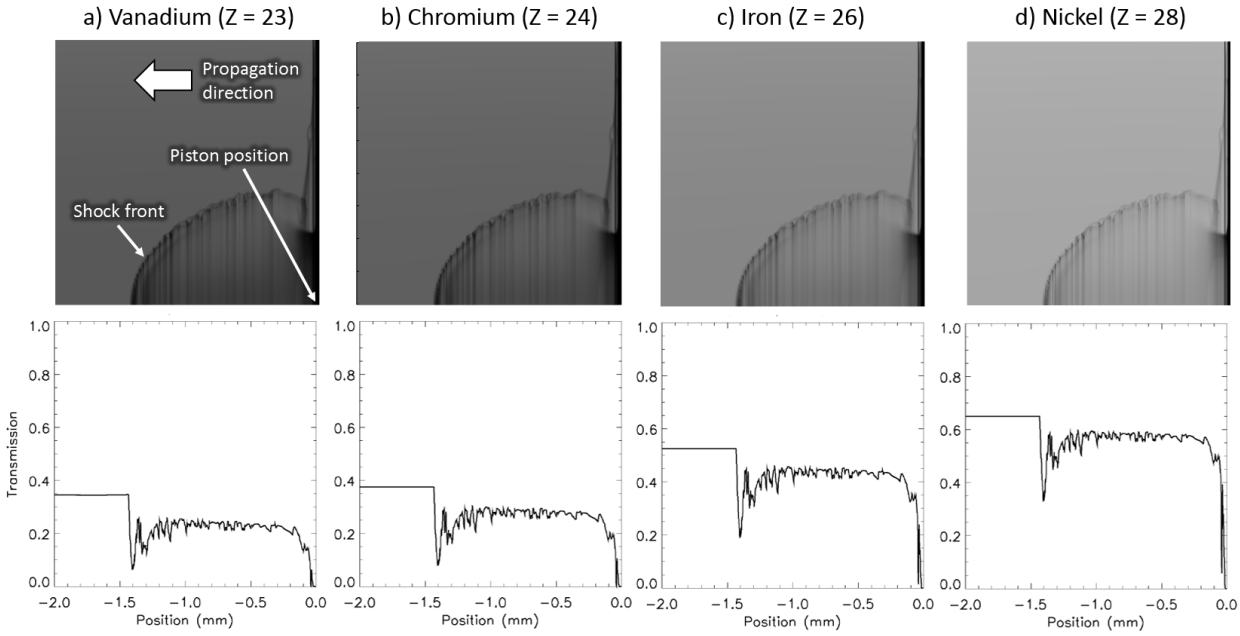


Figure 2.14: Simulated X-ray radiography images with different backlighter target materials with lineouts along the $y = 0$ (axis of the shock). All for targets filled with 0.3 bar of Xenon. Courtesy of Peter Graham, AWE.

Gas	**Density** (mg/cm^3)	**Material**	Z	**X-ray Energy** eV
Xenon	> 1.5	Iron	26	6398
Xenon	< 1.5	Vanadium	23	4949
Krypton	0.5	Iron	26	6398
Argon	> 0.7	Vanadium	23	4949
Argon	< 0.7	Scandium	21	4089
Neon	0.5	Scandium	21	4089

Table 2.5: X-ray backlighter material choices for different gas-fills and pressures used in these experiments.

The X-ray backlighting (XRBL) system used during the experiments on the Orion Facility was a point projection setup, where a pinhole is used to create a point-source of X-rays

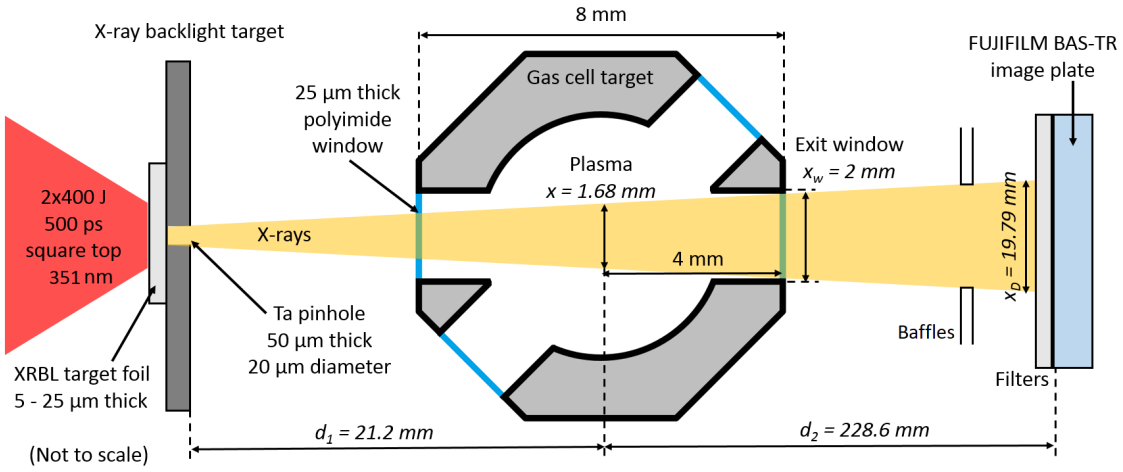


Figure 2.15: X-ray backlighting setup used for these experiments.

[Landen et al., 2001]. The gas filled target was then paced between the X-ray source and image plate as shown in Fig 2.15.

The X-ray source was produced by focusing the two Orion 'short pulse' laser beams, with a wavelength of 351 nm and pulse duration of 0.5 ns (described in detail in Section 2.1.1), onto a $5-25$ μm thick metal foil. Each beam delivered 250 J to ~ 250 μm diameter spot, achieving intensities of $\sim 1.6 \times 10^{15}$ W/cm^2. The laser-foil interaction produced a quasi-monochromatic X-ray source with a photon energy between $\sim 5-8$ keV, as described in Section 2.2.1.

To produce a point-source, the backlighter target foil was attached to a 50 μm thick sheet of Tantalum with a 20 μm diameter pinhole. Tantalum efficiently absorbs X-rays with a photon energy $5-8$ keV, with a transmission $T < 1 \times 10^{-6}$. The Tantalum sheet was coated with parylene which also filled the pinhole. This prevents the pinhole from closing when plasma from the XRBL target expanded. The gas cell target was located 21.2 mm from the XRBL target and had 2 mm by 2.3 mm windows with gas tight seals made of 25 μm thick polyamide to allow X-ray transmission, as described in Section 2.1.2.

Image plates were placed a further 228.6 mm from the gas cell target to record the intensity of transmitted X-rays. Fujifilm BAS-TR image plates were used in all experiments, which has a resolution of $\sim$94 μm and dynamic range $> 10^5$ [Gonzalez et al., 2002, Fiksel

et al., 2012]. These image plates are based on a thin layer of photostimulatable phosphor crystal $BaFBr : Eu^{2+}$. Ionizing radiation can liberate electrons from the Eu^{2+} ion which can become trapped in the lattice.

To reduce debris and avoid exposure to visible light (either during the experiment or handling) an 8 μm thick sheet of Aluminium coated polyimide was placed over the image plate. This is not opaque to the $\sim 4 - 8$ keV X-rays, having a transmission $T > 0.95$, but is opaque to visible light which could degrade the data stored on the image plate.

In addition, a metal foil of the same material as the backlighter target was placed over the image plate to act as a filter. This absorbed photons with energy above the K-edge (the energy required for inner most K-shell electrons to escape), so that the source can be treated as monochromatic. It also allowed for lower energy photons emitted by the plasma to be screened out. To prevent structures and crystals within the metal being imaged, two separate 12.5 μm foils were used so that impurities would overlap, resulting in a more homogeneous average density. In the case of Scandium backlighter targets, Titanium filters were used as they are more readily available and have a similar absorption spectrum to Scandium.

Image plates were scanned using a Fujifilm FLA-7000 scanner. Inside a light tight box a read laser, with a wavelength of 680 nm, is scanned over the surface of the image plate. In a process known as photostimulated luminescene, absorption of photons of the read laser cause the trapped electrons in the $BaFBr : Eu^{2+}$ lattice to recombine with the Europium ions and emit a photon of wavelength 390 nm [Gonzalez et al., 2002, Fiksel et al., 2012].The stimulated emission is then recorded by a photomultiplier tube (PMT). This reading process degrades the data recorded by the image plate. The image plate can be erased with white light so that it may be used again.

The output file is a 16-bit *.img file, with an associated *.inf file. The file records what Fujifilm refer to as Quantum Levels (QL), which have a logarithmic response to the intensity of stimulated photon emission, PSL, given by:

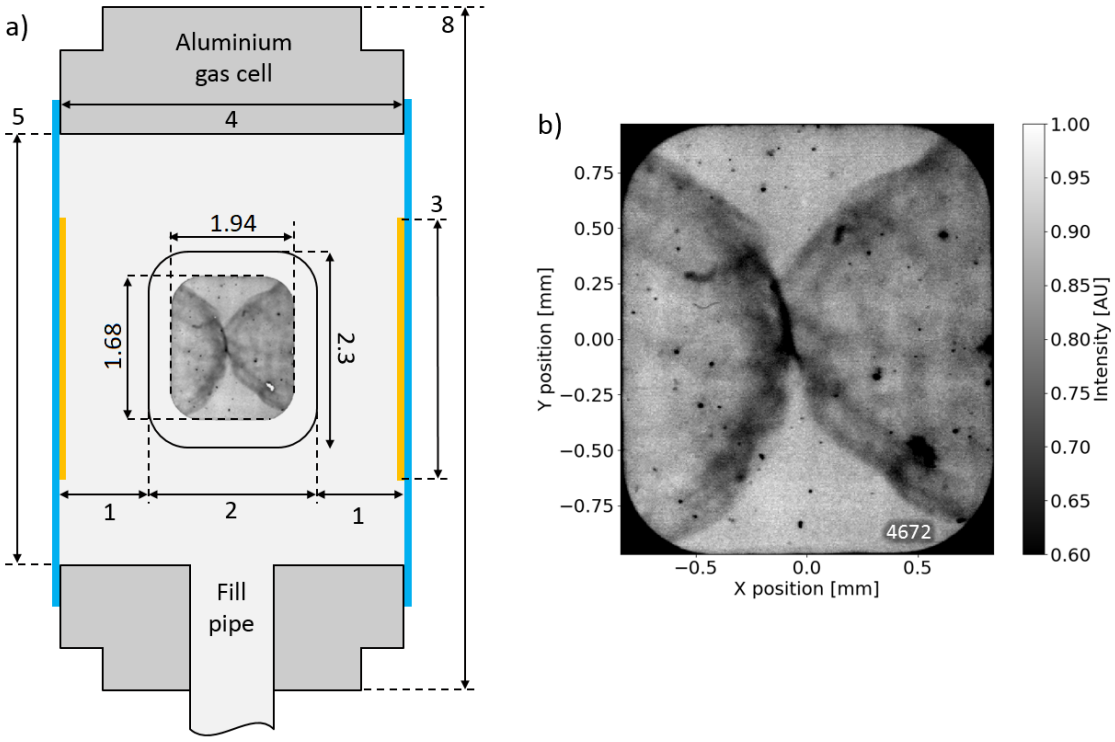


Figure 2.16: a) XRBL image location with respect to the experimental hardware. b) Example XRBL image from experiment #4672 with a Xenon gas-fill with an initial mass density of 1.84 mg/cm^3. Intensity has been normalized with respect to the unshocked region.

$$PSL = \frac{4000}{S}\left(\frac{R}{100}\right)^2 10^{\left[L\left(\frac{QL}{65535}-1/2\right)\right]} \tag{2.4}$$

where S is the sensitivity of the photomultiplier tube, R is the scan resolution and L is the number of orders of magnitude included in the 16-bit image, known as the latitude. For experiments performed in this thesis a sensitivity of $S = 4000$, resolution of $R = 50$ μm and latitude $L = 4$ were selected. An example XRBL image is shown in Fig 2.16, with intensity normalized with respect to the unshocked region.

Considering a triangle origination from the X-ray source, it can be shown that the ratio of height to distance from the source is equal along its entire length. The object, with height x, is placed a distance d_1 from the source and the image, with height x_D, is placed a distance $d_1 + d_2$ from the source. Therefore $x/d_1 = x_D/(d_1 + d_2)$. The X-ray source was placed a distance of $d_1 = 21.21$ mm, and the X-ray detector a distance of $d_2 = 228.6$ mm from the

centre of the target, therefore resulting in a magnification of $M = x_D/x = 11.8$. However, the X-ray image will be cropped by the exit window of the target, with dimensions $x_w = 2$ mm and $y_w = 2.3$ mm, as indication in Fig 2.15. Targets had a width of $t = 8$ mm from window to window and so:

$$\frac{x}{d_1} = \frac{x_D}{d_1 + d_2} = \frac{x_w}{d_1 + t/2} \tag{2.5}$$

This indicates that an object with size $x = 1.68$ mm by $y = 1.94$ mm was imaged with the XRBL system, forming an image with a size of $x_D = 19.79$ mm by $y_D = 22.85$ mm on the detector. The maximum resolution achievable with this setup can be calculated by dividing the scanning resolution, $S = 50$ μm, by the image magnification, $M = 11.8$. This yields a resolution of 4.2 μm at the gas cell centre. However, the image plate resolution is limited to ∼94 μm [Gonzalez et al., 2002, Fiksel et al., 2012], resulting in a resolution of ∼8 μm at the gas cell centre. However, the resolution at which features can be identified was determined is significantly coarser. This was determined by taking a horizontal profile of intensity from a background image. The window edge resembles a step function in intensity. By measuring the width of this step, between 10% and 90%, the resolution at which features can be determined was calculated to be much coarser at ∼25 μm.

An additional constraint on resolution is due to the effects of motion blur caused by the rapidly propagating shocks. The lasers that produced the X-ray source have a pulse width of 0.5 ns and the shocks were measured to move at 60 ± 10 km/s, measured in Section 2.3.1. This implies that the shock front is blurred by 30 ± 5 μm. Combining the motion blur further limits the resolution to ~ 40 μm.

2.2.2 Streaked self-emission

Optical self-emission from a 1-D line, along the axis of the gas cell, was recorded using a streak camera. This allowed the evolution of the shocks to be studied as a function of time.

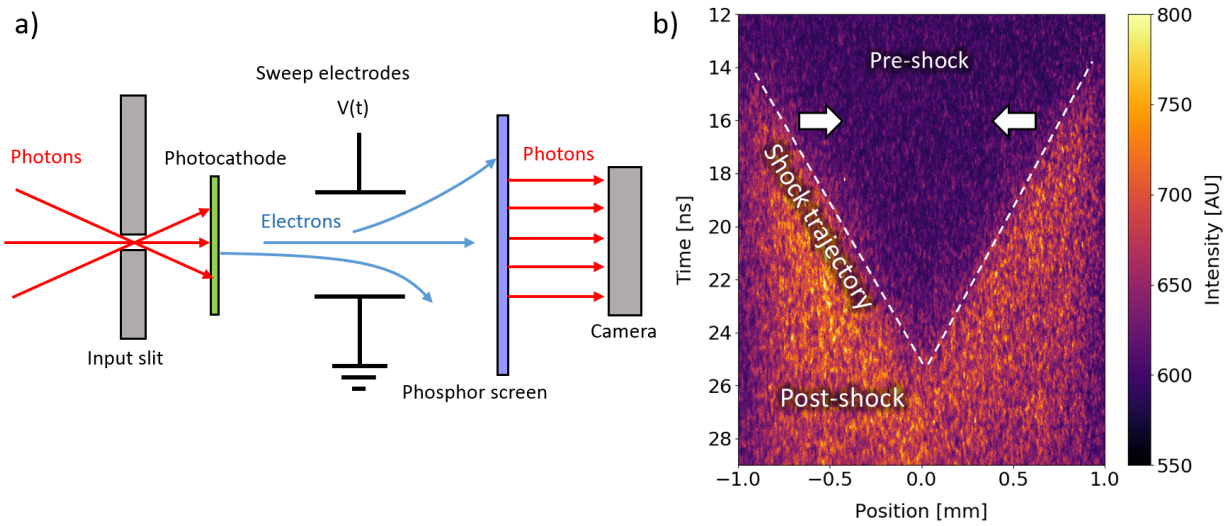


Figure 2.17: a) Description of how a streak camera operates. b) Example image with position in the horizontal axis and time in the vertical axis.

The operation of a streak camera is depicted in Fig 2.17.a. A slit is used to reduce the field of view to a 1-D line. Light that enters this slit is incident on a photo-cathode, liberating electrons via the photoelectric effect. These electrons are accelerated towards a detector or phosphor screen, converting the image back to photons and allowing it to be recorded by a CCD camera. By applying a time varying electric field perpendicular to the direction of acceleration, the electrons may be swept across the detector so that their vertical position varies with time. Thus this camera allows a 1-D image to be recorded as a function of time.

Temporal resolutions of images captured with this type of camera are of the order of sub-nanosecond, the streak cameras used for these experiment had an exposure of 100 ns. With an image size of 1000 pixels, this results in a temporal resolution of $\sim$0.1 ns. The slit of the streak camera was aligned with the axis of the gas-cell target, inline with the direction of shock propagation. This location was expected to best represent the 1-D evolution of the shocks.

An image produced with this diagnostic is shown in Fig 2.17.b with position in the horizontal axis and time in the vertical axis. The two shocks can be seen as bright emission propagating towards the centre of the gas cell, forming a V shape. After colliding, enhanced

emission expanding from the gas cell centre indicates the formation of a reverse shock. The spatial width of these images was found by identifying the edges of the window, known to be 2 mm across. To determine the timing of these streak images, timing experiments were performed where the drive lasers were focused onto a metallic target. Emission from this laser-target interaction was then used to identify the timing of the streak cameras relative to the drive lasers. Experiments took place over three weeks, each separated by several months, so start times could not be assumed to be consistent and so timing experiments were performed for both the second and third week. Fortunately the drive laser pulse is also visible in the majority of streak images recorded during the first week, providing a measurement of the streak cameras timing relative to the drive lasers.

2.2.3 Laser interferometry

Laser interferometry measures the change in refractive index integrated along the beam path while not perturbing the plasma. This can then be used to determine the plasma electron density, a product of ionization and ion density. This diagnostic was fielded on these experiments to measure the electron density ahead of the shock front in the radiative precursor.

Interferometry is performed by combining two laser beams, referred to as the probe and the reference beam, the former of which has accumulated an additional phase after passing through the plasma (typically these beams are produced by dividing a single laser beam). Constructive and destructive interference of the wavefronts of these two beams result in a fringe pattern (series of light and dark fringes) which may be used to infer changes in phase between the two beams. Both the probe and reference beam are modelled as propagating plane waves with an electric field $E_p(\mathbf{x}, t)$ and $E_r(\mathbf{x}, t)$ respectively. These are given by:

$$E_p(\mathbf{x}, t) = E_{p0} exp[i(\omega t - \mathbf{k_p}.\mathbf{x} + \delta\phi)] \tag{2.6}$$

$$E_r(\mathbf{x},t) = E_{r0}exp[i(\omega t - \mathbf{k_r}.\mathbf{x})] \tag{2.7}$$

where E_{p0} and E_{r0} are the electric field magnitudes, ω is the lasers angular frequency, $\mathbf{k}$ is the direction of propagation and $\delta\phi$ is any phase change obtained by propagating through the plasma. These two beams waves are recombined producing a total electric field of $E_T = E_p + E_r$. Imaging the recombined beam on a CCD records the intensity $I = |E_T|^2 = E_T E_T^*$ given by:

$$I(\mathbf{x}) = |E_{p0}|^2 + |E_{r0}|^2 + 2E_{r0}E_{p0}cos^2[(\mathbf{k_p} - \mathbf{k_r}).\mathbf{x} + \delta\phi] \tag{2.8}$$

The propagation direction of the two beams are offset by a slight amount ($\mathbf{k_p} \neq \mathbf{k_r}$) resulting in the solution shown in Fig 2.18 known as a Fresnel pattern. Constructive and destructive interference between the two beams results in a series of bright and dark fringes. Offsetting the beams further results in higher fringe densities recorded on the CCD. In these experiments the beams were offset so that a high fringe density of almost linear fringes could be imaged.

After passing through the plasma, the probe beam will accumulate a phase offset ϕ due to the varying refractive index of the plasma. For a cold plasma with moderate magnetic fields (so that the electron gyro-radius is less than the laser frequency) the dispersion relationship is given by:

$$\omega^2 = k^2c^2 + \omega_{pe}^2 \tag{2.9}$$

where c is the speed of light and ω_{pe} is the plasma frequency given by:

$$\omega_{pe}^2 = \frac{n_e e^2}{m_e \epsilon_0} \tag{2.10}$$

where n_e is the local electron density, e is the electron charge, m_e is the mass of an electron

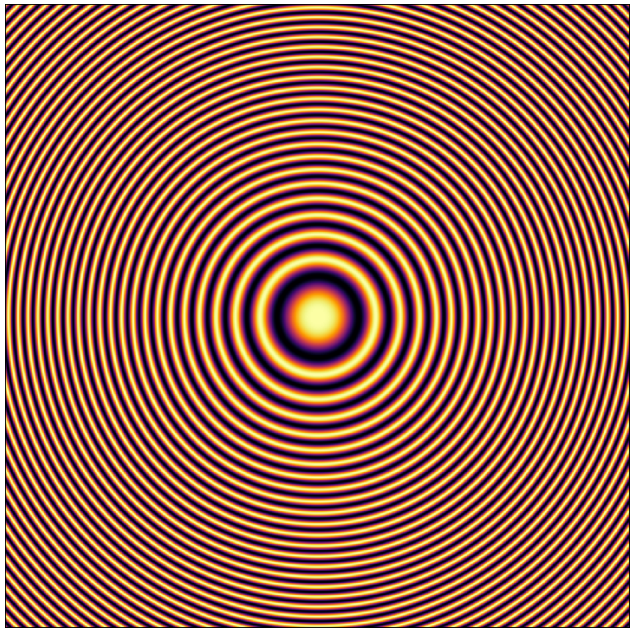


Figure 2.18: Solution to Equation 2.8 for two interfering beams as a function of offset in the x and y direction.

and ϵ_0 is the permittivity of free space. The total phase collected by the beam, through the plasma along a path **dl**, is:

$$\phi = \int \mathbf{k}.\mathbf{dl} \tag{2.11}$$

From Eq. 2.9 this can be shown to be:

$$\phi = \int \frac{1}{c}(\omega^2 - \omega_{pe}^2)^{1/2} dl = \int \frac{\omega}{c}\left(1 - \frac{\omega_{pe}^2}{\omega^2}\right)^{1/2} dl \tag{2.12}$$

As $\omega_{pe} \ll \omega$, a binomial expansion may be used to expand the square root. Ignoring high order terms allows this to therefore be expressed as:

$$\phi = \int \frac{\omega}{c}\left(1 - \frac{\omega_{pe}^2}{2\omega^2}\right) dl \tag{2.13}$$

Assuming the reference and probe beam have the same path length, the change in phase for passing through the plasma can be given by:

Wavelength λ [nm]	Line integrated electron density per fringe shift [cm^{-2}]
1034	2.16×10^{17}
532	4.21×10^{17}
355	6.30×10^{17}

Table 2.6: Electron density per fringe shift (phase change of 2π) for several common wavelengths.

$$\delta\phi = -\int \frac{\omega_{pe}^2}{2\omega c} dl = -\frac{e^2}{2\omega c\epsilon} \int n_e dl \tag{2.14}$$

The quantity $\int n_e dl$, the line integrated electron density, is usually refereed to as $n_e L$. In terms of the laser wavelength λ, the phase change is given as:

$$\delta\phi = -\frac{e^2 \lambda}{4\pi c^2} \int n_e dl \tag{2.15}$$

This phase change is measured using the previously mentioned fringe pattern with each fringe corresponding to a phase change of 2π. Thus the change in position of fringes, known as fringe shift, relative to those in an image taken without the plasma (a reference image) can be used to determine the line integrated electron density $n_e L$. Table 2.6 shows the electron density per fringe shift for commonly used probe lasers.

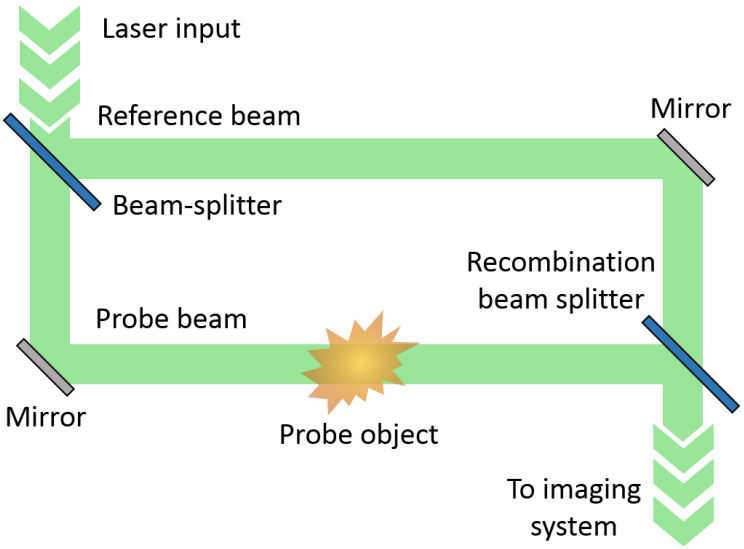


Figure 2.19: Schematic of a Mach-Zehnder laser interferometry setup.

A very widely used experimental setup is the Mach-Zehnder (used for experiments performed on both the Orion and MAGPIE facilities presented in this Thesis). A schematic of this instrument is shown in Fig 2.19. In a Mach-Zehnder laser interferometer the laser beam is separated into a probe and reference beam using a beam-splitter. These two beams follow different paths, the probe beam passing through the plasma and the reference beam through free space. These are then recombined on a second beam-splitter prior to the imaging system.

On the Orion laser facility laser interferometry was performed with a Mach-Zehnder setup using an optical laser with a wavelength of 532 nm, pulse length of 50 ns and total energy of $300 - 400$ mJ. 2-D time resolved images were recorded with four Gated Optical Intensifiers (GOI) cameras. Example images, referred to as 'interferograms', as shown in Fig 2.20.

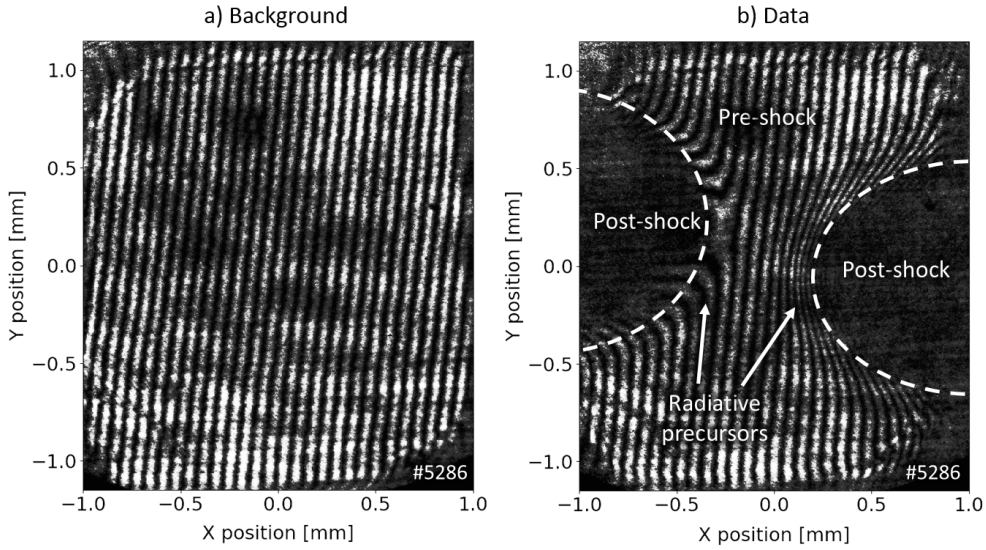


Figure 2.20: Example interferometry image recorded with a GOI camera from experiment #5286. a) Background image prior to the experiment. b) Data image taken during the experiment, 19 ns after the drive beams. The two shocks can be seen as dark semi-circular regions to the left and right of the image and the bending of fringes indicates a change in refractive index in the plasma.

Raw interferometry images, such as that shown in Fig 2.21.a,d are processed using methods described in [Swadling et al., 2013] to produce 2-D maps of line integrated electron density. However prior to this, the fringes of both the background and reference image are manually

traced in image editing software to produce a black and white bitmap such as that shown in Fig 2.21.b,e.

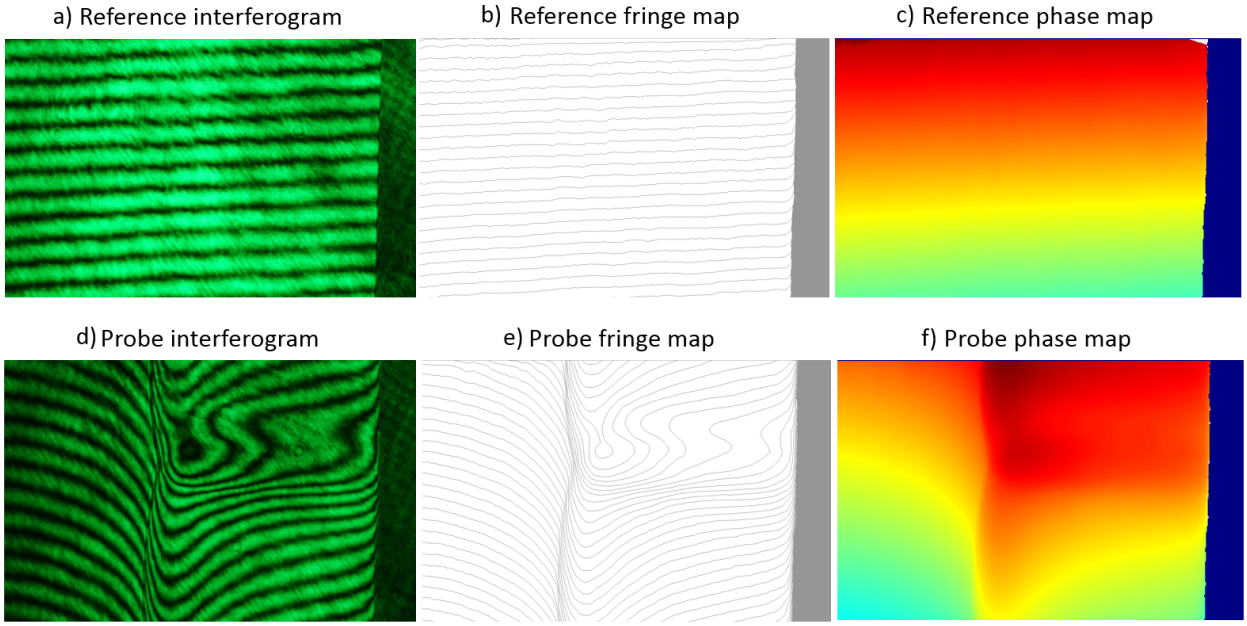


Figure 2.21: Steps involved in processing interferometry images to produce phase maps. For clarity, interferometry images from experiments detailed in Chapter 3 are shown. a,d) Raw interferogram images. b,e) Fringe map produced by tracing interferograms. c,f) Maps of phase map produced with the fringe numbering and interpolation software.

Both the traced probe and reference interferometry images are then loaded into a Matlab application. This application allows fringes to be manually numbered before performing an interpolation, producing a 2D phase map for both the reference and probe image, shown in Fig 2.21.c,f. Subtracting one phase map from the other yields a map of the phase difference incurred due to the plasma. Each whole fringe shift corresponds to a phase shift of 2π (π if both dark or bright fringes have been traced). Therefore allowing a map of integrated electron density to be obtained using Eq. 2.15.

However, this method is not able to determine integer fringe shifts and so a region of known plasma density (i.e. no plasma) is required, with a visible path connected to the region of interest. As no fringe shift will be recorded in this region it may be used as a baseline to measure other fringe shifts too. Without such a reference point only relative changes in

plasma density may be determined, as was the case with radially converging radiative shock experiments [Burdiak et al., 2014] (described in Section 1.7.2).

Ideally the spatial resolution of this diagnostic would be that of the camera, as small variations in phase (a fraction of a phase change) can be determined from variations in brightness. However, in reality the maximum and minimum of fringes cannot be determined to the accuracy of a single pixel, due to a combination of plasma self-emission, Schlieren effects and noise. Instead, this Thesis assumes a spatial error of half the distance between traced fringes, corresponding to a phase shift of π. Likewise, the error in measured values is assumed to be a phase shift of π (equivalent to $n_e L = 2.10 \times 10^{17}$ cm^{-2} for a wavelength of 532 nm).

In addition to capturing 2-D time resolved images on GOI cameras, a streak camera was employed to measure the temporal evolution of a 1-D lineout, on the gas-cell target axis and inline with the direction of shock propagation, with greater temporal resolution.

An example image is shown in Fig 2.22.a with position in the horizontal axis and time in the vertical axis. The region with no fringes below the V shape is post-shock material which is opaque to the 532 nm interferometry laser. The bending of fringes prior to this indicates a change in electron density.

These images were processed in a similar manner as those images with GOI cameras. The images were traced manually and then the fringe numbering program was used to produce 2D phase maps. For background images, the fringe pattern at time 0 was extrapolated to produce a series of vertical fringes. The resulting image shown in Fig 2.22.b shows the evolution of the line integrated electron density on the targets axis as a function of time.

As the beam passes through an extended object it integrates the electron density from different parts of the plasma. Fortunately, it is possible to determine the unbound electron density as a function of radius for cylindrically or spherically symmetric objects through an Abel inversion. For a quantity which is a function of radius, $f(r)$, the integrated and observed quantity, $F(x)$ is given by:

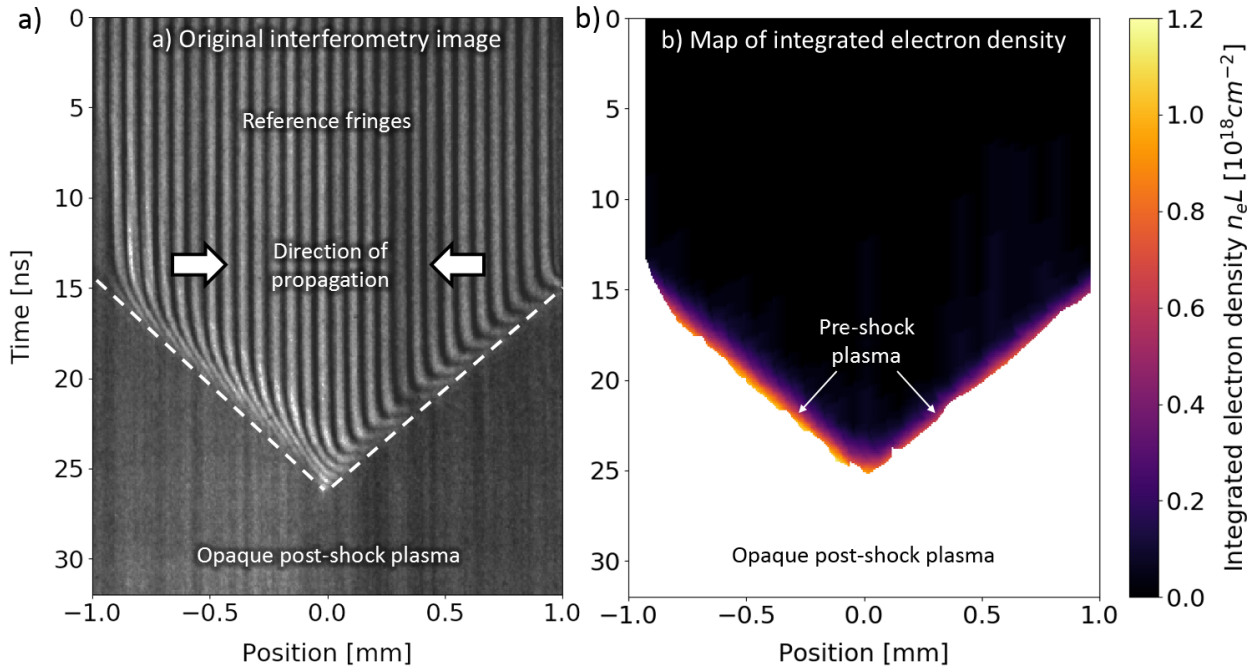


Figure 2.22: a) Raw streaked interferogram image. b) Processed image showing the evolution of the line integrated electron density over time.

$$F(y) = \int_x^\infty \frac{f(r) r dr}{\sqrt{r^2 - x^2}} \tag{2.16}$$

Assuming that $f(r)$ drops to zero quicker than $1/r$, it may be determined by the Abel inversion:

$$f(r) = -\frac{1}{\pi} \int_r^\infty \frac{dF}{dx} \frac{dx}{\sqrt{x^2 - r^2}} \tag{2.17}$$

In practise these integrals do not extend to infinity, but instead to the edge of the plasma, and these integrals are solved numerically. Consider a radially symmetric plasma with a density $n(r)$. This may be approximated as consisting of equal thickness bands with densities n_i each at a radius r_i, such as that shown in the top down image in Fig 2.23.

The line integrated density imaged at y_j, $f(y_j)$, will be equal to the sum of the density of each band multiplied by the path length, $2X_{j,i}$, where i refers to the band number and j the position of the image. Several such rays are indicated with red dashed lines in Fig 2.23.

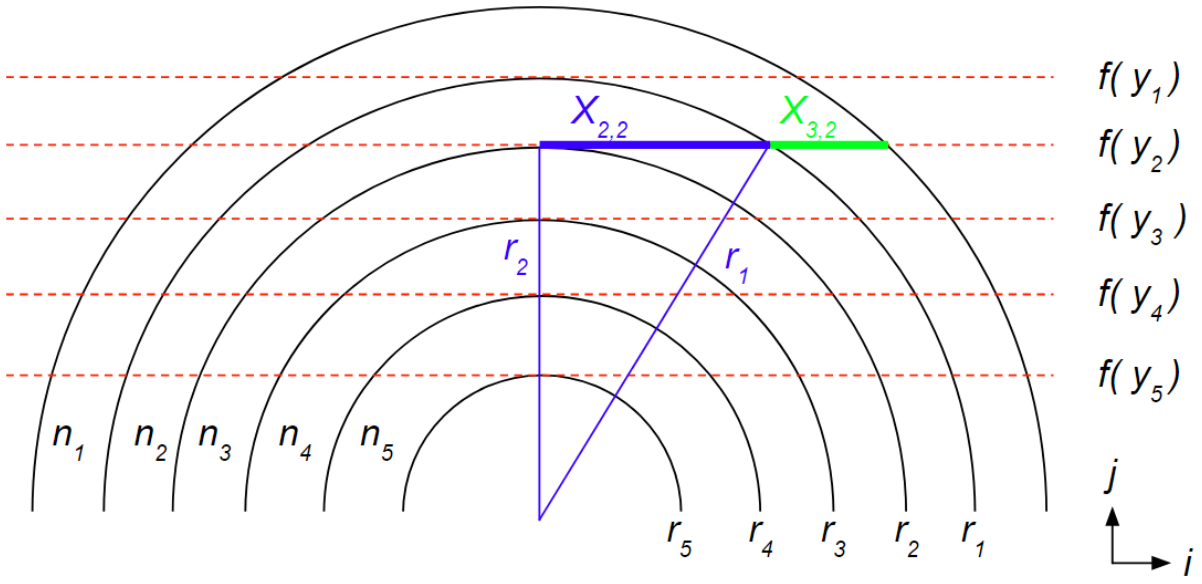


Figure 2.23: Diagram describing how Abel inverse transformations were performed numerically.

With $i = 1$ being the outer most band, these rays are seen to propagate through each band up to their j co-ordinate. Therefore:

$$f(y_i) = 2\sum_{j=2}^{i} n_j X_{ji} \tag{2.18}$$

When the j and i co-ordinates are equal the path length $X_{j,i}$ can be calculated simply using the Pythagoras theorem. Therefore $X_{2,2} = \sqrt{r_1^2 - r_2^2}$, shown in blue in Fig 2.23, and in general $X_{j,i} = \sqrt{r_{(j-1)}^2 - r_i^2}$. For path lengths where $i \neq j$, such as that shown in green in Fig 2.23, it can be shown that the general formula is:

$$X_{j,i} = \sqrt{y_{j-1}^2 - y_i^2} - \sqrt{y_j^2 - y_i^2} \tag{2.19}$$

Equation 2.18 may be expanded yielding:

$$f(y_i) = 2n_i X_{ii} + 2\sum_{j=2}^{(i-1)} n_j X_{ji} \tag{2.20}$$

Rearranging this yields and expression for n_i as a function of the measured integrated

density at $f(y_i)$ and densities at larger radii:

$$n_i = \frac{1}{X_{ii}} \left[\frac{f(y_i)}{2} - \sum_{j=2}^{i-1} n_j X_{ji} \right] \tag{2.21}$$

This can therefore be numerically solved by starting with the outermost radius, assumed to be zero density with $n_e = 0$, and systematically calculating the density at inner radii. This numerical method was tested against a known analytical example; a circle function, which once Abel inverted results in a step function. Fig 2.24 shows the result of performing an Abel inversion with different numbers of points, resulting in a faithful recreation of a step function. However, this fails at the axis, $r = 0$. In practise, calculated values closer to the axis will have increased errors due to integrating through larger regions of plasma.

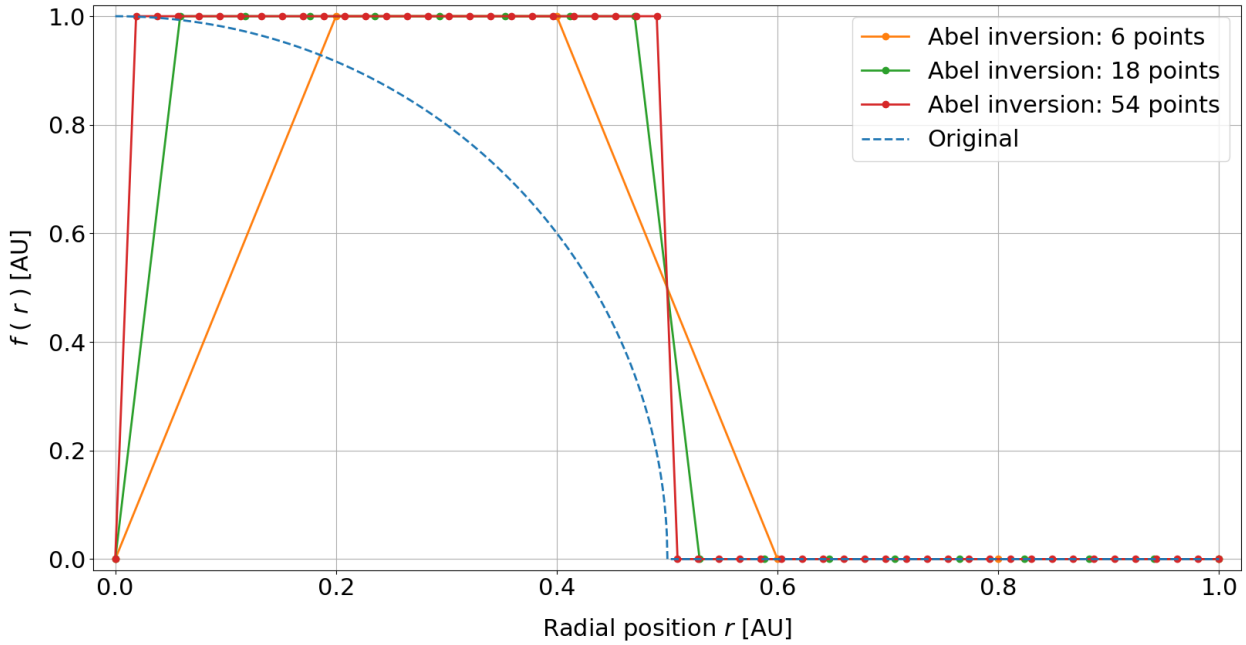


Figure 2.24: Test of the numerical Abel inversion method against a known analytical solution - a circle, shown in blue, which yields a step function.

2.3 Shock hydrodynamics

The experimental setup detailed in the Section 2.1 allowed counter-propagating radiative shocks to be launched into a gas-fill. This section investigates the shock hydrodynamics, e.g. velocity and evolution, primarily from experiments using a Neon gas-fill at $P_0 \sim 0.6$ bar. The initial mass density, ρ_0, may be determined using the ideal gas equation:

$$n_0 = \frac{P_0}{k_B T} \tag{2.22}$$

where n_0 is the particle number density, k_B is Boltzmans constant, T is the initial temperature (assumed to be 290 K) and P_0 is the fill pressure in Pascals (1 bar = 10^5 Pa). As Neon is a monatomic gas, the mass density, ρ_0 may be determined by multiplying the particle number density by the mass of each atom. Therefore:

$$\rho_0 = A m_p n_0 = \frac{P_0 A m_p}{k_B T} \tag{2.23}$$

where m_p is the proton mass and A is the atomic mass number ($A = 20.18$ for Neon). This yields a mass density of $\rho_0 = 0.5$ mg/cm^3 and atom density of $n_0 = 1.5 \times 10^{19}$ cm^{-3}.

Shock hydrodynamics were primarily studied with X-ray backlighting (XRBL) image, described in Section 2.2.1, which produced a single image in each experiment. A time sequence constructed from XRBL images, from seven different experiments, is shown in Fig 2.25. These experiments were all conducted with a Neon gas-fill with an initial mass density of 0.49 ± 0.01 mg/cm^3. To achieve optimal contrast in XRBL images a Scandium XRBL target was used, producing X-rays with an energy of $\sim$4.3 keV.

Darker regions of low X-ray intensity, indicate higher attenuation and thus higher mass density. No unattenuated X-rays were imaged and so each image was normalised to the intensity through the unshocked gas. The dark dots scattered across the images are a result of debris hitting the image plates, as indicated in Fig 2.25.b. The spatial scale was provided

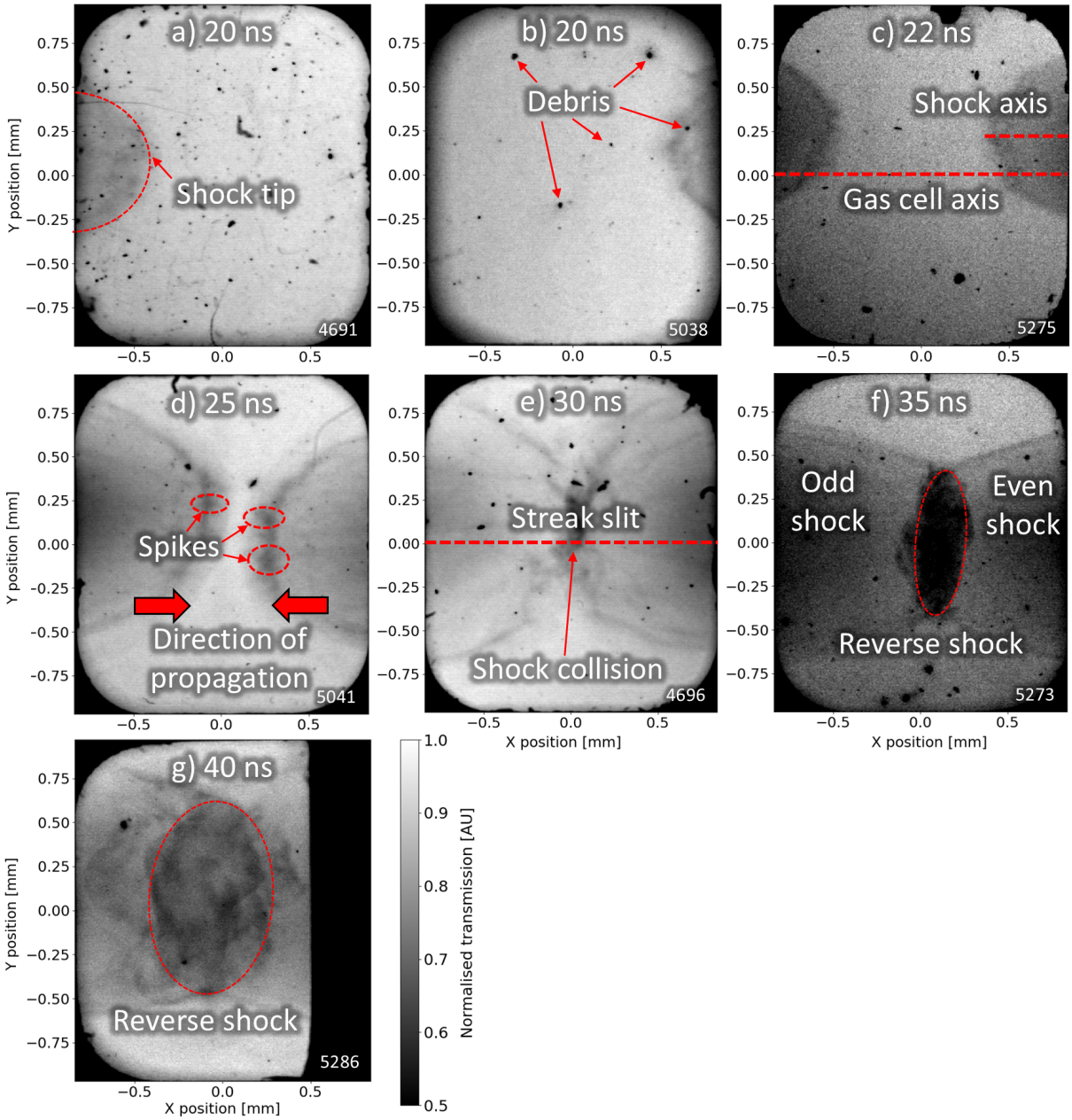


Figure 2.25: Time sequence constructed from seven normalised XRBL images of different experiments in Neon with an initial mass density of 0.5 mg/cm^3. The final image (g) was cropped possibly due to diagnostic misalignment. The origin is at the gas cell centre and the pistons are located at $x \sim \pm 2.2$ mm.

by the exit window size of 2 mm by 2.3 mm (scaled to accounting for point projection effects described in Section 2.2.1) and the centre of the gas cell has been defined as $x = y = 0$. The pistons are located at $x \sim \pm 2.2$ mm and so are not visible in these images, being obscured

by the gas cell body.

The two shocks can be seen as semi-circular structures, labelled in Fig 2.25.a, propagating towards the centre of the gas cell as indicated in Fig 2.25.d. Shocks collide after ∼30 ns, as seen in Fig 2.25.e, and a region of lower X-ray intensity forms in the centre of the gas cell, labelled 'reverse shock' in Fig 2.25.f-g. Slight offsets in the shocks axis from $y = 0$ and the collision from $x = 0$ are likely due to slight misalignments of the target. To compensate for this, analysis was performed on the shocks axis rather than the target axis, indicated in Fig 2.25.c. Shocks on the left of the image were produced by the Orion facilities odd numbered beam lines and so are refereed to as 'odd shocks', which shocks on the right of these images are refereed to 'even shocks', as labelled in Fig 2.25.f.

Shocks consist of a relatively high transmission region followed by a thin shell of low transmission, the latter of which is believed to be primarily composed of piston material. The structure of the post-shock material is investigated in detail in Section 2.3.2. The post-shock material is not uniform and possible instabilities are visible in the piston material, appearing as spikes of low transmission, labelled in Fig 2.25.d. In addition, the post-collision structure is non-uniform and asymmetric, particularly at later times as seen in Fig 2.25.g.

2.3.1 Shock velocity

An initial rough estimate of the shock velocity was calculated by measuring the distance the shock tip (labelled in Fig 2.25.a) had propagated from the piston, at $x \sim \pm 2.2$ mm (accounting for bulging in the piston due to the positive gas-fill pressure), and dividing by the time the image was taken. This yielded an average velocity of 82 ± 5 km/s prior to collision. However, this velocity may not be representative of the shock velocity at the time the XRBL images were taken as this assumes a constant velocity over time, and the shock velocity may change early in time when the shocks are obscured by the gas-cell.

To improve this estimate, and find the shock velocity just prior to collision, the distance the shock tip has propagated from the piston was plotted as a function of time in Fig 2.26. A

standard error in measuring the shock front position of 0.1 mm was assumed for these points. Position measurements, prior to and after the collision between the two shocks, both have positive correlations. An estimate of the velocity was determined by fitting linear trend-lines to these two series of points and taking their gradients. This yielded a shock velocity of 56 ± 10 km/s prior to collision and 38 ± 10 km/s after the collision.

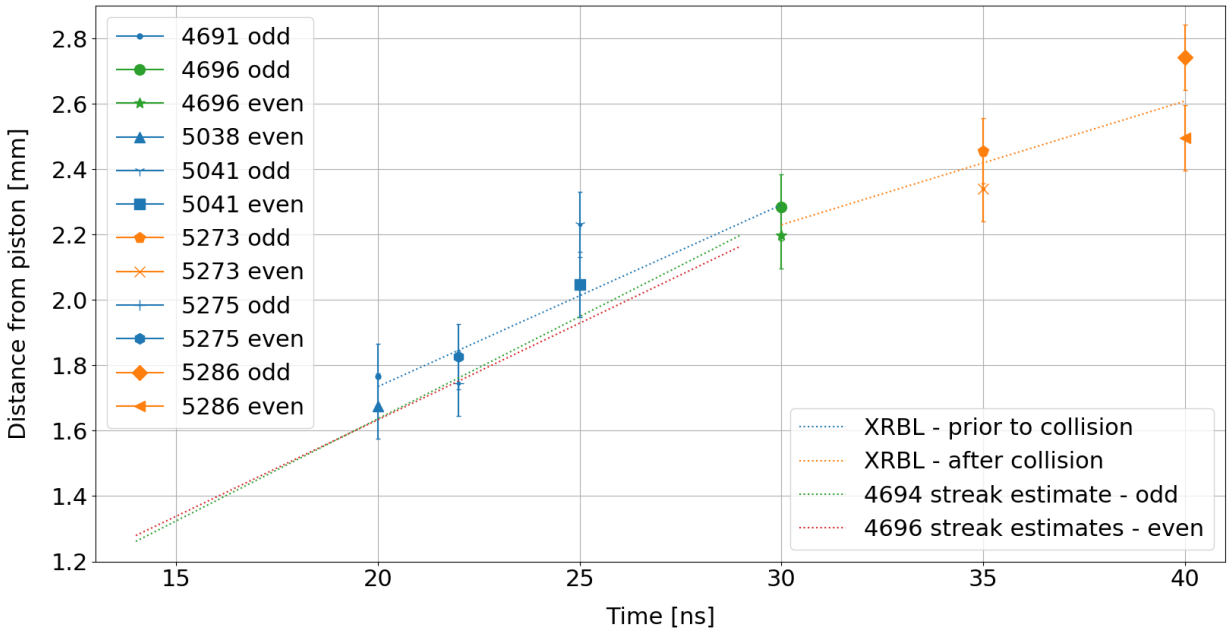


Figure 2.26: Position of the shock front tip in XRBL images from experiments with a Neon gas-fill with initial mass density of ~0.5 mg/cm^3. The points have been separated into pre-collision and post-collision, and both groups approximated by linear trend lines. The gradient of these trend lines was used to estimate the shock velocity and the reverse shock velocity. Shock trajectories determined from streak images in Fig 2.27 are also plotted.

The shock velocity was also measured using optical self-emission streak images. The streak camera recorded a 1-D lineout along the gas-cell axis, labelled 'Streak slit' in Fig 2.25.e. Fig 2.27 shows an optical self-emission streak image from experiment #4696, the corresponding XRBL image from this experiment is shown in Fig 2.25.e. Spatial position is shown on the horizontally axis and time vertically, intensity is recorded as pixel brightness. The shocks can be seen as regions of bright emission that enter the window (~1 mm from the pistons) ~14 ns after the drive lasers and propagate towards the collision point at the gas cell centre, at $x \sim 0$, by ~30 ns, matching the time of collision seen in XRBL images.

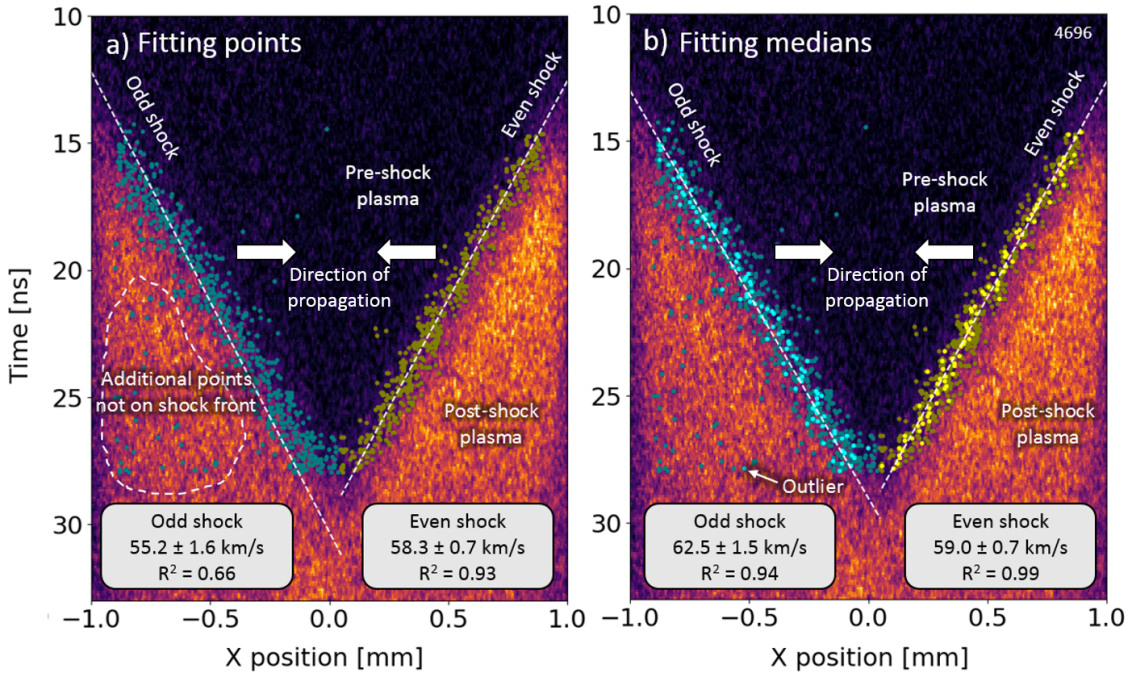


Figure 2.27: a) Self-emission streak image captured from the gas-cell axis (location shown in Fig 2.25.e) for experiment #4696, with a Neon gas fill and initial mass density of 0.47 mg/cm^3. Spatial position is shown horizontally and time vertically, intensity is recorded as pixel brightness. Shock velocity was measured by fitting linear trend-lines to isolated pixels with an intensity between $700 - 710$. Additional points not on the shock front distort this measurement. b) Shock velocity measured by fitting linear trend-lines to the median positions of isolated pixels.

The edge of emission in the optical self-emission streak image was used to determine the shock velocity. However, the shock front is not well defined, possibly due to emission from the radiative precursor and the broadband wavelength range of the streak camera. To systematically and reliably identify the edge of the shock front, a Python script was written to select pixels within a range of intensity values (shown in dark blue and yellow in Fig 2.27.a for the odd and even shocks respectively). An intensity range of $700 - 710$ was found to best correspond to visual approximations of the shock front position. Points were separated into the odd and even shocks by visually selecting the approximate shock collision position. This algorithm was run between $14 - 28$ ns, as the shock front is only visible for this approximate time, and between -0.9 to 0.9 mm in order to avoid the dimmer region adjacent to the window edge. These points were found to be reasonably well represented by linear trend

lines, the gradient of which was used to determine the shock velocity to be 55.2 ± 1.6 km/s and 58.3 ± 0.7 km/s for the odd and even shocks respectively.

However, several points in the post-shock plasma were also included by this method, highlighted in Fig 2.27.a. This resulted in a distortion to the gradient of the trend-line and thus an inaccurate velocity measurement. This is seen in the odd shock in Fig 2.27.a, the trend-line has a slightly steeper gradient than visually expected due to additional points in the post-shock material, and a low Pearson product-moment correlation squared $R^2 = 0.66$. To remove this effect, a median position was calculated for each vertical slice with at least 3 points in it (sufficient to select a meaningful median). These are shown in Fig 2.27.b with light blue and light yellow points. While outliers do still exist, highlighted in Fig 2.27.b, the vast majority of the points lie on the shock front. These points were found to be well represented by linear trend lines which visually matched the shock front position. The gradient of these trend-lines yields shock velocities to be 62.5 ± 1.5 km/s and 59.0 ± 0.7 km/s for the odd and even shocks respectively. These shock velocities are plotted on Fig 2.26 and are found to closely agree with estimates from XRBL images.

The consistent shock velocity of 60 ± 10 km/s, from both diagnostics allows the Mach number to be estimated. This is given by $M = u/c$, where u is the shock velocity and c is the sound speed in the cold, unshocked Neon. The sound speed was calculated by:

$$c_s = \sqrt{\gamma \frac{P_0}{\rho_0}} \tag{2.24}$$

where γ is the adiabatic index (assumed to be $\gamma = 5/3$), $P_0 = 6 \times 10^4$ Pa is the initial gas-fill pressure and $\rho_0 = 0.5$ mg/cm^3 is the initial mass density. This yielded a sound speed of $c_s = 450 \pm 4$ m/s and thus a Mach number of $M = 171 \pm 29$. However, the Mach number is expected to be reduced due to of the existence of a radiative precursor directly ahead of the shock front, which increases the local temperature and sound speed.

XRBL images were compared against self-emission streak images for experiments where both diagnostics were fielded, as are shown in Fig 2.28. XRBL images have been dived in

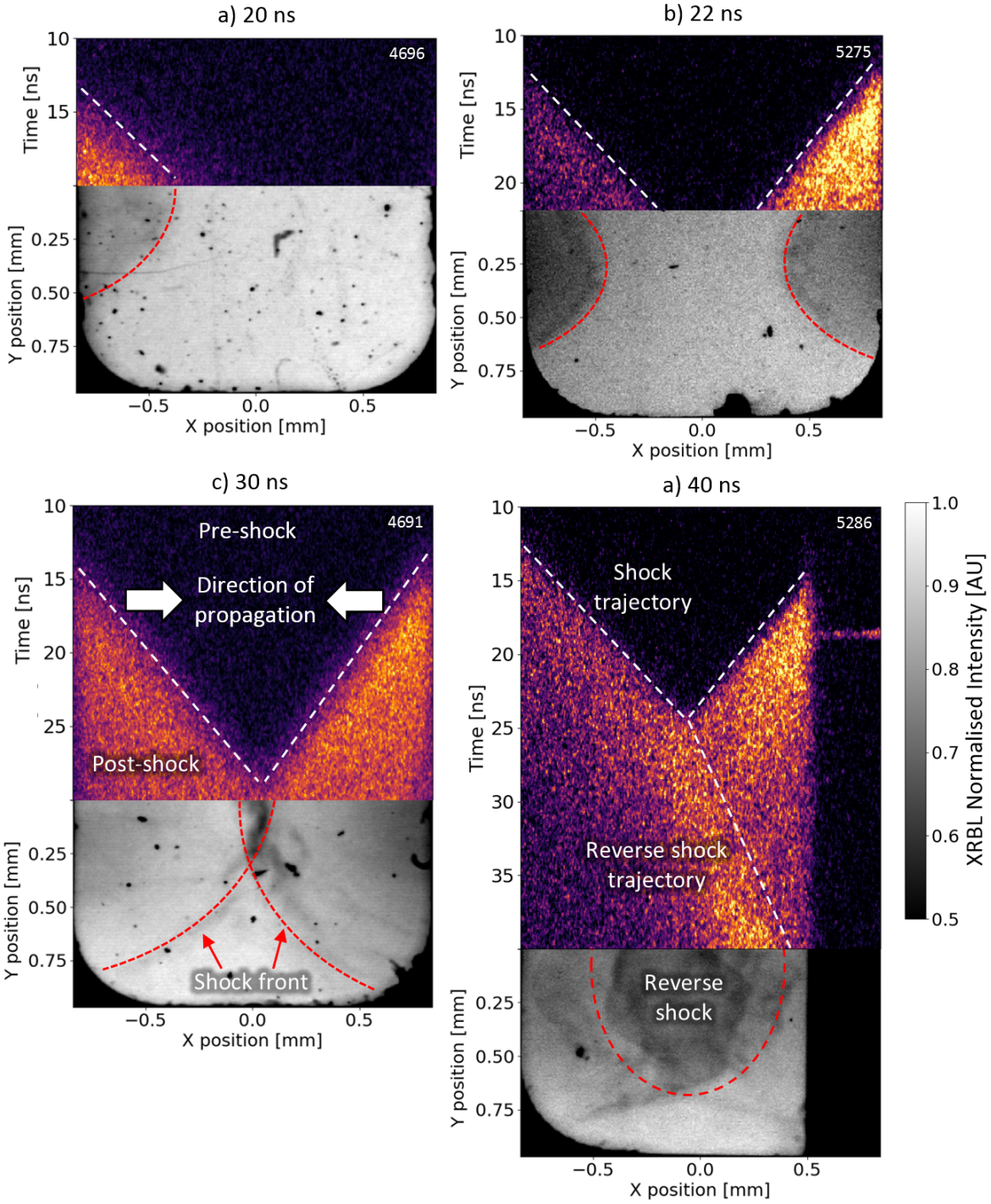


Figure 2.28: Self-emission streak images plotted with XRBL images from the same experiment. XRBL images have been dived in half so that their top edge matches the position of the streak slit and streak images have been cropped so that their bottom edge matches the time the XRBL image was taken.

half so that their top edge matches the position of the streak slit and streak images have been cropped so that their bottom edge matches the time the XRBL image was taken. The majority show good agreement in the position of the shock front between the XBRL and streak images. However, Fig 2.28.b (experiment #5275) shows poor agreement which could be due to a misalignment of the streak slit. After the shock collision, enhanced emission can be seen in the centre of the streak image, visible in Fig 2.28.d, corresponding with the reverse shock position. This is discussed in detail in Section 2.3.3.

Previous experiments to produce laser driven radiative shocks typically used narrow gas cells to confine the shock, and thus cause it to act as an approximately one dimensional expansion [Doss et al., 2010, Drake et al., 2011]. However, gas cells for these experiments were designed with a transverse width of 5 mm, significantly larger than the laser focal spot diameter of 600 μm, so that the shock was able to expand in three dimensions. XRBL images indicate that the shape of the shocks, prior to collision, are well approximated as semi-ellipsoids centred on the drive beams focal spot (obscured by the gas cell body) as shown in Fig 2.29. XRBL images show that, prior to colliding, the shocks exhibit an aspect ratio (semi-minor axis over semi-major axis) of $A_R \sim 0.4$.

To investigate how the shock evolves away from the axis, radial lines originating from the approximate piston position and passing through the shock front, were plotted at $\pm 10^\circ$ and $\pm 20^\circ$. These were used to help visually select the shock position in XRBL images. The shock front positions are plotted in Fig 2.30 as a function of time that the XRBL image was taken. A standard error in measuring the shock front position of 0.1 mm was assumed for all points.

A positive trend is visible in each of these series of points and so a linear trendline was fitted to each series to estimate the shock velocity. This yielded an expansion velocity of 55 ± 8 km/s at an angle of $\pm 10^\circ$, comparable to the axial shock velocity, and 16 ± 5 km/s at an angle of $\pm 20^\circ$, significantly slower than the axial velocity.

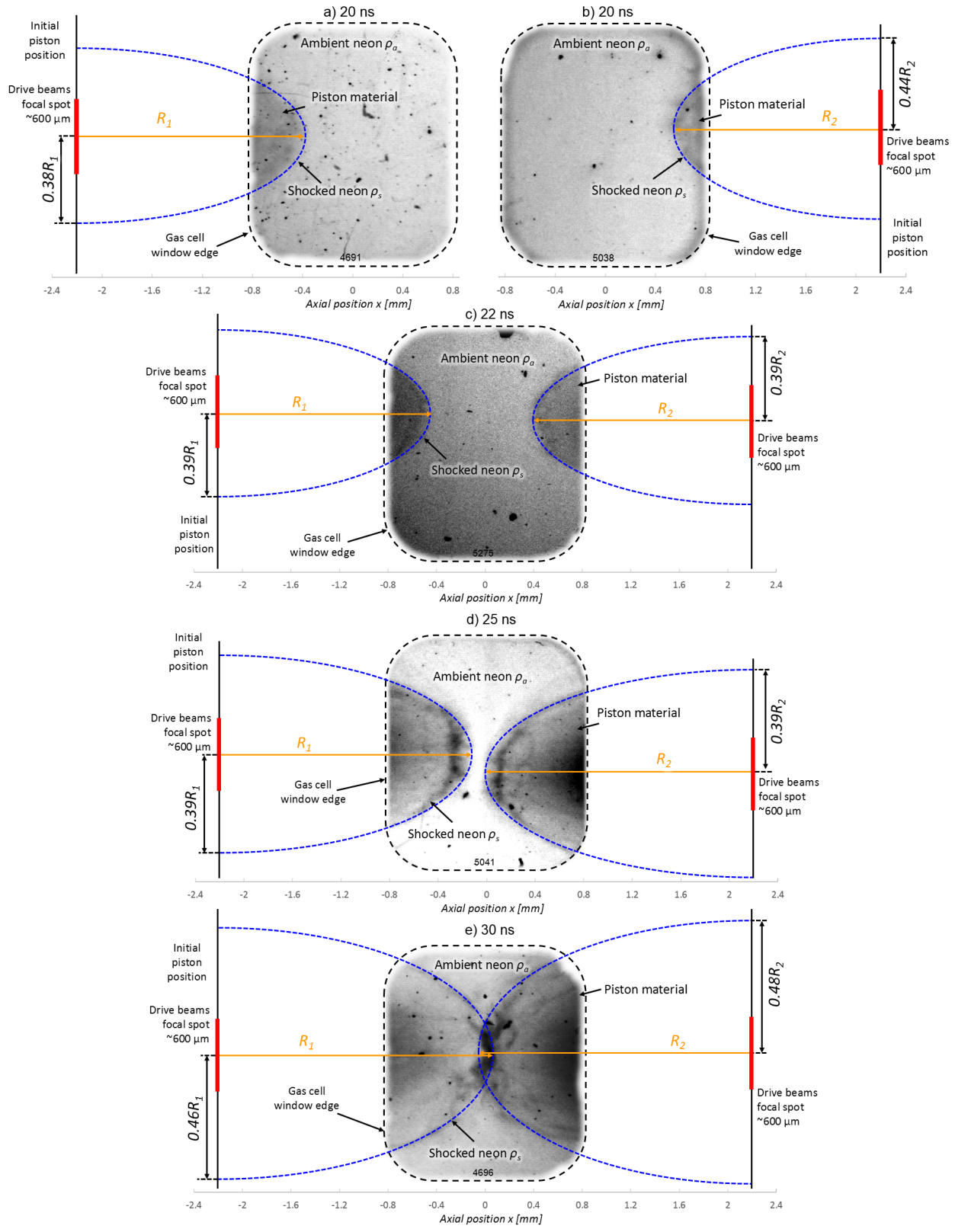


Figure 2.29: Prior to collision, shock were found to be well approximated as semi-ellipsoids centred on the drive beams focal spot with an aspect ratio of $A_R \sim 0.4$.

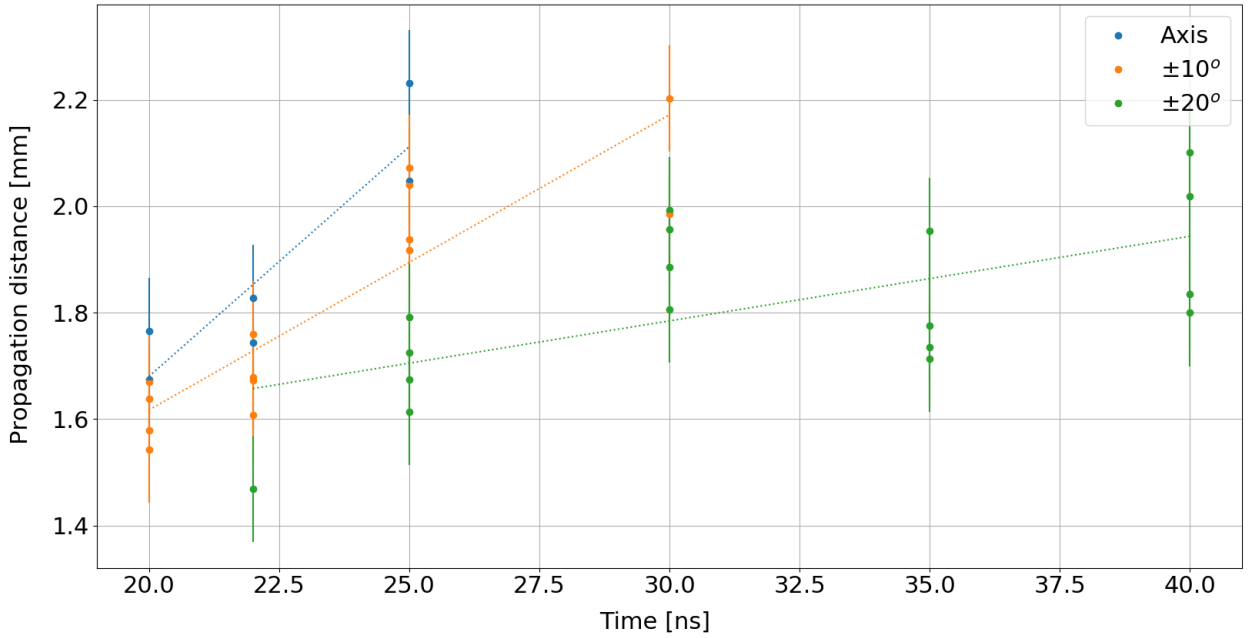


Figure 2.30: Shock front position as a function of time along radial lines originating at the piston position and passing through the shock front.

2.3.2 Post-shock compression

XRBL images were used to estimate the compression in the post-shock gas as this diagnostic is sensitive to changes in mass density. The following analysis assumes negligible mixing between the gas and piston material. 2-D radiative hydrodynamic simulations (detailed in Section 2.5) suggest this is a reasonable assumption for light elements, such as Neon investigated in this section, but is not the case for heavy elements such as Xenon studied in Section 2.3.4.

Profiles of normalised intensity were taken from the XRBL image of experiment #5041, with a Neon gas fill and initial mass density of 0.50 mg/cm^3, taken 25 ns after the drive beams. Profiles were taken along the approximate axis of the shock, $y = 0.15$ mm and $y = 0.05$ mm for the odd and even shocks respectively, and averaged over 100 μm. The location of these profiles is shown in Fig 2.31.a. Profiles were then shifted to the reference frame of the shock front (which was selected visually), with the even shock profile being flipped. These profiles are shown in Fig 2.31.b.

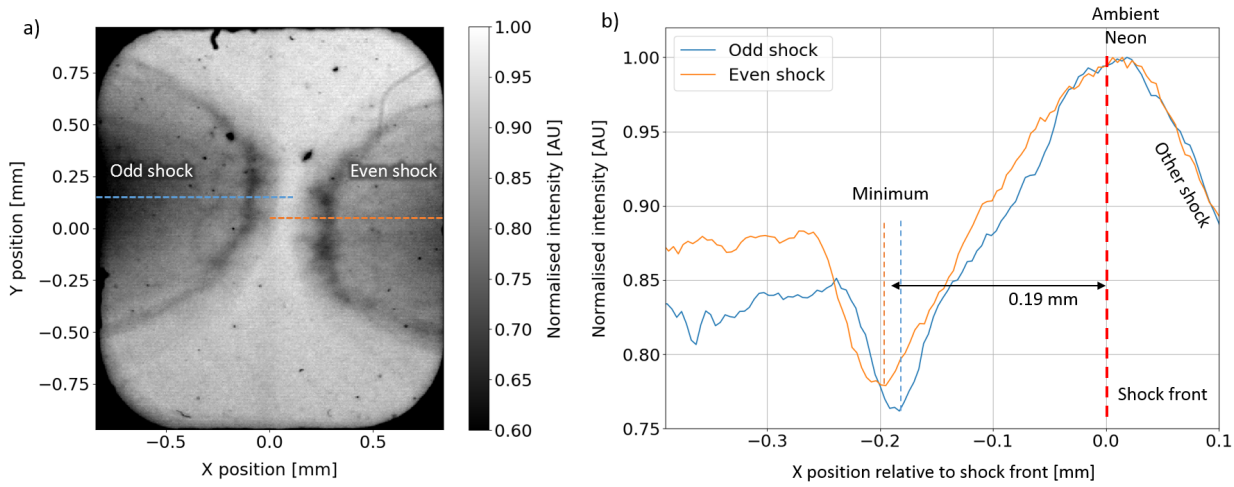


Figure 2.31: a) XRBL image of experiment #5041, with a Neon gas fill initially at 0.50 mg/cm^3, taken 25 ns after the drive beams. b) Profiles of normalised intensity along the approximate shock axis, averaged over 100 μm. Profile location indicated in a).

The unshocked, ambient material is identified on the right, with a normalised intensity of ∼1 (the reducing intensity to the far right of the profile is due to the opposite shock), followed by a region of decreasing intensity which is post-shocked material. The intensity decreases with distance from the shock front due to cylindrical symmetry, with X-rays closer to the piston passing through more shocked material and experiencing additional attenuation. In addition, radiative cooling in the post-shock region may lead to further increases in mass density away from the shock front and thus a steeper gradient. This region consists of shocked gas followed by shocked piston material (C_8H_7Br). However, the position of the boundary between the two is uncertain.

The average compression may be estimated by dividing the distance the shock has travelled, ∼2.1 mm, by the width of the shock region, assuming the shock acts approximately one-dimensionally on axis. The trough in intensity, labelled as *Minimum* in Fig 2.31.b, is also observed in simulations and is believed to be composed of piston material. Therefore, an upper bound for the shocked gas width was taken to be the distance between the unshocked gas with normalised intensity ∼1 and the minimum in intensity yielding a width of ∼0.19 mm. This yielded a lower bound for the post-shock compression of $\Gamma \sim \times 11$, corresponding

with a post-shock density of $\rho_{ps} \sim 5.5$ mg/cm^3. This compression is significantly higher than the compression limit of an adiabatic shock, $\times 4$, or even for a radiation dominated shock, $\times 7$ as shown in [Bouquet et al., 2000]. This suggests that ionization and radiative cooling (which are able to remove energy from the post-shock region) play a significant role in this experiment.

To more accurately approximate the post-shock compression, the XRBL profile was compared to calculated transmissions. These were calculated using the Beer-Lambert law given by Eq. 1.24. The photon energy of the XRBL was specifically selected to be monochromatic so that ionization would have minimal impact on the final transmission, thus the mass absorption cross section, σ, may be assumed to be constant through both unshocked and shocked gas. For experiments in Neon, Scandium backlighter targets were used which produced photons with an energy of $4086 - 4091$ eV. Values for the mass absorption cross section were determined using the online tool developed by the centre for X-ray Optics at Berkeley Laboratory [Henke et al., 1993]. This was used to estimate the transmission of photons, with the backlighters energy, after propagating through a small sample of gas. The mass absorption cross section for Neon was then calculated to be $\sigma = 171$ cm^2/g for photons with an energy of 4.09 keV. The intensity of X-rays not passing through the shocked material, I_a, is described by:

$$I_a = I_0 A e^{\sigma \rho_0 L} \tag{2.25}$$

where A describes any effect due to filters, ρ_0 is the density of the unshocked gas and L is the gas cell length. Fig 2.32 indicates how X-rays attenuated by the post-shock gas will have passed through predominantly unshocked gas and a region of post-shock gas with a length d. Assuming the post-shock gas has a constant mass density of ρ_{ps} the final intensity of the attenuated X-rays, I_s, is described by:

$$I_s = I_0 A e^{\sigma \rho_0 (L-d)} e^{\sigma \rho_{ps} d} \tag{2.26}$$

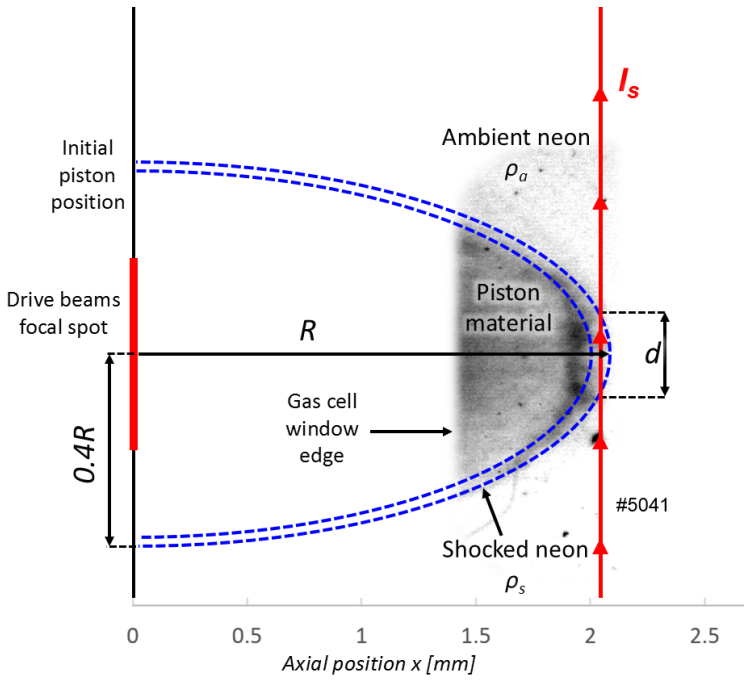


Figure 2.32: X-rays, at a position x from the drive beam focal spot, pass predominantly through unshocked ambient Neon and a region of post-shock Neon, with a length d. Due to cylindrical symmetry along the axis, rays coming out of the page experience similar attenuation as depicted in this figure.

Normalising the shocked intensity, I_s, with respect to the ambient intensity, I_a, results in:

$$\frac{I_s}{I_a} = e^{\sigma d(\rho_0 - \rho_{ps})} \tag{2.27}$$

By modelling the shock as a semi-ellipsoid with an aspect ration A_R, the length of the path through the post-shock region, d, at an axial position x, can be calculated as a function of the maximum distance of the shock front from the piston, R:

$$d = 2A_R\sqrt{R^2 - x^2} \tag{2.28}$$

The normalized intensity, I_s/I_a was calculated for several post-shock compressions and plotted on top of the profiles obtained from the XRBL image from experiment #5041, shown in Fig 2.33.a. However, plotting the transmission for a constant compression yields a curve which does not accurately represent the profile from the XRBL image. This is possibly

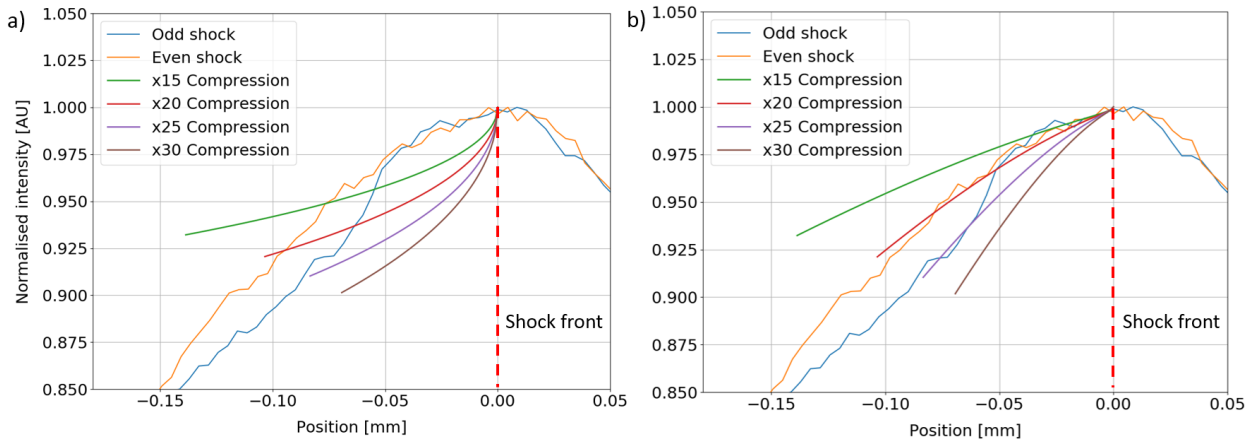


Figure 2.33: Calculated intensity for several post-shock compressions plotted on top of profiles obtained from the XRBL image shown in Fig 2.31. a) Assuming a constant compression. b) Assuming a linearly increasing compression.

because the mass density increases through the post-shock region due to radiative cooling. To improve upon this estimate, the post-shock mass density, ρ_{ps}, was modelled to be linearly increasing behind the shock front, this was approximated as the weighted average between the minimum and average mass densities, ρ_{min} and $\rho_{average}$:

$$\rho_{ps} = \frac{R-x}{W}\rho_{average} + \left(1 - \frac{R-x}{W}\right)\rho_{min} \tag{2.29}$$

where W is the thickness of the post-shock region. This was calculated assuming that on the axis the shock acts as if 1-D, and so the shock thickness is the distance the shock has travelled divided by the compression. The minimum mass density was taken to be the shock compression limit for an adiabatic shock, $\times 4$, multiplied by the ambient mass density, ρ_0 (however, the resulting transmission profile is not strongly dependant on this choice). The average mass density, $\rho_{average}$, was taken to be the post-shock compression multiplied by the ambient mass density.

With this new model the normalized intensity was again calculated for several post-shock compressions and plotted on top of the profiles obtained from XRBL images, shown in Fig 2.33.b. The resulting calculated curves closely follow the measured intensities. A compression of $\times 23 \pm 4$, was found to best approximate the measured intensity of the XRBL profiles, for

experiment #5041 after 25 ns. As the shocks are not 1-D, this estimate may not be valid away from the axis. To improve upon the accuracy of this estimate, numerical models are required, discussed in Section 2.5.

However, laser-target XRBL sources can produce a significant background of hard X-rays (> 10 keV) due to fast electrons interacting with the pinhole material [Krauland et al., 2012, Fein et al., 2014]. The 25 μm titanium filter placed over the image plate was transparent to X-rays above 9 keV and so these background X-rays could have a significant effect on these estimates. To reliably use XRBL images to infer densities, a method of accurately characterising these hard X-rays is required.

In summary, the average post-shock compression (25 ns after the drive beams) was estimated to be $\times 23 \pm 4$, corresponding to an average post-shock mass density of $\rho_{ps} = 11 \pm 2$ mg/cm^3. This compression is comparable to previous radiative shock experiments in 1-D shock tubes with Xenon gas fills [Drake, 2006, Stehlé et al., 2012].

These results were compared with the radiative shock model developed in Section 1.6.4. Assuming an initial mass density of $\rho_0 = 0.5$ mg/cm^3 and shock velocity of $v_s = 60$ km/s yielded a post-shock temperature of $T_{ps} = 13.4$ eV and post-shock ionization of $Z_{ps} = 3.0$. These are comparable to estimates from 2-D radiative hydrodynamic simulations of $T_{ps} \sim 15$ eV and $Z_{ps} \sim 4$ (detailed in Section 2.5). This model suggests that 62% of the kinetic energy of the incoming particles is dissipated as radiation, indicating that radiation plays a major role in this system. However, this model suggests a post-shock mass density of $\rho_{ps} = 3.5$ mg/cm^{-3}, significantly lower than the measured values of $\rho_{ps} = 11 \pm 2$ mg/cm^3.

2.3.3 The reverse shock

After the shocks collide ($\sim$30 ns after the drive beams) a darker region is visible on the XRBL images indicating a region of higher density, labelled as 'reverse shock' in Fig 2.25.f-g. In addition, self-emission streak images indicate an expanding region of enhanced emission, shown in Fig 2.34. It is assumed that the shocks collide collisionally, resulting in material

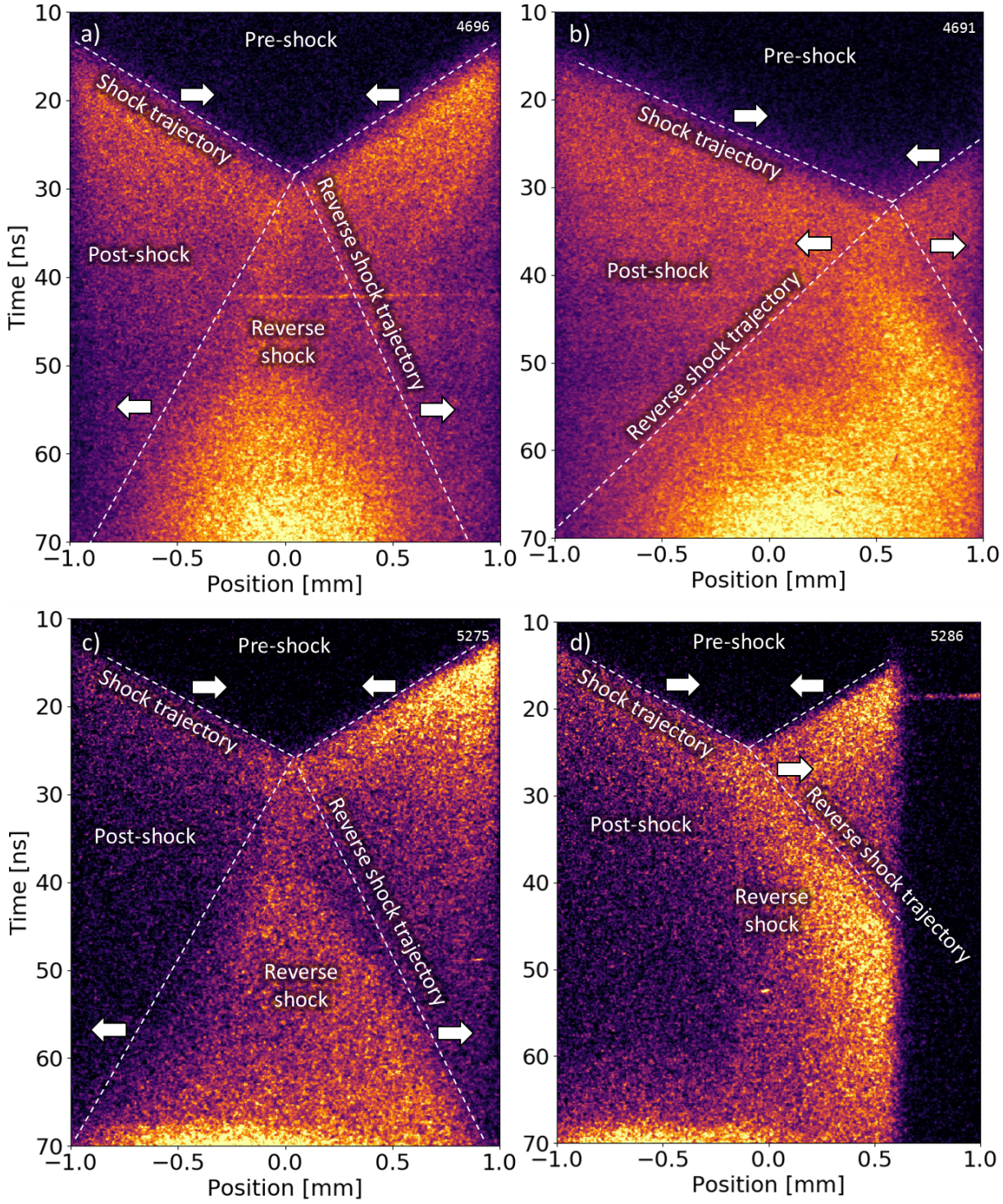


Figure 2.34: Self-emission streak images from four experiments with a Neon gas-fill with an initial mass density of at 0.5 mg/cm^3.

stagnating on the gas cell axis and forming a reverse shock. To ensure that this is the case the mean free path of particles may be calculated using the numerical estimate given by

[Park et al., 2012]:

$$\lambda_{mfp}(cm) \sim 5 \times 10^{-13} \frac{A^2}{Z_{ps}^4} \frac{[v_s(cm/s)]^4}{n_i(cm^{-3})} cos^4\left(\frac{\alpha}{2}\right) \tag{2.30}$$

where A is the atomic mass number, Z_ps is the average post-shock ionization, v_s is the shock velocity, n_i is the post-shock ion density and α is the angle the two shocks make, in this case $\alpha = 0$. For these experiments with a Neon gas-fill, $A = 20$, the shock velocity was measured to be $v_s \sim 6 \times 10^6$ cm/s and the post-shock mass density was measured to be $\rho_s \sim 11$ mg/cm^3. This yields an ion density of $n_i = \rho_{ps}/(m_p A) \sim 3 \times 10^{20}$ cm^{-3}. Estimates of the post-shock ionization as a function of velocity in Section 1.6.4 suggest $Z \sim 3$. This yields an interpenetrating mean free path of ~ 100 nm. This is far below the scale length of the experiment and so the shocks are expected to act collisionally with material stagnating on the axis and forming a reverse shock.

This reverse shock structure is asymmetric and non-uniform, as seen in the XRBL image shown in Fig 2.25.g. In addition, the post-shock self-emission streak images were unfortunately too noisy to determine the reverse shock velocity via the procedure performed in Section 2.3.1. Instead the reverse shock trajectory was visually identified, assuming a constant a linear velocity as shown in Fig 2.34. These four self-emission streak images yielded a reverse shock velocity of $v_{rs} \sim 25 \pm 10$ km/s, slower than the velocity estimates made from XRBL images, 38 ± 10 km/s, shown in Fig 2.26. Combining these estimates yields a final reverse shock velocity of 32 ± 14 km/s.

The mass density of material behind the reverse shock, ρ_{rs}, was directly measured from the intensity of XRBL images. Fig 2.35.a shows how X-rays passed through predominantly ambient gas and a length d through the reverse shock. Assuming that the material within this region is of relatively constant mass density and composed predominately of shocked gas with a constant mass absorption cross section, $\sigma = 171$ cm^2/g for Neon, the final intensity of the attenuated X-rays, I_{rs}, is given by:

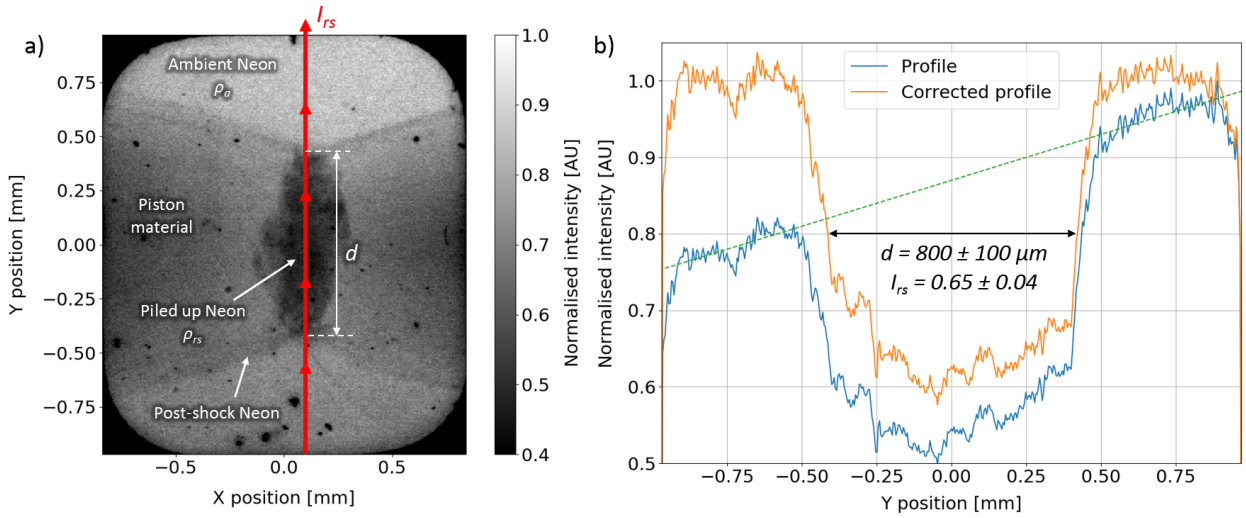


Figure 2.35: (a) XRBL image taken 35 ns after the drive lasers from experiment #5273, with a Neon gas-fill initially at 0.49 mg/cm^3. The two shocks from either side have collided resulting in material stagnating in the centre with a density of ρ_{rs}. X-rays passing through this region are attenuation over the length d, resulting in a final intensity of I_s. (b) Vertical profile of normalized intensity through the centre of the shock interaction at $x = 0.1$ mm.

$$I_{rs} = I_0 A exp\left[-\sigma\rho_0(L-d)\right] exp\left[-\sigma\rho_{rs}d\right] \tag{2.31}$$

where ρ_{rs} is the mass density of the reverse shock. By normalizing this with X-rays passing solely through the unshocked plasma, an expression for the mass density within the post-reverse shock region can be derived, found to be:

$$\rho_{rs} = \rho_0 - \frac{ln\left(I_{rs}/I_a\right)}{d\sigma} \tag{2.32}$$

Fig 2.35.b shows a profile of normalised intensity through the reverse shock region from experiment #5273. This was taken through the centre of the shock interaction (at $x = 0.1$ mm) and averaged over 100 μm. However, this profile shows significantly different intensities in the ambient Neon at positive and negative Y positions. These regions have not been perturbed by the shock and so are expected to have a normalized intensity of unity. This was found to be well approximated by a linear profile, shown with the green dashed line in Fig 2.35.b. Dividing by this linear profile yields a corrected profile which is correctly normalized,

shown in orange in Fig 2.35.b.

This corrected profile yields a reverse shock length of $d = 800 \pm 100$ μm with a normalised intensity of $I_{rs}/I_a = 0.65 \pm 0.04$. Equation 2.32 therefore yields a post-reverse shock mass density of 32 ± 9 mg/cm^3, corresponding with a total compression of $\times 64 \pm 18$.

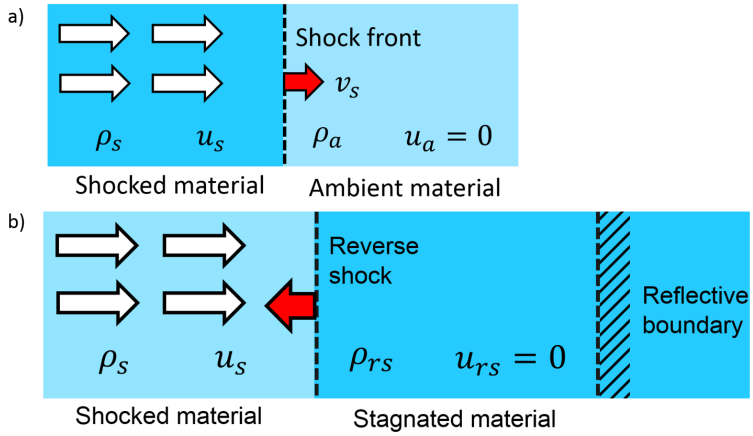


Figure 2.36: a) 1-D diagram of the formation of a shock. b) 1-D diagram of the formation of a reverse shock.

The mass density of the post-reverse shock region, ρ_{rs}, can also be estimated from the Rankine-Hugoniot equation for mass conservation, $\rho_1 u_1 = \rho_2 u_2$, where ρ_1 and ρ_2 are the mass densities and u_1 and u_2 are the particle velocities in the shock frame for the pre-shock and post-shock regions respectively. Particles in the unshocked, ambient gas have negligible initial velocities and so, in the shock frame, are moving at the shock velocity of v_s. Particles in the post-shock region have a velocity of u_s in the lab frame and so a velocity of $v_s - u_s$ in the shock fronts frame, indicated in Fig 2.36. Therefore:

$$v_s \rho_0 = (v_s - u_s)\rho_{ps} \tag{2.33}$$

and:

$$u_s = v_s - v_s \frac{\rho_0}{\rho_{ps}} \tag{2.34}$$

where ρ_0 is the mass density of the unshocked, ambient gas and ρ_{ps} is the mass density of

the post-shock gas. The reverse shock propagates with a velocity v_{rs}, into the post-shock region forming a reverse shock region in the centre of the gas-cell with a mass density ρ_{rs}, as shown in Fig 2.36. Particles in this region have stagnated at the gas-cell centre with negligible velocity, and so in the reverse-shock frame they move at the reverse shock velocity v_{rs}. Particles in the post-shock region therefore move at $u_s + v_{rs}$ towards the reverse shock. Using the mass conservation equation once again allows the mass density within the stagnated gas, ρ_{rs}, to be calculated:

$$\rho_{rs} v_{rs} = \rho_{ps}(u_s + v_{rs}) \tag{2.35}$$

Using Eq. 2.34 allows this to be expressed as:

$$\rho_{rs} = \frac{v_s}{v_{rs}} (\rho_{ps} - \rho_0) + \rho_{ps} \tag{2.36}$$

In Section 2.3.1 the shock velocity was determined to be $v_s = 60 \pm 4$ km/s. The reverse shock velocity was measured to be 32 ± 14 km/s from XRBL images in Fig 2.27. Section 2.3.2 found the average post-shock mass density to be $\rho_{ps} = 11 \pm 2$ mg/cm^3. With an initial mass density of $\rho_0 = 0.49 \pm 0.01$ mg/cm^3, a reverse shock mass density of $\rho_{rs} = 28 \pm 7$ mg/cm^3 was calculated, closely agreeing with the mass density measured from XRBL images. The average of these two measurements yields a reverse shock mass density of 31 ± 10 mg/cm^3, corresponding to a compression of $\times 62 \pm 20$ compared to the initial gas fill. However, the jump in density at the reverse shock front is only $\sim\times 3$, below the compression limit of an ideal, monatomic gas of $\times 4$.

Despite the similarity in density calculated from both of these methods, 2-D radiative hydrodynamic simulations (detailed in Section 2.5) indicate that the central region is primarily composed of piston material. Mixing between the Neon and piston material will result in significantly different X-ray transmission properties due to different mass absorption cross section. Thus the measured compression of $\sim \times 60$ may not be valid.

2.3.4 Experiments with Xenon gas-fills

In addition, a series of experiments were performed with a Xenon gas-fill with a higher initial mass density of $\rho_0 \sim 1.6$ mg/cm^3 ($P_0 \sim 0.3$ bar). These experiments were analysed in a similar manner to those performed in Neon.

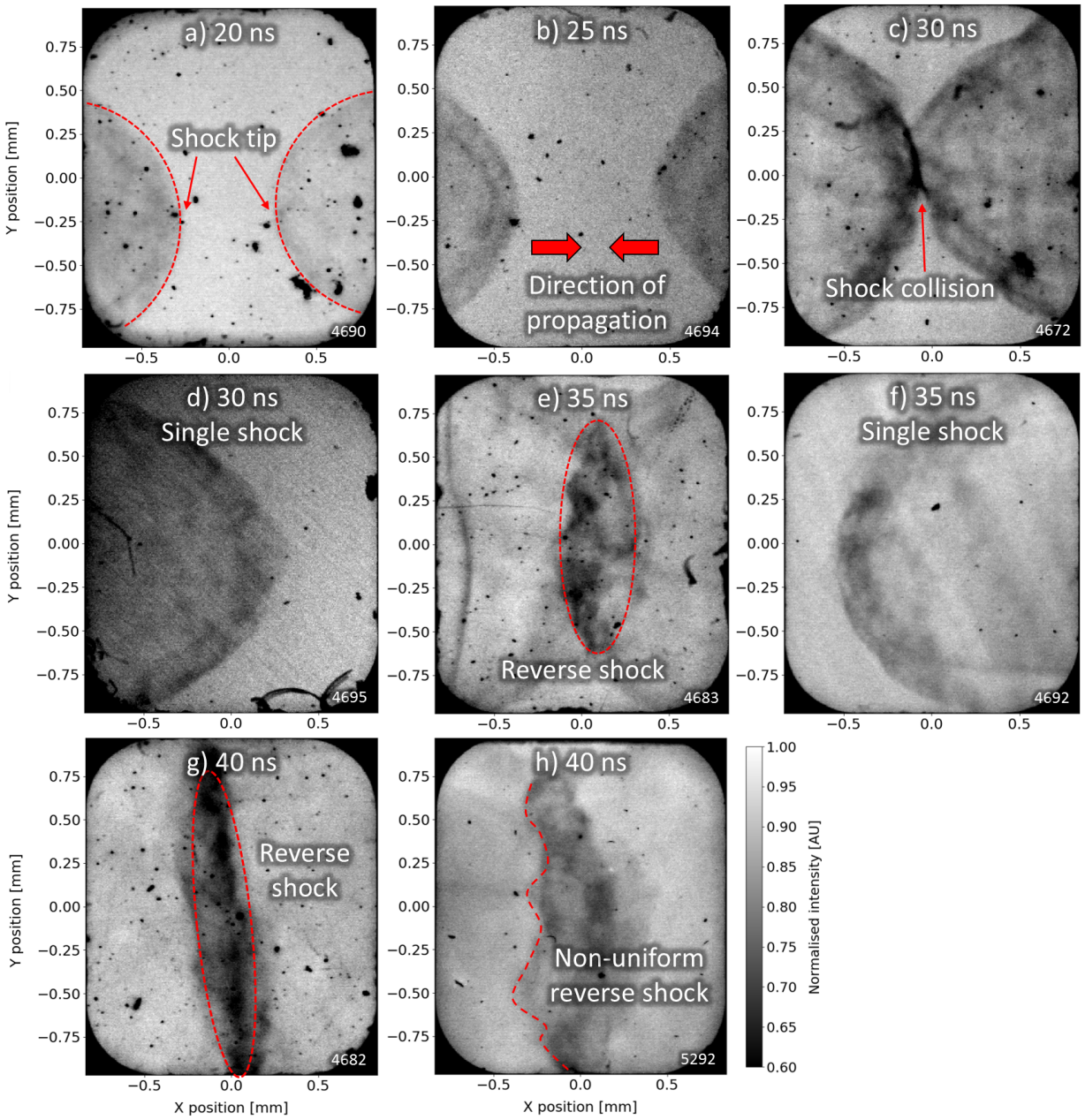


Figure 2.37: Time sequence constructed from several normalised XRBL images of different experiments with a Xenon gas-fill with an initial mass density of $\rho_0 = 1.6 \pm 0.2$ mg/cm^3 ($P_0 = 0.31 \pm 0.04$ bar).

A time sequence constructed from XRBL images, from eight different experiments, is shown in Fig 2.37. These images used the same X-ray backlighter setup as that in experiments with Neon except that an Iron backlighter targets were used, achieving an approximately monochromatic X-ray source with a photon energy of 6.7 keV.

The images shown in Fig 2.37 are similar to those taken with Neon gas fills (shown in Fig 2.25) and normalized against the unshocked regions. Darker regions correspond with regions of higher X-ray absorption and thus higher mass density and the two shocks are visible to the left and right of the image as dark semi-circular regions, labelled in Fig 2.37.a. The shocks propagate towards the centre of the image and collide at ∼30 ns, seen in Fig 2.37.c. The formation of a reverse shock is then observed in the centre of the image at 35 ns in Fig 2.37.e. This reverse shock structure then evolves in a very non-uniform manner, as seen in Fig 2.37.h.

An initial estimate of the shock velocity was made by dividing the distance the shock has travelled between Fig 2.37.a and Fig 2.37.c, visually measured to be ~ 0.25 mm, by the 5 ns interval between the frames. This yielded a velocity of $v_s \sim 75 \pm 25$ km/s. Similarly, the velocity of reverse shock was estimated by dividing the distance the shock has travelled between Fig 2.37.b and Fig 2.37.c, $d = 0.25$ mm and 0.5 mm, which yielded a value of $v_{rs} \sim 30$ km/s.

An improved estimate of the shock velocity immediately prior to collision was made in a similar fashion to the methodology described in Section 2.3.1. Shock front tip positions were measured from all of the XRBL images shown in Fig 2.37. These positions were divided into pre-collision and post-collision and plotted against time in Fig 2.38. This yielded a shock velocity prior to collision of $v_s = 53 \pm 15$ km/s and reverse shock velocity of $v_{rs} = 25 \pm 11$ km/s. This was confirmed using optical self-emission streak images, shown in Fig 2.39. A similar analysis to that performed in Section 2.3.1 was performed to estimate the shock velocity. This yielded a shock velocity of $v_s = 64.4 \pm 1.8$ km/s for the odd shock and $v_s = 56.0 \pm 0.8$ km/s for the even shock.These shock trajectories are plotted in Fig 2.38 and agree with the previous shock velocity estimated from XRBL images.

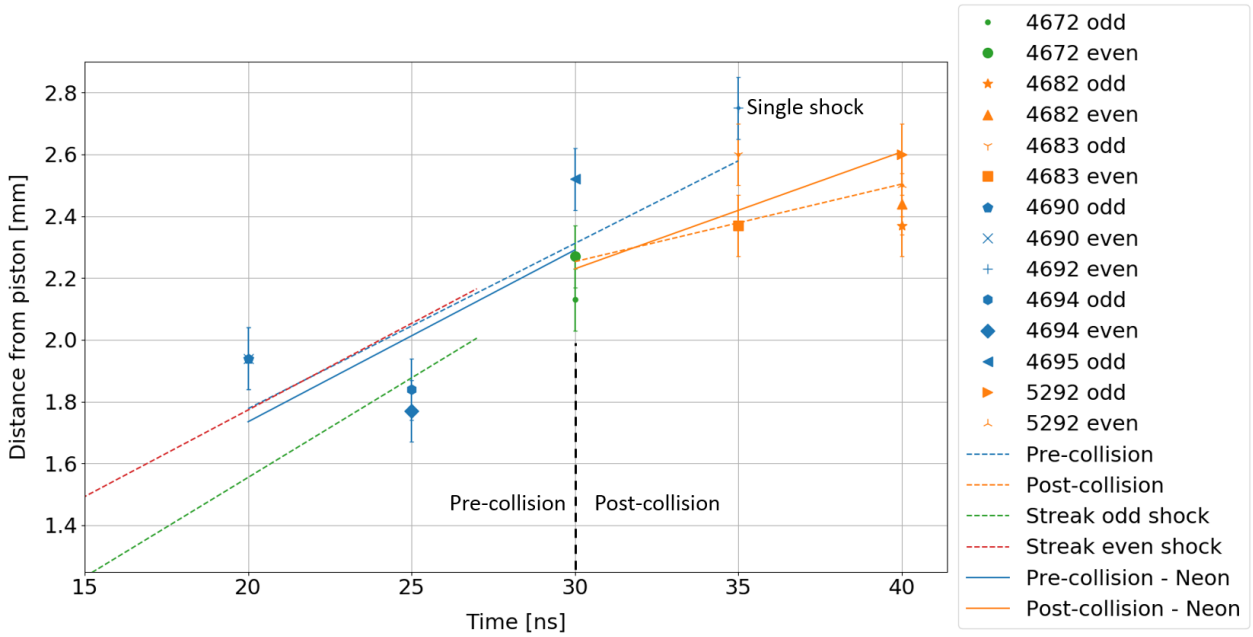


Figure 2.38: Position of the shock front tip in XRBL images from experiments in Xenon. The points have been separated into pre-collision and post-collision, and both groups approximated by linear trend lines. Shock trajectory measured from self-emission streak images and XRBL images of Neon are also shown.

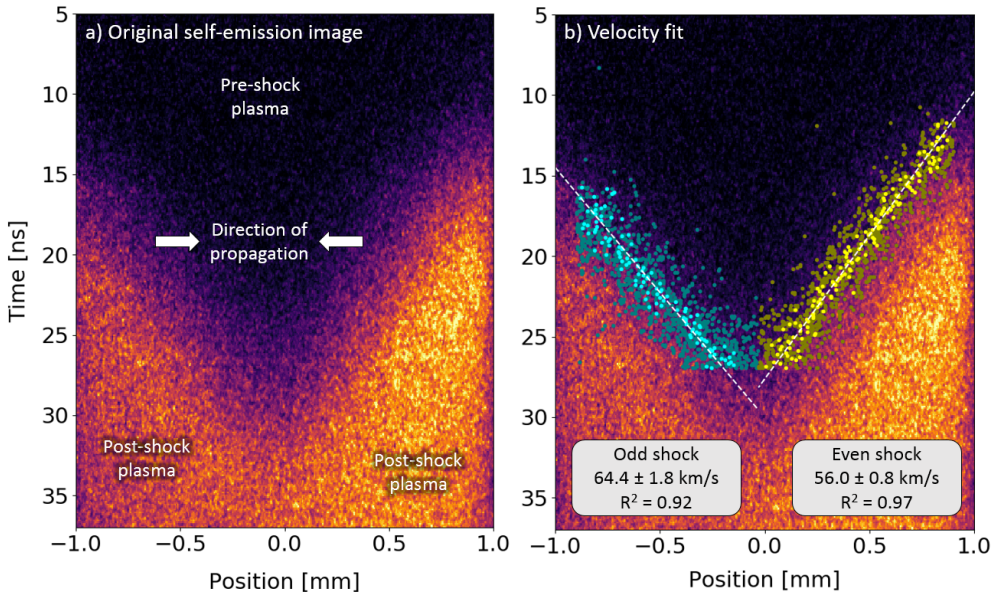


Figure 2.39: Shock velocity measured from a self-emission streak image from experiment #4694, with Xenon gas-fill with an initial mass density of 1.47 mg/cm^3 (0.28 bar).

Therefore an average shock velocity of $v_s = 58 \pm 15$ km/s and reverse shock velocity of $v_{rs} = 25 \pm 11$ km/s was measured for these experiments with Xenon gas-fills initially at 1.6

mg/cm^3. This is very similar to velocities measured in Neon experiments with an initial mass density of 0.5 mg/cm^3. The shock trajectories for experiments in Neon, determined from XRBL images, are plotted with solid lines in Fig 2.38 and show excellent agreement with shock trajectories determined for experiments with Xenon gas-fills despite having a third of the initial mass density. While a higher mass density gas-fill will cause the shock to loose more energy over time, causing it to more rapidly decelerate, in these experiments the piston was significantly more massive and so was negligibly effected by the gas-fill. The pistons had an areal mass density of $\sim$10 mg/cm^2, significantly higher than the area mass density of half the gas cell, $0.1 - 0.3$ mg/cm^2 for the experiments with Neon and Xenon respectively. In both series of experiments the Orion beam energy remained constant, with variation of $\sim$10% , resulting in a consistent piston ablation velocity and therefore similar shock velocity.

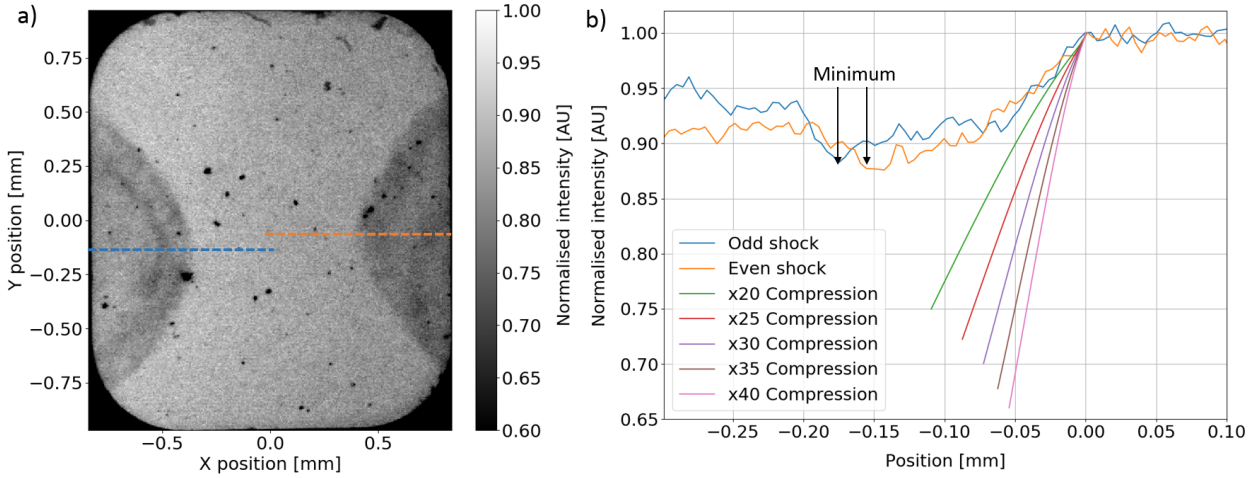


Figure 2.40: Profiles of X-ray normalized intensity through the shock front. a) Position of profiles. b) Profiles offset to the shocks frame. Calculated normalized intensities for different compressions are plotted on top.

To estimate the post-shock density, ρ_{ps}, a similar analysis to that in Section 2.3.2 was performed on XRBL images from Xenon experiments. Horizontal profiles, averaged over 100 μm, were taken along the shocks axis from XRBL images at a position of $y = -0.17$ mm for the odd shock and $y = -0.07$ for the even shock, as shown in Fig 2.40.a. These profiles were shifted to the shock fronts reference frame and are shown in Fig 2.40.b. Transmission for different average compression, assuming a linearly increasing density, were calculated using

	Neon	**Xenon**
Atomic mass	20	132
Fill pressure [bar]	0.6	0.3
Initial mass density [mg/cm^3]	0.5	1.6
Post-shock mass density ρ_{ps} [mg/cm^3]	12 ± 2	unknown
Post-shock compression	$\times 23 \pm 4$	unknown
Reverse shock mass density ρ_{rs} [mg/cm^3]	31 ± 10	unknown
Reverse shock compression	$\times 62 \pm 20$	unknown
Shock velocity v_s [km/s]	60 ± 10	58 ± 15
Reverse shock velocity v_{rs} [km/s]	32 ± 14	25 ± 11

Table 2.7: Comparison of key parameters between experimental series performed with Neon and Xenon gas-fills.

the methodology described in Section 2.3.2. Using the online tool developed by the centre for X-ray Optics at Berkeley Laboratory [Henke et al., 1993], a mass absorption cross section of $\sigma = 556$ cm^2/g was calculated for Xenon. The resultant transmissions are shown in Fig 2.40.b, however none of these calculated profiles match the XRBL profiles. Profiles calculated for lower compressions are also not plausible as they would yield a post-shock Xenon layer that extends past the minimum transmission, which simulations indicate is composed of piston material.

It is possible that the post-shock Xenon layer is not visible if its thickness is below the minimum resolution of the XRBL system, found to be $\sim$40 μm in Section 2.2.1 (including effects of motion blur). Assuming an approximately 1-D compression at the shock tip, compressions of $\Gamma > \times 50$ would be challenging to resolve with this system. Secondly, 2-D radiative hydrodynamic simulations, discussed in Section 2.5, show significant mixing of post-shock and piston material which would significantly effect the X-ray transmission and thus could make this method ineffective at determining the post-shock mass density in this system.

A comparison between the experimental series performed with Neon and Xenon gas-fills, with an initial mass density of 0.5 mg/cm^3 and 1.6 mg/cm^3 respectively, is shown in Table 2.7.

2.4 The radiative precursor

This section investigates the precursor observed ahead of the shock front in counter-propagating radiative shock experiments performed on the Orion laser facility. While XRBL provides information about the post-shock region, it is not sensitive to the precursor ahead of the shock front. This region has the same mass density as the initial gas-fill, but is heated and ionized by radiation emitted from the shock front. Therefore laser interferometry (described in Section 2.2.3) was used to measure the electron density integrated along the path of the probe beam, $n_e L$ (units of cm^{-2}).

2.4.1 Precursor structure

Fig 2.41.a-d shows four Gated Optical Intensifier (GOI) images, all from the same experiment, #5286, with a Neon gas-fill and initial mass density of $\rho_0 = 0.48$ mg/cm^3 ($P_0 = 0.59$ bar). The orientation of these images is similar to that of the XRBL images in Fig 2.25, however these images do not need to be corrected for point projection scaling as the laser probe beam is collimated. This diagnostic measures changes in the refractive index integrated along the path of the probe beam. Shifts in the fringe position from their original vertical lines, shown in the background image in Fig 2.41.i, indicates a change in refractive index and thus a change in electron density.

The shocks appear as dark semi-circular shaped regions to the left and right of each image, labelled in Fig 2.41.a, as the dense post-shock material is opaque to the laser probe beam with an electron density greater than the critical plasma density $n_c = 3.9 \times 10^{21}$ /cm^3. In addition, strong gradients in the refractive index ahead of the shock front cause the probe beam to be refracted out of the collection optics, making the region directly ahead of the shock front appear opaque even when below the electron critical density. This is expected to slightly increase the apparent shock size and means the exact location of the shock front is unknown. Bending of the fringes directly ahead of the shocked plasma indicate a non-zero

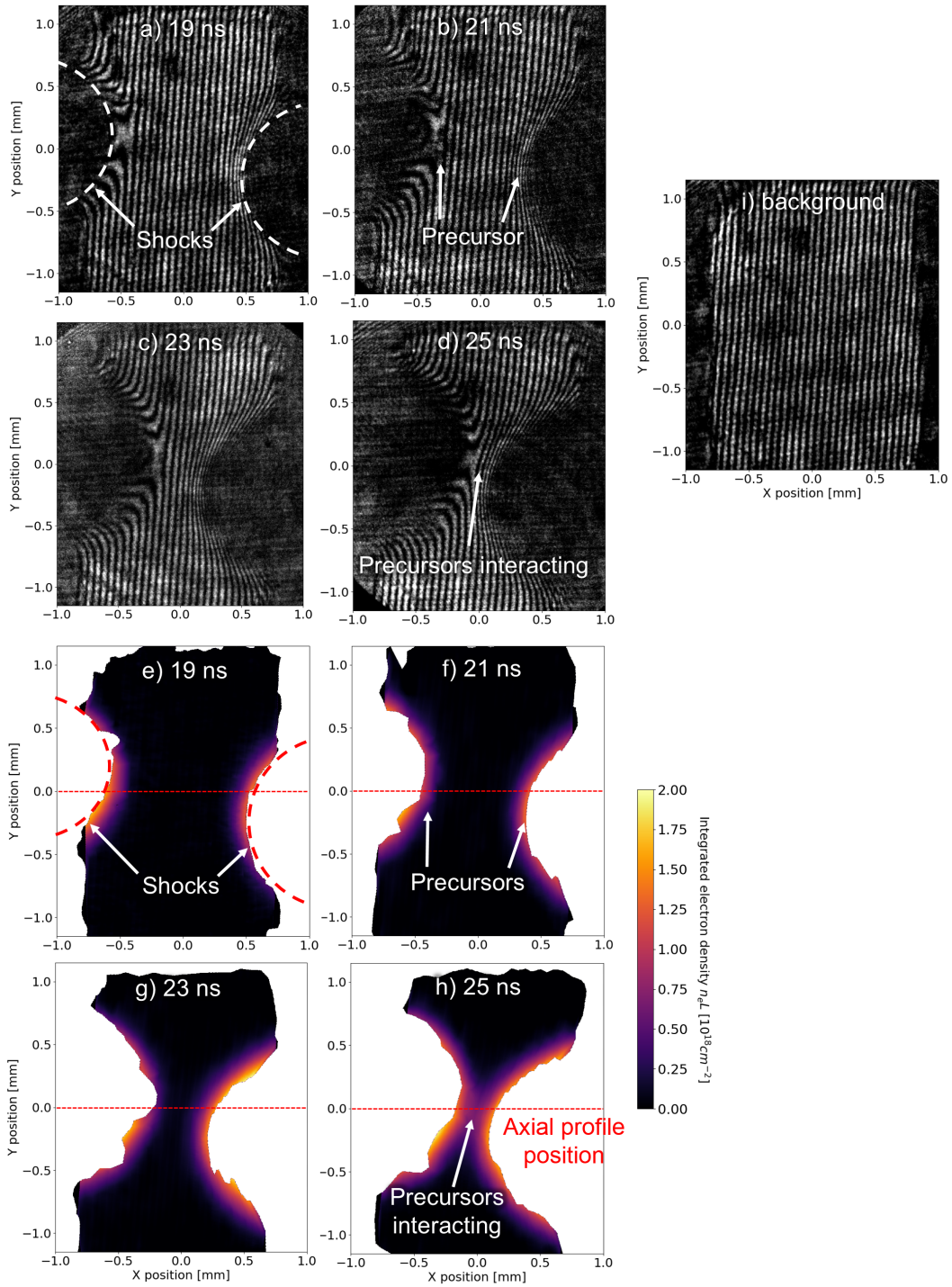


Figure 2.41: a-d) Four GOI interferometry images, taken at different times, from experiment #5286 with a Neon gas-fill and initial mass density of $\rho_0 = 0.48$ mg/cm^3 (with a mass density of $P_0 = 0.59$ bar). e-h) Processed maps of electron density integrated along the path of the probe laser beam, $n_e L$. i) Background fringes taken before the experiment.

electron density and thus the presence of a precursor proceeding the shock. Over time the shocks propagate towards the centre of the gas cell, resulting in the precursors interacting at $\sim$ 25 ns, as seen in Fig 2.41.h.

Fringes in the interferometry images and reference images, an example of which is shown in Fig 2.41.i, were traced and processed using the methodology described in Section 2.2.3. This yielded 2-D maps of n_eL shown in Fig 2.41.e-h. The opaque regions, where fringes could not be traced, have been coloured white. These images show a smooth gradient in electron density outlining the shock front and extending for $\sim$200 μm. The resolution of this diagnostic is limited to roughly half the inter-fringe spacing, limiting the spacial resolution to $\sim$32 μm and resolution of n_eL to 2.1×10^{17} cm^{-2}. As the observed precursor is smooth, there is no internal structure larger than the resolution of this diagnostic, $\sim$32 μm.

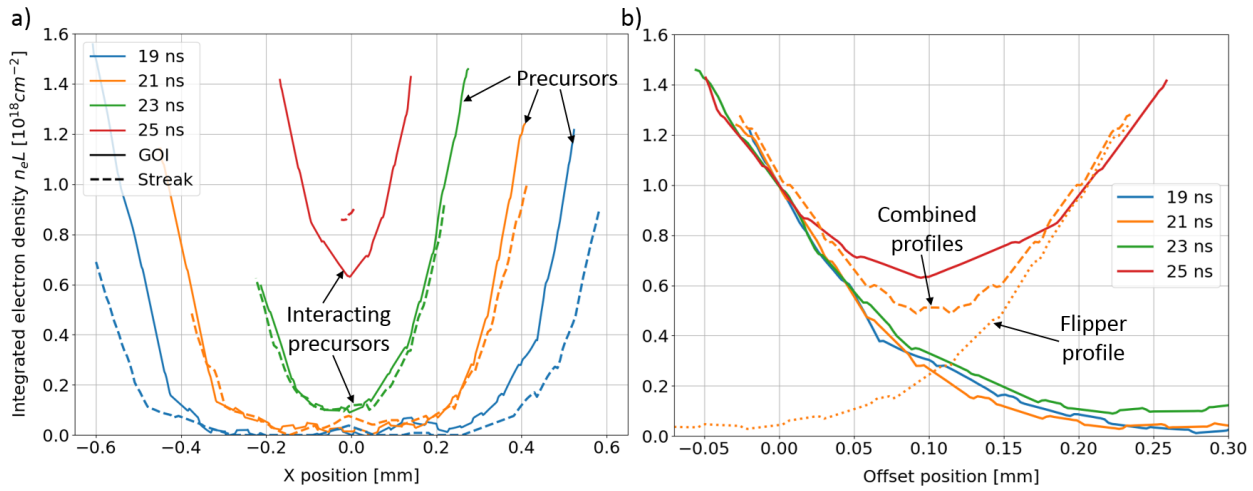


Figure 2.42: a) Solid lines, profiles from 2-D maps of n_eL shown in Fig 2.41.e-h. Dashed lines, profiles from streak maps of n_eL shown in Fig 2.45.b. b) Profiles shifted so they overlap. Dotted line shows the profile at 21 ns inverted so it overlaps with the right hand side of 25 ns. Dashed line is the sum of the two profiles at 21 ns.

Axial profiles were taken from Fig 2.41.e-h and are plotted in Fig 2.42.a. The two precursors can be seen on the left and the right as steep gradients in n_eL. Early time profiles, taken at 19 ns and 21 ns, show zero electron density in the centre of the gas cell. However, later time profiles, taken at 23 ns and 25 ns, show the precursors interacting - resulting in enhanced electron density at the centre of the as cell.

To investigate how the radiative precursor evolves over time, the profiles were shifted to the approximate shock frame. As the shock front position is unknown in these images this was approximated by offseting the profiles to intercept when $n_eL = 1 \times 10^{18}$ cm^{-2}, shown in Fig 2.42.b. Note that the right hand side (even shock) of the profiles in Fig 2.42.a were used as these include measurements of n_eL closer to the shock front. Profiles at 19 ns, 21 ns and 23 ns show very similar shapes and closely follow one another over a distance of 0.2 mm. However, the profile taken at 25 ns, red line in Fig 2.42.b, shows the two precursors interacting strongly and reaches a minimum integrated electron density of $n_eL = 0.63 \times 10^{18}$ cm^{-2}.

To investigate how the two radiative precursors interact, the profile taken at 21 ns was flipped and offset so that it intercepts the right hand side of the profile taken at 25 ns when $n_eL = 1 \times 10^{18}$ cm^{-2}, shown with the dotted orange line in Fig 2.42.b. These two offset profiles from 21 ns were summed resulting in the orange dashed line in Fig 2.42.b. As the beam path remains constant, this may then be compared to the profile taken at 25 ns. The calculated profile closely follows the profile taken at 25 ns but with a lower minimum value of $n_eL \approx 0.49 \times 10^{18}$ cm^{-2}. The difference in minimum value of $\sim 0.14 \times 10^{17}$ cm^{-2} corresponds to a third of a fringe shift and so is comparable to the error in these measurements. This indicates that when the two precursor interact the enhanced electron density is approximately the sum of the two separate precursors.

To investigate how the precursor is structured off-axis, radial profiles were taken at angles of $\pm 10^\circ$ and $\pm 20^\circ$ from the 2-D map of n_eL from experiment #5286 after 21 ns. These profiles originated from the approximate piston position at $x \approx -2.2$ mm with $y \approx 0.16$ mm (the approximate axis of the off shock), and their location is indicated in Fig 2.43.a. The resulting profiles are shown in Fig 2.43.b, plotted as a function of distance from the initial piston position. The profiles from different angles shown in Fig 2.43.b bear remarkable similarities to one another. Fig 2.43.c plots the same profiles off-set so that they intercept at an integrated electron density of $n_eL = 1 \times 10^{18}$ cm^{-2}, demonstrating how similar these

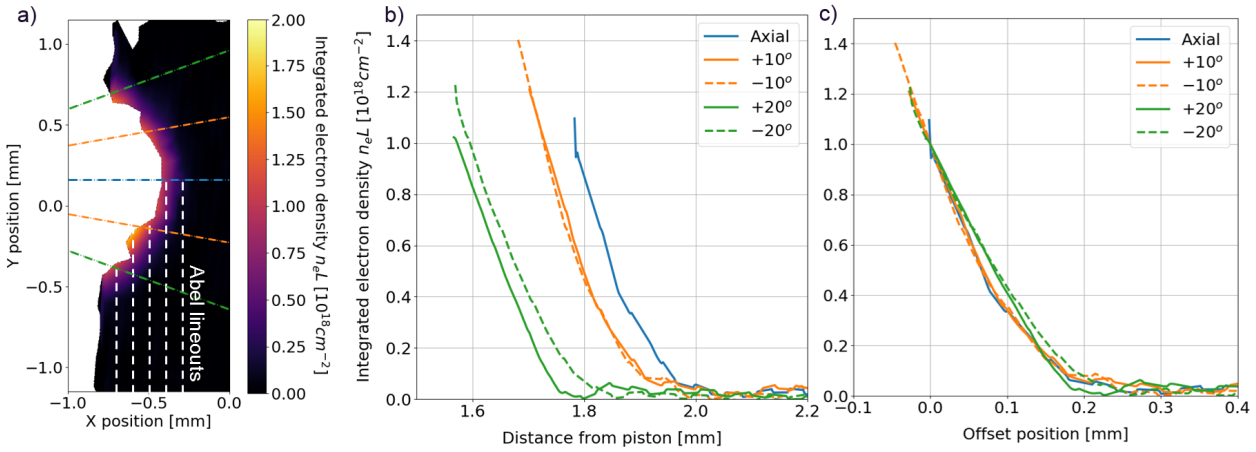


Figure 2.43: a) Radial profiles originating from the approximate piston position $x \sim -2.2$ mm with $y \approx 0.16$ mm, the approximate axis of the odd shock. Plotted on top of Fig 2.42.e. b) Resulting radial profiles of n_eL, from experiment #5286 after 21 ns, plotted as a function of distance from the piston position. c) Radial profiles offset so that they intercept at an integrated electron density of $n_eL = 1 \times 10^{18}$ cm^{-2}.

profiles are. Despite the slower off-axis expansion velocity, the precursor extends the same distance on the shock axis and radially.

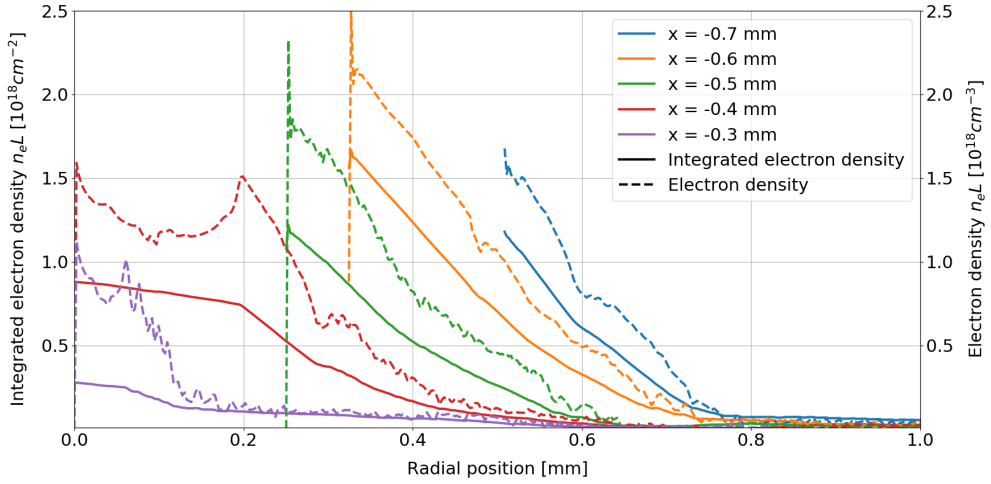


Figure 2.44: Abel inversions of vertical profiles taken from the 2-D GOI map of n_eL taken at 21 ns, indicated in Fig 2.43.a.

The shocks propagate with cylindrical symmetry around the shock axis ($y \approx 0.16$ mm) and therefore the electron density as a function of radial distance from the axis may be determined using an Abel inversion, as described in Section 2.2.3. Vertical profiles were taken from the 2-D map of n_eL, taken at 21 ns, and are labelled as 'Abel lineout' in Fig 2.43.a.

The Abel inversions of these profiles are shown with solid lines in Fig 2.44 while the original profiles are shown with dotted lines. The Abel inversion profiles follow similar shape to the original profiles and indicate that the electron density decreases gradually with distance from the shock front.

2.4.2 Evolution of the precursor

In addition to GOI cameras, a streak camera recorded a 1-D line of interferometry from the gas-cell axis, inline with the shock direction of propagation (as detailed in Section 2.2.3). This location is the same as the axial profile location indicated in Fig 2.41.e-h. The original streak interferometry image, from experiment #5286 is shown in Fig 2.45.a. The 1-D axial lineout is plotted in the horizontal axis and time in the vertical axis. The two shocks are seen as dark regions, as the post-shock plasma is opaque to the probe laser probe, on the left and right of the image. These two shocks enter the image at ∼16 ns and propagate towards the centre of the gas cell, forming a V shape, similar to that seen for self-emission streak images in Section 2.3.1. the shift in fringe position ahead of the shock front indicates ionization and therefore the presence of a precursor.

This was processed in a similar way to the GOI images (with the full methodology described in Section 2.2.3) to produce a map of line integrated electron density, $n_e L$, shown in Fig 2.45.b. As seen in the GOI images in Fig 2.41, the shocks are proceeded by a gradually decaying electron density. To compare these two diagnostics, horizontal profiles were taken from the processed streak interferometry images at the times the GOI images were captured, as indicated in Fig 2.45.b. These are shown in Fig 2.42.a with dashed lines. These show excellent agreement, with the exception of profiles at 25 ns (possibly due to limited resolution of the streak camera).

Profiles were taken taken 2 ns apart between 16 ns and 22 ns, location shown in Fig 2.45.b. These were then shifted to intercept when $n_e L = 4 \times 10^{17}$ and are plotted in Fig 2.45.c. All of these profiles closely follow the same shape suggesting that the radiative precursor remains

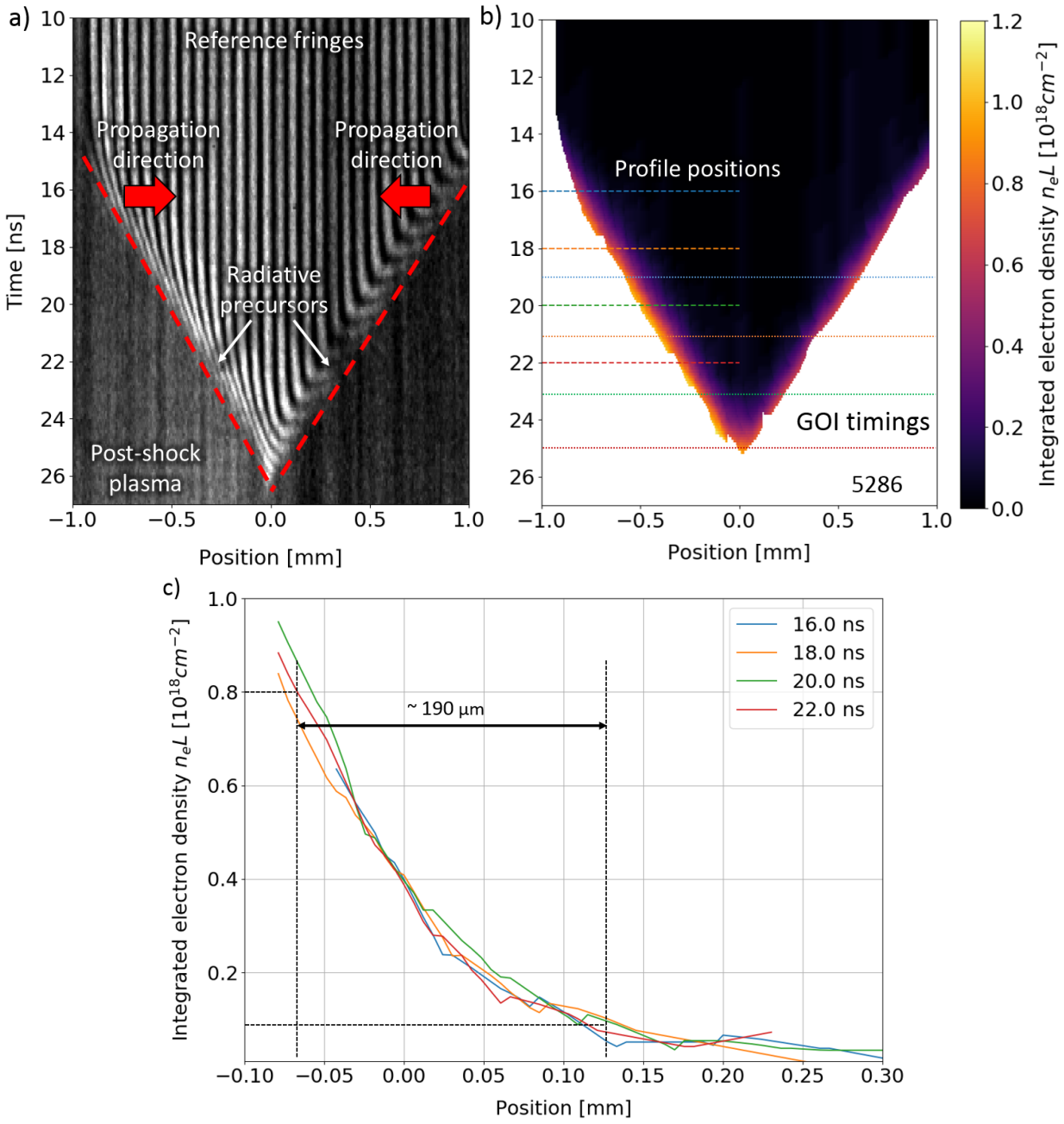


Figure 2.45: (a) Interferometry streak image along the axis for a experiment in Neon. Shifts in fringe position indicate changes in refractive index and thus a change proportional to the free electron density, n_e. The shocked plasma region was identified visually as the region opaque to the probe laser. (b) Processed map of line integrated electron density n_eL. c) Profiles of n_eL taken 2 ns apart between 16 ns and 22 ns, location shown in Fig 2.45.b, and shifted to intercept at $n_eL = 4 \times 10^{17}$.

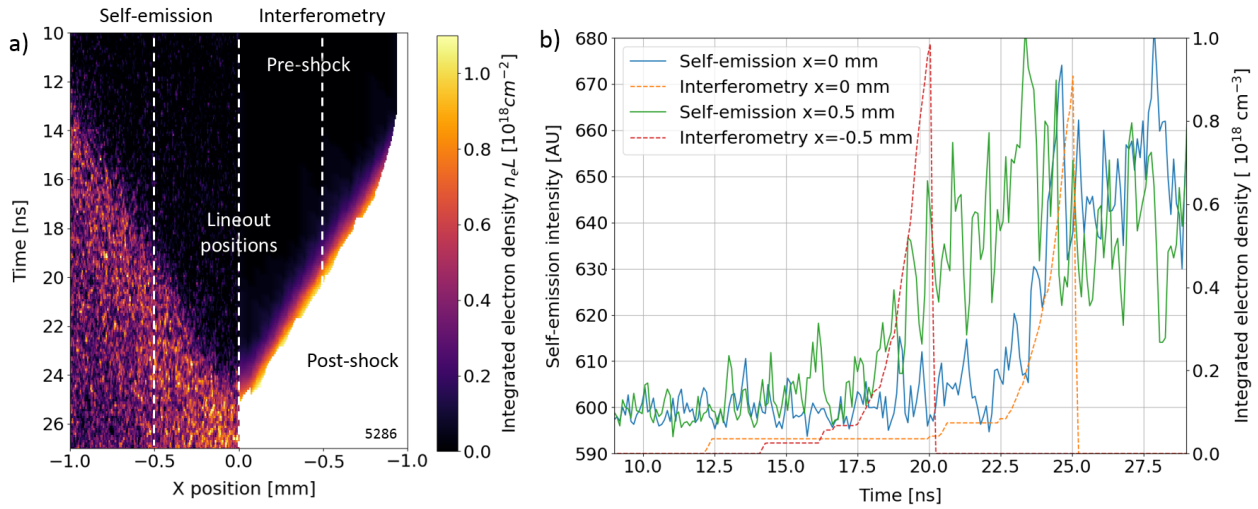


Figure 2.46: Comparison between a self-emission streak image and interferometry streak map of n_eL from the same experiment.

constant for over 6 ns, matching conclusions from GOI images. As the precursor remains constant it can be characterised by a spatial width, defined as between 0.8×10^{17} cm^{-2} and 8×10^{17} cm^{-2} (a $\times$10 increase), selected to be above the noise floor and sufficient below the opaque post-shock plasma. Visually selecting these points yielded a radiative precursor width of 190 ± 30 μm for Neon gas-fills with an initial mass density of $\rho_0 = 0.5$ mg/cm^3.

The streak interferometry maps of n_eL were compared against streak self-emission images from the experiment #5286. Fig 2.46.a shows the self-emission image and map of n_eL from the odd shock, with the map of n_eL being flipped. This shows very good qualitative agreement between the self-emission and interferometry streak images with both shocks entering the field of view at $\sim$14 ns and reaching the gas cell centre at $\sim$24 ns. Profiles at constant position were taken from the gas cell centre and at $x = -0.5$ mm and plotted in Fig 2.46.b. The interferometry profiles closely follow the rising edge of the self-emission profiles, indicating that the radiative precursor is sufficiently hot to radiate photons. In addition, the electron density profiles are cut off when the self-emission profiles begin to level off, indicating a transition to the opaque post-shock material.

2.4.3 Formation mechanism

The precursors observed in these experiments are expected to have formed due to reabsorption of radiation emitted by the hot shock front. The shock velocity required to produce a radiative precursor may be estimated using Eq. 1.80. Using post-shock ionization predicted by the radiative shock model developed in Section 1.6.4, $Z_{ps} \sim 3$, and assuming $\gamma = 5/3$ and $\epsilon_0 = \epsilon_1 \eta \sim 1$ yields a shock velocity of $v_s \sim 26$ km/s. This is significantly bellow the shock velocity measured for these experiments, $v_s = 60 \pm 10$ km/s, and so a radiative precursor is expected to form. However, precursors ahead of the shock may also form due to particles reflected by the shock front or due to thermal conduction [Drake, 2006].

To determine if electron or ion acceleration plays a role, the electron and ion mean free path were calculated using Eq. 1.17 and Eq. 1.18. Post-shock temperature and ionization estimates were taken from 2-D radiative hydrodynamic simulations (detailed in Section 2.5) yielding $T_e \sim 15$ eV and $Z \sim 4$. The electron density was approximated as the ion density (equal to the initial gas-fill atom density of $n_i = 1.5 \times 10^{19}$ cm^{-3}) multiplied by the ionization, resulting in $n_e = 5.9 \times 10^{19}$ cm^{-3}. The Coulomb logarithm was estimated using Eq. 1.12, yielding a value of $\Lambda \sim 1.2$. This yielded mean free paths of $\lambda_e \sim 150$ nm and $\lambda_i \sim 10$ nm for the electron and ions respectively, both of which are significantly smaller than the observed precursor, indicating it is not formed due to accelerated particles. This also suggests that the post-shock front is in local thermodynamic equilibrium (LTE), with thermal energies of particles well represented by a single Boltzmann distribution. In addition, it suggests that the shock front is very thin, with ions and electrons thermalizing in a very narrow region region below the resolution of the diagnostics.

However, to fully discount particle acceleration as the formation mechanism, the mean free path was recalculated for ions travelling at the shock velocity of $v_s \sim 60$ km/s. Neon ions travelling at this velocity will have a kinetic energy of ∼380 eV. Recalculating the ion mean free path for this temperature yields a value of $\lambda_i \sim 1.2$ μm, still significantly smaller

than the precursor observed in these experiments. Therefore this mechanism may be ignored in this experiment.

To determine if thermal conduction was responsible for the formation of the precursor, the thermal diffusion was approximated as a Marshak wave. The thermal conductivity, k_{th}, is given by [Drake, 2006]:

$$k_{th} = 2 \times 10^{21} \frac{[T_e(eV)]^{5/2}}{\Lambda Z(Z+1) n_i(cm^{-3})} C_p \rho_0 \tag{2.37}$$

where C_p is the heat capacity at constant pressure ($\sim 5.2 \times 10^6$ erg/g/K for Neon [Kramida et al., 2015]) and ρ_0 is the mass density (in g/cm^3) of the unshocked medium. Using the previous estimates for temperature and ionization, $T_e \sim 15$ eV and $Z \sim 4$, yields a thermal conductivity of $k_{th} \sim 1.2 \times 10^7$ gcm/s^{3}K. The position of the thermal wave front, x_0, in a Marshak wave as a function of time, t, is given by:

$$x_0 = \frac{\sqrt{n+2}}{n+1} \sqrt{\frac{2k_{th}}{\rho C_V}} \sqrt{2t} \tag{2.38}$$

Where n is a dimensionless number, $\sim$4 in high density materials [Drake, 2006], and C_V is the heat capacity at constant volume. Using the electron thermal conductivity previously calculated, and assuming the process is approximately adiabatic (so that $C_V = C_P/\gamma$ where $\gamma \sim 1.67$) indicates the Marshak wave has propagated $\sim$140 μm after 25 ns. However, this model does not take into account the motion of the shock front itself and thus is likely to be a significant overestimate. Therefore this is unlikely to account for the large precursor observed ahead of the shock front, 190 μm. However, this may be resolvable by the interferometry diagnostic and may partially contribute to the ionization observed directly ahead of the shock front.

As these formation mechanisms are unable to account for the larger precursors observed in these experiments, they are therefore assumed to be formed due to the reabsorption of radiation emitted by the shock front.

2.4.4 Precursor in Xenon gas-fills

Fig 2.47.a-d shows GOI images from experiment #5292, with a Xenon gas-fill and initial mass density of $\rho_0 = 1.43$ mg/cm^3 ($P_0 = 0.27$ bar). These images are similar to those shown in Fig 2.41 and the shocks appear as dark semi-circular shaped regions to the left and right of each image, labelled in Fig 2.47.a. Bending of the fringes directly ahead of the shocked plasma indicate a non-zero electron density and thus the presence of a precursor proceeding the shock. The dark shape to the top of the interferograms was a splinter of metal, labelled in 2.47.i. This did not have any noticeable effects on the shock or precursor evolution.

Fringes in the interferometry images and reference images, an example of which is shown in Fig 2.47.i, were traced and processed using the methodology described in Section 2.2.3. This yielded 2-D maps of n_eL shown in Fig 2.47.e-h. The opaque regions, where fringes could not be traced, have been coloured white. These images show a smooth gradient in electron density outlining the shock, similar to that seen in experiments in Neon. However, the precursor observed in these experiments extends significantly further than that in Neon, $\sim$500 μm as opposed to $\sim$200 μm in Neon.

Horizontal profiles were taken along the gas cell axis, as indicated in Fig 2.47.h, and are plotted in Fig 2.48. There is a slight asymmetry in the shocks in this experiment, with the collision point being at $x = -0.08$ mm. This is likely due to the variation in laser power, 1423 J for the odd beams (left hand side) and 1565 J for the even beams (right hand side), or perhaps due to a slight target misalignment.

The radiative precursor in these experiments was found to extend significantly further than those performed in Neon, so that just 20 ns after the drive beams the radiative precursors are already beginning to overlap. To characterise the free expansion of a single radiative precursor, off-axis profiles were taken at an angle of 25° as shown in Fig 2.49.a. Off-axis profiles from all four GOI images from experiment #5292 are shown in Fig 2.49.b, shifted to intercept one another when $n_eL = 2 \times 10^{18}$ cm^{-3}. These profiles were found to be very

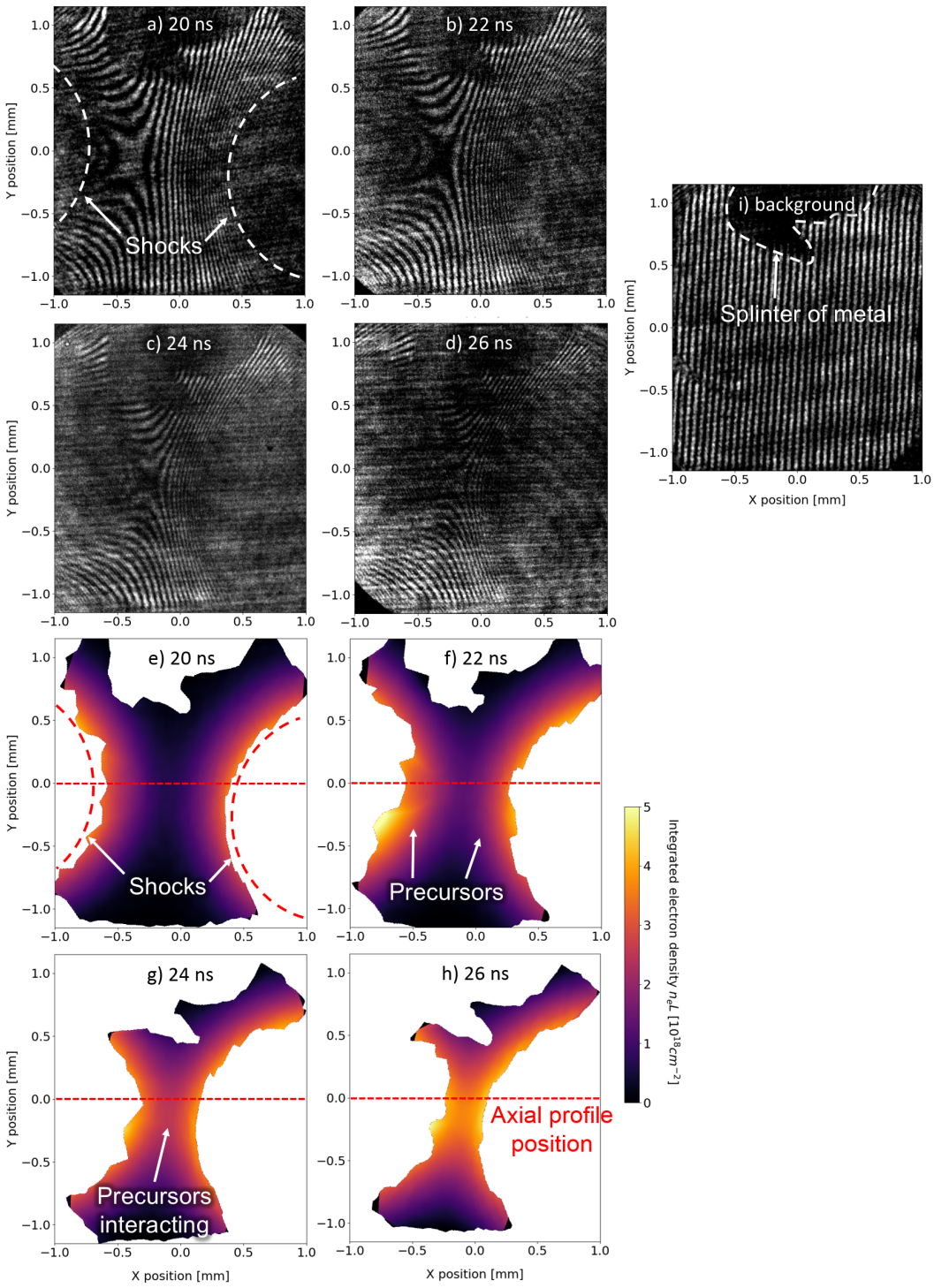


Figure 2.47: a-d) Four GOI interferometry images, at different times, from experiment #5292, with a Xenon gas fill at 0.27 bar (yielding a mass density of 1.43 mg/cm^3). e-h) Processed maps of electron density integrated along the path of the probe laser beam, $n_e L$. i) Background fringes taken before the experiment.

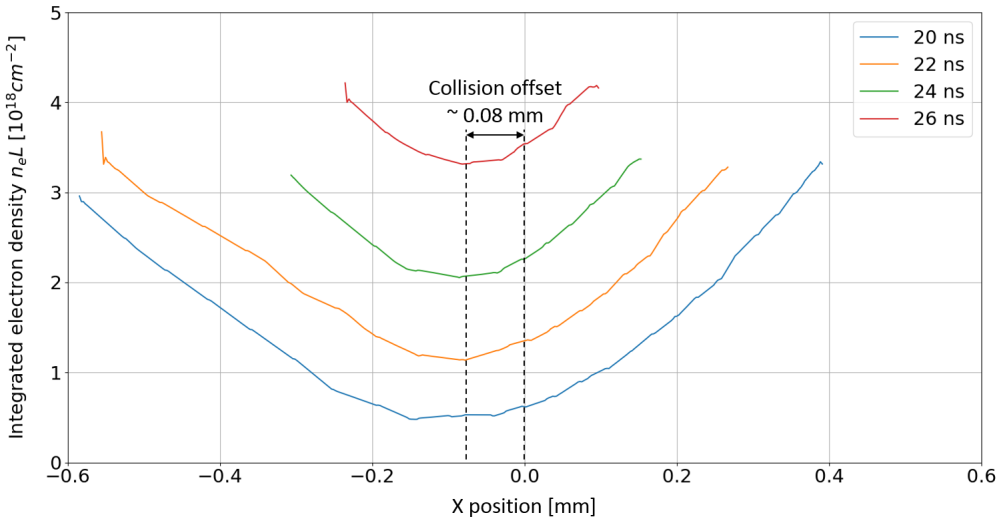


Figure 2.48: Axial profiles from 2-D maps of integrated electron density shown in Fig 2.47.e-h.

similar to the axial profile from 20 ns, plotted with a dashed line in Fig 2.49.b, and thus are assumed to be representative of the precursor in a single shock. As with experiments in Neon, these profiles were found to remain constant over the observed period.

The radiative precursor width in Neon was approximated as the distance between a $\times 10$ jump in integrated electron density. In a similar fashion the precursor width was measured between $n_eL = 0.25 \times 10^{18}$ /cm^{-3} and $n_eL = 2.5 \times 10^{18}$ /cm^{-3}. Visually selecting these points yields a width of 430 ± 30 μm. This is significantly larger than estimates from precursors seen in Neon, 190 ± 30 μm.

2.4.5 Variation with gas species

A series of experiments was performed with four different noble gas-fills (Neon, Argon, Krypton and Xenon) while maintaining a similar mass density of $\rho \sim 0.5$ mg/cm^3. This allowed each experiment to exhibit similar shock velocities and hydrodynamics but different radiative effects. A constant mass density was achieved by varying the initial gas pressure that the gas-cell was filled to. The required fill pressure, P_0, was calculated using Eq. 2.23, assuming the gas-fill acted like an idea gas. The desired fill pressures for different gases are shown in Table 2.8. Experiments were not performed using Helium as it is not expected to

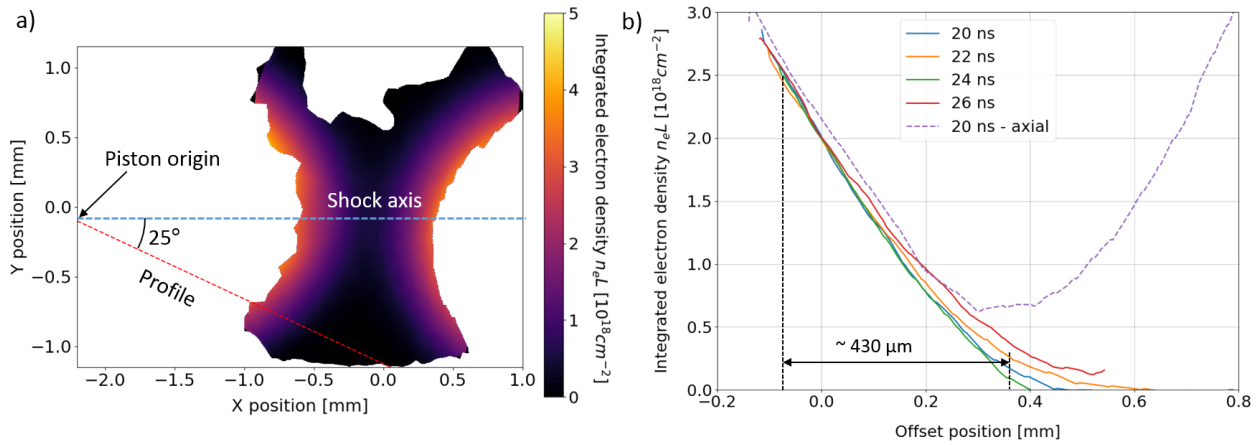


Figure 2.49: Profiles were taken at 25° to the shock axis from maps of n_eL shown in Fig 2.47. a) Location of profiles. b) Profiles from all four GOI images shifted to intercept at $n_eL = 2 \times 10^{18}$ cm^{-3}.

Gas	**Atomic mass**	**Fill pressure P_0**
Neon ($Z = 10$)	20.18	599 mbar
Argon ($Z = 18$)	39.95	303 mbar
Krypton ($Z = 36$)	83.80	144 mbar
Xenon ($Z = 54$)	131.29	92 mbar

Table 2.8: Fill pressure required to reach a mass density of $\rho_0 \sim 0.5$ mg/cm^3 for different noble gases.

exhibit significant radiative effects, leaks too rapidly and requires pressure to high for the gas-cell target to support. Experiments were also not performed with Radon as it is highly radioactive and so may not be used due to safety concerns.

Self-emission streak images from experiments using four different noble gases are shown in Fig 2.50. All of these shocks enter the field of view at ∼14 ns and collide in the centre at ∼25 ns. Therefore, by maintaining a constant gas density but varying the gas species, hydrodynamics and shock velocity may be kept constant.

Laser interferometry from the gas cell axis was recorded with a streak camera on experiments performed with these four gas-fills. These images were processed, using the methodology described in Section 2.2.3, to produce maps of integrated electron density, n_eL, shown in Fig 2.51. Horizontal profiles taken at 16, 18 and 20 ns are shown in Fig 2.52 with their location

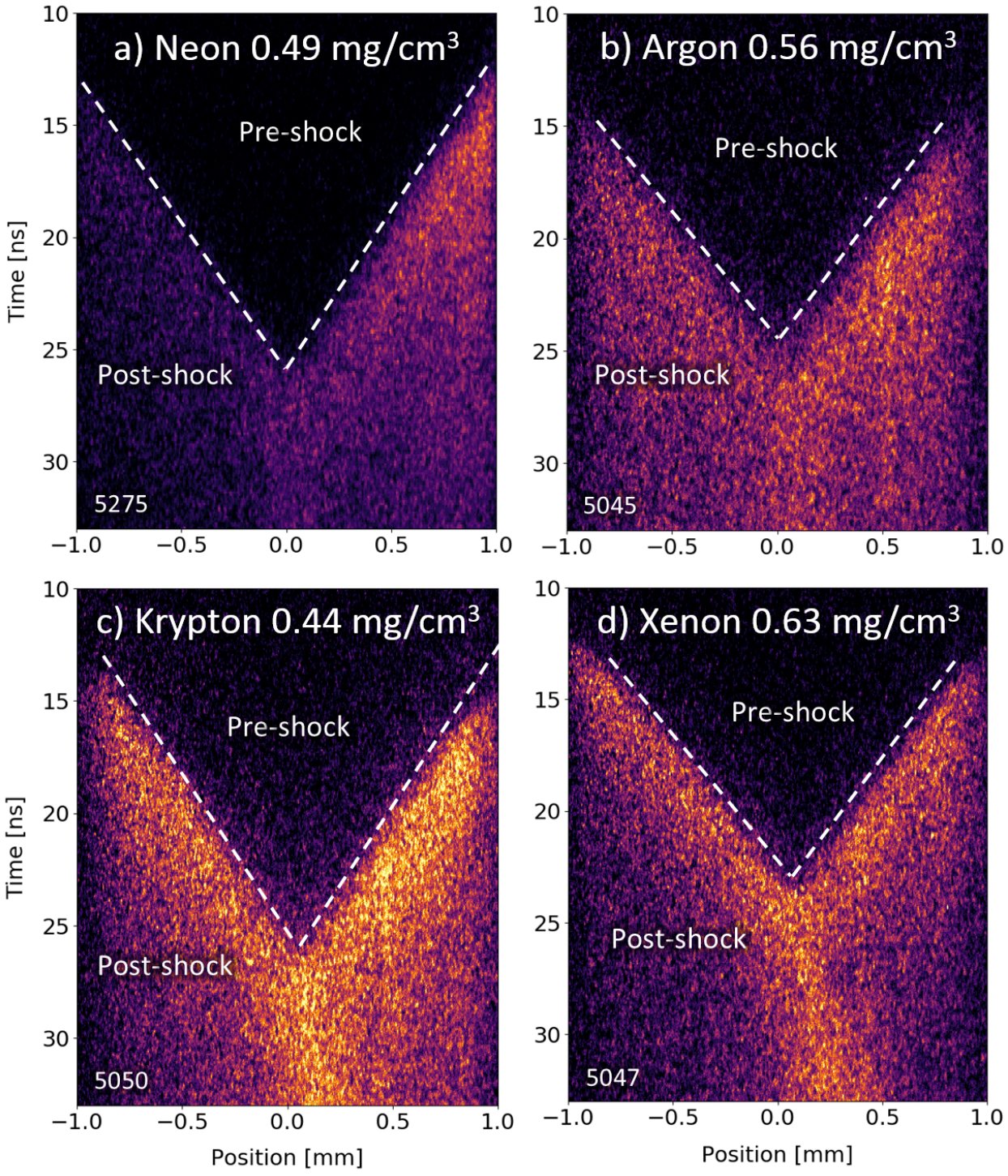


Figure 2.50: Self-emission recorded from experiments with different gas species.

shown with red dashed lines in Fig 2.51. Radiative precursors observed in heavier elements, such as Krypton and Xenon, are seen to extend significantly further than those in lighter

gases such as Neon and Argon.

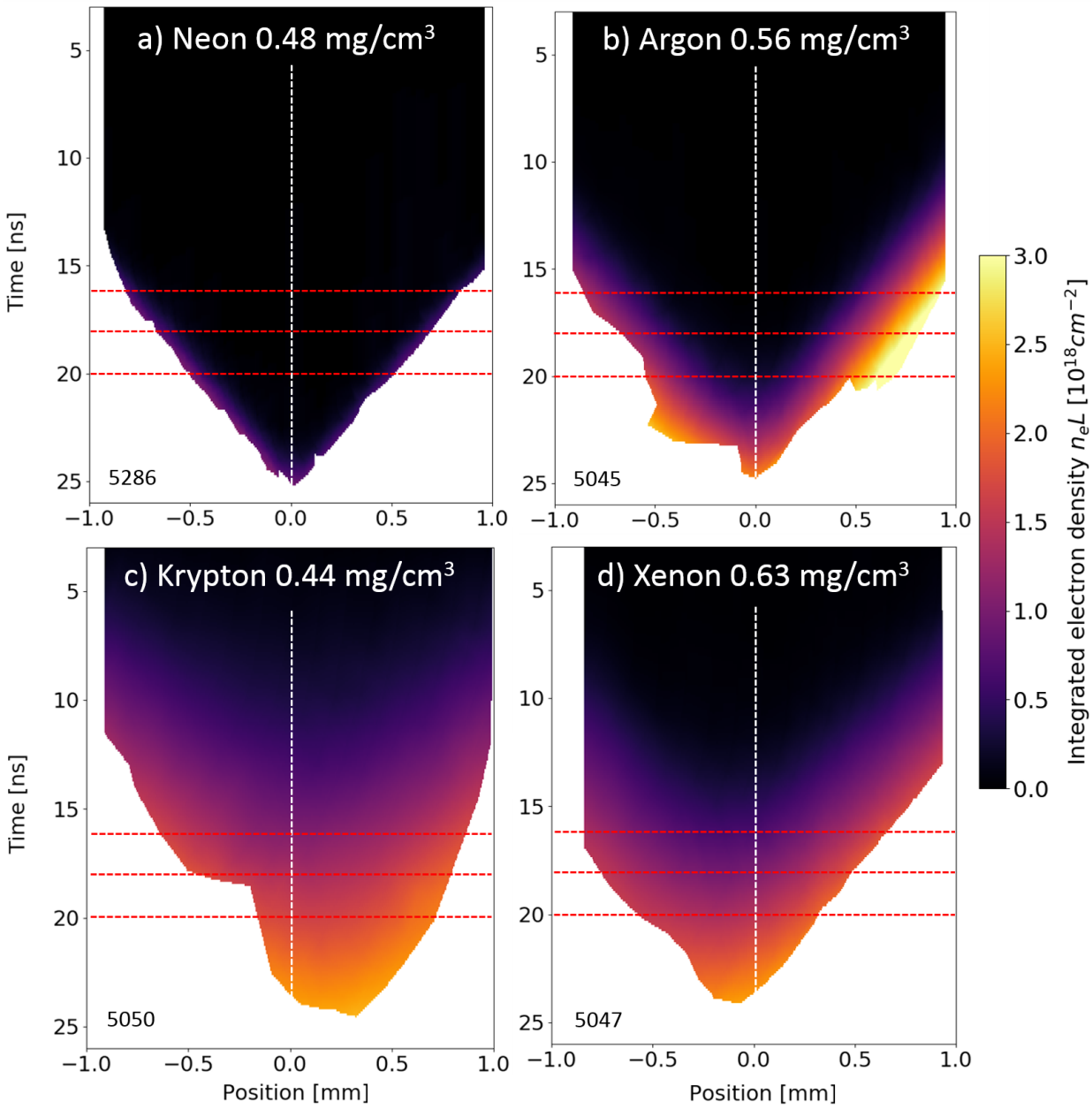


Figure 2.51: Maps of n_eL produced from interferometry streak images from experiments with different gas species by similar mass densities.

As the radiative precursors for heavier gases extend for a larger distance than the window of the gas cell, horizontal profiles could not be used to estimate the radiative precursor width. Fortunately, as the shocks travel at a constant velocity of $v_s \sim 60$ km, an estimate of the radiative precursor width may be made by taking vertical profiles and multiplying the width

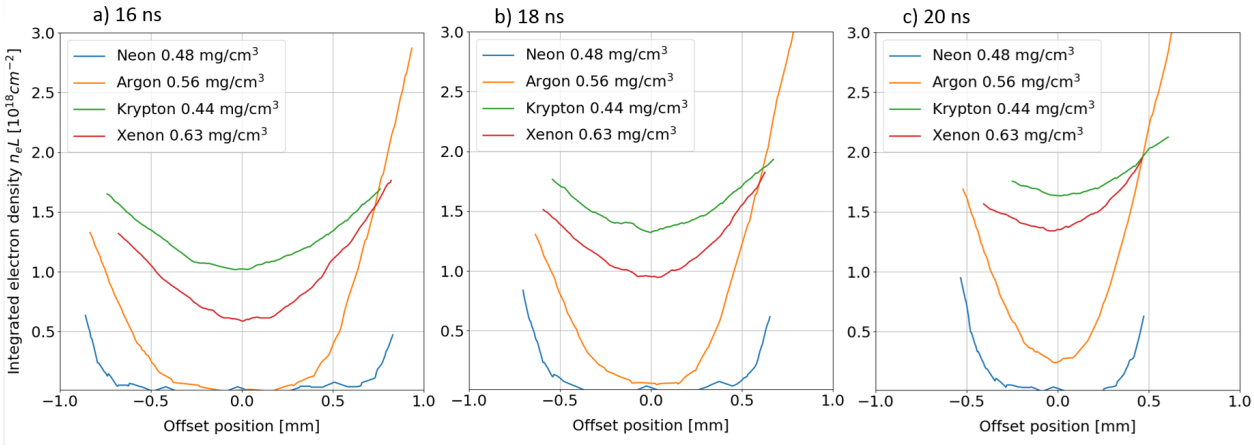


Figure 2.52: Horizontal profiles of n_eL taken at different times, location indicated with red dashed lines in Fig 2.51.

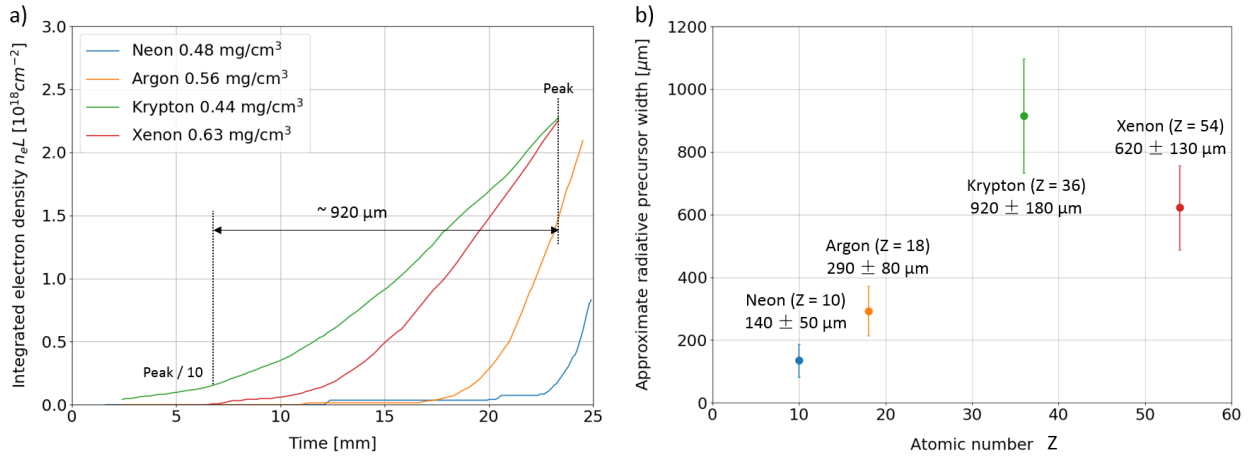


Figure 2.53: a) Vertical profiles of n_eL taken from the gas cell centre, location indicated with white dashed lines in Fig 2.51. b) Estimated radiative precursor widths as a function of atomic number.

by the shock velocity. Fig 2.53.a, shows vertical profiles taken from the centre of the gas cell, with the location shown in Fig 2.51 with white dashed lines. Radiative precursor widths were estimated by taking the distance between the peak of a profile and where the profile drops by a factor of ten, indicated in Fig 2.53.a. This yielded similar values to those already determined for Neon and Xenon, thus indicating this is a viable approximation. The resulting radiative precursor widths for each gas species are plotted as a function of atomic number in Fig 2.53.b. An error of ±10 km/s was assumed for the velocity, yielding an error of 17%. An addition ~ 30 μm of error was assumed (matching previous approximations in this estimate).

The radiative precursor width is found to increase with atomic number. This matched expectations that higher atomic number elements radiate more photons and are significantly easier to ionize. However, the radiative precursor in Krypton is larger than that observed in Xenon, despite Xenon being more readily ionized.

2.5 Comparison to numerical simulations

2.5.1 HELIOS 1-D simulations

The radiative-hydrodynamic simulation software HELIOS (developed by PRISM Computational Sciences Inc) [MacFarlane et al., 2006] was used to perform 1-D simulations of the experiments. This is a Lagrangian simulation code, where the grid moves with the fluid, which includes models for simulating laser energy deposition and multi-group diffusive radiation transport. Material equations of state (EOS) and opacity were simulated using PRism OPACity Equation of State (PROPACEOS) data sets.

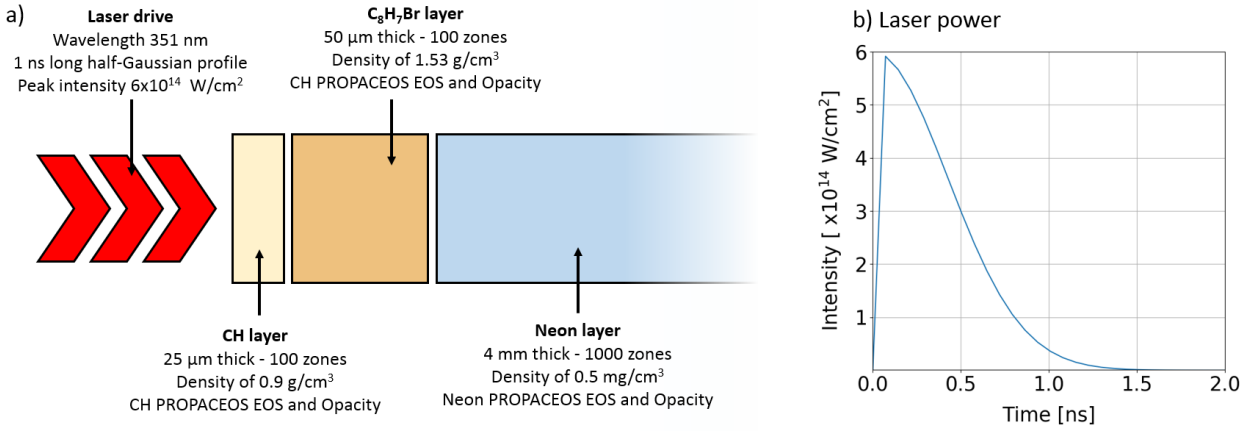


Figure 2.54: a) Setup of 1-D HELIOS for simulating the evolution of a single shock, similar to those observed in experiments. b) Laser power as a function of time.

The evolution of a single shock, similar to those observed in experiments, was simulated for a Neon gas-fill with an initial mass density of 0.5 mg/cm^3. A schematic of the simulation is shown in Fig 2.54.a. The target piston, consisting of a 25 μm thick layer of CH and a 50

μm thick layer C_8H_7Br, was simulated as two layers each with 100 zones, a mean atomic mass of 6.5 (assuming approximately equal parts Carbon and Hydrogen) and mass densities of 0.9 g/cm^3 and 1.53 g/cm^3 respectively. Equation of state and opacity were simulated with PROPACEOS models of CH for both layers. Therefore the effect of doping the second layer with Bromine, to act as an X-ray shield, was not simulated. The Neon gas-fill was simulated as a 4 mm long region, with 1000 zones, Neon PROPACEOS models of equation of state and opacity, a mean atomic weight of 20 and mass density of 0.5 mg/cm^3 (matching experiments performed with Neon gas fills). The simulation was run with non-LTE mode, with $T_{ion} \neq T_{electron}$, with a diffusion model for radiation transport and 50 frequency groups.

Initially simulations were run with a peak laser power of 600 TW/cm^2 to match the average laser intensity, assuming 1600 J is delivered to a 600 μm diameter focal spot on the piston. The drive laser was approximated as half of a 1 ns long Gaussian temporal profile, shown in Fig 2.54.b, whereas experiments used an approximately square temporal profile. This resulted in a total of ~840 J being delivered to the focal spot, slightly less than the ~1000 J estimated for experiments in Section 2.1.3.

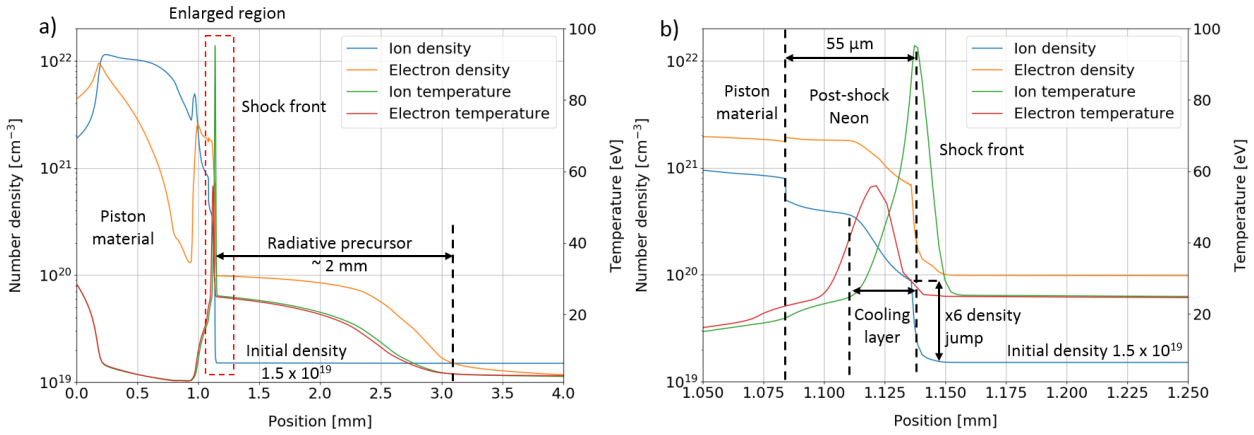


Figure 2.55: Electron and ion densities and temperatures predicted by HELIOS simulations with a Neon gas-fill with an initial mass density of 0.5 mg/cm^3 and peak laser intensity 600 TW/cm^2. a) Plot at 8 ns. b) Enlargement of the highlighted region in (a) showing the post-shock structure.

The output of these simulation, 8 ns after the drive beams, is shown in Fig 2.55.a. The shock is propagating from left to right and the shock front is defined as the peak in ion

temperature at $x \sim 1.12$ mm. Despite the similar drive beam these shocks propagate at $v_s \sim 125$ km/s, significantly faster than shock velocities of $v_s = 60 \pm 10$ km/s measured for experiments in Section 2.3.1. An enlarged view of the shock front is presented in Fig 2.55.b. At the shock front the ions are rapidly heated to 95 eV before thermalizing with the electrons over ~ 100 μm. The ion density at the shock front jumps by a factor of $\Gamma \sim \times 6$, significantly above the $\times 4$ limit for a strong shock in a monatomic gas. The effective adiabatic index, γ, may be determined by rearranging Eq. 1.58 to yield:

$$\gamma = \frac{\Gamma + 1}{\Gamma - 1} \tag{2.39}$$

This yields an effective adiabatic index of $\gamma = 1.4$ at the shock front, reduced from the monatomic value of $\gamma = 1.67$ due to ionization.

Due to radiative cooling, the post shock ion density increases rapidly in a cooling layer, mirrored by a reduction in ion and electron temperature. As the post-shock material becomes optically thick, radiative cooling reduces, resulting in the ion density increasing at a slower rate. The Neon post-shock region extends a total of $\sim$55 μm, reaching a maximum ion density of 5×10^{20} cm^{-3} at the interface with the piston material, corresponding with a total compression of $\times 33$. The average compression in the post-shock region was found to be $\Gamma = \times 20$, similar to the value of $\Gamma = \times 23 \pm 4$ measured for experimental data in Section 2.3.2. Running these simulation with radiation transport turned off resulted in a decrease in post-shock compression and an increase in post-shock width.

Ahead of the shock front the mass density is unperturbed but significant heating is observed while the mass density remains unchanged, indicating the formation of a precursor. This precursor region was confirmed to be formed due to radiative effects by running the simulation with radiation transport turned off, which resulted in the electron temperature ahead of the shock front remaining zero. However, the radiative precursor observed in these simulations is significantly larger, at $\sim$2 mm, than those observed in experiments, measured to be $\sim$190 μm wide in Section 2.4.2. In addition, the shape does not resemble that observed in

	Experiments	HELIOS high energy	HELIOS low energy
Peak laser intensity [TW/cm^2]	∼710	600	150
Laser energy in focal spot [J]	∼1000	∼840	∼210
Shock velocity v_s [km/s]	60 ± 10	∼125	∼65
Average post-shock compression Γ	$\times 23 \pm 4$	$\times 20$	$\times 12$
Radiative precursor width [μm]	190 ± 30	∼2000	∼1000

Table 2.9: Comparison of key parameters between experiments and HELIOS 1-D simulations with different laser powers.

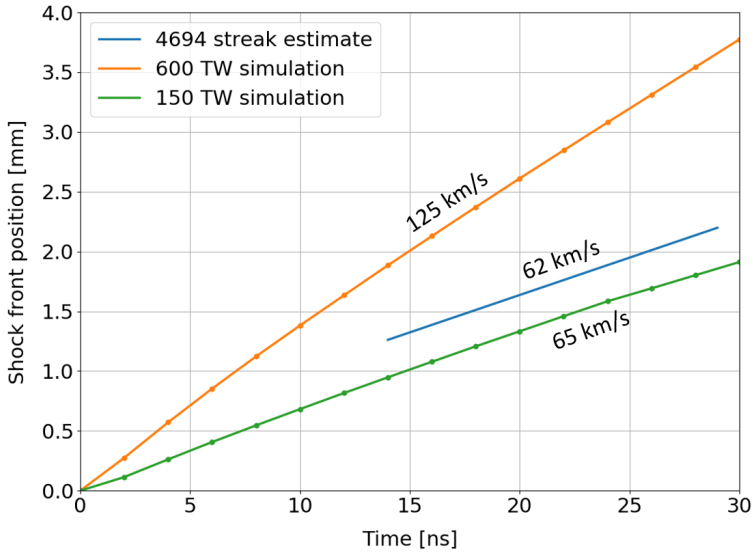


Figure 2.56: Shock front position as a function of time in experiment #4694 with a Neon gas fill with initial mass density of 0.5 mg/cm^3, estimated from self-emission streak images. Shock front positions predicted by HELIOS simulations are also plotted, run with peak laser powers of 600 TW and 150 TW.

experiments. In Section 2.4.1it was shown that the radiative precursor had an approximately linear gradient of electron density whereas these simulations suggest the precursor has a relatively constant electron density for ∼1.5 mm before rapidly decreasing. A comparison of key parameters measured in experiments and these simulations is shown in Table 2.9, with results from these simulation labelled as 'HELIOS high energy'.

To achieve better agreement with experiments, HELIOS simulations were run with reduced laser power until shock velocities approximately matched those observed in experiments. A peak laser intensity of 150 TW/cm^2, corresponding with a total energy of ∼210 J (∼20% of

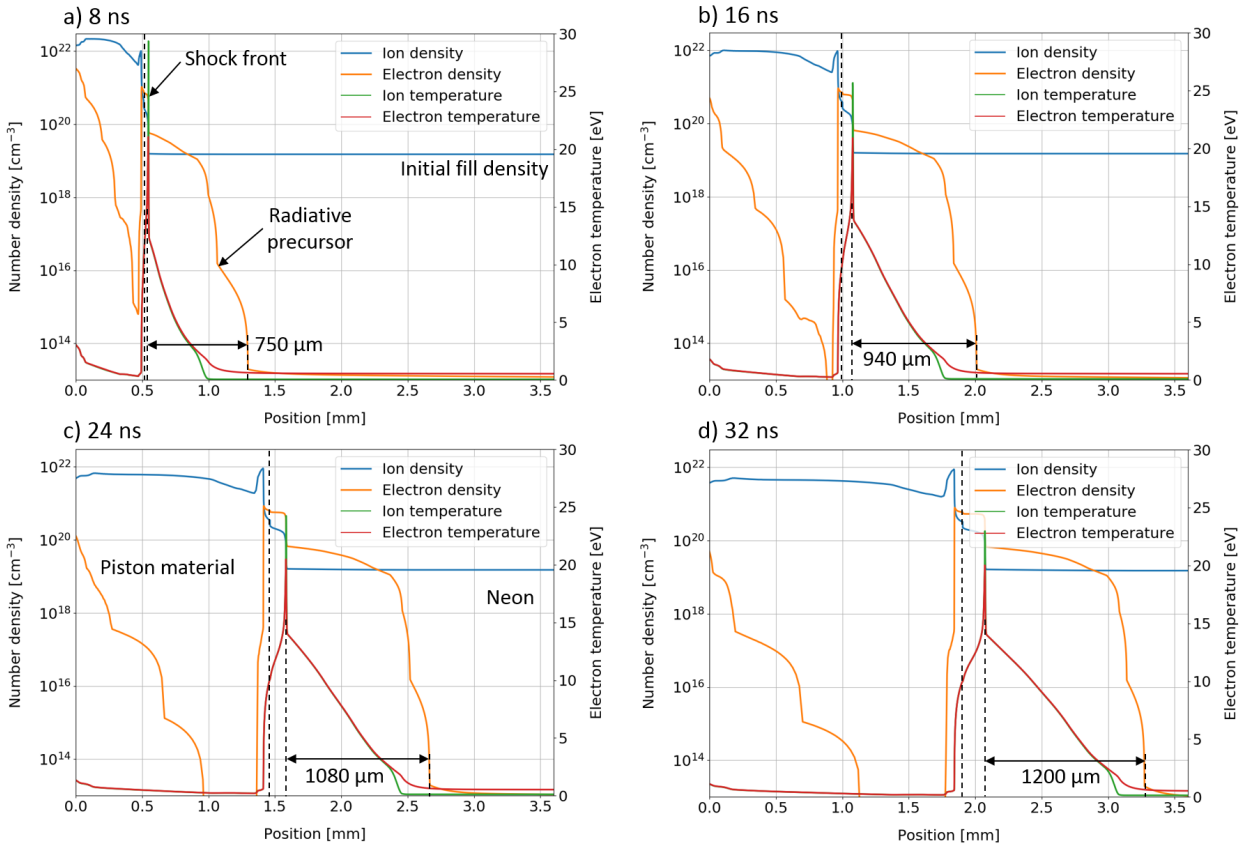


Figure 2.57: Output from HELIOS simulations of a Neon gas-fill with an initial mass density of 0.5 mg/cm^3 and peak laser intensity 150 TW/cm^2 (total energy of ∼210 J, ∼20% of that delivered in experiments).

that delivered in experiments) was found to yield a similar post-shock velocity of $v_s \sim 65$ km/s. Shock position as a function of time is plotted in Fig 2.56 for experiments (estimated from the self-emission streak image from experiment #4694) and for both HELIOS simulations with 600 TW/cm^2 and 150 TW/cm^2 of laser energy.

Electron and ion temperatures and densities from this simulation are shown for several different times in Fig 2.57. A similar post-shock structure to that seen in Fig 2.55.b is observed, with post-shock material experiencing radiative cooling. An average post-shock compression of $\Gamma = \times 13$ is achieved at 8 ns, reducing to $\Gamma = \times 11$ by 32 ns. This is significantly lower than compressions estimated from XBRL of $\Gamma = \times 23 \pm 4$. These simulations also predict more conservative post-shock temperatures of $T_{ps} = 20 - 25$ eV, decreasing slowly over time. In addition, the radiative precursor observed in these lower energy simulations is

significantly smaller than previous high energy simulations, extending ∼750 μm at 8 ns and growing to ∼1200 μm by 32 ns. However, this is still many times larger than that observed in experiments. A summary of key parameters measured from these simulations with reduced laser power is shown in Table 2.9, labelled as 'HELIOS low energy'. Inaccuracies in these HELIOS 1-D simulations demonstrate the importance of experimental data for understanding radiative shocks and benchmarking simulation codes.

2.5.2 NYM - PETRA 2-D simulations

Prior to performing these experiment, two-dimensional radiative-hydrodynamic simulations were run with two different codes, NYM and PETRA, to estimate conditions in the plasma and to help determine XRBL target materials. The author does not have access to these simulation codes and so simulations were performed by Peter Graham at AWE.

Simulations were initialized with a piston matching those in experiments, a 25 μm thick layer of polypropylene (CH) followed by a 50 μm thick layer of brominated polypropylene (C_8H_7Br). Only one quadrant of the gas cell was simulated, a 2 mm by 2 mm square with reflective boundaries. The laser was modelled as a 1 ns long square pulse, with a wavelength of 351 nm, focal spot diameter of 600 μm and total laser energy of 1.6 kJ (corresponding with four of the Orion beams). This achieved an intensity of 600 TW/cm^2, ∼60% higher than estimated for experiments.

The first few nanoseconds (∼5 ns) were simulated with the Lagrangian radiative-hydrodynamic code NYM [Roberts et al., 1980]. Lagrangian codes anchor the computational mesh to the material so that it moves with it and thus maintains material interfaces precisely and roughly maps more complex regions with more computational cells. It is frequently beneficial to model laser target interactions with Lagrangian codes as they typically assign more computational cells to important regions. The NYM simulation code includes models for the laser energy deposition and so the laser interaction with the target pistons is explicitly modelled rather than initializing the simulation with a hot, fast piston. To avoid mesh tangling, the evolution

and shock dynamics after 5 ns were then simulated with the Eulerian code PETRA [Youngs, 1984]. In contrast to Lagrangian methods, Eulerian methods have a fixed grid and move particles between cells.

Both simulations used equations of state and opacities taken from SESAME tables. Radiation transport was simulated with multiple-groups (allowing materials to have a difference response to different photon frequencies) and Monte-Carlo X-ray transport. The Monte-Carlo method models radiation transport by spawning a large number $(100 - 1000)$ of macro-particles, each representing many photons, and simulating their propagation through the plasma. These are generated randomly so as to fit a distribution based on local plasma properties.

A time sequence of simulations, run with a Xenon gas-fill, with an initial mass density of 1.6 mg/cm^3 and total laser energy of 1.6 kJ, is shown in Fig 2.58. A combination of mass density, electron temperature and material are shown for four different times. The two shocks propagate from the left and right pistons, located at ± 2 mm (piston bulging due to the positive fill pressure was not taken into account in these simulations), towards the gas cell centre at $x = 0$ mm. The two shocks collide before 28 ns and form a reverse shock region of increased density at the gas cell centre, which expands outwards. The majority of the semi-elliptical post-shock structure is composed of brominated polypropylene piston material.

The post-shock Xenon is confined to a thin layer $\sim$30 μm thick. The interface between the Xenon and piston layer is not smooth and instead perturbations grow over time on the shock front. At the front of the shock spikes of the dense piston material are observed pushing into the Xenon layer and at the side of the shock larger perturbations are observed which curl back on themselves. These perturbations appear to have a degree of vorticity and may have formed due to the sheer between the shock and ambient gas, indicating that these are possibly Kelvin-Helmholtz instabilities. At the time of collision these perturbations have grown to a scale of $\sim$150 μm. This is above the minimum resolution of the XRBL diagnostic, of ~ 80 μm, but yet these perturbations are not seen in experiments. This is discussed further

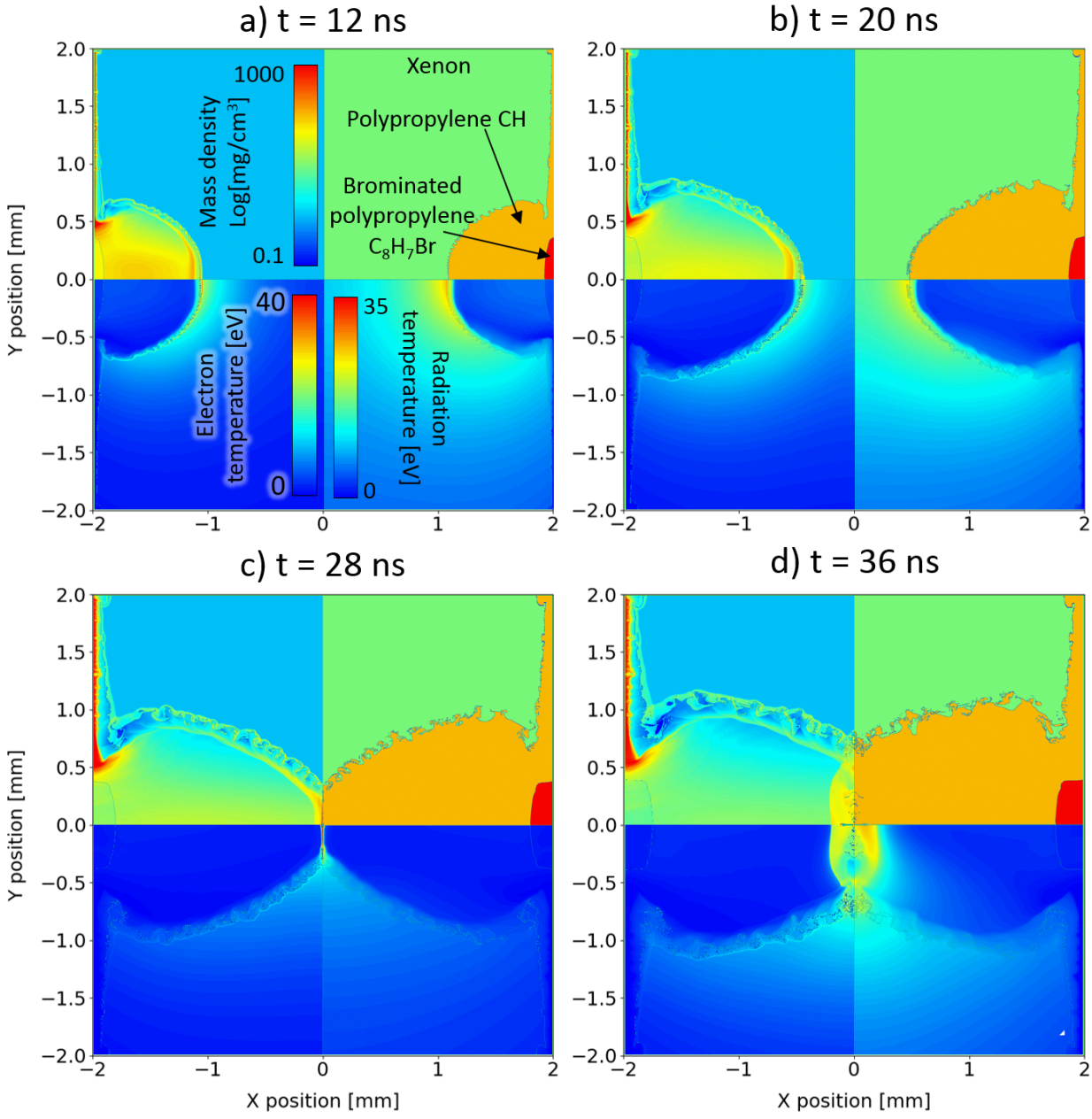


Figure 2.58: Time sequence created from the output of NYM/PETRA simulations with a Xenon gas-fill with an initial density of 1.6 mg/cm^3 and laser energy of 1.6 kJ. Each image is divided into four quadrants. Top left: mass density with a logarithmic scale. Top right: colour coded to show the different materials. Bottom left: electron temperature, T_e. Bottom right: radiation temperature.

in Section 4.2.1.

XRBL images from experiments with similar gas-fills are compared against these simulations in Fig 2.59. Synthetic XRBL images were produced from simulation outputs of mass density, one of which is shown in Fig 2.59.b. These synthetic images were calculated by assuming cylindrical symmetry around the gas cell axis, $y = 0$, and so perturbations in the Xenon resulted in a striped pattern along the length of the shock. Therefore these are a result of the 2-D nature of the simulations and are not seen in experimental XRBL images. These synthetic XRBL images assisted in selecting X-ray backlighter material (and thus photon energy) by allowing the contrast of different materials to be observed.

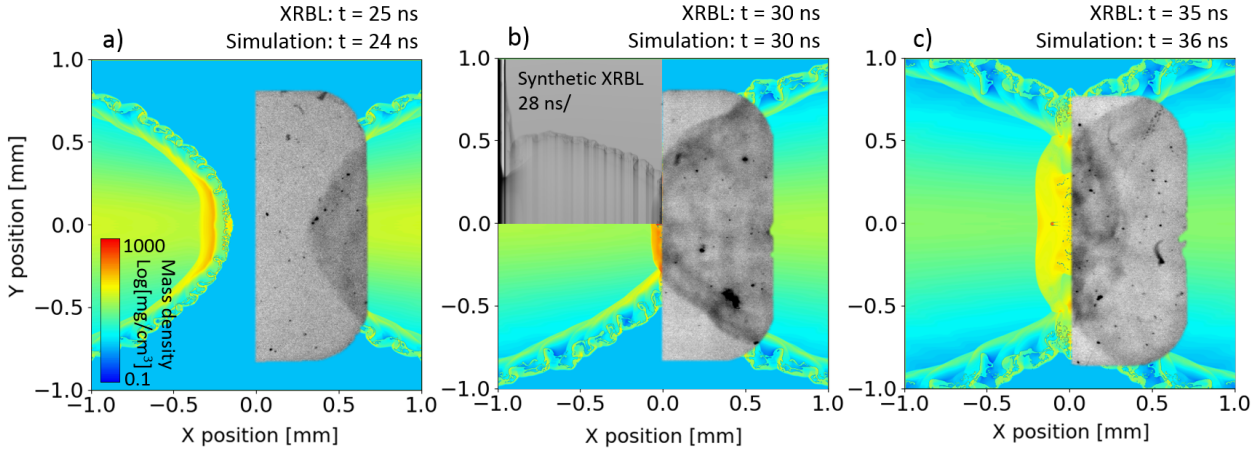


Figure 2.59: XRBL images from experiments with a Xenon gas-fill with an initial density of 1.6 mg/cm^3 compared against mass density predictions from 2-D simulations (with a laser energy of 1.6 kJ), on a logarithmic scale. A synthetic XRBL image from 28 ns is shown in the top left quadrant of (b).

Prior to the experiments, simulations of both Neon and Xenon gas-fills were performed with an increased laser energy of 2 kJ, the maximum Orion energy delivered with all five beam lines. Fig 2.60 shows profiles of mass density and electron temperature taken along the gas cell axis. Results are shown from simulation with Neon and Xenon gas-fills, with initial mass densities of 0.5 mg/cm^3 and 1.6 mg/cm^3 respectively, as was used in experiments. Due to the lower mass density which offered less resistance to the piston, the shock in Neon propagates at a faster velocity of ∼105 km/s while the shock in Xenon propagates at ∼82

km/s. However, experiments measured a constant, slower shock velocity of $v_s \sim 60$ km/s in both gas fills.

These simulations predict a peak compression in Neon-gas fills of $\sim\times 30$, not dissimilar to the value of $\times 23 \pm 4$ measured for experimental data in Section 2.3.2. A higher post-shock compression of $\sim\times 70$ is predicted for Xenon gas fills. This difference is due to increased radiative cooling in the Xenon post-shock material. These simulations show a gradual decrease in the post-shock mass density and compression over time as the shocks loose energy.

To investigate the radiative precursor and its evolution, the electron density and temperature were plotted together, offset to the reference frame of the shock front. This is shown for simulations with a Neon gas-fill, with initial mass density of 0.5 mg/cm^3 and total laser power of 2 kJ, in Fig 2.61. Ahead of the shock front, the electron density decays gradually over $\sim$360 μm to a minimum of 3×10^{19} cm^{-3} (the reason for this minimum is not fully understood and may indicate a level of pre-ionization due to X-rays produced in the laser-piston interaction). However, experiments estimated a radiative precursor width of 190 ± 30 μm in similar experiments, significantly smaller than predictions from simulations. Despite this overestimate, these 2-D simulations have performed significantly better than 1-D HELIOS simulations which predict a different radiative precursor shape and width $1000 - 2000$ μm. The radiative precursor remains relatively unchanged over the initial evolution of the shock. However, when the radiative precursors from the two shocks begin overlapping, both the electron density and temperature is increased, as seen in the green curves at 16 ns in Fig 2.61.

This analysis was repeated for a Xenon gas-fill, with initial mass density of 1.6 mg/cm^3 and total laser power of 1.6 kJ, as shown in Fig 2.62. However, in these simulations the radiative precursor extends beyond the simulation region after just 16 ns (i.e. the radiative precursor of the two shocks is already interacting). Therefore a vertical profile of electron density was taken from $x = 1$ mm, as shown in Fig 2.62.a. This shows a very gradual decay in Fig 2.62.b, yielding a radiative precursor length of $\sim$1470 μm. This is significantly larger

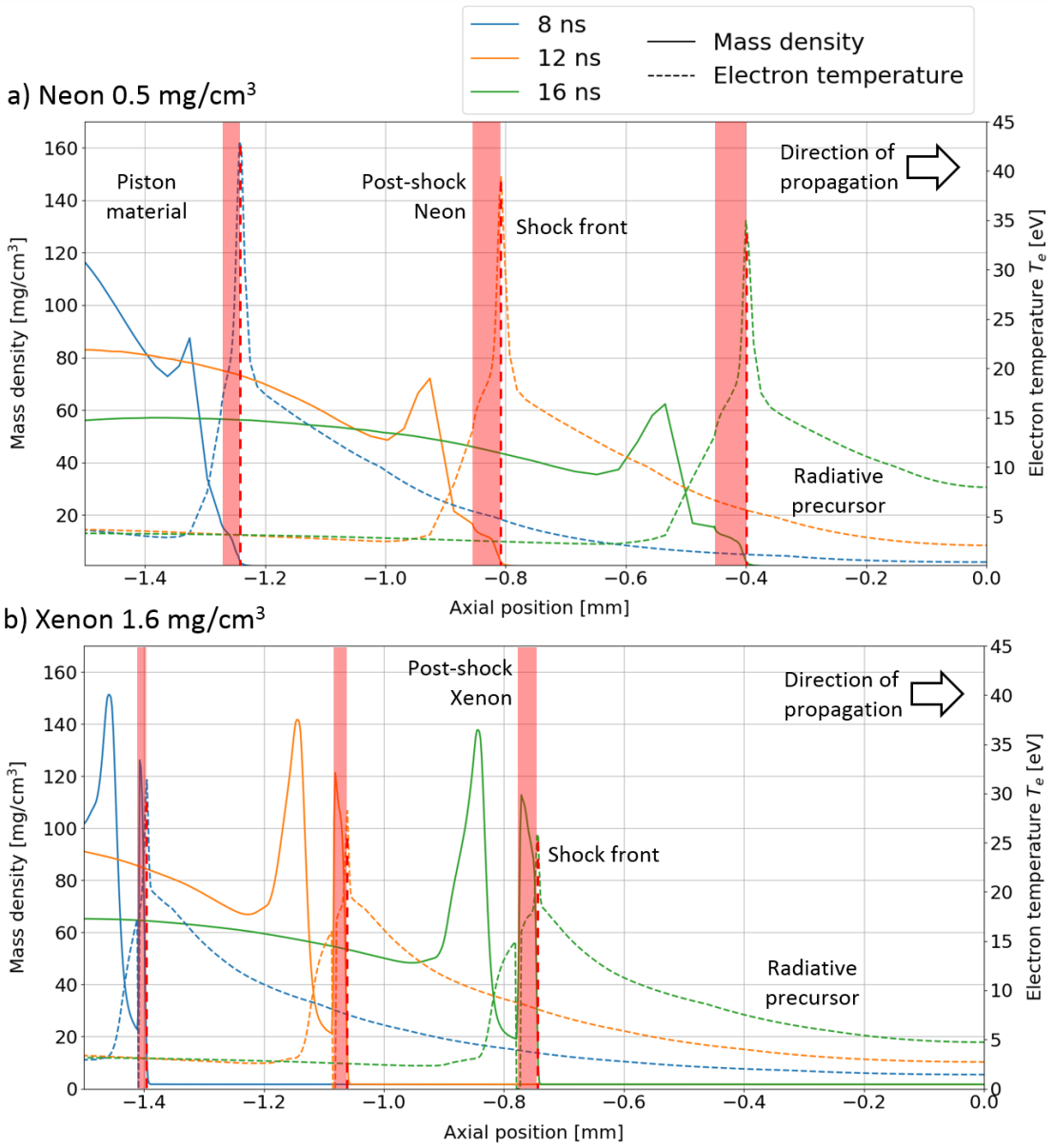


Figure 2.60: Axial profiles of mass density and electron temperature from 2-D simulations, run with a total laser energy of 2 kJ, at several times. The post-shock gas is highlighted in red. a) Simulations with a Neon gas fill with initial mass density of 0.5 mg/cm^3. b) Simulations with a Xenon gas fill with initial mass density of 1.6 mg/cm^3.

than measurements of 430 ± 30 μm from experiments.

A comparison of key parameters measured in experiments and these simulations is shown in Table 2.10. Generally better agreement is observed between experiments and these 2-D simulations than with 1-D HELIOS simulations. Higher velocities and post-shock compressions

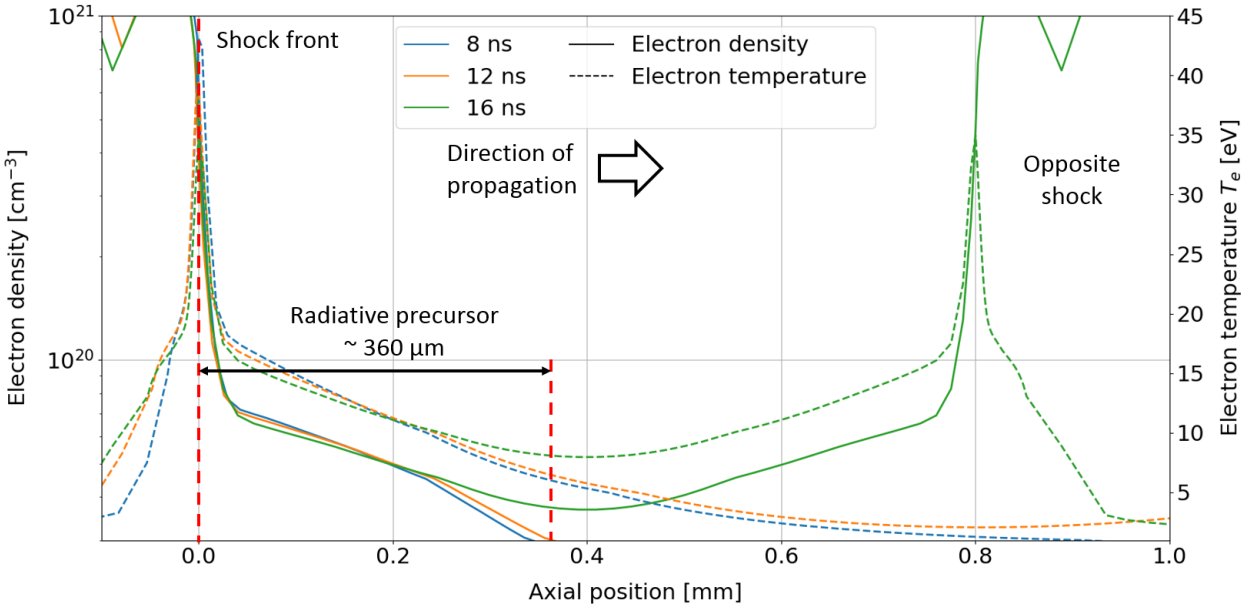


Figure 2.61: Axial profiles of electron density and temperature from 2-D simulations of Neon gas-fills with an initial mass density of 0.5 mg/cm^3 and laser energy of 2 kJ. These profiles have been offset to the reference frame of the shock front for comparison.

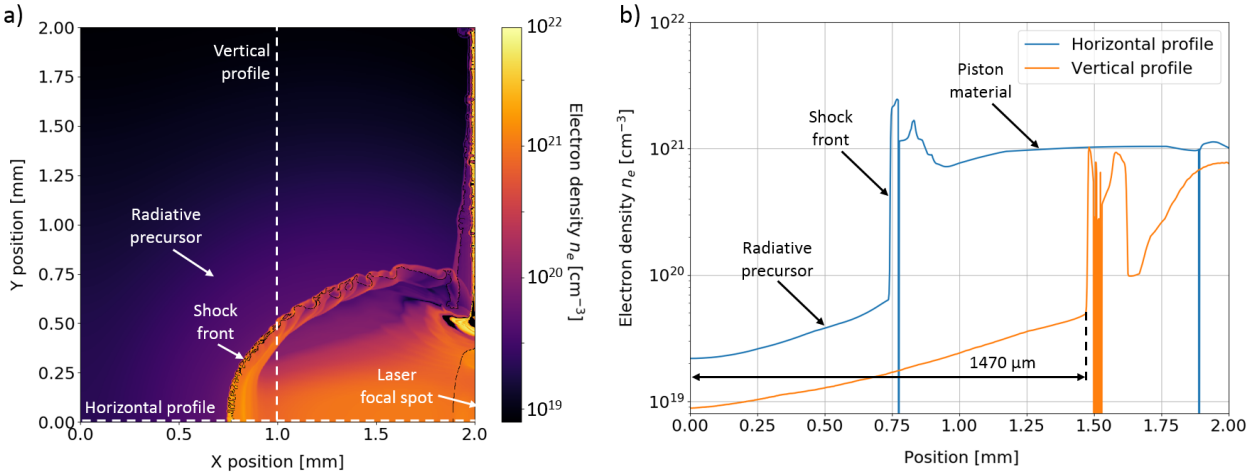


Figure 2.62: a) 2-D map of electron density from 2-D simulations, taken at 16 ns, of a Xenon gas-fill with an initial mass density of 1.6 mg/cm3 and laser energy of 1.6 kJ. b) Horizontal and vertical profiles from the positions marked in (a).

are observed,which may in part be due to the higher drive laser energy. These simulations also significantly overestimate the radiative precursor width, albiet not as drastically as HELIOS 1-D simulations.

	Neon 0.5 mg/cm^3	
	Experiment	**NYM/PETRA**
Shock velocity v_s [km/s]	60 ± 10	$\sim$105
Average post-shock compression	$\times 23 \pm 4$	$\sim\times$30
Radiative precursor width [μm]	190 ± 30	$\sim$360
	Xenon 1.6 mg/cm^3	
	Experiment	**NYM/PETRA**
Shock velocity v_s [km/s]	$\sim$60	82
Average post-shock compression	unknown	$\sim\times$70
Radiative precursor width [μm]	430 ± 30	$\sim$1470

Table 2.10: Comparison of key parameters between experiments and NYM/PETRA 2-D simulations.

Chapter 3

Radially expanding shock experiments

This chapter describes cylindrically expanding radiative shock experiments, performed on the MAGPIE pulsed power facility at Imperial College London, UK. These experiments build upon previous work conducted by G. C. Burdiak (described in Section 1.7.2) by offering improved diagnostic access and allowing radiative shocks to propagate further. This allows the full extent of the radiative precursor to be observed and electron density determined with interferometry diagnostics. These experiments have resulted in a publication which has been submitted to the seventh Special Issue of IEEE Nuclear and Plasma Sciences Society, as a conference proceeding from the 10th International Conference on Dense Z-Pinches.

Section 3.1 provides an overview of the MAGPIE facility. Section 3.2 describes the experimental setup and investigates how the liner is expected to respond to the MAGPIE current. Section 3.3 describes the diagnostic suite used to investigate this experiment, which includes current and magnetic probes, optical self-emission imaging, laser interferometry and optical spectroscopy. Section 3.4 investigates optical self-emission images to study how the shocks evolve over time, finding they expand with a constant velocity of $\sim$10 km/s, and investigates possible mechanisms for launching the shocks. Finally, Section 3.5 investigates laser interferometry images to study the structure the shock and the radiative precursor. Optical spectroscopy measurements are compared against PrismSPECT simulations to

determine the shock temperature to be ∼2.5 eV.

3.1 Overview of the MAGPIE facility

Experiments presented in this Chapter of the Thesis were performed on the Mega Ampere Generator for Plasma Implosion Experiments (MAGPIE) facility at Imperial College London. This section describes the operation of MAGPIE and is primarily based on information found in the Review of Scientific Instruments paper by I. H. Mitchell et al. [Mitchell et al., 1996] as well as several PhD thesis from students working in the MAGPIE laboratory e.g. [Suzuki-Vidal, 2009, Swadling, 2011, Burdiak, 2012, Hare, 2017].

MAGPIE is a pulsed-power generator that delivers a current pulse with a peak of up to ∼1.4 MA and rise time of ∼240 ns. A schematic of the generator shown in Fig 3.1. The generator was designed with a high internal impedance of 1.25 Ω, allowing current to be discharged through a wide variety of high impedance loads with negligible change in current. This permits a wide variety of experiments that may not be possible on smaller machines.

MAGPIE was initially designed and built for Z-pinch experiments with cryogenic Deuterium fibres [Mitchell et al., 1996, Lebedev et al., 1998]. The current delivered by the MAGPIE generator was designed so that a Deuterium fibre Z-pinch would radiatively collapse, where the radiative losses would exceed temperature increases due to compression and Ohmic heating. It was hoped this would allow the Deuterium to be compressed to conditions where nuclear fusion could occur. However, Z-pinches were found to subject to instabilities preventing this from being realized.

More recently, the MAGPIE facility has been used to conduct laboratory astrophysics experiments using conical wire arrays and radial foils to generate plasma jets, e.g. [Lebedev et al., 2005, Suzuki-Vidal et al., 2010], and study their interaction with gases e.g. [Suzuki-Vidal et al., 2012, Skidmore, 2013, Suzuki-Vidal et al., 2015]. Inverse wire array exploders have been used to create uniform magnetised plasma flows and their interaction with obstacles

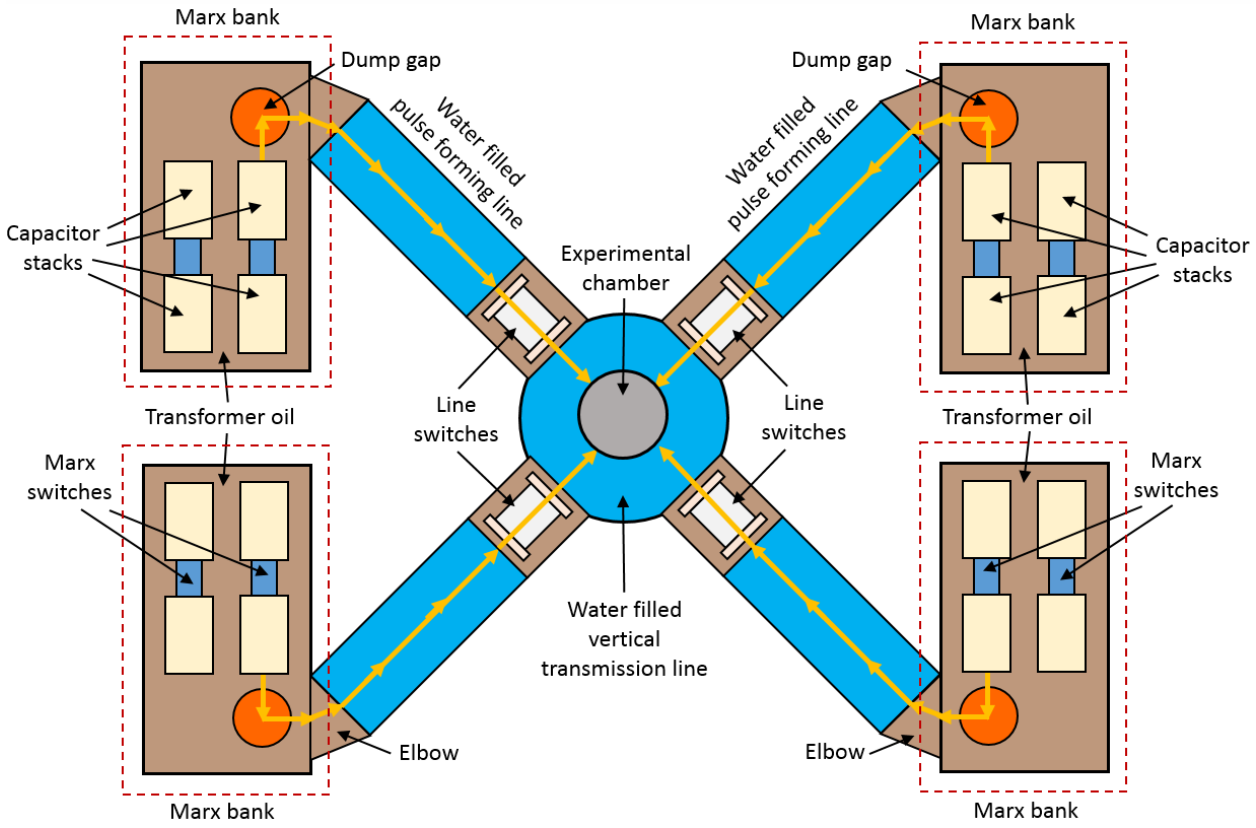


Figure 3.1: Diagram of the MAGPIE pulsed power facility. Sections filled with transformer oil are coloured brown. Sections filled with deionized water are coloured blue.

has been studied e.g. [Lebedev et al., 2014, Burdiak et al., 2017]. Two parallel wire array exploders have been used to create converging plasma flows with opposite embedded magnetic fields allowing for the study of magnetic reconnection e.g. [Suttle et al., 2016, Hare et al., 2017b, Hare et al., 2017a, Hare et al., 2018].

3.1.1 Marx banks

MAGPIE consists of four Marx capacitor bank (labelled in Fig 3.1), originally based on those used in the Hermes III at Sandia National Laboratories in the USA. Each Marx bank contains 24 capacitors (each with a capacitance of $C = 1.3\ \mu$F) in a bipolar configuration, as shown in the circuit diagram in Fig 3.2. These are arranged in four columns, each with six capacitors.

One group of capacitors is charged to +65 kV and the other group to −65 kV by two

Glassman High Voltage pb/pk 100N040 units. These are connected through RG218 high voltage cables to a series of diodes (to prevent discharge back to the charging units). These were located in a barrel filled with transformer oil, to prevent electrical breakdown. This is then connected to another transformer oil filled barrel which contains 4-way splitters, allowing a positive and negative high voltage cable to be sent to each Marx bank. Pneumatic pistons within these barrels allow these charging cables to be connected to high power grounded resistors, allowing the Marx banks to be quickly discharged in the event of an emergency.

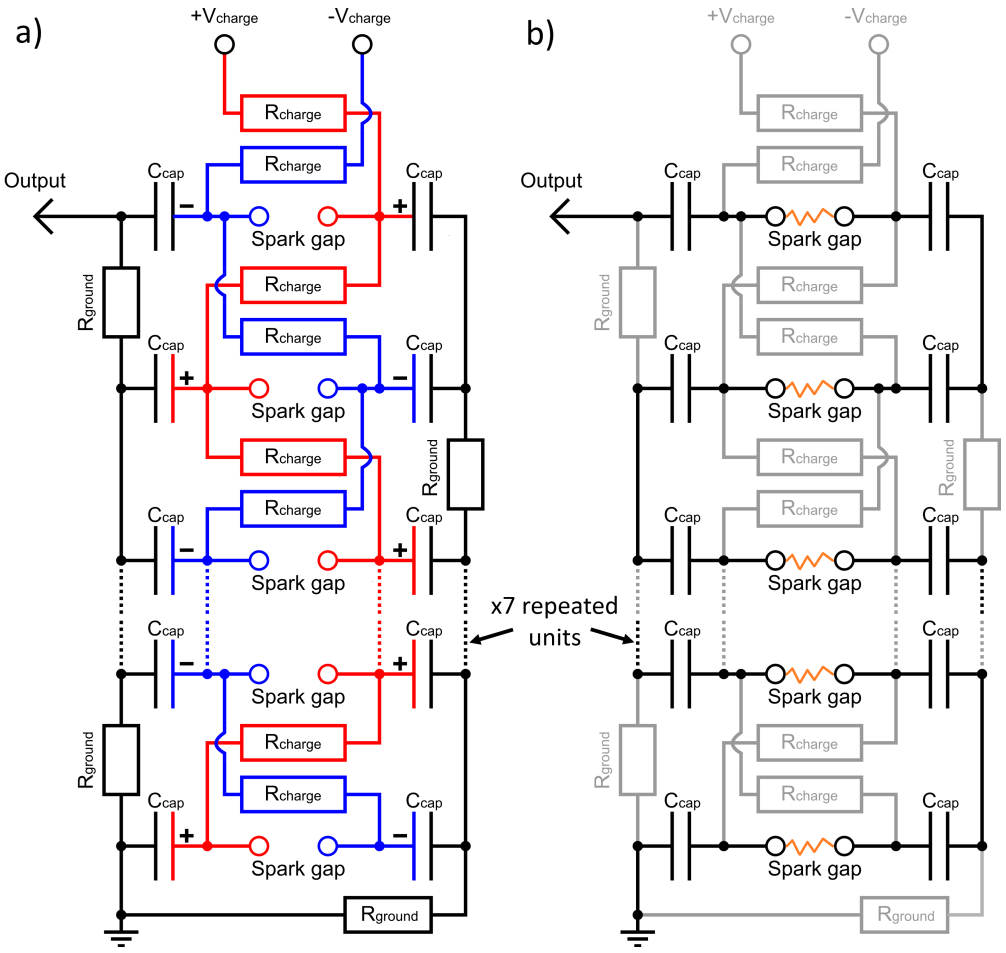


Figure 3.2: Circuit diagram of a bipolar Marx bank. Dotted lines indicate seven repeat units, each with two capacitors and a spark gap. a) Capacitors are charged in parallel to ±65 kV. b) Once erected the capacitors discharge in series.

When charged, to the nominal charging voltage of $V = \pm 65$ kV, each capacitor stores $E = 2.7$ kJ, given by:

$$E = \frac{1}{2}CV^2 \tag{3.1}$$

The capacitors are charged in parallel over ∼5 minutes. The total capacitance of the Marx bank is yielded by summing the individual capacitances (31.2 μF per Marx bank and 124.8 μF for all of MAGPIE). This yields a total energy storage of 66 kJ stored per Marx bank, or 264 kJ for all four banks in MAGPIE.

The capacitors are charged through 20 kΩ resistors, labelled as R_{charge} in Fig 3.2, that isolate the charging circuit and prevent discharge between capacitors when firing MAGPIE. Due to the high power of the MAGPIE charging system inch diameter resistors were made from Tygon tubes filled with a copper-sulphate solution, the concentration of which is controlled to achieve the desired resistance.

Between the two groups of capacitors in each Marx bank are twelve spark gaps filled with SF_6 gas at ∼1.8 bar, labelled in Fig 3.2. When triggered, low resistance plasma arcs bridge these switches reconfiguring the Marx bank to the series circuit in Fig 3.2.b. In this configuration the Marx bank is said to have 'erected' and the capacitors are connected in series. This reduces the total capacitance of the Marx bank to $C_{Marx} = 54.2\ nF$, given by:

$$C_{Marx} = \left[\Sigma C_{cap}^{-1}\right]^{-1} = \frac{C_{cap}}{N} \tag{3.2}$$

where $C_{cap} = 1.3\ \mu$F is the capacitance of each capacitor and $N = 24$ is the number of capacitors in the Marx bank. The energy at the end of charging and just prior to discharge remains unchanged and so, using Eq. 3.1:

$$E = \frac{1}{2}NC_{cap}V_{charge}^2 = \frac{1}{2}C_{Marx}V_{Marx}^2 \tag{3.3}$$

where $|V_{charge}| = 65$ kV is the charging voltage and V_{Marx} is the final output voltage. Substituting in Eq. 3.2 allows an expression for the final output voltage to be calculated:

$$V_{Marx} = NV_{charge} = 24 \times 65\ kV = 1.56\ MV \tag{3.4}$$

Upon firing, the switches are triggered by a smaller Marx bank, refereed to as the Trigger Marx. This consists of ten 0.15 μF capacitors arranged in a similar bipolar configuration to the main Marx banks. These are charged in parallel to $\pm$30 kV by a custom built power supply, storing a total of 675 J. Upon firing MAGPIE, a high voltage pulse is delivered to the switches inside the Trigger Marx. In a similar manner to the Marx bank, this reconfigures the Trigger Marx bank so that the capacitors are connected in series and thus their voltages add. This results in a +300 kV pulse that is fed to each of the four Marx banks using identical lengths of cable, ensuring identical transmission times. The +300 kV pulse is delivered to a brass ring between the two electrodes in the first five spark gaps in each Marx bank. This results in electrical breakdown between the ring and the negatively charged capacitor which in turn results in breakdown across the switch, connecting the positive and negatively charged capacitors.

A 100 Ω resistor at the end of each trigger Marx cable prevents the higher voltage of the Marx bank being discharged back to the Trigger Marx. When connected in series the voltage of the capacitors add (as shown in Eq. 3.4), resulting in a total voltage of 390 kV across the sixth switch. This high voltage is sufficient to initialize electrical breakdown in this and proceeding switches without external triggering. Previous experiments determined that erection of the Marx bank takes $\sim$250 ns, with increased amplitude in the trigger pulse having minimal effect.

3.1.2 Pulse forming lines

To conduct the initially proposed radiative collapse studies, a pulse length of $\sim$200 ns was required with a line impedance of 1.25 Ω. Therefore MAGPIE was designed so that the four Marx banks each discharge into separate $\sim$5 Ω coaxial transmission lines, labelled as pulse

forming lines (PFLs) in Fig 3.1. These act as capacitors for intermediate energy storage before being discharged to the load. In doing so the $\sim\mu$s discharge of Marx banks is temporally compressed. When triggered, these discharge into into a single vertical transmission line (VTL) which is impedance matched to the four PFLs, achieving the required 1.25 Ω

The final pulse length will be twice the transit time of the PFLs (sufficient for a wave to travel down the PFL and be reflected off the back surface). Thus, to achieve a pulse length of $\sim$200 ns the transit time of the PFLs must be $\tau_{PFL} \sim 100$ ns. The pulse velocity in a coaxial transmission line is given by: $c/\sqrt{\epsilon_r}$ where ϵ_r is the insulators relative permittivity and c is the speed of light. Therefore, to reduce the pulse velocity so that practical length transmission lines may be used, deionized water was used as a dielectric, with $\epsilon_r \approx 80$ yielding a length of $d = 3.3$ m. The impedance, Z, of the coaxial cable is given by:

$$Z = \sqrt{\frac{\mu_r \mu_0}{\epsilon_r \epsilon_0}} \frac{1}{2\pi} ln\left(\frac{b}{a}\right) \tag{3.5}$$

where μ_0 is the vacuum permeability, μ_r is the dielectrics relative permeability (assumed to be unity), ϵ_0 is the vacuum permittivity, a is the inner radius and b is the outer radius. Therefore, to achieve the desired impedance of $Z_{PFL} = 5\ \Omega$ a ratio of $b/a \sim 2$ is required. To avoid high electric field strengths, which could ionize the dielectric leading to electrical breakdown, $a = 0.26$ m and $b = 0.5$ m were selected. In addition, charging the inner conductor of the PFL to negative potentials reduced the likelihood of electrical breakdown across the deionized water. This is because any streamers formed of liberated electrons will diverge as they propagate towards the outer conductor.

Separating the PFL and Marx banks was an oil filled 'elbow' section consisting of several bellows which allowed for thermal expansion and directed the PFLs towards the experimental chamber at the centre of the laboratory, labelled in Fig 3.1. Two 50 mm thick high density polythene diaphragms were used to separate the elbow from the Marx bank and PFL. These are slightly elastic so do not fail when shocked. At these points the inner conductor radius was only 0.15 m, increasing the electric field above the threshold for electrical breakdown

across the diaphragms surface. To counter this, field shapers were installed to increase the effective radius and therefore reduce the electric field strength at this point.

Between each PFL and the VTL sits a large switch, labelled in Fig 3.1. These are embedded in transmission oil which has a low relative permittivity and so reduces capacitive coupling between the PFL and VTL, preventing a pre-pulse from reaching the load. Once the PFLs have been charged these switches are simultaneously triggered, allowing all four PFLs to discharge into the VTL. The switches consist of two stainless steel electrodes in an SF_6 gas-fill at $3-5$ bar. The electrode on the VTL side had an axial hole to accommodate a trigger pin, shown in Fig 3.3. Separating the two electrodes, and forming the pressurized gas cell, were a series of rings of acrylic separated by steel rings. These steel rings help to ensure a uniform field between the anode and cathode by capacitively coupling to one another. This helps to reduce localised field stress on the insulator.

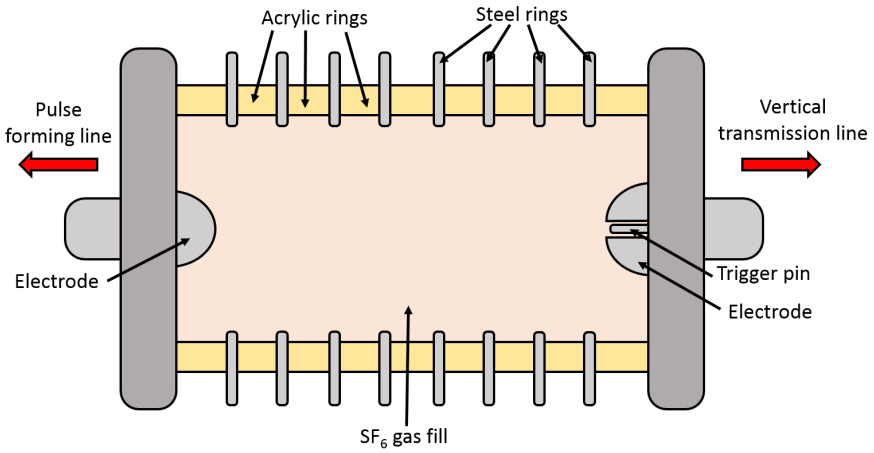


Figure 3.3: Cross section of one of the four MAGPIE line switches located between each PFL and the VTL.

These four switches were triggered by a single 0.7 μ F capacitor, known as the line gap trigger (LGT), charged to 40 kV by a custom built power supply. A single spark gap allows the LGT to discharge into four RG218 50 Ω cables connected to the trigger pin. These cables are coiled around the inside of the VTL, providing $\sim$50 μH of inductance to prevent the PFLs discharging into the LGT.

The high potential difference across the small gap between the trigger pin and electrode

results in electrical breakdown which in turn causes breakdown across the two electrodes, allowing the PFLs to discharge. Previous experiments determined that these switches have a jitter rate of ±8 ns, significantly shorter than the MAGPIE pulse and therefore allowing MAGPIE to produce a repeatable current. However, these switches are prone to self-breakdown due to the high potential difference between the PFL and VTL. When this occurs the MAGPIE current delivered to the load is reduced and the pulse length increased, as was seen in several experiments.

3.1.3 Vertical transmission line

The four PFLs converge on a central vertical transmission line (VTL) which delivers current to the load. The VTL is also a coaxial cable using de-ionised water as a dielectric with an outer radius of 1 m and inner radius of 0.83 m, achieving the required line impedance of 1.25 Ω, given by Eq. 3.5. The VTL has a length of 2.17 m and thus a transit time of 65 ns. This is sufficient to remove asymmetry introduced from the four separate PFLs. During the MAGPIE pulse of ∼500 ns current is able to reflect several times within the VTL which acts to slightly boost the peak current.

At the top of the VTL is a conical magnetically insulated transmission line (MITL), shown in Fig 3.4. This spatially concentrates the current from the 0.83 m inner radius of the VTL to 0.02 m, to which the experimental load can be directly connected.

At the top of the MITL the distance between the anode and cathode is only 10 mm. However, the strong magnetic fields generated by the MAGPIE current result in very small electron gyro-radii which inhibits electron conduction across the gap. The toroidal magnetic field, B, in this region may be calculated using Ampere's law (minus Maxwell's extension) which states that the magnetic field, $B(t, r)$, around a closed loop, ds, is proportional to the current flowing through it, $I(t)$:

$$\oint \mathbf{B}(t, r).\mathbf{ds} = \mu_0 \mu_r I(t) \tag{3.6}$$

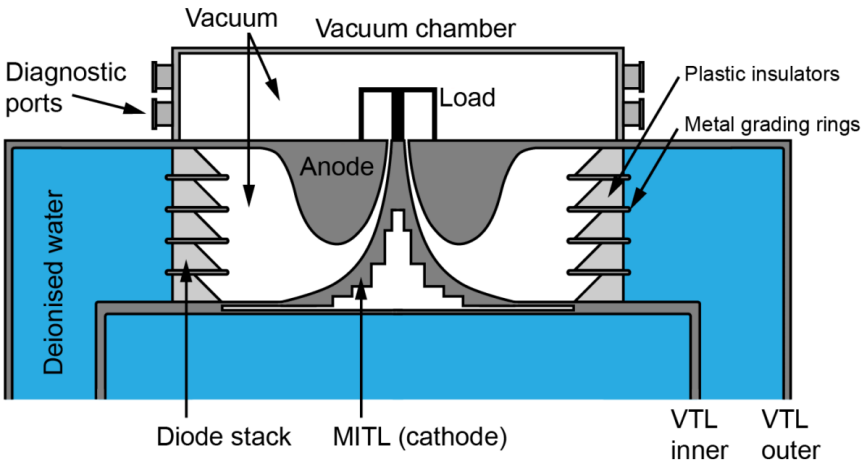


Figure 3.4: Cross section of the top of the MAGPIE VTL, containing the magnetically insulated transmission line and diode stack. Reproduced from [Burdiak, 2012]

Integrating around a circle with radius r (with the relative permeability of water $\mu_r \approx 1$) yields:

$$\mathbf{B}(t, r) = \frac{\mu_0 I(t)}{2\pi r} \tag{3.7}$$

For a peak current of $I = 1.2$ MA and radius of $r = 0.02$ m this yields a peak field of 12 T. The electron gyroradius, r_g may then be calculated with [Zel'dovich and Raizer, 2002]:

$$r_g = \frac{m_e v}{|q|B} \tag{3.8}$$

where m_e and q are the electron mass and charge respectively. Taking the upper limit for the velocity, v, of the speed of light yields an electron gyroradius of $\sim$140 μm. Electrons emitted by the negatively charged cathode will not be able to propagate much further than this distance and thus conduction across the anode-cathode gap is severely limited.

The high voltages and electric fields achieved at the top of VTL prohibit the use of a single insulator, as breakdown would occur along its surface, a phenomenon known as flashover. Instead a series of four stainless steel rings separated by layers of perspex is used, known as the diode stack and labelled in Fig 3.4. The steel rings ensure a uniform field between the

anode and cathode by capacitively coupling to one another. This helps to reduce localised field stress on the insulator.

The insulators surface is angled by 45° towards the load. This aims to direct liberated electrons away from the insulators surface, thus reducing the likelihood of an avalanche breakdown and thus flashover. Liberated electrons are accelerated both upwards, by the strong electric field between the anode and cathode, and inwards due to $E \times B$ drift. However after the current peak, when the electric field reverses, these processes reverse and so the diode stack can fail.

High energy photons, emitted for example by stagnating Z-pinches, are also able to liberate electrons from the diode stacks surface which can result in flashover. The large bulge in the anode seen in Fig 3.4 acts as shielding and thus helps to prevent this.

In atmosphere avalanche electrical breakdown would be able to occur across the 10 mm gap between the anode and cathode at the top of the MITL. In addition, a gas would interfere with the plasma evolution. To prevent this, a cylindrical vacuum chamber, with an internal diameter of 710 mm and internal height of 270 mm is located at the top of the MITL, labelled in Fig 3.4. This is evacuated to a pressure of $\sim 2 \times 10^{-4}$ mbar. The volume of this chamber allows for a wide variety of plasma experiments to be performed and sixteen customizable radial ports provide line of sight for a wide range of diagnostics. In addition, laser probes can be focused through the top of the chamber to probe experiments in the axial ('end on') direction [Swadling et al., 2014].

3.2 Experimental setup

Previous experiments with liners to produce radiative shocks, discussed in Section 1.7.2, had limited diagnostic access. In addition radiative effects occurred on spacial scales larger than the experiment, limiting studies of the radiative precursor and making it impossible to determine absolute electron densities with interferometry diagnostics. To solve these

problems the 'inverse liner z-pinch' experimental configuration was designed to produce radially expanding radiative shocks, shown in Fig 3.5. In this configuration the gas-fill surrounds the liner while the interior is under vacuum.

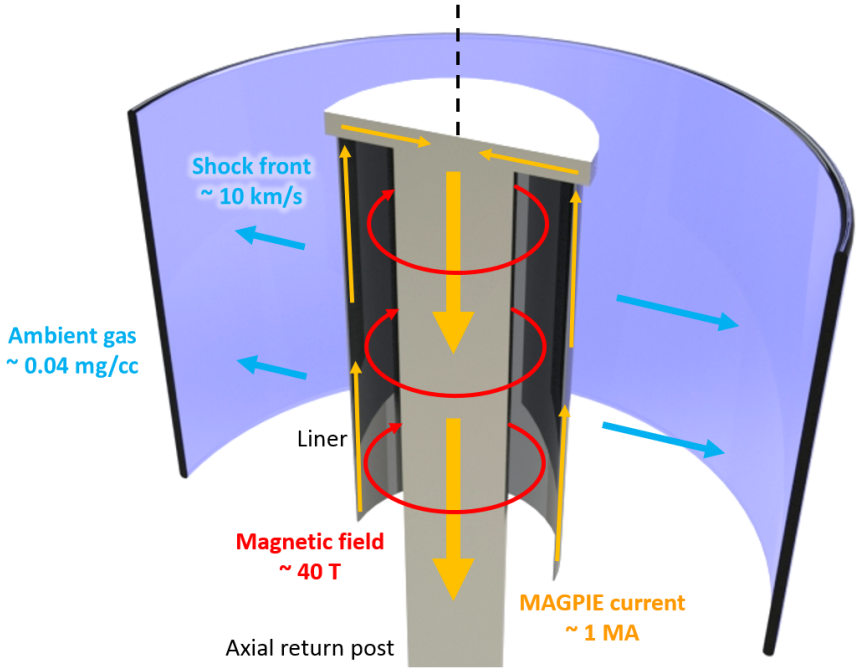


Figure 3.5: 3D diagram showing a cutaway of the 'inverse liner z-pinch' experimental configuration, highlighting the current path in yellow, toroidal magnetic field in red and radially expanding shock in blue.

The ∼1 MA output of the MAGPIE generator was used to drive a current through the liner, as shown in Fig 3.6.a. Current returned down the axial return post generating a strong toroidal magnetic field within the liner. This resulted in a cylindrically symmetric, radially expanding radiative shock being launched into the gas-fill, as shown in Fig 3.6.b. The reason this shock is launched is not yet fully understood and possible mechanisms are discussed in Section 3.4.2. In addition, secondary shocks were launched from where the liner joins the rest of the experimental hardware, which expand at a similar velocity. These are investigated in Section 3.5.3.

This experimental configuration offers several advantages over the converging shock geometry discussed in Section 1.7.2. Firstly, as dynamics are located outside of the liner, the

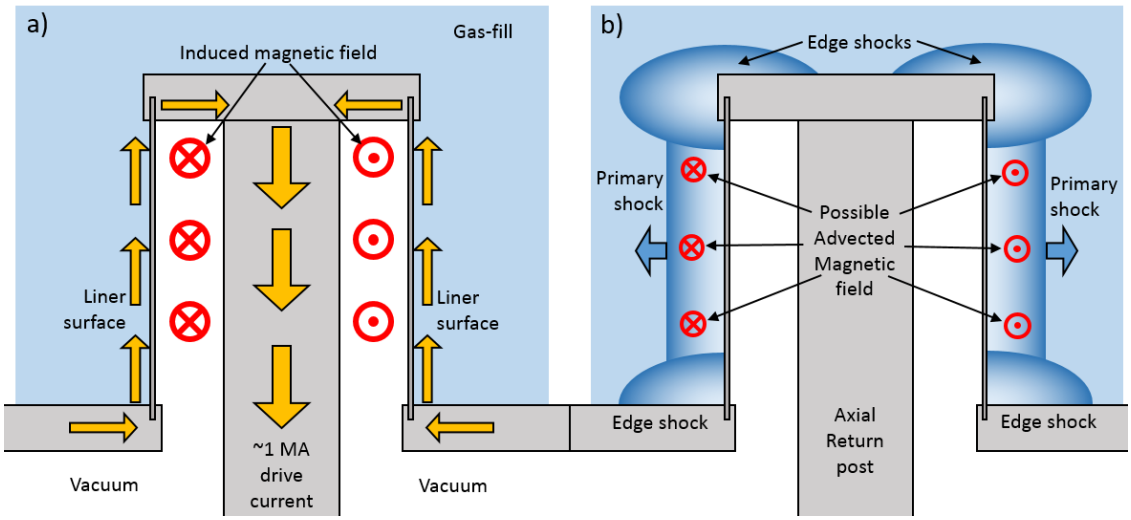


Figure 3.6: Diagram showing the formation of the radiative shock. a) The ∼1 MA MAGPIE current is discharged through the liner and returned down the axial return post resulting, producing a magnetic field inside the liner. b) Quasi one dimensional cylindrically expanding shocks are launched, labelled as 'primary shock'. Additional shocks are sometimes launched where the liner joins the rest of the hardware, labelled as 'edge shocks'.

experiment can be probed side-on as well as end on. This prevents Schlieren effects, from imaging through long regions of plasmas, refracting probe beams out of collection optics. In addition, this prevents having to probe through edge effects, such as the shocks launched from joins between the liner and surrounding hardware, which may be interpreted as additional radial shocks. Secondly, the radially expanding shocks were able to evolve uninterrupted over a long distance and period of time. This is especially important when considering radiative effects as photon path lengths can be of the same order of magnitude as the liner diameter. Fig 3.7 show transmission, as a function of photon energy, after passing through 1 mm of gas at a density of 0.04 mg/cm^3 (used in these experiments), calculated using the online tool at [Henke et al., 1993]. These transmissions were used to calculate the approximate distance required to absorb 90% of the radiation, using Eq. 1.24. These plots show that at these densities several centimetres of gas are required to fully absorb the radiation and observe the full extent of the radiative precursor.

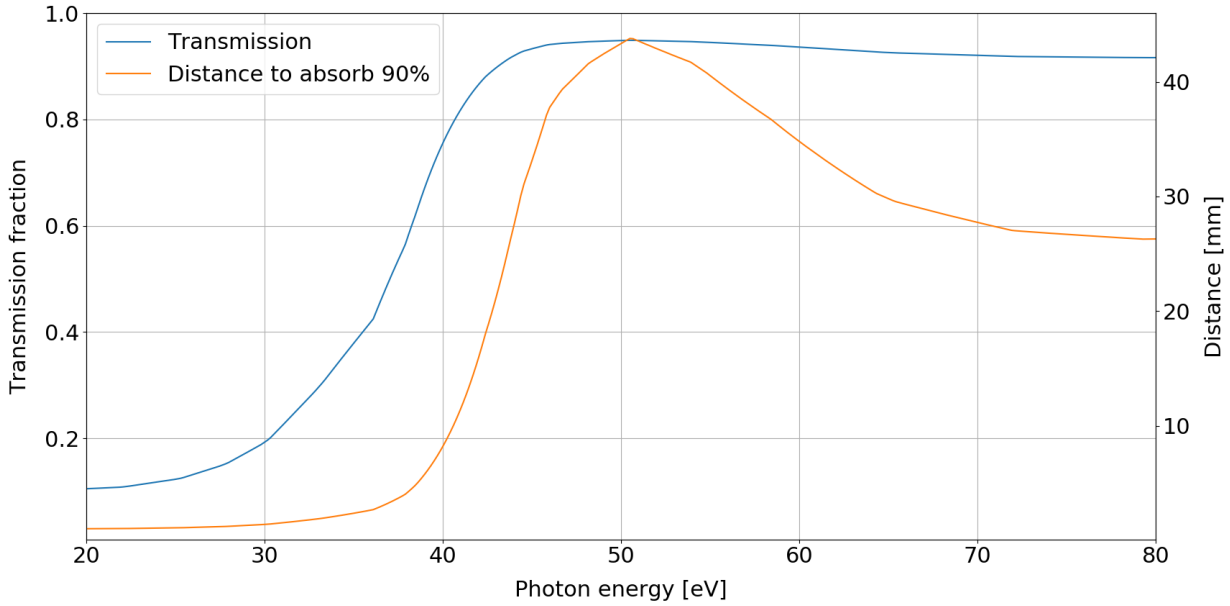


Figure 3.7: Transmission and distance required to absorb 90% of photons in an Argon gas, with a mass density of 0.04 mg/cm^3, as a function of photon energy.

3.2.1 Technical description

Previous work on converging shocks suggested that a thin walled stainless steel liner would launch a single, magnetically driven shock into the gas fill [Burdiak et al., 2015]. However, to accommodate a central return post with a diameter of 5 mm (so that an M3 bolt could be screwed into its end) a larger diameter liner was required. A stainless steel liner with an inner diameter of 11 mm was selected, allowing for a vacuum gap of 3 mm between the liner and return post (sufficient to prevent electrical breakdown inside the liner), and a similar wall thickness of 100 μm was selected. The liner is shown in the cutaway 3D CAD model in Fig 3.8. Liners were made of AISI 321 stainless steel which, in addition to Iron, contains $17-19\%$ Chromium and $9-12\%$ Nickel.

Initially the liner was selected to be 16 mm in length, similar to those used in converging shock experiment. However, it was found that shocks were launched from the ends of the liner (dubbed 'edge-shocks' and investigated in greater detail in Section 3.5.3), disrupting the otherwise cylindrically expanding primary shock. These persisted despite efforts to minimise

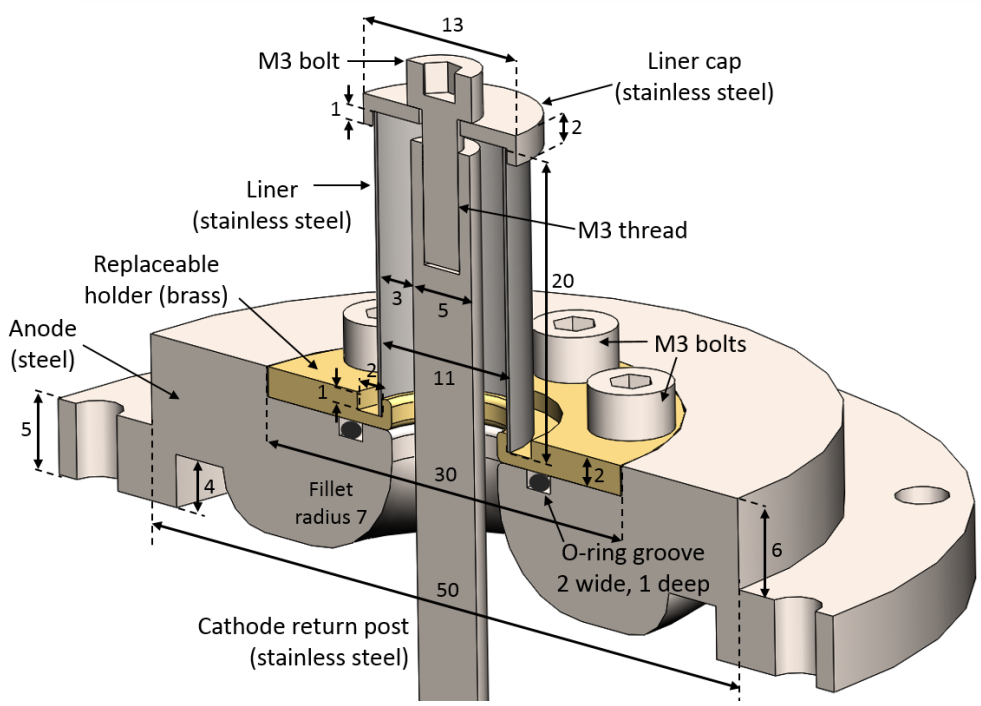


Figure 3.8: Cutaway view of a 3D CAD model of the liner. All dimensions in milimeters.

them and so the liner length was increased to 20 mm for the majority of experiments. This left a region of the primary shock undisrupted at the time of imaging. Although this increase in length slightly increased the inductance and resistance of the load, the high impedance of the MAGPIE generator resulted in negligible change to the current discharged through the liner.

A cross-sectional cut of the entire hardware is shown in Fig 3.9. The additional height added due to the brass structure at the bottom of the hardware, labelled as 'Current return' in Fig 3.9, allowed the plasma to be brought into line with diagnostics which were being used for other experiments performed during the same period [Suttle et al., 2016, Hare, 2017, Burdiak et al., 2017]. This structure was designed to mimic the MITL current feed of MAGPIE with a similar vacuum gap, thus helping to minimise the increase in hardware inductance. However, the region directly above this, labelled 'Rogowski probe location' in Fig 3.9, extends radially outwards resulting in a significant increase in the inductance of the hardware. This provided locations to attach two Rogowski probes, described in Section 3.4.1,

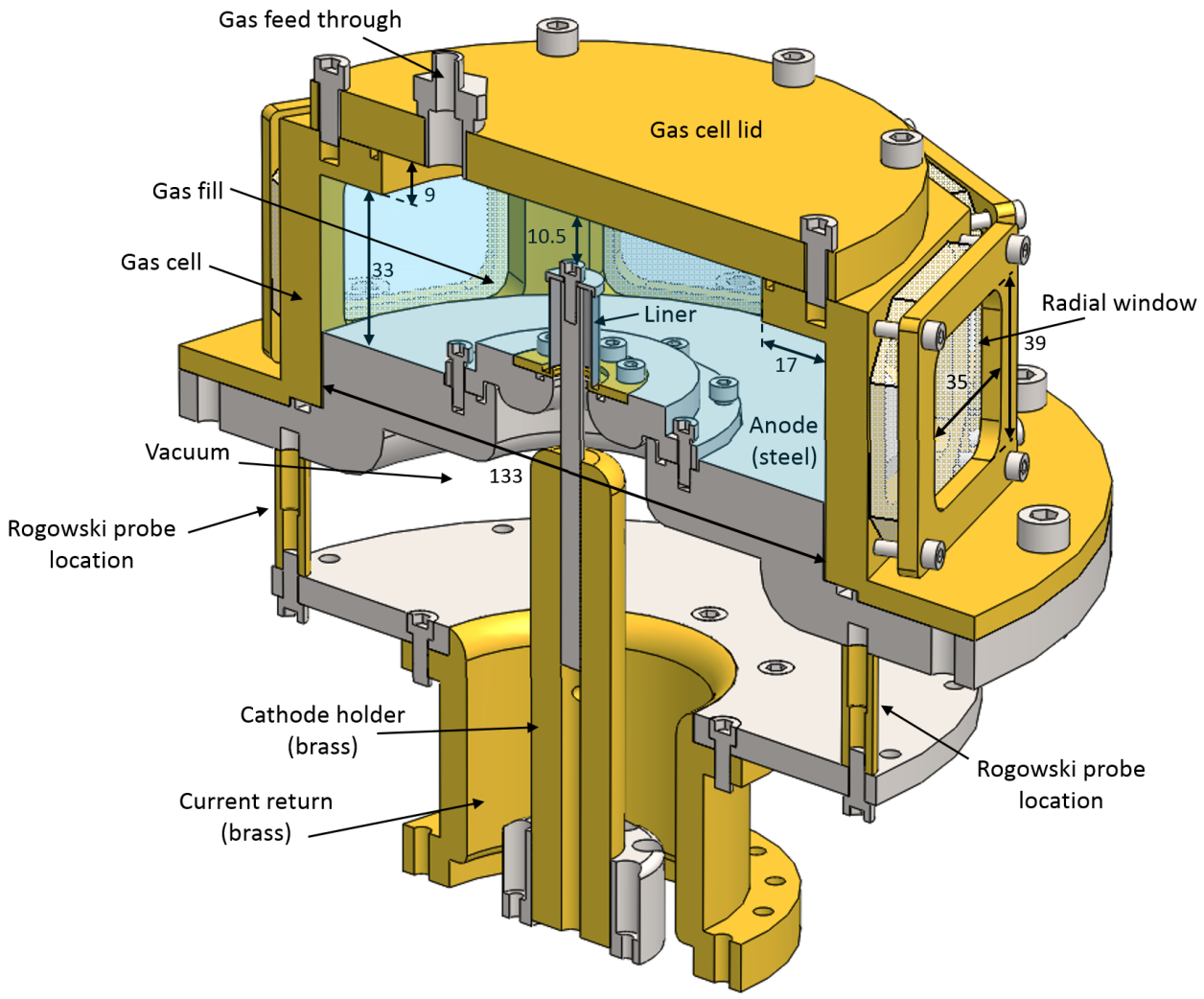


Figure 3.9: Cutaway view of a 3D CAD model of the entire hardware used for this experiment. The region of gas-fill is highlighted in blue. All dimensions in millimetres.

for monitoring the current delivered to the liner.

The MAGPIE transfer line (MITL) delivering current to the liner is kept under vacuum and filling the entire MAGPIE vacuum chamber with gas would result in electrical breakdown. Previous experiments on this facility have used a supersonic gas nozzel to deposit gas immediately prior to firing, so that the gas did not have time to diffuse into the MITL [Suzuki-Vidal et al., 2012]. However, this resulted in a non-uniform gas density which was challenging to determine. For this reason a gas cell was installed within the larger MAGPIE vacuum chamber.

The gas cell used for these experiments was developed by J. Skidmore for experiments involving plasma jets from radial foils [Skidmore, 2013]. This gas cell provided a large volume with an internal radius of 66.5 mm and height of 33 mm. The exterior was octagonally shaped, with a face to face distance of 143 mm, allowing for 8 radial windows with a height of 35 mm and width of 39 mm. A 3D CAD model is shown in Fig 3.10.a and a picture of the gas cell is shown in Fig 3.10.b. The gas cell body was milled from brass due to it's low cost and ease to machine while the gas cell base was milled from steel.

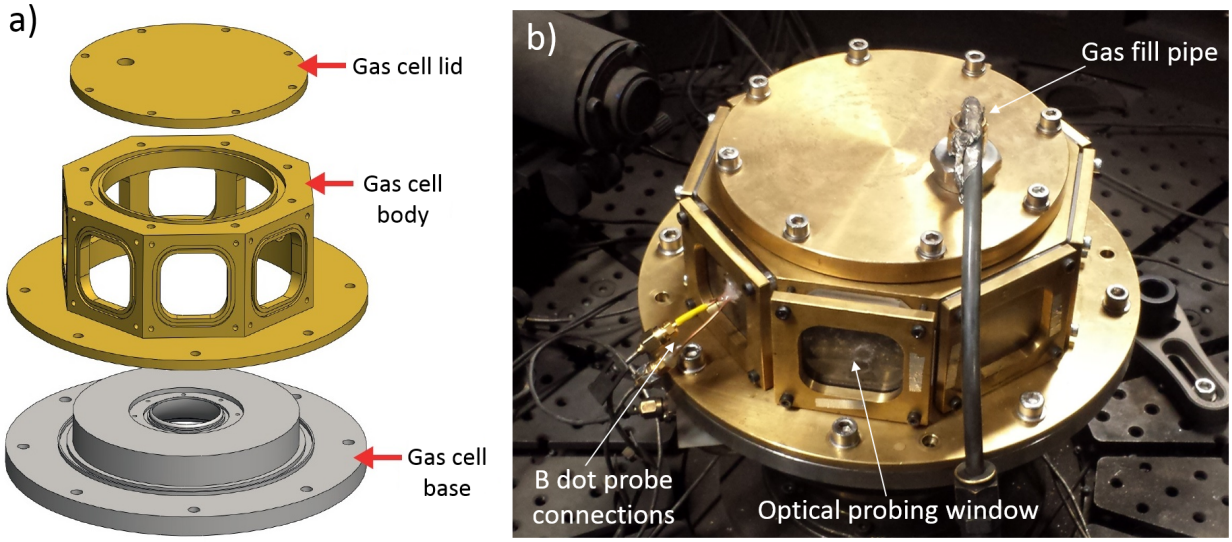


Figure 3.10: a) Exploded 3D CAD model of the gas cell, reproduced from [Skidmore, 2013]. b) Picture of the gas cell used in these experiments inside the MAGPIE vacuum chamber. In this image the original metal lid is used.

Electrical breakdown was observed between the top of the liner and gas cell lid, diverting current away from the liner. This is discussed in detail in Section 4.2.2. To prevent this, later experiments replaced the metal lid was replaced with a 5 mm thick laser cut acrylic insulating lid which did not show signs of electrical breakdown.

A gas filling system allowed the gas cell to be evacuated and filled in situ inside the MAGPIE vacuum chamber. A diagram of the gas filling system is shown in Fig 3.11. A flexible 1/4 inch hose was connected to a Swagelok fitting on the lid of the gas cell while the other end was connected to the gas filling system. Firstly a valve connecting the hose to the

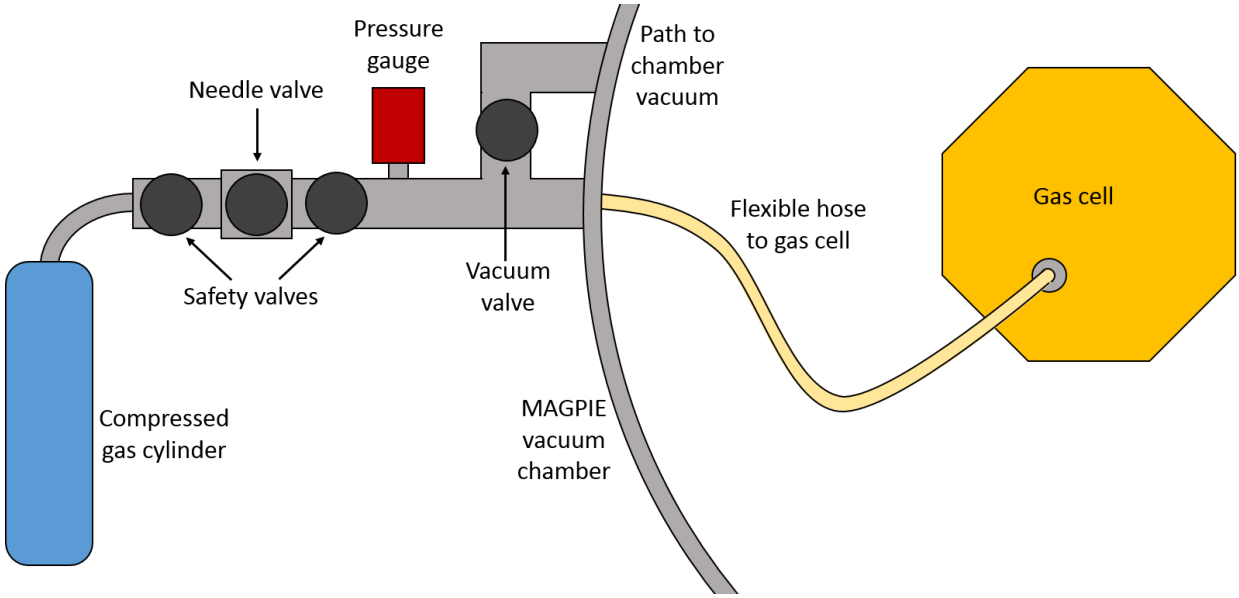


Figure 3.11: Diagram of the gas filling rig. A combination of pressure gauge and needle valve were used to fill the gas cell to a specific pressure while under vacuum. A valve connected to the vacuum chamber allowed the interior of the gas cell to be evacuated.

MAGPIE vacuum chamber was opened, allowing the gas cell to be brought to high vacuum. This valve was then closed and a small amount of gas, from a pressurized bottle, was fed into the chamber through a needle valve. A high accuracy pressure gauge was attached to the gas cell side of the gas filling system which allowed the pressure inside the gas cell to be monitored to 4 significant figures between 100 mbar and $\sim 10^{-2}$ mbar. The additional safety valves shown in Fig 3.11 were installed to prevent the MAGPIE vacuum chamber being accidentally opened directly to the pressurized bottle.

As the interior of the liner was under vacuum, a gas tight seal had to be made with the surrounding hardware. Initial attempts involved using rubber O-rings which could be compressed under screw clamps to make a seal against the liner surface. A picture of this setup is also shown in Fig 3.12.a. However, these were later replaced with a layer of glue, which was found to also provide a gas tight seal. Araldite Instant, a two-component epoxy adhesive [Go-Araldite, 2017], was applied to the top and base of the liner as shown in Fig 3.12.b. This simplified the experimental setup, reducing the hardware surrounding the load, and helped to mitigate the size of 'edge-shocks'. After application, the glue had to be left to

set for ∼30 minutes prior to evacuating the chamber. Failure to do so would result in the tacky glue partially boiling, forming air bubbles within the glue which could break the gas tight seal.

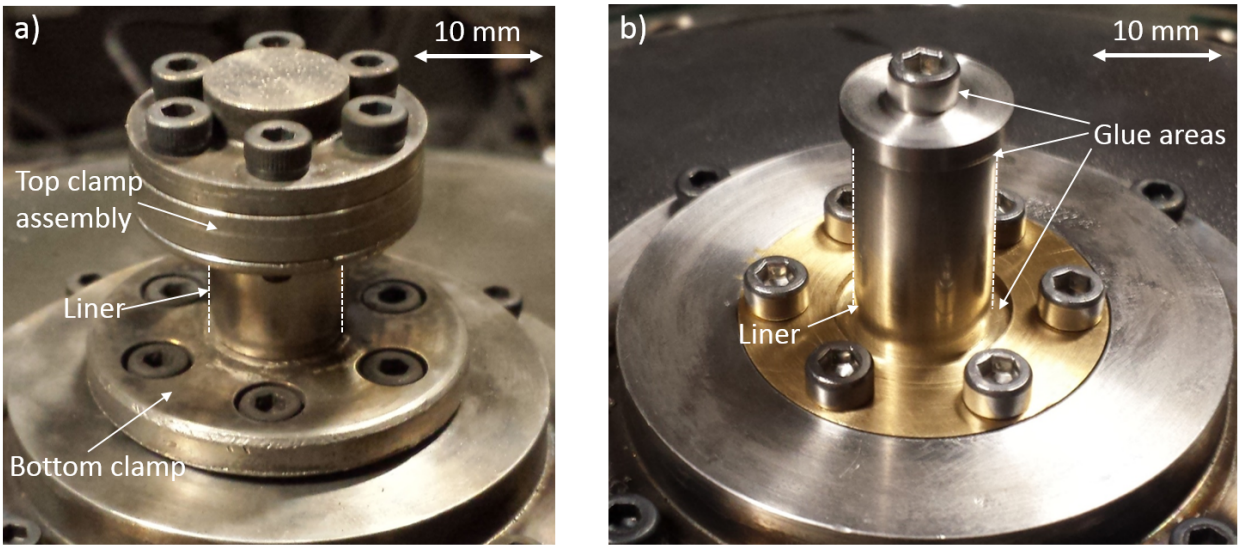


Figure 3.12: a) Picture of the liner held in place with the O-ring clamps. b) Picture of the liner prior to applying Araldite glue.

Although these experiments were initially inspired by work performed by G. Burdiak (detailed in Section 1.7.2 [Burdiak et al., 2015]), several major modifications were introduced and are summarised in Table 3.1. A similar liner length and thickness were used in both experiments but this work used liners with a significantly increased diameter to accommodate a central return post. This decreased the current density in the liner. Although both experiments were performed with Argon gas-fills, this work used much higher fill pressures in order to make the shocks more visible to self-emission and interferometry diagnostics when probing side on.

3.2.2 Circuit model of the liner

To understand how the MAGPIE current flows through the experimental hardware, the liner and return post were modelled as the simple circuit shown in Fig 3.13.

As resistance is inversely proportional to the cross section of a conductor, the thin wall

	These experiments Expanding shocks	Previous experiments Converging shocks
Liner material	Stainless steel (AISI 321)	Aluminium (AL 6061)
Liner inner-diameter [mm]	11	5.8
Liner outer-diameter [mm]	11.2	6
Liner wall thickness [μm]	100	90
Liner length [mm]	16/20	14
Gas species	Argon	Argon
Gas fill pressure P_0 [mbar]	24	7
Gas fill mass density ρ_0 [mg/cm^3]	0.04	0.01

Table 3.1: Comparison between these experiments on radially expanding shocks and previous work on radially converging shocks detailed in Section 1.7.2.

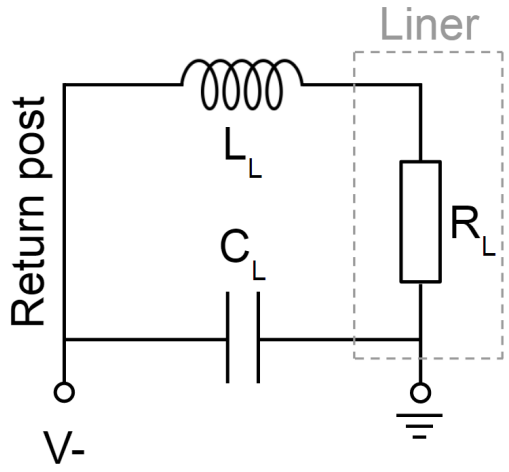


Figure 3.13: Circuit diagram of the liner and return post modelled as a resistor R_L, capacitor C_L and inductor L_L.

of the liner acts as a resistor of R_L while the return post and surrounding hardware have negligible resistance. In addition, the liner and return post can be thought of as a current loop and so act as an inductor with an inductance L_L. Finally, the voltage drop across the liner could result in charge build up at the base of the liner and return post causing it to act as a capacitor with a capacitance C_L.

The initial resistance through the liner can be calculated as the resistance of stainless steel, 7.2×10^{-7} Ωm [ASM Aerospace Specification Metals Inc., 2017], multiplied by the height of the liner, h, and divided by its cross-sectional area. The cross sectional area of the liner, CSA, can be calculated by subtracting the area of a circle of the liner inner radius,

r_1, from a circle of the liner outer radius, r_2, yielding $CSA = \pi r_2^2 - \pi r_1^2$. With an inner radius of $r_1 = 5.5$ mm and outer radius of $r_2 = 5.6$ mm, this yields a cross sectional area of $CSA = 3.4 \times 10^{-6}\ m^2$. With a liner height of $h = 0.02$ m this yields a total resistance of 0.005 Ω. However, during the current pulse the liner will heat up resulting in an increase in resistance, as discussed in Section 3.2.3.

The ∼1.2 MA discharge of the MAGPIE generator resulted in large toroidal magnetic fields being generated inside the liner. The magnitude of this field as a function of radius may be calculated using Eq. 3.7 and is plotted for a peak current of 1.2 MA in Fig 3.14. This predicts a peak field of 96 T on the surface of the 5 mm diameter return post (at $r = 2.5$ mm) and 44 T on the inner surface of the liner at $r = 5.5$ mm. However, outside of the liner this field is expected to drop to zero as the current in the liner is equal but opposite to the current on the return post. Assuming current flows uniformly through the liner, the magnetic field decays linearly through the liner wall.

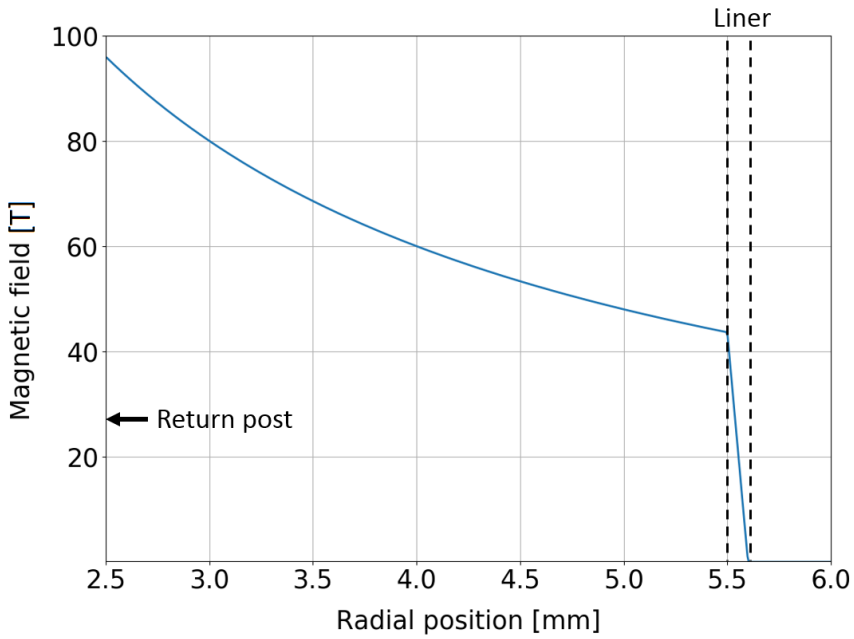


Figure 3.14: Toroidal magnetic field strength in the liner, generated by the MAGPIE 1.2 MA discharged, as a function of radial position from the axis.

Capacitance

As voltage is dropped across the liner, charge builds up at the base of the liner and return post causing it to act as a cylindrical capacitor. The capacitance of the liner can be found by considering the electric field between the liner and return post. Gauss' law states that the electric field, $\mathbf{E}(r,t)$, integrated over a closed surface is proportional to the enclosed charge, Q:

$$\oiint \mathbf{E}(r,t).d\mathbf{A} = \frac{Q}{\epsilon_0} \tag{3.9}$$

where ϵ_0 is the vacuum permittivity, 8.85×10^{-12} F/m. Integrating over a cylindrical surface of radius r and height h containing a charge Q, the electric field will be given by:

$$\mathbf{E}(r,t) = \frac{Q}{2\pi\epsilon_0 r h}\ \hat{\mathbf{r}} \tag{3.10}$$

Integrating the electric field between the return post, at a radius r_0, and liners inner surface, at a radius r_L, yields the electric potential, V, between the two:

$$V = \int_{r_0}^{r_L} |\mathbf{E}(r,t)| dr = \int_{r_0}^{r_L} \frac{Q}{2\pi\epsilon_0 r h} dr = \frac{Q}{2\pi\epsilon_0 h} ln\left(\frac{r_L}{r_0}\right) \tag{3.11}$$

The capacitance is defined as the total charge divided by this potential difference $C = Q/V$ and thus the total capacitance can be stated as:

$$C_L = \frac{2\pi\epsilon_0 h}{ln\left(\frac{r_L}{r_0}\right)} \tag{3.12}$$

An upper bound for the capacitance in this system can be approximated using the liner length $h = 20$ mm and substituting in values for the liner and return post radii, $r_0 = 2.5$ mm, $r_L = 5.5$ mm. This yields a total capacitance of 1.4 pF which is not expected to have a significant effect on the MAGPIE current.

Inductance

The liner and return post act as a current loop and the time varying magnetic field within the liner causes it to act as an inductor, with an inductance L_L, inducing a voltage, $V(t)$, across the liner:

$$V(t) = -L_L \frac{\partial I(t)}{\partial t} \tag{3.13}$$

The inductance, L_L, may be calculated using Faraday's law which states that the voltage across the component is proportional to the rate of change of magnetic flux, ϕ, given by:

$$V(t) = -\frac{\partial \phi(t)}{\partial t} \tag{3.14}$$

The magnetic flux is the total field integrated over half the cross section of the liner, and is therefore given by:

$$\phi(t) = \int_{r_0}^{r_L} \int_0^h B(r,t) dr dz \tag{3.15}$$

Eq. 3.7 can then be used to replace B yielding:

$$\phi(t) = \int_{r_0}^{r_L} \int_0^h \frac{\mu_0 I(t)}{2\pi r} dr dz \tag{3.16}$$

Solving this integral yields:

$$\phi(t) = \frac{\mu_0 I(t) h}{2\pi} ln\left(\frac{r_L}{r_0}\right) \tag{3.17}$$

Once substituted into Eq. 3.14 this yields:

$$V(t) = -\frac{\mu_0 h}{2\pi} ln\left(\frac{r_L}{r_0}\right) \frac{\partial I(t)}{\partial t} \tag{3.18}$$

which can be equated to Eq. 3.13 to yield the inductance of the liner:

$$L_L = \frac{\mu_0 h}{2\pi} ln\left(\frac{r_1}{r_0}\right) \tag{3.19}$$

For this experimental configuration $r_0 = 2.5$ mm, $r_L = 5.5$ mm and $h = 20$ mm which yields an inductance of 3.2 nH. As the liner does not move on the time scales of the experiment this inductance remains constant throughout the entire current pulse.

Impedance

Ohm's law for direct current can be expressed as the product of the resistance, R, and current, $I(t)$. However, for a time varying current additional terms for capacitance, C, and inductance, L are introduced and Ohm's law becomes:

$$V(t) = I(t)R + i\omega L\frac{\partial I(t)}{\partial t} - \frac{i}{\omega C}\int I(t)dt \tag{3.20}$$

Approximating the current as a sinusoidal wave, with an angular frequency ω, given by:

$$I(t) = I_0 exp\,(i\omega t) \tag{3.21}$$

therefore yields:

$$V(t) = RI(t) + i\omega LI(t) - \frac{i}{\omega C}I(t) \tag{3.22}$$

The voltage across the capacitor and inductor are imaginary, labelled with an i. This is because these terms represent energy storage in the system and thus are 90° out of phase with the drive current. It is common to combine all of the terms on the right hand side by introducing the impedance, Z, of an electrical circuit, given by:

$$Z = R + i\omega L - \frac{i}{\omega C} \tag{3.23}$$

Fig 3.13 shows how the liner can be approximated as a resistor of $R_L = 0.005\ \Omega$ and

inductor with $L_L = 3.2$ nH in series. Adding the first and second term on Eq. 3.23 in quadrature yields the magnitude of the impedance through the liner, given by:

$$|Z| = \sqrt{R + (\omega L)^2} \tag{3.24}$$

Approximating the MAGPIE pulse (with a duration of ~ 500 ns) as half a sinusoidal wave yields a frequency of $\omega = 6.28 \times 10^6$ rad/s. This yields a total impedance of 0.021 Ω, dominated by the inductance term which is a factor of $\sim\times 3$ larger than the resistive term.

Note the capacitance term in Eq. 3.23 which allows rapidly varying electric fields to transfer current across a capacitor. As shown in Fig 3.13, this would allow current to bypass the liner. However, with a capacitance less than 1.4 pF, the impedance across this current path is 114 kΩ, several orders of magnitude larger than the total impedance of the liner. Thus $> 99\%$ of the MAGPIE current will pass through the liner in the absence of electrical breakdown.

3.2.3 Current and magnetic skin depth

High frequency currents do not flow uniformly through a conductor, instead the majority of the current flows close to the surface. This minimises the inductance by reducing the area of the current loop. In addition, the induced magnetic field establishes eddy currents which resist the diffusion of the current. Both the current and magnetic field strength decay exponentially with depth into the conductor with a skin depth, δ, defined as the depth at which the current and magnetic field magnitude have decayed to $1/e \approx 37\%$. The following derivation of the skin depth follows that found in the book 'Magnetic Fields' [Knoepfel, 2000].

The magnetic diffusion equation can be derived starting from the differential form of Faraday's law of induction; which states that the curl of the electric field vector, $\mathbf{E}(t)$, is equal to the time derivative of the magnetic field vector, $\mathbf{B}(t)$:

$$\nabla \times \mathbf{E}(t) = -\frac{\partial \mathbf{B}(t)}{\partial t} \tag{3.25}$$

Next consider Ohm's law for current density, which states that the current density vector, $\mathbf{j}(t)$ is equal to the product of the conductivity, σ, and electric field vector:

$$\mathbf{j}(t) = \sigma \mathbf{E}(t) \tag{3.26}$$

This may be substituted into Faraday's law, replacing the electric field vector and yielding:

$$\nabla \times \left(\frac{\mathbf{j}}{\sigma}\right) = -\frac{\partial \mathbf{B}}{\partial t} \tag{3.27}$$

Next consider the differential form of Ampere's law:

$$\nabla \times \mathbf{B} = \mu \mathbf{j} + \epsilon \frac{\partial \mathbf{E}}{\partial t} \tag{3.28}$$

where μ is the magnetic permeability and ϵ is the electric permittivity. However, in a good conductor the electric field is able to diffuse at near the speed of light, crossing the 100 μm thick liner wall in $\sim$0.3 ps - approximately instantaneous on the time scale of these experiments. Therefore the electric field can be assumed to be constant through the liner and the time derivative of the electric field can be neglected. This allows Ampere's law to be substituted into Eq. 3.27 to replace the current density, yielding:

$$\nabla \times \left(\frac{\nabla \times \mathbf{B}}{\sigma \mu}\right) = -\frac{\partial \mathbf{B}}{\partial t} \tag{3.29}$$

Using the vector identity $\nabla \times (\nabla \times \mathbf{A}) = \nabla.(\nabla \mathbf{A}) - \nabla^2 \mathbf{A}$, yields the magnetic diffusion equation, with magnetic diffusivity coefficient $1/\kappa = \sigma\mu$:

$$\nabla^2 \mathbf{B} = \frac{1}{\kappa} \frac{\partial \mathbf{B}}{\partial t} \tag{3.30}$$

Taking the curl of this equation, and using the vector identity $\nabla \times (\nabla^2 \mathbf{A}) = \nabla^2(\nabla \times \mathbf{A})$, yields:

$$\nabla \times \left(\frac{\nabla \times \mathbf{B}}{\sigma \mu} \right) = -\frac{\partial \mathbf{B}}{\partial t} \tag{3.31}$$

Ampere's law (Eq. 3.28) can then be substituted into this equation (ignoring the time derivative of the electric field again). This yields the current diffusion equation which is identical in form to the magnetic diffusion equation, Eq. 3.30:

$$\nabla^2 \mathbf{j} = \frac{1}{\kappa} \frac{\partial \mathbf{j}}{\partial t} \tag{3.32}$$

Both the magnetic and current diffusion equations have the same diffusion coefficient, $1/\kappa$, and therefore the same skin depth. The solutions to both of these equations follow the form:

$$\mathbf{B}(x,t) = \mathbf{B}_0 exp\left(-\frac{x}{\delta}\right) exp\left(-\frac{t}{\tau}\right) \tag{3.33}$$

$$\mathbf{j}(x,t) = \mathbf{j}_0 exp\left(-\frac{x}{\delta}\right) exp\left(-\frac{t}{\tau}\right) \tag{3.34}$$

where δ and τ are the characteristic length and time. Substituting Eq. 3.33 into Eq. 3.30 yields an expression for the characteristic length, known as the magnetic/current skin depth, δ, given by:

$$\delta = \sqrt{\kappa \tau} = \sqrt{\frac{\tau}{\sigma \mu}} \tag{3.35}$$

The magnetic field and current will exponentially decay with depth into the conductor so that they have decayed to 37% after a distance equal to the skin depth.

To calculate the skin depth of the liner the current pulse of MAGPIE was approximated to be a sinusoidal wave with a period double the pulse length $\tau = 2 \times 500$ ns. For stainless steel, with a conductivity of 1.38×10^6 /Ωm [ASM Aerospace Specification Metals Inc., 2017]

and magnetic permeability within 1% of the vacuum permeability, so that $\mu \approx 4\pi \times 10^{-7}$ H/m, this yields a skin depth of ∼420 μm. As this is far greater than the wall thickness of the liner, 100 μm, the current can be assumed to flow approximately uniformly through the liner but close to the surface of the return post. The current density on the outside surface of the liner is expected to be ∼61% of the maximum on the inside surface.

However, this value assumes a constant conductance over the entire current pulse. In reality the large MAGPIE current Ohmically heats the liner resulting in a decrease in conductivity and therefore changing how current flows through the liner. This has significant consequences for how current flows through the liner. The power deposited in the liner is given by $Power = \frac{j^2}{\sigma}$ This may be inserted into the thermal equation [Knoepfel, 2000], yielding:

$$\nabla.\left[k\nabla T(x,t)\right] + \frac{j^2}{\sigma} = c_v \frac{\partial T(x,t)}{\partial t} \tag{3.36}$$

The first term represents thermal conduction: where $T(x,t)$ is the temperature, k is the thermal conductivity with typical values of 16 W/m/K for steel [ASM Aerospace Specification Metals Inc., 2017]. The second term represents the power deposited through Ohmic heating. The term on the right hand side represents the rise in temperature: where c_v is the specific heat capacity, with typical values of ∼500 J/kg/K for steel [Engineers Edge LLC, 2017].

However as the liner is heated, the conductivity decreases resulting in increased Ohmic heating and thus an exponential decrease in conductivity over time. This leads to a set of nonlinear equations. At sufficiently high temperatures the conductivity, $\sigma(x,t)$ of the liner may be approximated as:

$$\sigma(x,t) = \frac{\sigma_0}{\alpha T(x,t)} \tag{3.37}$$

Where σ_0 is the conductivity at room temperature (∼300 K), α is the temperature coefficient of resistance and T is the temperature. For steel, α has a typical values of 0.003 K

[Kuphaldt, 2017] and σ_0 has a typical value of 1.39×10^6 Ωm [ASM Aerospace Specification Metals Inc., 2017]. This approximation, along with the assumption that the heat conduction, k, is negligible on the time scales of interest allows Eq. 3.36 to be expressed as:

$$\frac{j^2 \alpha T(x,t)}{\sigma_0} = c_v \frac{\partial T(x,t)}{\partial t} \tag{3.38}$$

For simplicity, the geometry shown in Fig 3.15.a is adopted. The conductor extends from $x = 0$, the magnetic field points in the z direction and the current points in the y direction.

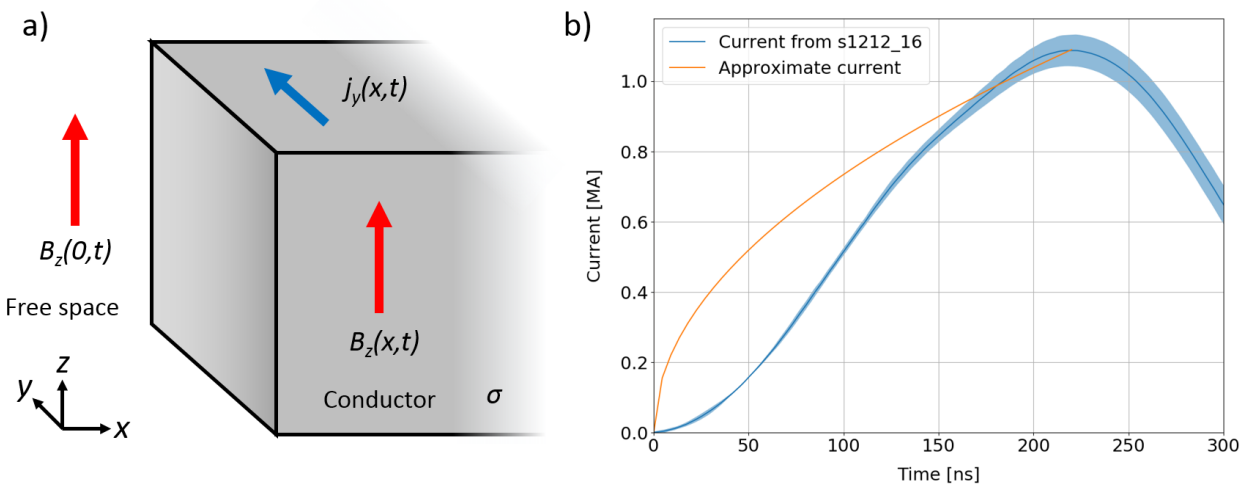


Figure 3.15: a) Geometry used in the derivation of an analytical solution to Ohmic heating of the liner. The conductor extends from $x = 0$, the magnetic field points in the z direction and the current points in the y direction. Based on [Knoepfel, 2000] b) Current from MAGPIE experiment s1212_16 compared against the approximate magnetic field on the conductor surface used to determine Ohmic heating, scaled to match the current.

This geometry allows Eq. 3.29 to be expressed in terms of scalars:

$$\frac{\partial B_z(x,t)}{\partial x} = -\frac{\sigma_0}{\alpha T(x,t)} \mu E_y(x,t) \tag{3.39}$$

In addition, Faraday's law (Eq. 3.25) may now be expressed as:

$$\frac{\partial E_y(x,t)}{\partial x} = -\frac{\partial B_z(x,t)}{\partial t} \tag{3.40}$$

Substituting Ampere's law, Eq. 3.28 (ignoring the timer derivative of the electric field)

into the current density in to the thermal equation, Eq. 3.38, yields:

$$c_v \frac{\partial T(x,t)}{\partial t} = -\frac{\alpha T(x,t)}{\sigma_0} \left(\frac{\partial B_z(x,t)}{\partial t} \right)^2 \tag{3.41}$$

To derive an analytical solution the following boundary conditions must be applied:

$$x = 0 \quad t \geq 0 \quad : \quad B_z(0,t) = B_0(t) \tag{3.42}$$

$$t = 0 \quad x \geq 0 \quad : \quad B_z(x,0) = 0 \tag{3.43}$$

Where B_0 is the initial magnetic field on the conductors surface. In addition, the magnetic field on the conductor surface is approximated as being proportional to the square-root of the time, t.

$$B_0(t) = b_c \sqrt{\frac{t}{t_0}} \tag{3.44}$$

Where t_0 is the duration of the rising pulse and b_c is the characteristic field, a material property that represents the field at which the conductivity is reduced to half it's initial value. This may be expressed as:

$$b_c = \sqrt{\frac{2\mu c_v}{\alpha}} \tag{3.45}$$

This approximation roughly follows the rising MAGPIE current pulse, as shown in Fig 3.15.b. In addition, it is assumed that the magnetic field on the surface of the conductor exceed $b_c \sim 0.65$ T, which is easily achieved using the MAGPIE generator. This leads to the following solutions for the magnetic field, current and energy deposited:

$$B_z(x,t) \sim b_c \left(\frac{t}{t_0} - \frac{x}{\delta_0} \right)^{1.2} \tag{3.46}$$

$$Q(x,t) \sim \frac{\alpha}{c_v}\left(\frac{t}{t_0} - \frac{x}{\delta_0}\right) \tag{3.47}$$

$$j_y(x,t) = \frac{b_c}{2\delta_0}\left(\frac{t}{t_0} - \frac{x}{\delta_0}\right)^{-1/2} \tag{3.48}$$

where δ_0 is the initial skin depth. These solutions are valid up to a depth of $x = \delta_0(t/t_0 - 1)$ after which the magnetic field and current decay exponentially. The solution for the magnetic field and current in a stainless steel conductor are plotted in Fig 3.16 for several times. As time progresses, the magnetic field and current both propagate deeper into the conductor. However, these profiles are significantly different from those predicted with Eq. 3.33 and Eq. 3.34. Instead, the current density peaks within the conductor, avoiding hotter material closer to the surface which is significantly more resistive.

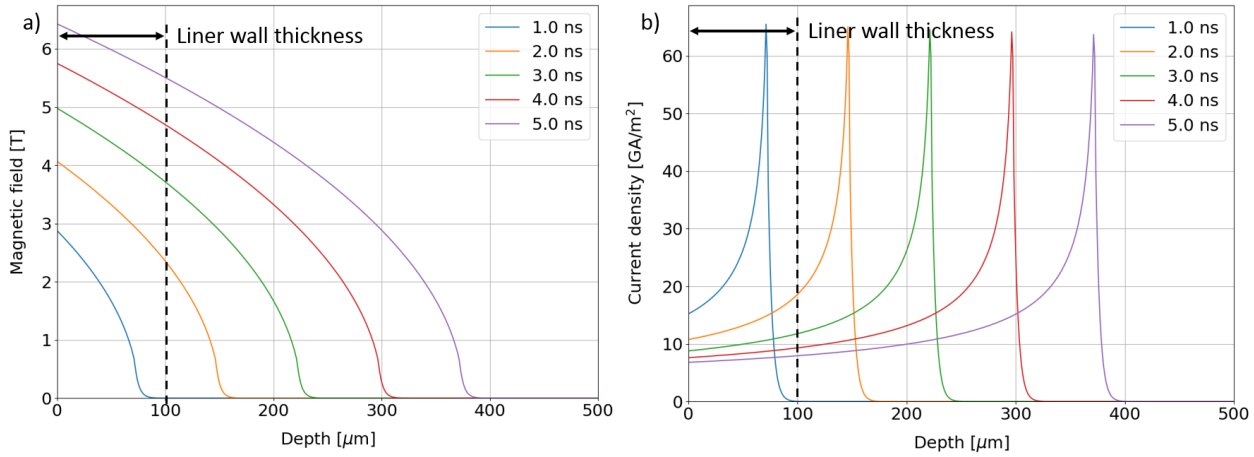


Figure 3.16: Analytical solution for the diffusion of magnetic field and current within the liner. a) Solutions to 3.46 showing magnetic field. b) Solutions to 3.46 showing current density.

These solutions show that within ~2 ns, significantly shorter than the MAGPIE pulse length, the majority of the magnetic field and current will have diffused through the liner wall and so it is appropriate to assume the current flows uniformly through the liner wall. However, this model assumes an infinite liner wall and does not model the interface with the gas-fill.

3.3 MAGPIE diagnostic suite

A schematic of diagnostics fielded in these experiments is shown in Fig 3.17. Rogowski current probes and magnetic probes embedded in the MITL measured the current delivered to the load (discussed in Section 3.3.1). Magnetic probes were used to determine if any magnetic fields were advected by the shock front (discussed in Section 3.3.2). The large octagonal gas cell offered good diagnostic access for optical diagnostics. Laser interferometry with wavelengths of 532 nm and 355 nm was performed using a Mach-Zehnder setup (discussed in Section 3.3.4). Optical self-emission was recorded using a fast multi-frame camera (discussed in Section 3.3.3). Finally, optical self-emission was captured by a fibre bundle to perform spectroscopy (discussed in Section 3.3.5). Interferometry, optical spectroscopy and self-emission imaging were all performed along the same line of sight with the same focal plane allowing for close comparison between images.

3.3.1 Current probes

Magnetic fields can be measured using induction probes, made from simple coils of wire. A changing magnetic field within the coil results in a voltage being induced across the coil which may be recorded on an oscilloscope. Placing an induction probe near to a current carrying conductor also allows the current to be indirectly determined non-intrusively by measuring the induced magnetic field. The induced voltage, $V(t)$, is given by Faraday's law:

$$V(t) = -NA\frac{\partial \phi(t)}{\partial t} + V_{cap}(\mathbf{x}, t) \tag{3.49}$$

where $\phi(t)$ is the magnetic flux (magnetic field multiplied by probe area $B(t)A$) and N is the number of turns of the coil. This voltage may then be measured on an oscilloscope to determine the time differential of the current. By integrating the voltage with respect to time the magnetic field may be estimated.

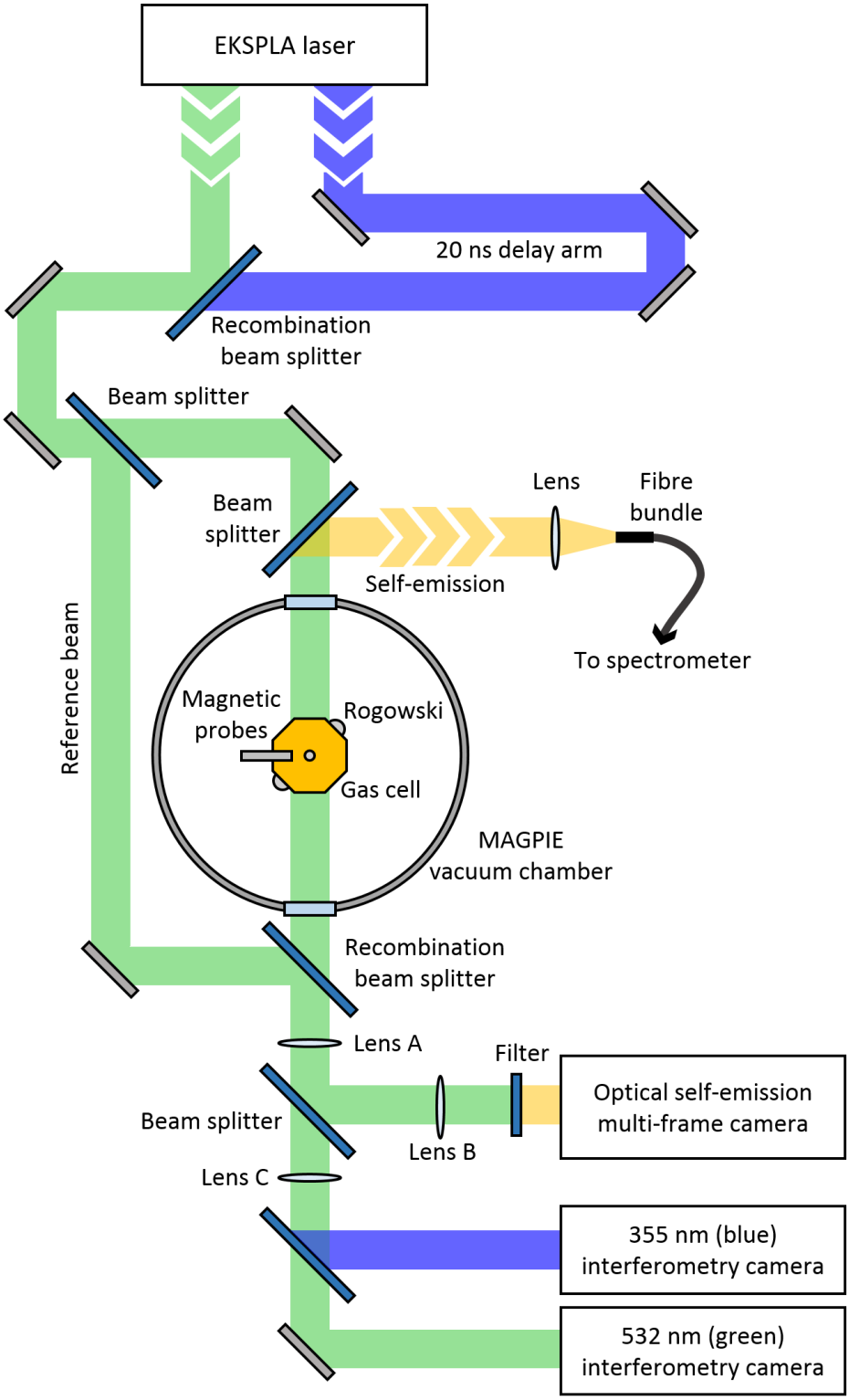


Figure 3.17: Diagnostic setup for experiments performed on the MAGPIE facility. Some mirrors and beam conditioning optics prior to the chamber are omitted for clarity of presentation.

The additional term $V_{cap}(\mathbf{x}, t)$ refers to an electrostatic component due to capacitive coupling with the MAGPIE generator. The impedance of the load is dominated by the inductance (as shown in Section 3.2.2) so the voltage through the load will be proportional to $dI(t)/dt$. As this is a scalar, it may be isolated using two oppositely wound coils which record voltages $V_1(t)$ and $V_2(t)$. The time differential of the magnetic field and voltage due to capacitive coupling are then given by:

$$\frac{\partial \phi(t)}{\partial t} = \frac{1}{2NA}(V_1(t) - V_2(t)) \tag{3.50}$$

$$V_{cap(\mathbf{x},t)} = \frac{1}{2}(V_1(t) + V_2(t)) \tag{3.51}$$

To measure the current passing through the load, a mixture of Rogowskii and magnetic induction probes were used. Two Rogowski probes were placed around current return posts in each experiment and four magnetic induction probes were located inside the MITL as shown in Fig 3.18.

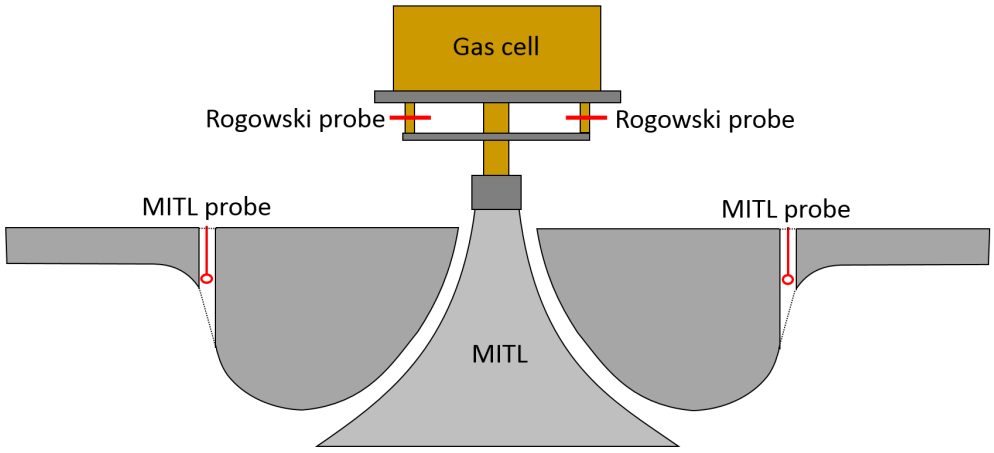


Figure 3.18: A cross section of the MAGPIE MITL with the locations of the Rogowski probes and two of four the magnetic induction probes are shown.

The Rogowski probes used on the MAGPIE facility were machined from a 34 mm diameter disk of brass with a 15 mm diameter axial hole and an asymmetric toroidal groove, shown in Fig 3.19. A pin radially bridges the groove and is connected to an SMA cable, creating

a conducting loop. This probe surrounds a current carrying conductor so that a toroidal magnetic field is induced in the groove.

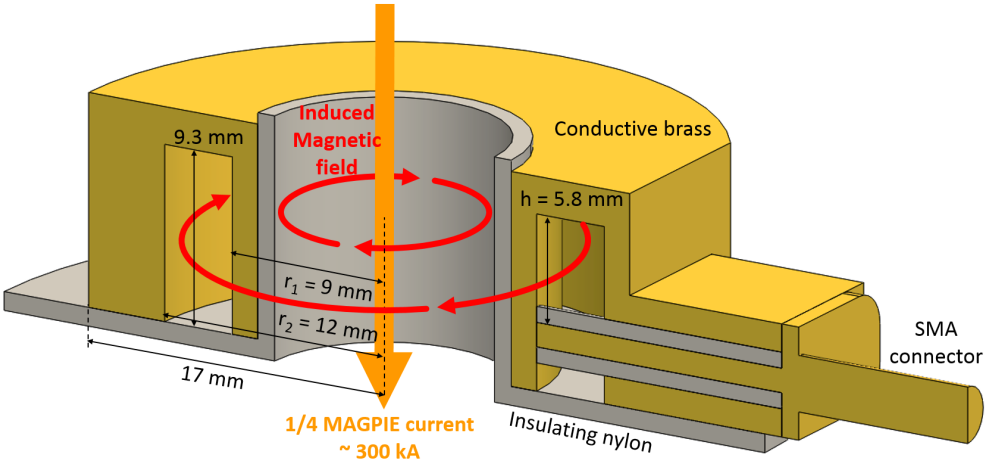


Figure 3.19: Cutaway of the Rogowski probes used on the MAGPIE facility. Axial current, indicated in orange, generates a toroidal magnetic field inside the Rogowski groove, indicated in red. This induces a voltage on the SMA cable.

A change in current through the axial conductor results in a change in magnetic field threading the Rogowski groove. This results in an induced voltage around the conductive loop which can be recorded by connecting the SMA cable to an oscilloscope. The toroidal magnetic field, B, created by the central conductor is given as a function of radius, r, is given by Eq. 3.7. For a groove of depth h, inner radius r_1 and outer radius r_2 the magnetic flux, Φ, is therefore given as:

$$\Phi(t) = \int \mathbf{B}(t).d\mathbf{A} = \int_0^h \int_{r_1}^{r_2} \frac{\mu_0 I(t)}{2\pi r} dr dz \tag{3.52}$$

which yields:

$$\Phi(t) = \frac{\mu_0 I(t)}{2\pi} h \int_{r_1}^{r_2} \frac{1}{r} dr = \frac{\mu_0 I(t) h}{2\pi} ln\left(\frac{r_2}{r_1}\right) \tag{3.53}$$

Using Faraday's law, Eq. 3.14, for the induced voltage around the loop of the Rogowski probe yields:

$$V(t) = -\frac{\partial \Phi(t)}{\partial t} = -\frac{\mu_0 h}{2\pi} ln\left(\frac{r_2}{r_1}\right) \frac{\partial I(t)}{\partial t} \tag{3.54}$$

where the number of coil turns is set to one, $N = 1$, and the electrostatic component has been ignored. Rearranging for the current at time, $I(t)$, yields:

$$I(t) = -\frac{2\pi}{\mu_0 h ln\left(r_2/r_1\right)} \int_0^t V(\tau) d\tau \tag{3.55}$$

The two Rogowski probes used on the MAGPIE facility have an inner radius of $r_1 = 9$ mm, outer radius of $r_2 = 12$ mm and groove depth of $h = 5.8$ mm so that the final current may be given as:

$$I(t) = -3 \times 10^9 \int_0^t V(\tau) d\tau \tag{3.56}$$

The voltage recorded by the oscilloscope, $V_{scope}(t)$, is further attenuated by $A_{scope} = 100$. In addition, the Rogowski only measures current passing through the conductor on it's axis and so, assuming current is even distributed between the return posts, this must be multiplied by the number of return posts, $N_{posts} = 4$. Therefore:

$$I(t) = -2.3 \times 10^9 A_{scope} N_{posts} \int_0^t V_{scope}(\tau) d\tau \tag{3.57}$$

A typical Rogowski signal, from experiment s1212_16, is shown in Fig 3.20.a. This signal has both a positive and negative peak, indicating a rising and falling current i.e. a single current pulse. The two signals are inverted, as one probe is placed upside down so that the signals could be later subtracted and the electrostatic component removed.

Performing the integration in Eq. 3.57 for each probe independently yields the current as a function of time, shown in Fig 3.20.b. The two Rogowskis predict a peak current of 0.85 to 1.63 MA at 1750 ns. Averaging these two signals, to remove the electrostatic component, yields an current of ∼1.24 MA. The current rarely returns to zero due to errors accumulated

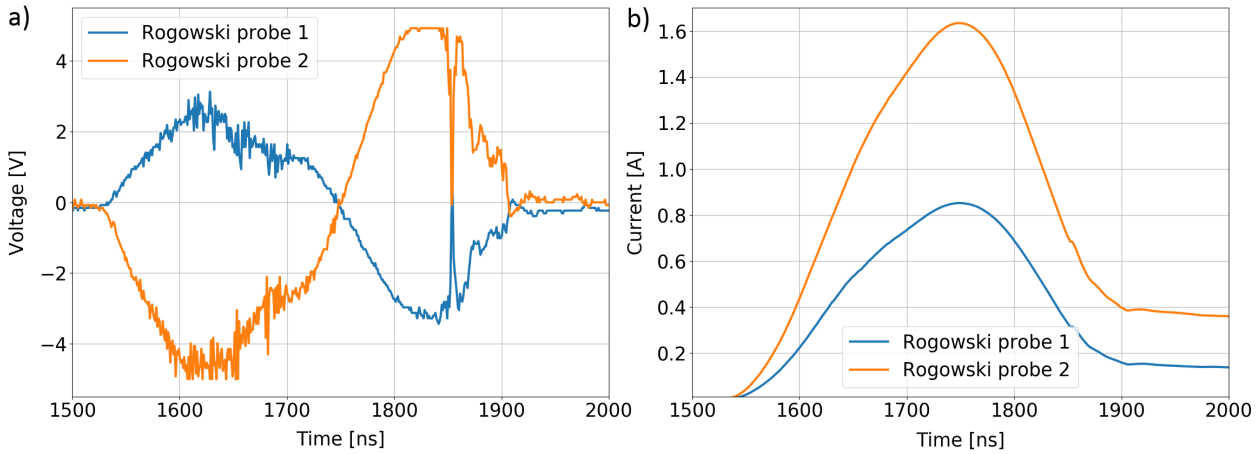


Figure 3.20: a) Voltage recorded from Rogowski proves on experiment s1212_16. b) Current as a function of time for experiment s1212_16 determined from Rogowski probes.

from integrating the noisy Rogowski signals. After peak current, when the voltage across the load reverses, electric breakdown can occur across the MAGPIE diode stack which may be the cause of the spike seen at ∼1850 ns. As a result current measurements after the peak current are less reliable.

The measurements and current from the both Rogowski probes show significant variation, shown in Fig 3.20. This is thought to not a result of current being distributed asymmetrically through the load but due to electrostatic pickup and variation between experiments in Rogowski probe placement. As one of the probes is placed upside down the electrostatic noise can effectively be cancelled out by averaging the current determined by each probe. However, this still results in significant uncertainty in the measured current.

Instead the current was measured with the four magnetic induction probes located inside the MITL, as shown in Fig 3.18. These were not modified between experiment and so offer a more reliable reading of the current passing through the load. These probes operate in a similar way to the Rogowski probes, but consist of a single loop and no Rogowski groove, and so the voltage recorded is also proportional to the current differential. Example signals, from experiment s1212_16, are shown in Fig 3.21.a. In several experiments, signals were not recorded from one or two of the probes (this could be due to several faults, such as a poor connection to the oscilloscope). When this was the case, these probes were excluded from

the following analysis.

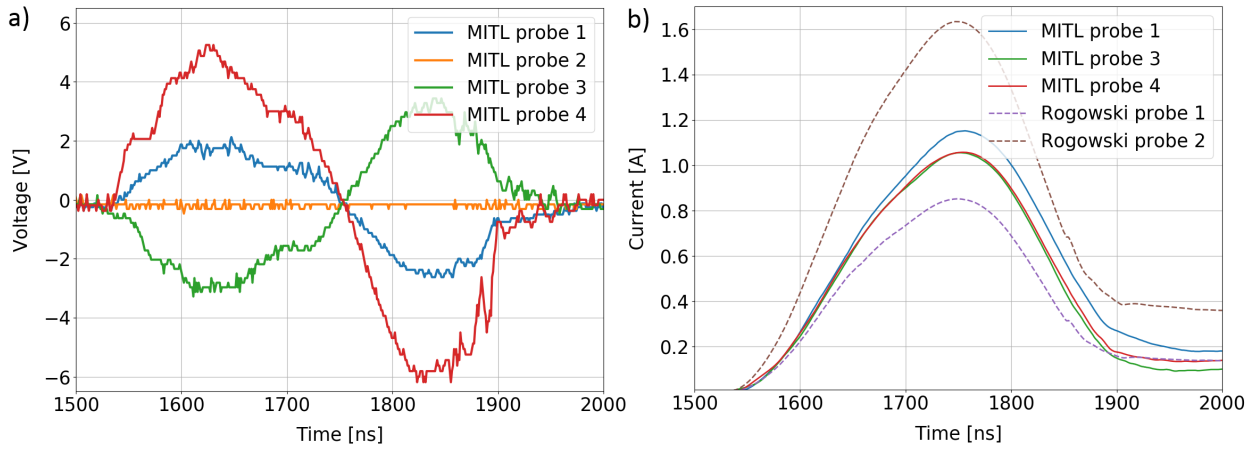


Figure 3.21: a) Voltage recorded from magnetic induction probes located inside the MITL on experiment s1212_16. In this, and several other experiments, no voltage was recorded on probe 2 and so it was excluded from further analysis. b) Current as a function of time for experiment s1212_16, estimated from MITL and Rogowski probes.

However, the sensitivity of these probes was unknown and could not be determined geometrically as the probes are partially shielded by virtue of their location. Instead, measurements from Rogowski probes, from many experiments to compensate for any variation between experiments, were used to calibrate these probes. The maximum voltage was measured from MITL probes for each experiment, averaged over 40 ns to remove noise. These were then plotted against the maximum time derivative of the current, dI/dt, (the average of the two Rogowski probes multiplied by their respective attenuations). The result for MITL probe 1 is shown in Fig 3.22.

As the voltage the MITL probes measure is expected to be proportional to the time derivative of the current, a linear trend line intercepting the origin was fitted to these points, as indicated with the dotted line in Fig 3.22. The gradient of this trend-line is the scale factor that the MITL probe must be multiplied by to obtain the current. The resulting current determined by these probes for experiment s1212_16 is shown in Fig 3.21, which yields a peak current of 1.09 ± 0.04 MA.

A Python script was written to automatically analyse the signals from the magnetic

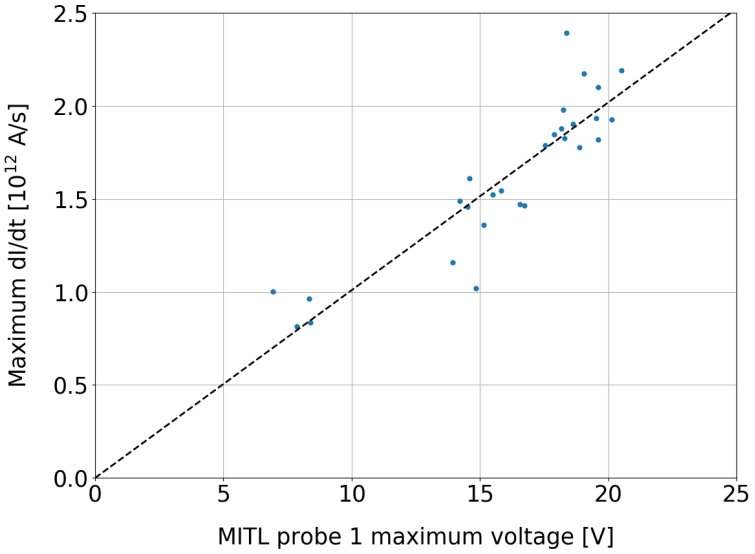


Figure 3.22: Maximum of the time derivative of the current, measured with Rogowski probes, plotted against the maximum voltage recorded by the MITL probe 1.

induction probes. Firstly any offset in the data was removed by subtracting the mean of the noise preceding the MAGPIE signal (selected to be the first 1000 points). In addition, the noise maximum and noise range (difference between minimum and maximum) were calculated from these points.

To determine the current start, the script iterated through the points until the signal consistently exceeded the noise maximum for 100 points (arbitrarily selected). The current start for an experiment was then obtained by averaging the current start for each magnetic induction and Rogowski probe. This yielded values which systematically agreed with visually selected current starts, yielding 1534 ± 4 ns for the example shown in Fig 3.21.

In addition, maximum current, time of peak current and full-width-half-maximum were determined from the current estimates from each magnetic induction and Rogowski probe. Averaging these (barring the less reliable Rogowski probe maximum current estimates) yielded the current parameters shown in Table 3.2 for experiment s1212_16, with the error being the standard deviation of each measurement.

Current start	1534 ± 4 ns
Maximum current	1088 ± 45 kA
Time of peak current	1752 ± 3 ns
Full-width-half-maximum	207 ± 3 ns

Table 3.2: Current parameters determined for experiment s1212_16.

3.3.2 B-dot probes

Similar to the magnetic induction coils used to measure the MAGPIE current, induction probes were used to measure the local magnetic field. These simple probes have the advantage of making time dependent, spatially resolved measurements. However, they can physically disrupt the plasma, resulting in a local environment which may not well represent the unperturbed plasma. A typical design is to have the probe consist of two counter-wound coils. A circuit diagram of such a probe is shown in Fig 3.23.a. As described in Section 3.3.1, the magnetic field will induce a voltage $V_{a-probe}$ in the first coil and a voltage $-V_{b-probe}$ in the oppositely wound coil. The time differential of the magnetic field may then be calculated by subtracting these two voltages, as shown in Eq. 3.50, and the electric field calculated by summing these two voltages, as shown in Eq. 3.51. However, this method can suffer from systematic errors if the coils do not have exactly the same area or are at slight angles to one another. In addition, spacial separation of the coils can limit the spacial resolution of this diagnostic.

The author developed high precision, counter-wound magnetic induction probes capable of making measurements with a spatial resolution of $\sim$0.5 mm. An annotated photo of the probe is shown in Fig 3.23.b. These probes were inspired by the three axis probes produced by Everson et al. [Everson et al., 2009]. However, these probes were designed with a minimal profile, so as to reduce perturbations to the plasma, and so measured magnetic field in a single axis. Unlike the Everson probes, subtraction of the signals was not performed by the device and instead two signals were recorded which allowed the electrostatic field component to also be measured and so helped to remove uncertainty in the device. The tip of the probe

consisted of two counter-wound wire loops with a diameter of 0.5 mm, setting the spatial resolution. The time resolution of these probes is limited either by the signal crossing time, < 0.1 ns, or, in the case of a plasma flow, the crossing time.

Loops were made from enameled copper wire, with a thickness of 68 μm, and the distance between the two loops was < 0.1 mm so as to have minimal impact on the spatial resolution. To reduce the sensitivity to electrostatic fields and protect the probe, the tip of the probe was silver painted. A 30 mm long aluminium tube, with an outer diameter of 1 mm, shielded wires from the probe tip. Within this tube the wires were braided so as to minimise the cross-sectional area away from the probe tip to prevent an inducing additional voltage. A steel box shielded the wires from inducing additional voltages when connecting to SMA connectors.

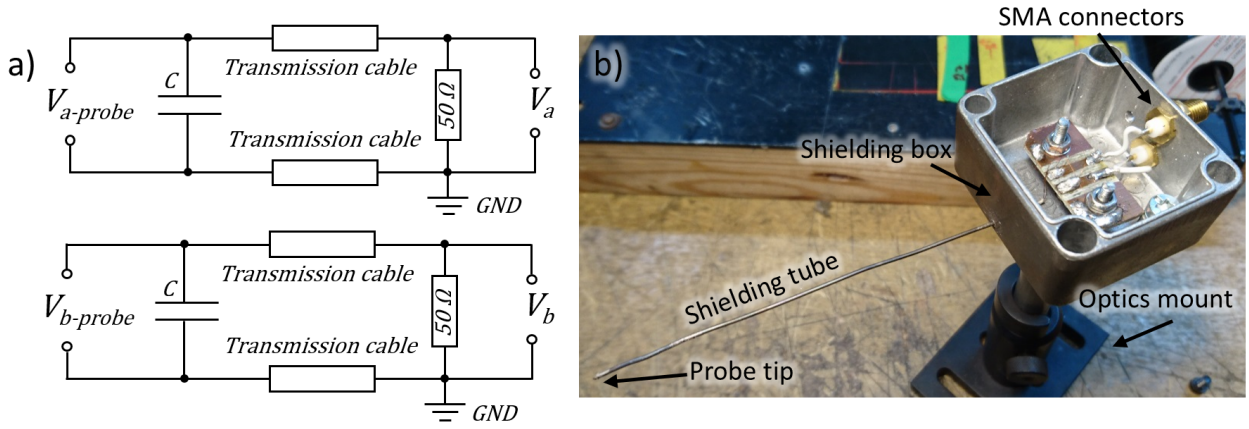


Figure 3.23: a) Circuit diagram of a counter-wound magnetic induction probe. b) Picture of the high precision counter-wound magnetic induction probes developed for the MAGPIE facility.

However, these probes did not provide reliable signals when placed inside the gas cell. Strong capacitative coupling between the probe and gas cell resulted in signals from these probes being dominated by an electrostatic component during the MAGPIE current pulse. As a result, a new type of probe know as a 'bipolar magnetic inductance probe', shown in Fig 3.24, was developed based on discussions with Dr. George Swadling. These probes consisted of a single coax wire. The tip of the probe is formed by removing a portion of

the outer ground shielding and bending the exposed inner to produce a loop. The ground shielding of both ends of the wire is fused directly behind the loop. The voltage on both ends of the wire are then recorded on an oscilloscope. These probes operate in a similar manner to counter-wound probes and the magnetic field is determined by subtracting two recorded voltages. However, these probes have two major advantages. Firstly, the current measurement is made from a single loop, removing systematic errors due to variation in the loop size in a counter-wound probe. Secondly, these probes were found to have a negligible electrostatic component, allowing them to be used within the gas-cell.

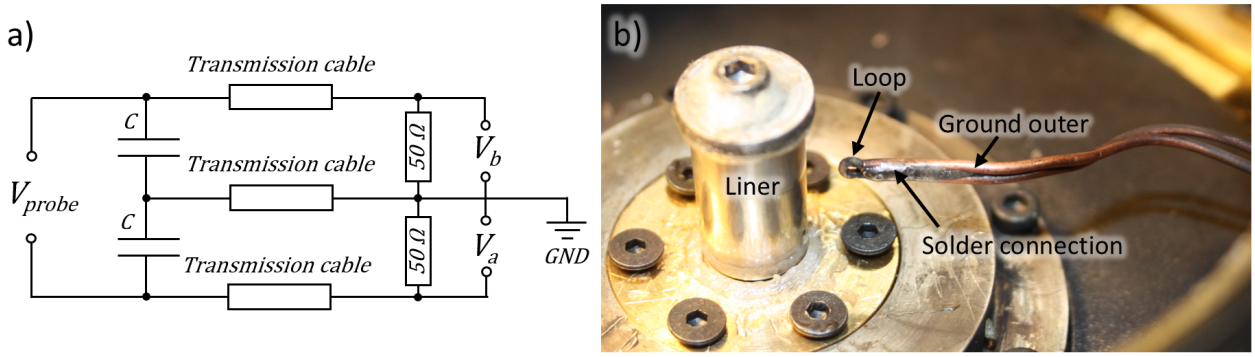


Figure 3.24: a) Circuit diagram of a bipolar magnetic induction probe. b) Picture of the bipolar magnetic induction probes developed for the MAGPIE facility.

3.3.3 Multiframe optical self-emission camera

A fast multiframe camera (Invisible Vision U2V1224) recorded optical self-emission from the plasmas and shocks, allowing the evolution of the shocks to be studied. This multiframe camera was capable of recording twelve separate images, with a minimum exposure time of 5 ns for each frame.

The camera was fielded on the same line of sight as the laser interferometer and optical spectrometer, with an image plane at the chamber centre. A low pass filter was inserted in front of this camera to block the laser light and so this diagnostic was sensitive to wavelengths > 600 nm. A two lens system with focal lengths $f_A = 750$ mm or 1000 mm and $f_B = 1000$ mm or 750 mm, labelled as 'Lens A' and 'Lens B' respectively in Fig 3.17, were used to

achieve a magnification of ×0.75 or ×1.33. Example images are shown in Fig 3.25 and are studied in detail Section 3.4.

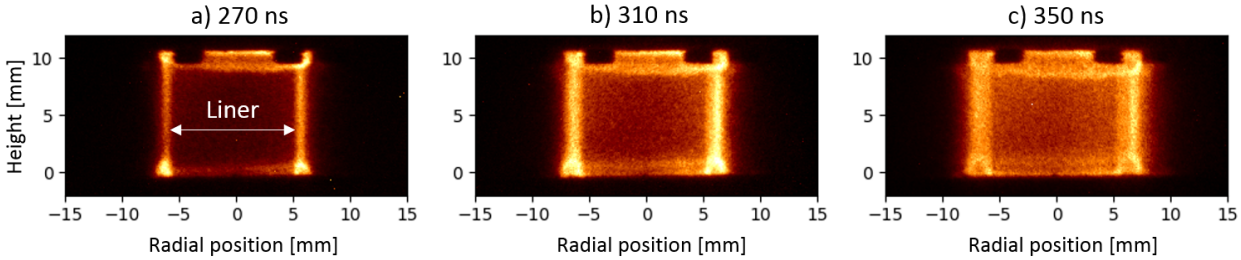


Figure 3.25: Optical self-emission from experiment s0623_16 was recorded using a fast multiframe camera, with an exposure time of 10 ns. The liner is located in the centre, labelled in (a), and the shock propagates radially outwards.

Prior to firing a experiment, preshot images were recorded with a longer exposure of 1.3 ms and backlit by a torch. An example preshot image is shown in Fig 3.26.a. These were used to calculate the scale of the image for aligning the individual images of the multiframe camera which were slightly misaligned relative to one another.

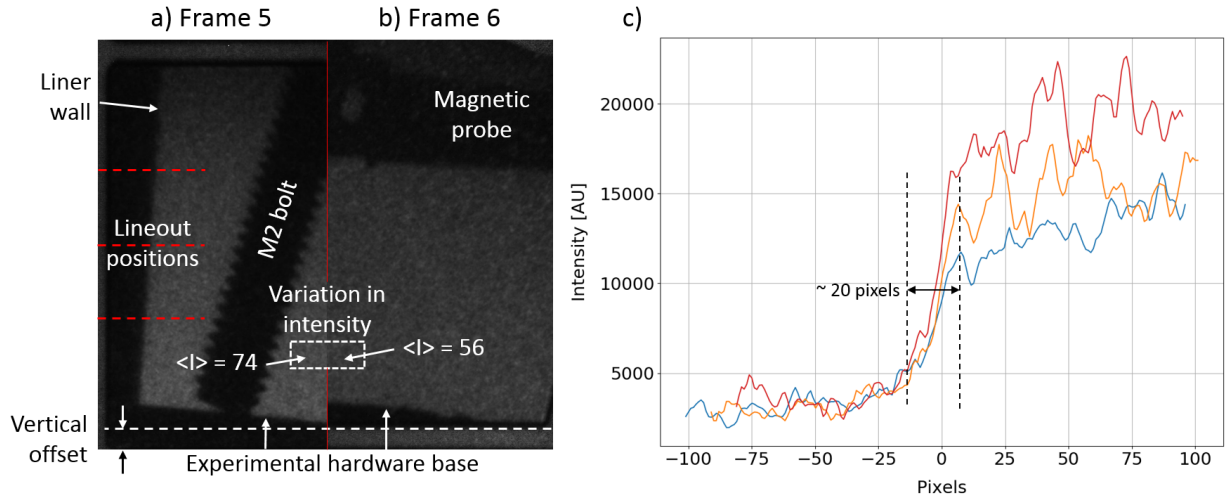


Figure 3.26: a-b) Preshot images of an M2 bolt in the focal plane of the multiframe camera. Half of each image is shown, divided along the red solid line, to allow for each comparison. Each image is offset differently and has slight variations in background intensity. c) A lineouts across the liner surface produce a 'step function', the width of which implies the minimum resolution at which features can be resolved.

To align these images they were initially rotated until the liner wall (labelled in Fig 3.26.a)

was vertical. This rotation was found to be constant between each image. To determine relative offsets initially common points on each image were visually selected. However, this was found to produce erroneous results due to slight misalignments.

In order to produce a systematic and consistent alignment procedure, a Python script was written to automatically align the rotated images using the sharp edge of the liner and experimental hardware, labelled on the bottom of Fig 3.26.a-b. For each image this script produced horizontal lineouts, averaged over the entire height of the image, and vertical lineouts, averaged over the entire width of the image. The edge of the liner and hardware were evident as steep edges in the lineouts and by identifying their position the relative offsets could be determined. This edge was identified by calculating the gradient of each pixel, defined as the value of pixel to the left minus the value of the pixel to the right. To avoid erroneous measurements due to noisy data, these values were averaged over 30 pixels. The pixel with the largest gradient was identified as the common point on each image. This method effectively minimised the effect of spikes in the noisy data and aligned images more reliably than by visually selecting points.

These preshot images also displayed slight variations in overall intensity. Therefore a Python script was used to calculated the average intensity for each preshot image to normalize images taken during the experiment.

An M2 bolt, with a diameter of 2 mm and pitch of 0.4 mm, was placed in the focal plane of the camera, labelled in Fig 3.26.a, in order to calculate the images scale. This indicated that each pixel corresponds to $\sim$11 μm. However the actual resolution at which features can be resolved is significantly coarser. The maximum resolution was determined by measuring the width of a step function in intensity, i.e. the edge of the liner. Several lineouts were taken across the liner edge, plotted in Fig 3.26.c. The width of the step was visually approximated to be $\sim$20 pixels, corresponding with an estimated minimum resolution of $\sim$250 μm.

With exposures of 10 ns a degree of motion blur is expected in these self-emission images. At typical shock velocities of $\sim$10 km/s (derived in Section 3.4.1) the shock will propagate

$\sim$100 μm while a single image is exposed. This level of motion blur is bellow the minimum resolution of $\sim$250 μm and thus is not expected to have significant impact on any conclusions drawn from these images.

3.3.4 Laser interferometry

The MAGPIE facility uses a Mach Zehnder style optical laser interferometer, the theory of which is described in Section 2.2.3. A schematic of the interferometer is shown in Fig 3.17. The second and third harmonics of an SBS compressed, pulsed Nd-YAG laser (EKSPLA SL321P) were used to produce two $\sim$0.5 ps pulse with a wavelength of 532 nm and 355 nm respectively. The path of the 355 nm pulse is longer so that the beam is delayed by a further 20 ns, allowing the plasma to be probed at two different times. While useful for experiments which evolve on shorter time scales, for this series of experiments these two frames are approximately coincidental. Both pulses are spatially combined at a dichroic beamsplitter before entering the Mach-Zehnder system and so image an identical region of plasma.

The laser is separated into a probe and reference beam, both with similar path lengths. The probe beam passes through the plasma picking up a variation in phase. While the reference beam passes through freespace above the chamber. Recombining these two beams allows for constructive and destructive interference, due to the variation in beam phase, to produce a 2-D series of fringes known as an interference pattern, as described in Section 2.2.3.

After the probe and reference beam lines are recombined, the 532 nm and 355 nm pulses are separated using a dichromatic beamsplitter and focused onto two separate commercial Canon DSLR cameras. Neutral density filters were placed in front of the cameras to prevent over-saturation. To make the camera sensitive to the 355 nm beam the internal UV filter was removed, which resulted in 355 nm appearing yellow. To achieve optimal contrast between fringes the probe and reference beam require similar intensities. This was achieved with neutral density filters and visually comparing intensities recorded by the cameras. The laser

is significantly brighter than the plasma self-emission integrated over the entire experiment and so the cameras had an exposure much greater than the experiment duration, with the image being time gated by the 0.5 ns laser pulse.

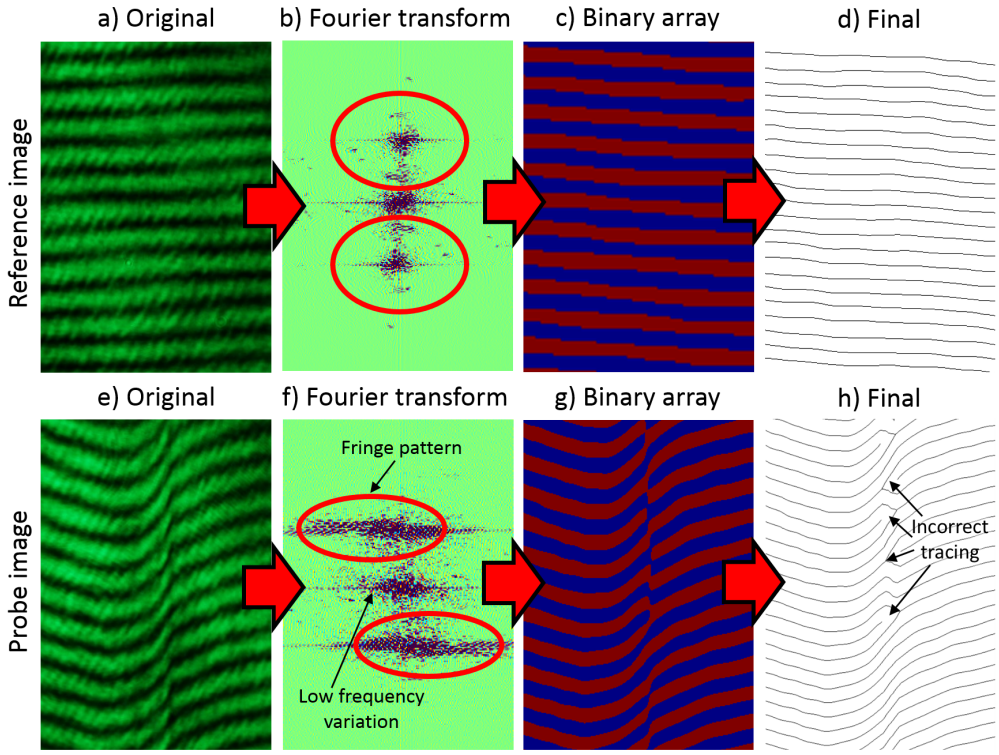


Figure 3.27: Example of the automated fringe tracing algorithm. a-d) Regularly spaced fringes, such as reference images are correctly traced. e-h) Traces of complex fringe geometry, such as shock fronts, requires manual corrections.

Interferometry images were processed using the methodology described in Section 2.2.3. However, instead of manually tracing the fringes in an image editing software this process was partly automated using a Matlab script developed by Ji Ming Ma. The steps this algorithm performs are shown in Fig 3.27. Firstly a 2-D fast Fourier transform is performed on the raw interferograms, as shown in Fig 3.27.b,f. An elliptical region of the Fourier map is then selected (along with it's complex conjugate) and isolated, thus removing high and low frequency noise. An inverse Fourier transform is applied to this map and it is converted to a binary array by choosing a threshold value, as shown in Fig 3.27.c,g. A thinning algorithm and a hole filling algorithm are applied to this to produce a black and white map where both

light and dark fringes have been traced, such as that shown in Fig 3.27.d,h.

This algorithm is efficient at tracing regularly separated fringes, such as those ahead of the shock or in the background image, as shown in Fig 3.27.a-d. However, it is unable to trace complex fringe geometries, such as shock fronts, as shown in Fig 3.27.e-h. These images therefore had to be manually corrected in an image editing program. In addition, a gray mask was manually added to the image, removing regions that are not of interest or could not be traced.

The analysis in this Thesis assumes a spatial error of half the distance between traced fringes. As these interferometry images were double traced, tracing both light and dark fringes, the minimum spacial resolution is therefore 1/4 of a fringe shift, corresponding to a phase shift of $\pi/2$. Likewise, the error in measured values is assumed to be a phase shift of $\pi/2$ (equivalent to $n_e L = 1.05 \times 10^{17}$ cm^{-2} for a wavelength of 532 nm).

3.3.5 Optical spectroscopy

Optical spectroscopy was fielded to measure ionization and determine the plasma temperature. Self-emission was recorded using a bundle of fourteen 100 μm diameter optical fibres, arranged in a 3.25 mm long line. A single 250 mm focal length achromatic lens was used to focus emission from fourteen collection volumes in the plasma. The lens was placed $u \sim 350$ mm from the plasma and $v \sim 880$ mm from the fibre bundle, resulting in a magnification of $v/u \sim 2.5$. Collection volumes therefore had a diameter of $\sim$250 μm and resulted in a field of view of $\sim$8.1 mm and separation of $\sim$580 μm. The collection volumes were arranged radially outwards from the liner, from $r = 5.5$ mm to $r = 13.6$ mm, and the opposite end of the fibre bundle was imaged onto a spectrometer (Andor SR500). The light was dispersed with a 300 lines/mm grating and imaged on to a CCD centred on 400 nm, imaging spectrum between $\sim$310 nm and $\sim$490 nm.

In these experiments the optical spectrometer was fielded down the same line of sight as the interferometry and multiframe cameras with the same focal plane. This allowed the

position of the collection volumes to be accurately determined by focusing a low powered laser pointer into the other end of the fibre and recording the emission on the interferometry cameras. This was performed for several fibres prior to every experiment which fielded this diagnostic. The position of all fibres could then be determined on the interferometry image by interpolating between the measured positions, yielding a map as shown in Fig 3.28.

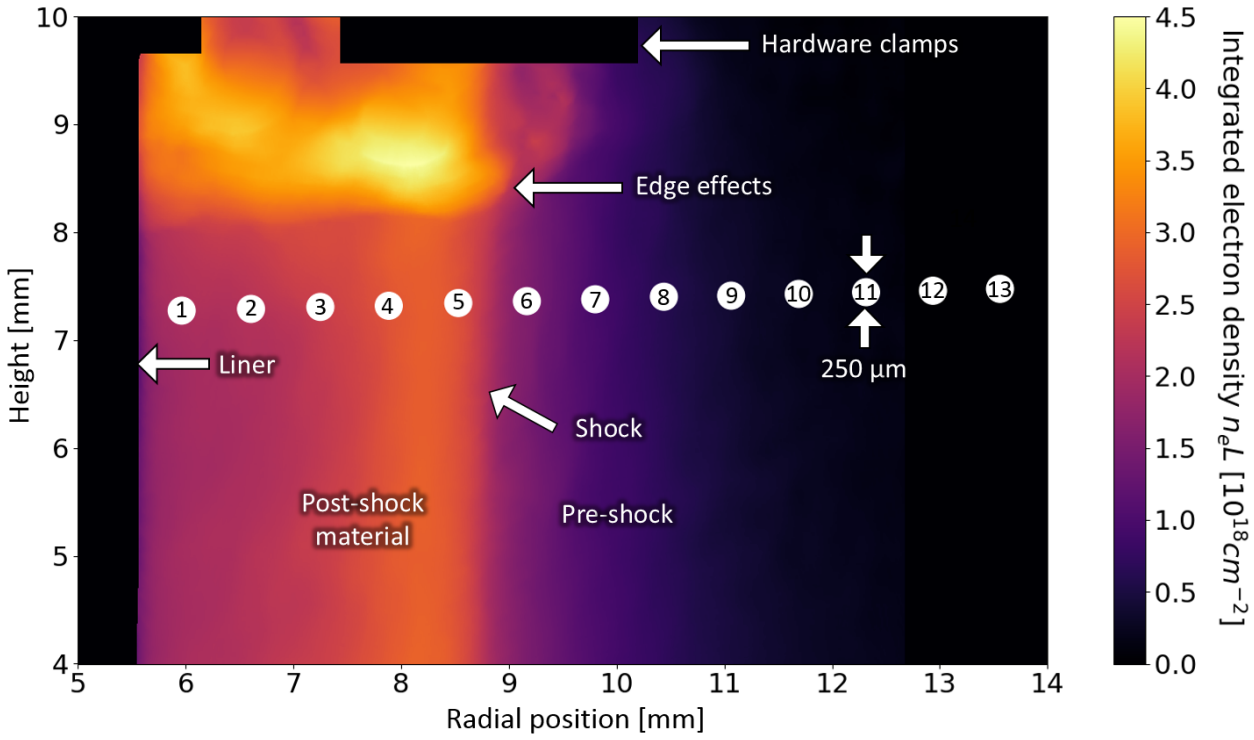


Figure 3.28: Locations of collection volumes for optical spectroscopy, drawn on top of a processed interferometry image.

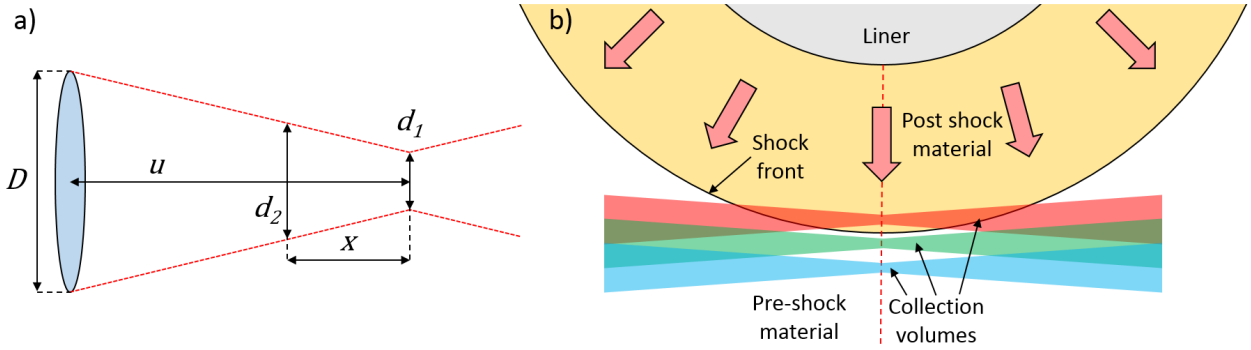


Figure 3.29: Shape of the optical spectroscopy collection volumes. a) Diagram indicating how the fibres were focused. b) Scale image of several neighbouring collection volumes.

Self-emission from a double conical region, depicted in Fig 3.29.a, will be focused onto the collection fibre and imaged by the spectrometer. Using this geometry it can be shown that over a scale length x, the diameter of this cone, d_2 is may be estimated to be:

$$d_2 = \frac{x}{u}(D - d_1) + d_1 \tag{3.58}$$

where D is the diameter of the lens and d_1 is the diameter of the focal spot. For this experimental setup $u = 350$ mm, $D = 50$ mm and $d_1 = 0.25$ mm. These experiments occur on a centermeter scales and so with $x = 10$ mm this yields $d_2 = 1.67$ mm. Three neighbouring collection volumes are shown to scale on top of a shock that has propagated 4 mm from the liner surface in Fig 3.29.b. This demonstrates how collection volumes focused behind the shock front record emission from both post-shock regions and regions ahead of the shock front while collection volumes focused ahead of the shock do not record emission from the post-shock material.

Although the spectrometer has been calibrated by Andor, this calibration was confirmed through the use of a Mercury lamp, which outputs a distinctive and well-documented spectrum. Slight rotation or offset of either the fibre bundle or any internal elements of the spectrometer could result in systematic errors to the recorded spectrum. Therefore, prior to each experiment series, the Mercury lamp was connected to the chamber facing ends of the optical fibres and its output recorded, allowing for any offset on the CCD to be measured and included in all further analysis.

3.4 Shock evolution

The experimental setup detailed in the Section 3.2 allowed cylindrically expanding radiative shocks to be launched into a gas-fill. This section investigates the shock hydrodynamics, e.g. velocity and evolution, from experiments using an Argon gas-fill at $P_0 = 24$ mbar. The initial mass density, ρ_0, may be determined using the ideal gas equation, Eq. 2.23. This yields a

mass density of $\rho_0 = 0.04$ mg/cm^3 and atom density of $n_0 \sim 6 \times 10^{17}$ cm^{-3}.

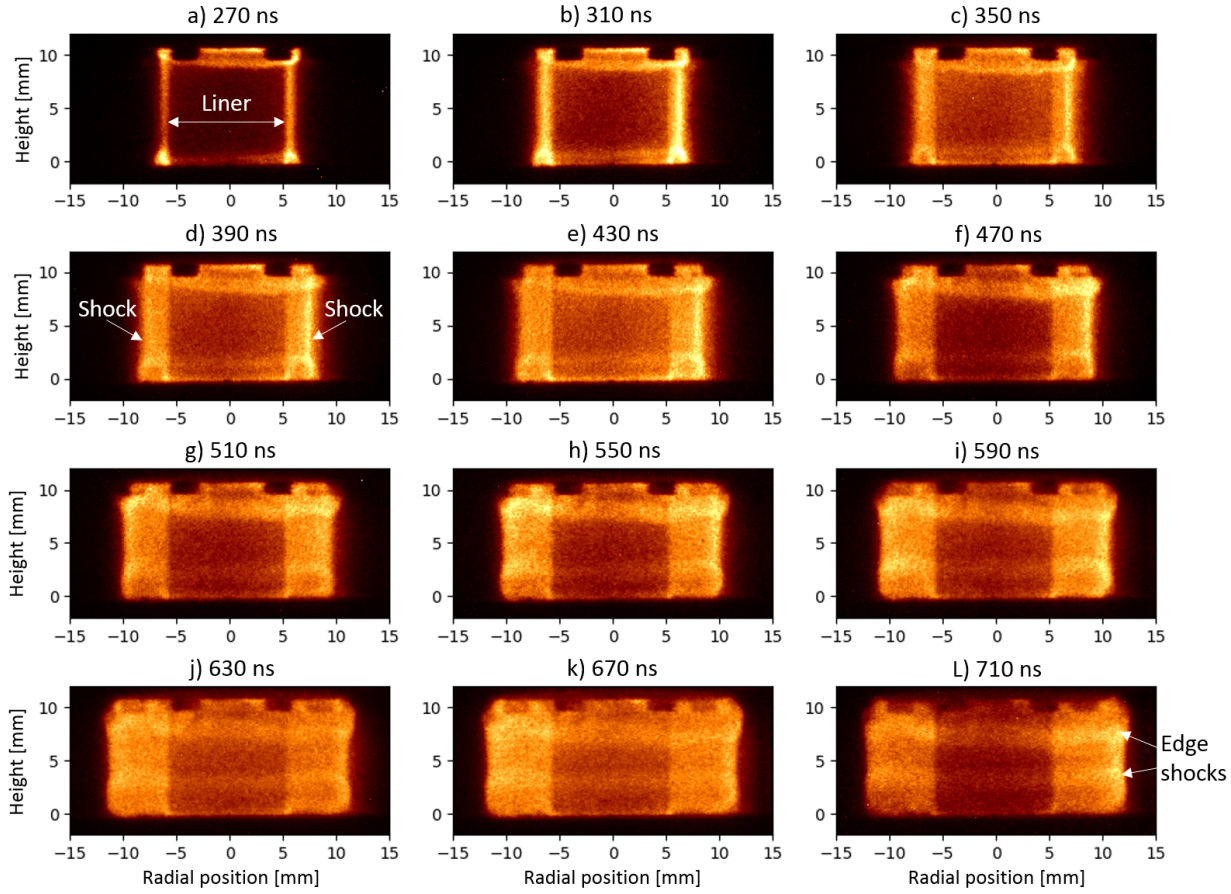


Figure 3.30: Optical self-emission images from experiment s0623_16. The times of each frame are approximate times after the start of the MAGPIE current. The liner wall is labelled in (a), and the shock propagates radially outwards, labelled in (d).

The evolution of shocks produced with this experimental platform was primarily studied by recording the optical self-emission with a multiframe camera, detailed in Section 3.3.3. A time-sequence covering 440 ns from a single experiment, s0623_16, is shown in Fig 3.30, with an inter-frame time of 40 ns and exposure of 10 ns per frame. This experiment was performed with the early experimental hardware, with a 16 mm tall liner and O-ring clamps, which reduced the exposed liner height to ∼10 mm. Brighter regions correspond to increased optical self-emission and the liner (with an outer-diameter of 11.2 mm) is visible as a dark region in the centre, labelled in Fig 3.30.a. The shock propagates radially outwards from the liner and is seen as bright emission to the left and right of the liner, labelled in Fig 3.30.d. A

resolution of ∼750 μm was measured for these images using the methodology described in Section 3.3.3.

Self-emission images in Fig 3.30 are symmetric, demonstrating that the shocks evolved with cylindrical symmetry. Therefore, to study the shock with improved resolution the multiframe camera (and other diagnostics) were focused onto a single side of the liner with a higher magnification and resolution of ∼250 μm. A time-sequence is shown in Fig 3.31 from experiment s1212_16 which used the same gas-fill, but a liner height of 20 mm and glue instead of O-ring clamps. In these images the liner surface is visible on the left on the image, labelled in Fig 3.31.a, and the shock propagates to the right, labelled in Fig 3.31.i.

The intensity of images in both Fig 3.30 and Fig 3.31 was normalised against preshot images, as discussed in Section 3.3.3, and thus variations in intensities can be compared qualitatively. The self-emission from the shock increases in intensity from the first few frames, < 270 ns, and then remains relatively constant for the remaining duration of the experiment. However, the self-emission is dependent on several plasma parameters (such as temperature and mass density) and so it is non-trivial to infer measurements of these properties from just these images.

The shock can be seen to bend slightly towards the edges of the liner, possibly due to the influence of the surrounding hardware. Thus all measurements were made from the centre of the liner. Additional shocks, labelled as 'edge shocks' in Fig 3.30.L and Fig 3.31.i, were launched from the top and base of the liner. These expand radially outwards, forming a region of enhanced emission when interacting with the primary shock. This feature varied significantly between experiments and is discussed in greater detail in Section 3.5.3.

3.4.1 Shock velocity

To determine the shock front position, horizontal profiles were taken from near the centre of the liner, at a height of $y = 8$ mm as indicated in Fig 3.31.d. Due to high levels of noise in these images, profiles were averaged over a width of 200 μm (18 pixels). Profiles

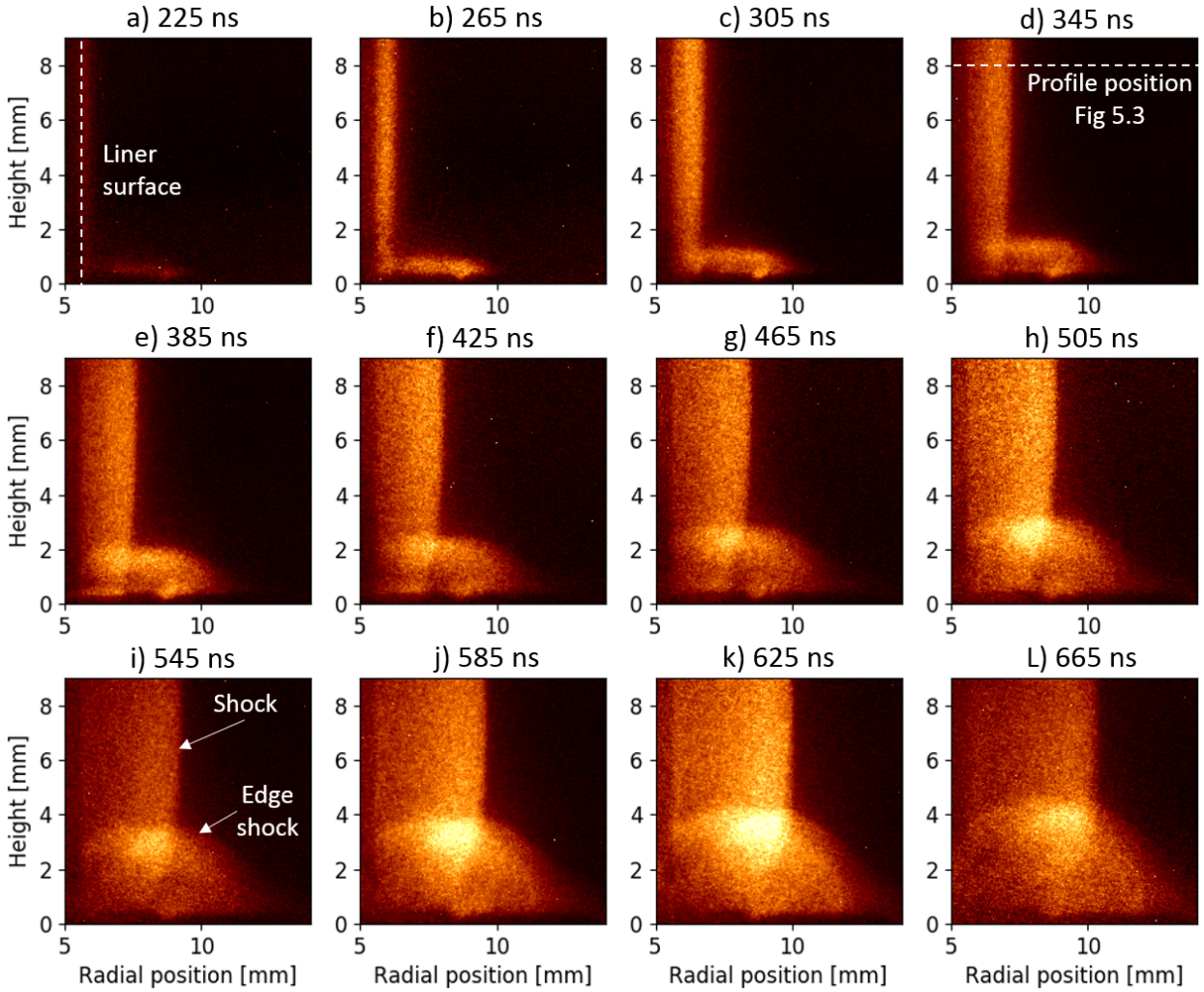


Figure 3.31: Optical self-emission images from experiment s1212_17. The liner wall is located on the left, labelled in (a), and the shock propagates to the right, labelled in (i). The times of each frame are approximate times after the start of the MAGPIE current.

from experiment s1212_16 are shown in Fig 3.32. All profiles exhibit a similar overall shape. Directly in-front of the liner a slow increase in intensity is observed followed by a rapid decrease. Ahead of the shock front the intensity does not decay entirely to zero for another few millimetres, instead decaying gradually. This is expected to be due to radiative effects, discussed in detail in Section 3.5.2, causing in material ahead of the shock front to be heated, resulting in emission of radiation.

To measure the shock velocity the approximate position of the peak in intensity from profiles was measured visually, and plotted in red in Fig 3.33.a. A linear trendline may be fit

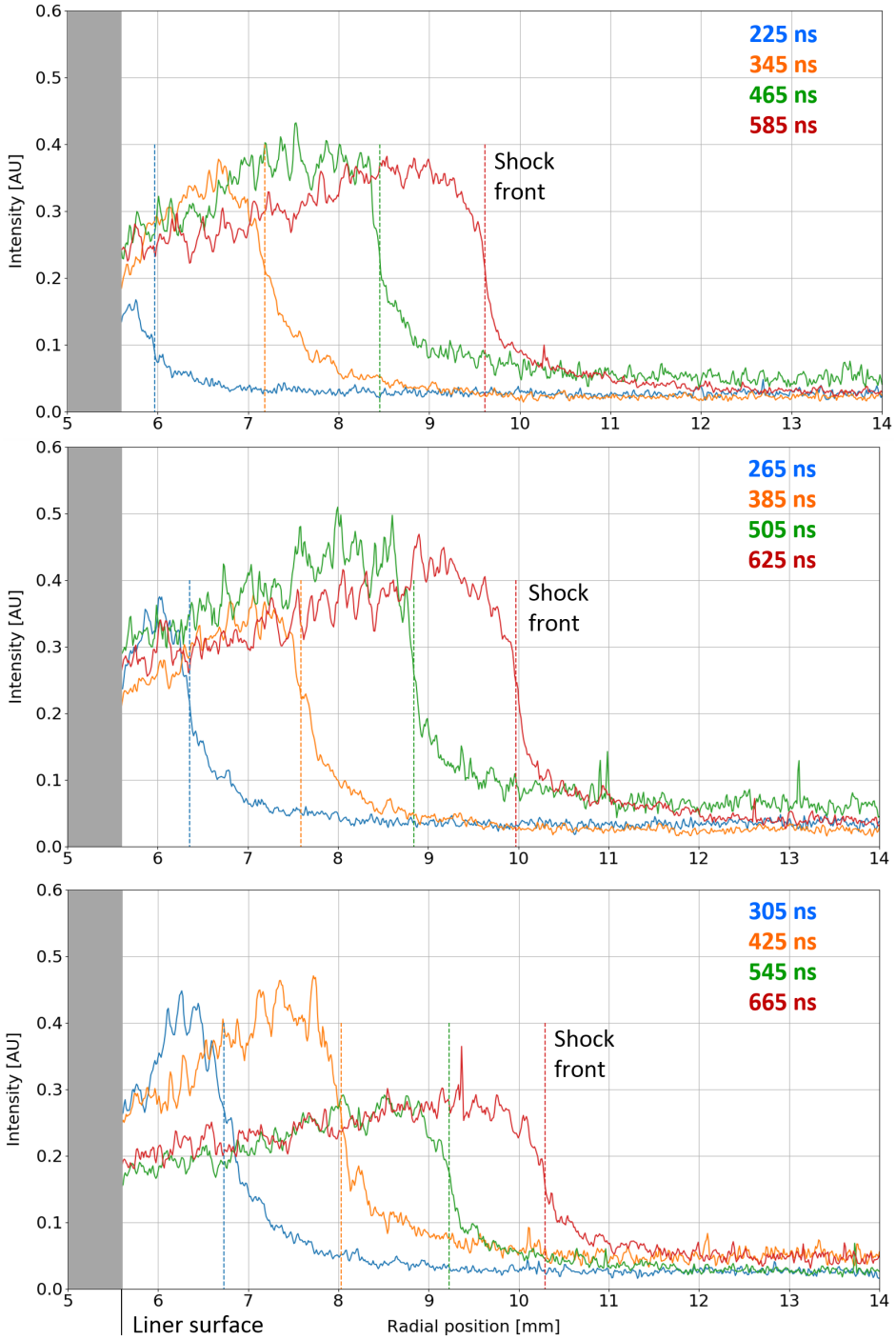


Figure 3.32: Horizontal profiles of self-emission intensity from experiment s1212_16, shown in Fig 3.31. Dashed lines indicate the shock front position measured by the Python script. The location of the profiles is indicated in Fig 3.31.d.

to these points, the gradient of which yields the shock velocity of $\sim 8.0 \pm 0.6$ km/s. However, the peak in self-emission is unlikely to correspond with the actual shock front. As the shock

is expanding cylindrically, images of regions directly behind the shock front will contain self-emission from a much thicker region of post-shock material and thus appear brighter. Therefore, the shock front position is expected to be at the rapid decrease in intensity seen in Fig 3.32, confirmed with laser interferometry in Section 3.5.

A Python script was developed to reliably, and without bias, identify the shock front position in all profiles. The script identified this region by finding the maximum gradient in a similar manner to the automatic aligning script described in Section 3.3.3. The gradient was calculated for each pixel, by subtracting the average of pixels to the right from the average of pixels to the left. Averages were taken over 30 pixels to avoid spikes in the noisy data being falsely identified as the shock front. The value of 30 pixels was selected to be above the threshold where noise spikes influence the measurements. A plot of how the measured shock front position varied with the selection of this value is shown in Fig 3.34. The measured shock position varies slightly depending on the number of pixels selected and this was used to estimate the error in shock front position to be ± 70 μm. This is smaller than the minimum resolution of the multiframe camera, defined to be ~ 250 μm in Section 3.3.3, indicating the choice in this value is of little consequence.

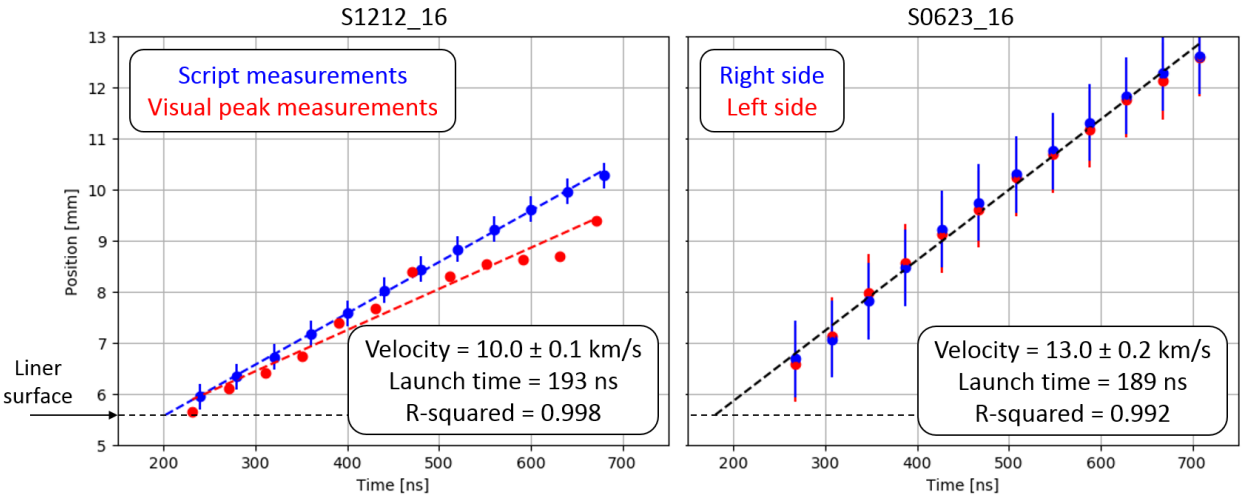


Figure 3.33: Shock front positions plotted as a function of time. Linear trendlines, shown with dashed lines, closely fit the data allowing the shock velocity and launch time to be determined. a) Experiment s1212_16, showing measured positions from the Python script and visual measurements of the peak intensity. b) Experiment s0623_16.

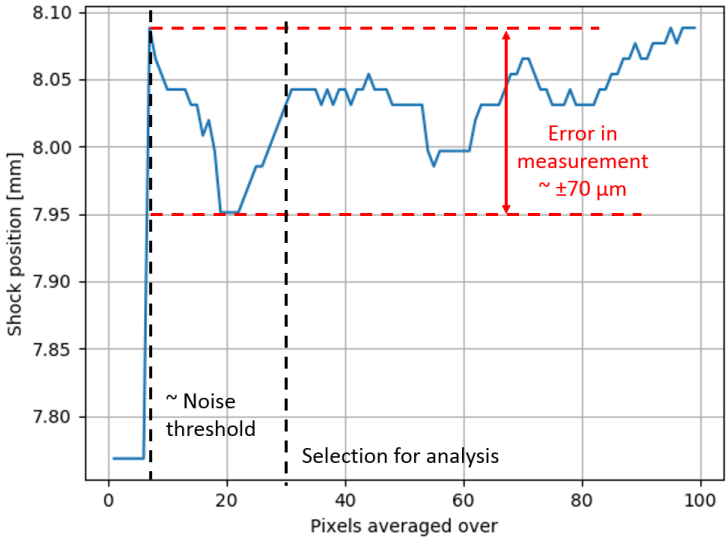


Figure 3.34: Shock front position measurements from the Python script plotted as a function of how many pixels were used to calculate averages. These measurements were made from a profile of self-emission from experiment s1212_16, taken 385 ns after current start (shown in Fig 3.31.e).

Script measured positions of the shock front were then plotted as a function of the time in Fig 3.33. These positions closely follow linear trendlines with a Pearson product-moment correlation squared (R-squared) of > 0.99. The gradient of these trendlines yields a shock velocity of 10.0 ± 0.1 km/s for experiment s1212_16, as shown in Fig 3.33.a. The close fit to the linear trend lines indicates that the shock velocity remains constant over the observed period of time and any possible change in velocity during the experiment is below the resolution of this diagnostic. For experiments where both sides of the liner were visible, the shock position could be measured twice in each frame (once on the left and right), albeit with a lower resolution. Points from both measurements were combined to derive a single shock velocity, found to be 13.0 ± 0.2 km/s for experiment s0623_16, shown in Fig 3.33.b. The error in the velocity was determined from the standard error in the gradient of these trendlines.

The Mach number of the shocks may be determined by dividing the shock velocity by the sound speed in the ambient gas-fill. Assuming an ideal gas, the sound speed, c_s is given as the product of the adiabatic index, γ, temperature, T, divided by the particle mass, $m_p A$:

$$c_s = \sqrt{\frac{\gamma k_B T}{M}} \tag{3.59}$$

where k_B is the Boltzmann constant and m_p is the proton mass. For an initial temperature of $T = 290$ K and gas-fill of Argon (with $A = 40$) and an adiabatic index of $\gamma = 5/3$ (for a monatomic gas). This yields a sounds speed, $c_s = 316$ m/s which in turn yields a Mach number of 31.6 ± 0.3 for experiment s1212_16 and 41.1 ± 0.6 for experiment s0623_16. With Mach numbers far larger than unity, this shock fulfils the strong shock criteria (described in Section 1.5.2) and the pressure of the material ahead of the shock can be assumed to have minimal impact.

The time the shock is launched after current start was determined by extrapolating the trendline back to the position of the liner surface, at $x = 5.6$ mm. This yielded a launch time of $\sim 181 \pm 10$ ns and $\sim 190 \pm 10$ ns after current start for experiment s1212_16 and experiment s0623_16 respectively. The error in this value was defined as half the difference between minimum and maximum launch times. These were found by fitting trendlines, with gradients equal to the velocity plus/minus the error in velocity measurements, and extrapolating the shock position to the liner surface.

This analysis was repeated for nine experiments with mass densities between 0.0382 mg/cm^3 and 0.0396 mg/cm^3. Despite these similar mass densities and identical liners, shock velocities were found to range from $6.9 - 13.8$ km/s and launch times ranged from $135 - 179$ ns. A variety of different noble gases (Ne, Ar, Kr, Xe) were used as gas-fills but this had no noticeable effect as long as the mass density remained consistent between experiments, as will be shown in Section 3.5.4.

This relatively wide range in shock velocities and shock launch times is possibly due to the high variability in the MAGPIE current, with peak currents ranging from 0.59 to 1.20 MA. This variation occurred for a variety of reasons such as line or dump switches firing early or late. The MAGPIE drive current was recorded through the use of up to four magnetic induction probes located in the MITL, as described in Section 3.3.1, whose signal

is proportional to the time derivative of the current. By integrating these signals the total current passing through the hardware could be determined as a function of time.

It is expected that higher MAGPIE currents would deliver more energy to the liner, resulting in an increase in shock velocity. To investigate this, the shock velocity was plotted against the peak MAGPIE current, shown in Fig 3.35.a. A positive trend is visible indicating that increased currents do result in faster shock velocities. A similar analysis was performed for the shock launch time, plotted against the peak MAGPIE current in Fig 3.35.b. No conclusive trend is evident, however if s1215_16 is an outlier then the remaining points may be represented by a negative trend. This analysis suggests that additional factors (possibly also related to the MAGPIE drive current) are primarily responsible for the variation in shock launch time.

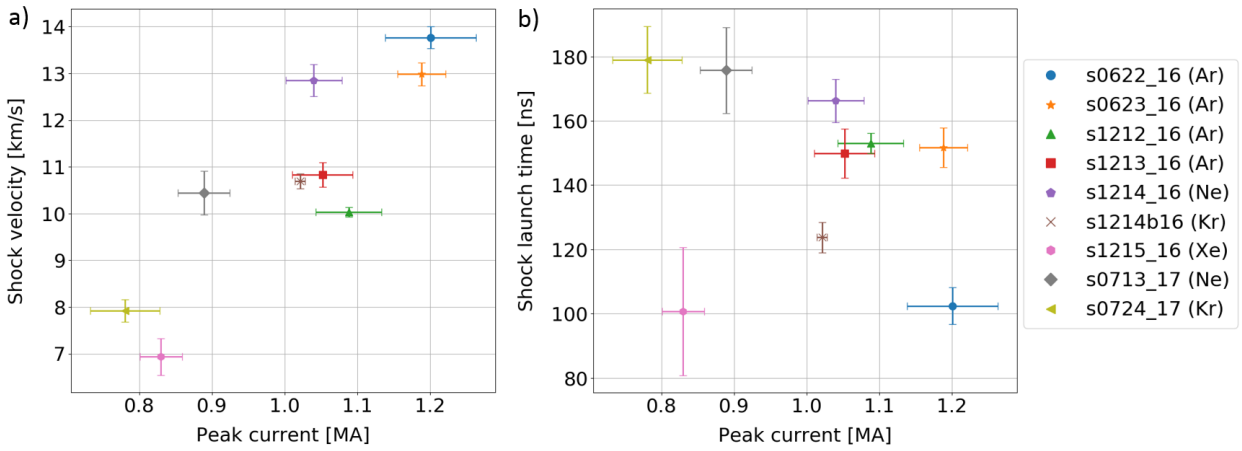


Figure 3.35: a) Shock velocity plotted as a function of peak MAGPIE current for nine experiments with a similar mass density between 0.0382 to 0.0396 mg/cm^{-3}. b) Shock launch time plotted as a function of peak MAGPIE current for the same set of experiments.

3.4.2 Shock launch mechanism

Previous experiments on radially converging shocks launched from liners (described in Section 1.7.2) observed multiple shocks being launched by two different mechanisms [Burdiak et al., 2015]. The first shock was mechanically driven and launched due to the magnetic pressure exceeding the yield strength of the liner material, resulting in spalling. The second shock

was magnetically driven and launched by melting of the liner. This causing its resistance to increase, allowing the magnetic field to diffuse through the liner wall and the current to switch to the gas. The current carrying plasma could then be accelerated by inwards by the Lorentz force. However, these launch mechanism may not responsible for the shocks observed in this thesis due to the change in geometry and larger liners, with a diameter of 11 mm compared to 6 mm. In a similar manner to [Burdiak, 2012], the variability of the MAGPIE current was used to investigate these possible launch mechanisms.

Firstly, the mechanically driven shock is considered, caused by magnetic pressure exceeding the yield strength of the liner material. The magnetic pressure, P_B is given by:

$$P_B = \frac{B^2}{2\mu_0} \tag{3.60}$$

where B is the magnetic field, given by Eq. 3.7, and μ_0 is the vacuum permeability. At the liner surface, r_L, the magnetic field generated by the current, $I(t)$, results in a magnetic pressure of:

$$P_B(t) = \frac{\mu_0 I(t)^2}{8\pi^2 r_L^2} \tag{3.61}$$

Using currents measured by the MITL induction probes (described in Section 3.3.1), the magnetic pressure at the inner surface of the liners, $r_L = 5.6$ mm, was plotted as a function of time for the same nine experiments with similar mass densities and is shown in Fig 3.36.a. The time the shock is launched is plotted, showing errors in the magnetic pressure at that time. The ultimate tensile strength (UTS) for AISI 321 stainless steel is 620 MPa [ASM Aerospace Specification Metals Inc., 2017] and is indicated with a black dashed line. Errors in time are a combination of error in MAGPIE start time and shock launch time (added in quadrature). The errors in the magnetic pressure are derived from errors in the current at the minimum and maximum shock launch time.

The shock is always launched prior to the peak current and prior to the magnetic pressure

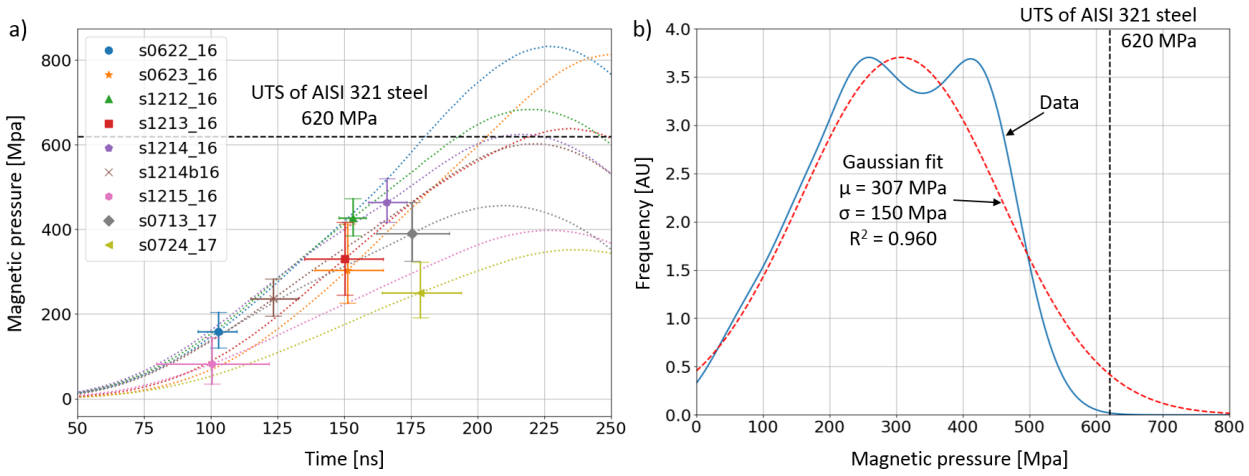


Figure 3.36: a) Magnetic pressure experienced by the liner as a function of time for nine experiments with an initial mass density of ∼0.04 mg/cm^3. The times the shocks are launched are also plotted. b) Sum of magnetic pressures at the shock launch time (modelled as Gaussian distributions) plotted with a blue line. This may be approximated with a single Gaussian distribution with a mean of 307 MPa and standard deviation of 150 MPa, plotted with a red dashed line. The ultimate tensile strength for stainless steel is plotted in both with a black dashed line.

exceeding the UTS of steel. The values of magnetic pressures at the shock launch time were modelled as a Gaussian distribution, (with σ equal to their error) and their sum is plotted in Fig 3.36.b with a blue line. This sum may be reasonably well approximated with a single Gaussian distribution found by iterating through possible mean and sigma values to find which achieved the highest correlation. The resulting fit achieved an $R^2 = 0.960$ and is plotted in Fig 3.36.b with a red dashed line. This analysis suggests that shocks are launched when the magnetic pressure experienced by the liner exceeds 307 ± 150 MPa. This value does not incorporate the UTS of stainless steel and these large errors indicate that a different process is contributing to the shocks launch time.

Secondly, the magnetically driven shock is considered, caused by melting of the liner. Previous experiments on stainless steel liners, with a smaller diameter of 6 mm, resulted in shocks driven by this mechanism [Burdiak et al., 2015]. To determine if this mechanism was responsible for launching the shocks observed in this Thesis the energy deposited in the liner, characterising by the action integral, J, was calculated, given by:

$$J = \int_0^{T_{shock}} j(t)^2 dt \tag{3.62}$$

where $j(t)$ is the current density, obtained by dividing the current, $I(t)$ by the cross sectional area of the liner, 3×10^{-4} m^2. The action integral was calculated as a function of time for the same nine experiments with similar mass density gas-fills and is shown in Fig 3.37.a. The time the shock is launched is plotted, showing errors in the action integral at that time.

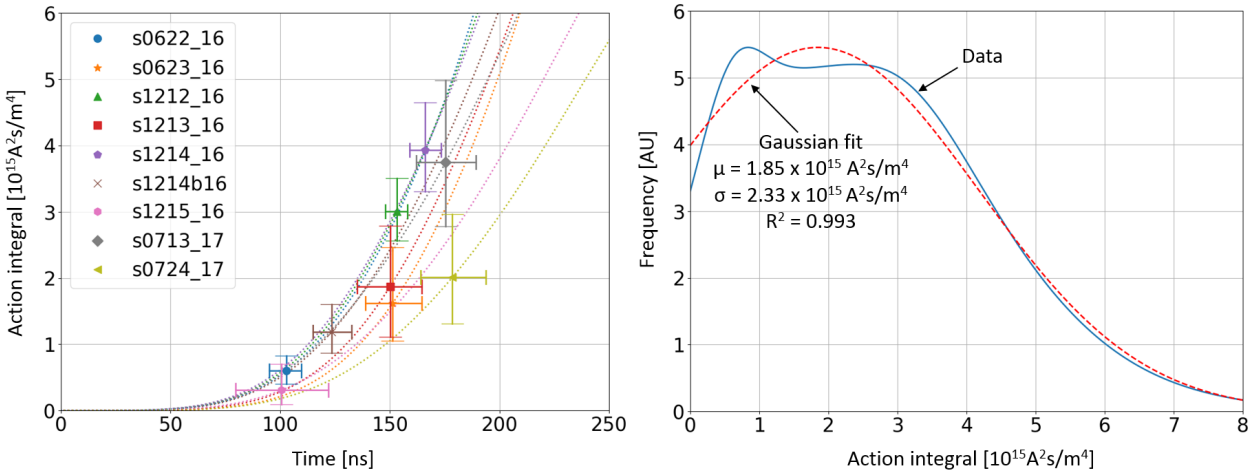


Figure 3.37: a) Action integral as a function of time for nine experiments with an initial mass density of ∼0.04 mg/cm^3 plotted with dotted lines. The times the shocks are launched are also plotted. b) Sum of action integral at the shock launch time (modelled as Gaussian distributions) plotted with a blue line. This may be approximated with a single Gaussian distribution with a mean of 1.85×10^{15} A^{2}s/m^4 and standard deviation of 2.33×10^{15} A^{2}s/m^4, plotted with a red dashed line.

Action integral values to take room temperature stainless steel to melting point were not found in the literature but similar action integrals values were found to vaporize Aluminium and stainless steel in wire explosion experiments [Chemezova et al., 1998]. This suggests that the action integral to melt stainless steel is not too dissimilar from Aluminium, $\sim 32 \times 10^{15}$ A^{2}s/m^4 [Knoepfel, 2000]. However, the measured action integrals at the shock launch times are an order of magnitude lower than this value. In addition, no signs of melting were visible in the liners after an experiment. Therefore, this mechanism is not likely to be the cause of

the shocks observed in this thesis.

A similar analysis to that performed in Fig 3.36.b was performed on this data. The action integrals at the shock launch time were modelled as a Gaussian distribution and their sum is plotted in Fig 3.37.b in blue. Fitting a single Gaussian, by iterating through possible mean and sigma values, achieved a correlation of $R^2 = 0.997$ and indicates that shocks are launched when the action integral exceeds $1.85 \pm 2.33 \times 10^{15}$ $\mathrm{A^2s/m^4}$. These very large errors suggest that a different process is responsible for the shocks launch time. The mechanism for driving these shocks is therefore not yet understood and will be the subject of future investigations.

3.4.3 Magnetisation of the shocks

A strong toroidal magnetic field of ∼40 T is expected to form inside the liner, as described in Section 3.2.2, which will quickly diffuse through the 100 μm thick liner wall. If a portion of this current flows through the hot post-shock plasma then the magnetic field will diffuse out of the liner, where it may then be advected by the shocks. To determine if this is the case, a bipolar magnetic induction probe, described in Section 3.3.2, was placed ∼5 mm radially outwards from the liners surface and midway along its height. The voltage recorded from the magnetic probe in experiment s0727_17 is shown in Fig 3.38.a along with a Rogowski signal from the same experiment. The shock is launched close to maximum voltage on both the Rogowski and Bdot probe at ∼250 ns. For the first ∼500 ns these two signals very closely follow one another, possibly due to capacitative coupling between the hardware and magnetic probe. However, after the current pulse has ended, and the Rogowski probes record zero voltage, a signal can still be seen in the magnetic probes. In particular the magnetic probes signal crosses zero at ∼800 ns, indicating a maximum in the magnetic field approximately when the shock collides with the probe.

These two signals were integrated to obtain the current and magnetic field as a function of time, using the methodology detailed in Section 3.3.2, and are plotted in Fig 3.38.b. A shorter period of time is shown in this figure as the errors in the magnetic field increase over time

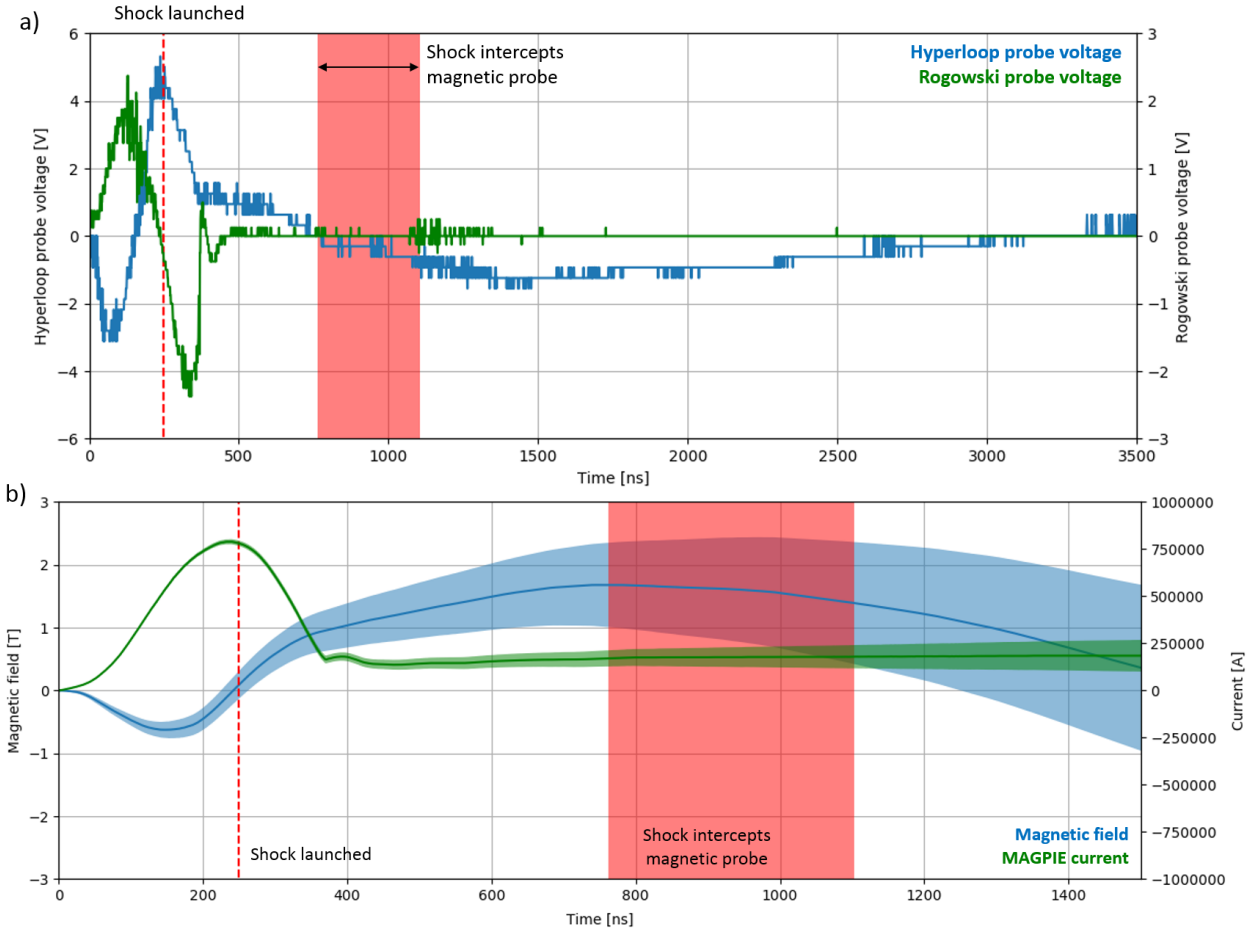


Figure 3.38: a) Voltage recorded from both the bipolar magnetic induction probes (in blue) and Rogowski current probe (in green) as functions of time after current start from experiment s0727_17. The red dotted line indicates the launch time of the shock and the region highlighted in red indicates the approximate time that the shock is in contact with the magnetic probe. b) Integrated signals showing the magnetic field (in blue) and current (in green) as a function of time after current start. The shaded blue and green regions indicate the error in these measurements.

and so result in unreliable readings. Despite these large errors, the measured magnetic field reaches a maximum of $1-2$ T when the shock collides with the magnetic probe. However, if the shock were carrying a significant current then a large dB/dt signal would be expected when the shock interacts with the magnetic probe. Therefore, it is unlikely that the hot plasma in the shock-front is carrying a current to support this magnetic field.

3.4.4 Snowplough trajectories

The shock trajectory measured for experiment s1212_17 was compared against a cylindrical snowplough model, given by Eq. 1.67. This was solved numerically with initial values corresponding with the second measurement of the shock front position from the optical self-emission camera, shown in Fig 3.33.a. This yielded a time of $t_0 = 280$ ns, radius of $r_0 = 6.35$ mm and velocity of 10 km/s. The mass of the snowplough, m, was assumed to be the total mass swept up by the shock, given by:

$$m(r) = h\pi\rho_0(r(t)^2 - r_L^2) \tag{3.63}$$

where h is the height of the shock, ρ_0 is the initial gas-fill mass density, $r_L = 5.6$ mm is the outer radius of the liner and $r(t)$ is the radius of the shock. Assuming the shock was not driven, with $F = 0$ in Eq. 1.67, yields the trajectory shown with a blue solid line in Fig 3.39. This is significantly slower than the observed trajectory and has propagated approximately half the distance by 700 ns. Therefore this indicates that either the shock is being driven, with $F > 0$, or additional mass is ablated by the liner, adding a term of m_0 to the right hand side of Eq. 3.63.

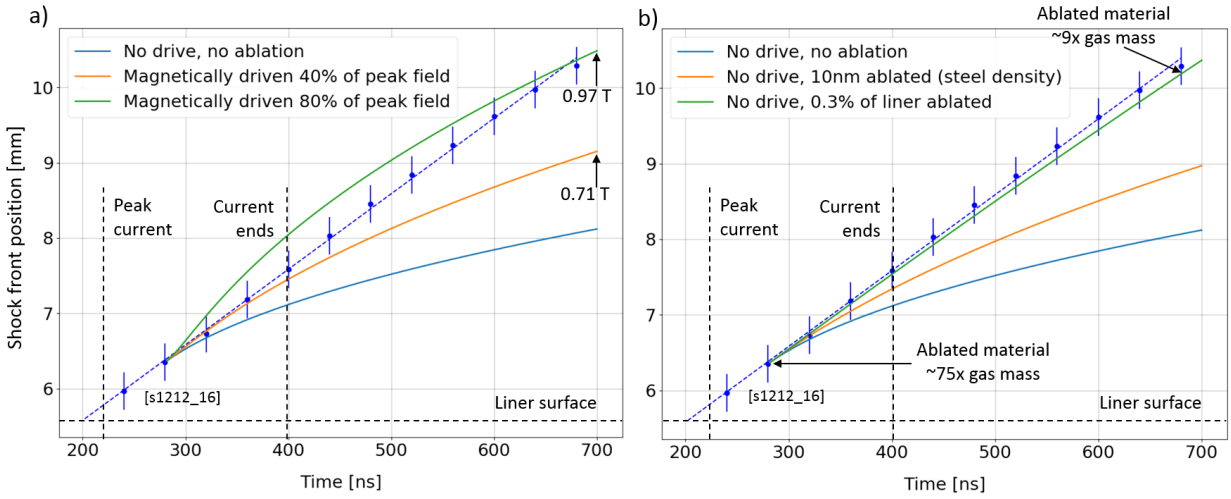


Figure 3.39: Comparison between snow-plough models and measured shock trajectories. a) For a magnetically driven shock. b) For an over-dense shock.

Firstly a magnetically driven shock is considered. The MAGPIE current pulse duration is significantly shorter than the evolution of the shock, with peak current shortly after the shock is launched and the current pulse ending shortly after, at ∼400 ns. To achieve a continual driving force it was assumed that a portion of the magnetic field generated at peak current would be frozen into the plasma, with a constant magnetic flux, Φ, This represents a current loop between the shock front and the liner surface with a magnetic flux given by:

$$\Phi = const. = \int_{r_L}^{r(t)} hr' B(r', t) dr' \tag{3.64}$$

Using Eq. 3.7 for the magnetic field, B, and integrating yields:

$$\Phi = \frac{h\mu_0 I(t)}{2\pi} ln\left(\frac{r(t)}{r_L}\right) \tag{3.65}$$

Equating this to the magnetic flux at peak current, when $r(t) = r_0$ and $I(t) = I_0$, and using Eq. 3.7 again yields an expression for the magnetic field evolution:

$$B(t) = \frac{\mu_0 I_0}{2\pi r(t)} \frac{ln(r_0/r_L)}{ln(r(t)/r_L)} \tag{3.66}$$

where I_0 is the portion of current flowing through plasma in the shock at time t_0. The force acting on the shock front may then be calculated by multiplying the magnetic pressure, given by $P_B = B^2/2\mu_0$, by the surface area of the shock front (assuming it is a cylinder of radius $r(t)$ and height h. This yields:

$$F(t) = \frac{\pi r(t) h B(t)^2}{\mu_0} \tag{3.67}$$

Inserting this expression into Eq. 1.67 and solving numerically yields the solutions shown in Fig 3.39.a. This indicates that if ∼80% of the peak magnetic field, generated by the MAGPIE current pulse, is frozen into the plasma then a similar shock position may be achieved at ∼700 ns. When the shock has propagated ∼5 mm, this magnetic field will have

dropped to ∼1 T. While this is comparable with estimates from magnetic field probes placed at this distance, no dB/dt signal was observed indicating the shock front was not carrying a current. In addition, this results in a trajectory that does not well represent the observed linear shock trajectory. This indicates that this driving mechanism does not dominate the system and the shock is not carrying a substantial current.

Secondly, an massive shock is considered, which will result in a situation more similar to the experiments performed on the Orion laser facility described in Chapter 2, where the gas fill is significantly less dense than the shock front or its piston and so offers little resistance. This was modelled by adding an additional term, m_0, to the right hand side of Eq. 3.63. This additional mass may come from contaminants blown off the outer surface of the liner. Work performed in [Cuneo et al., 1997] suggests that the surface is coated in ∼100 monolayers, ∼10 nm, of loosely bound surface contaminants (primarily H_2O, adsorbed atmospheric gases or small polymers). To discount this as a source, a layer of $d = 10$ nm of steel, with mass density $\rho = 8050$ kg/m^3, was included in the model, with a mass $m_0 = 2\pi\rho_0 r_L dh = 5.7 \times 10^{-8}$ kg. This trajectory was solved numerically and is plotted in Fig 3.39.b. This trajectory is still significantly slower than the observed trajectory and so the shocks are assumed to not be launched by contaminants on the surface of the liner. However, ablation of just $> 0.3\%$, ∼300 nm, of the liner resulted in trajectories which closely match measurements (with more ablated materials resulting in even straighter trajectories). As the liner is significantly distorted and damaged during the experiment, it was not possible to measure the post-shock liner thickness to a level of accuracy that would confirm this as a drive mechanism.

3.5 Shock structure

The structure of the shock was studied with laser interferometry imaging (the principles of which are discussed in detail in Section 2.2.3 and Section 3.3.4) which allows the electron density, a product of ion density and ionization, to be determined. A raw interferogram and

map of integrated electron density is shown in Fig 3.40, taken 405 ns after current start from experiment s1212_16, which had an Argon gas-fill with an initial mass density of $\rho_0 = 0.04$ mg/cm^3 ($P_0 = 24$ mbar). This image is from the same experiment and along the same line of sight as the self-emission images shown in Fig 3.31. However, this diagnostic offers improved resolution of ~67 μm (~1/4 of a fringe shift as both light and dark fringes were traced) instead of ~250 μm achieved with the multiframe camera.

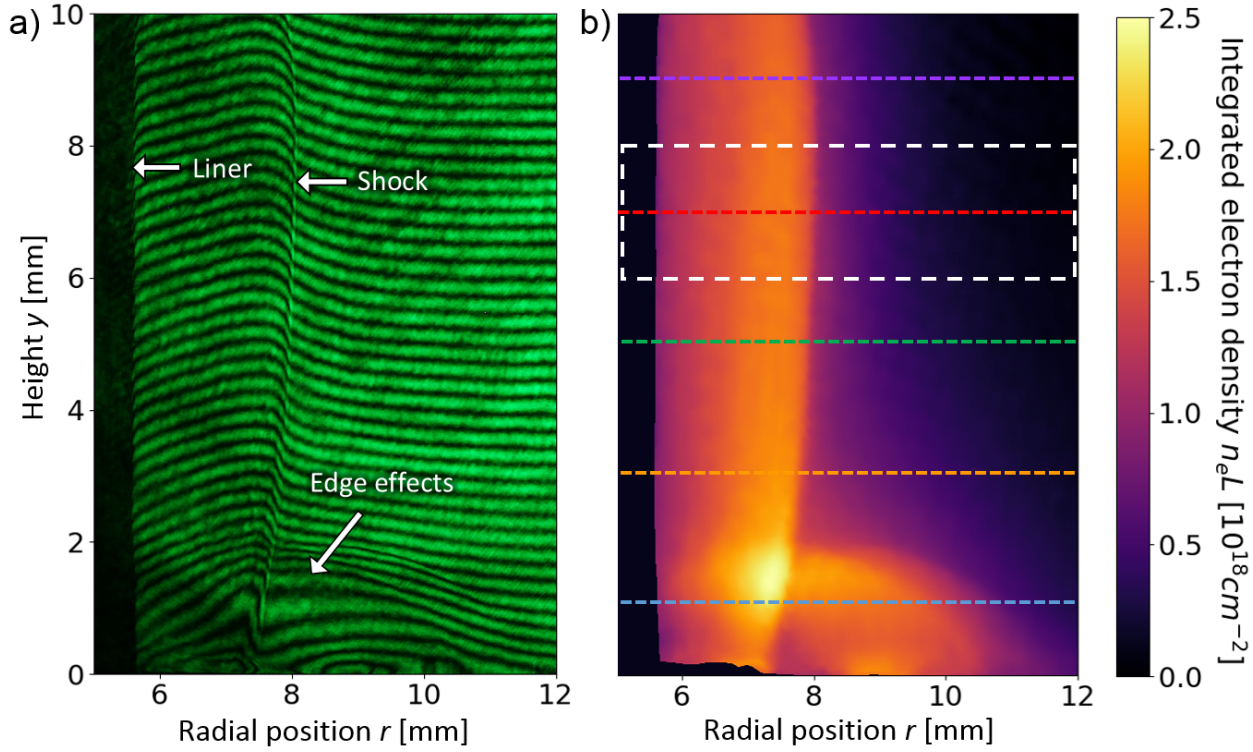


Figure 3.40: a) Interferometry image, with a wavelength of 532 nm, taken 405 ns after current start from experiment s1212_16, which had an Argon gas-fill with an initial mass density of 0.04 mg/cm^3. b) Map of integrated electron density yielded by processing the image using the methodology described in Section 2.2.3 and Section 3.3.4.

In the raw interferogram the fringes are initially horizontal and shifts in fringes indicate the presence of electrons and hence ionization. Above a height of $y \sim 2$ mm the fringe pattern shown in Fig 3.40.a is approximately uniform along the length of the liner. The fringe shift gradually increases with distance away from the liner surface, at $r = 5.6$ mm, to a maximum at $r \sim 7.5$ mm. This is followed by a rapid decrease in fringe shift at $r \sim 8.0$ mm. The fringe shift then continues to decrease gradually for a further ~3 mm. Although the fringe pattern

is uniform along most of the entire length of the liner, the formation of an 'edge shock' is visible bellow $y \sim 2$ mm, discussed in greater detail in Section 3.5.3. In addition, the pattern bends towards the edges of the liner, deviating the approximately 1-D expansion.

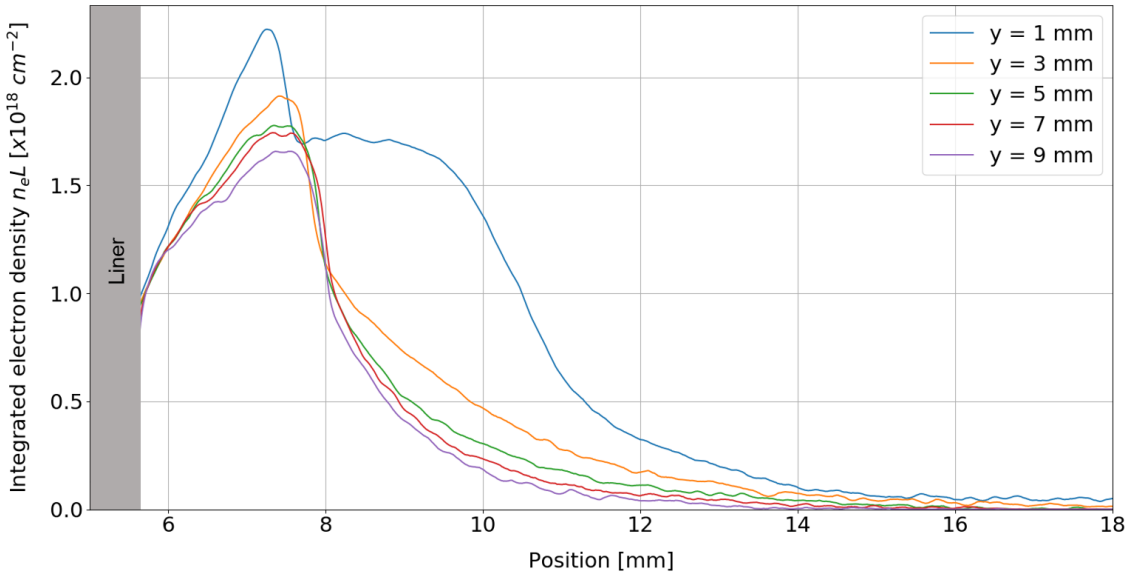


Figure 3.41: Horizontal profiles of integrated electron density from several heights along the length of the liner, locations indicated in Fig 3.40.b.

The interferometry fringe pattern was processed using the methodology described in Section 2.2.3 and Section 3.3.4. This yielded a map of electron density integrated along the path of the probe beam, n_eL, shown in Fig 3.40.b. The same structure previously described also be seen in this image as the fringe shift and integrated electron density are linearly proportional. Horizontal profiles were taken at different heights along the length of the liner, at $y = 3, 5, 7, 9$ mm. The location of these profiles are shown as dotted lines in Fig 3.40.b and the profiles are shown in Fig 3.41. Profiles at $y = 1$ mm and $y = 3$ mm showing enhanced electron density in both their peaks and in the precursor region due to interaction with the edge shock. However, near the centre of the liner ($y = 5 - 9$) mm, the shock evolves approximately 1-D with cylindrical symmetry and so this uniform region was used for analysis.

The electron density as a function of radius can be determined using an Abel inversion, as described in Section 2.2.3, with the result shown in Fig 3.42. For reference, the initial atom

density of $n_{i0} = 5.8 \times 10^{18}$ cm^{-3} is indicated with the red dashed line. This shows a similar pattern to the initial fringe shifts shown in Fig 3.40, with an increasing electron density with distance from the liners surface to a peak electron density of $\sim 2.5 \times 10^{18}$ cm^{-3} at $r = 7.95$ mm. This peak electron density corresponds with the shock front where temperatures and densities are highest. The electron density then gradually decays till reaching the noise floor at $r \sim 12$ mm.

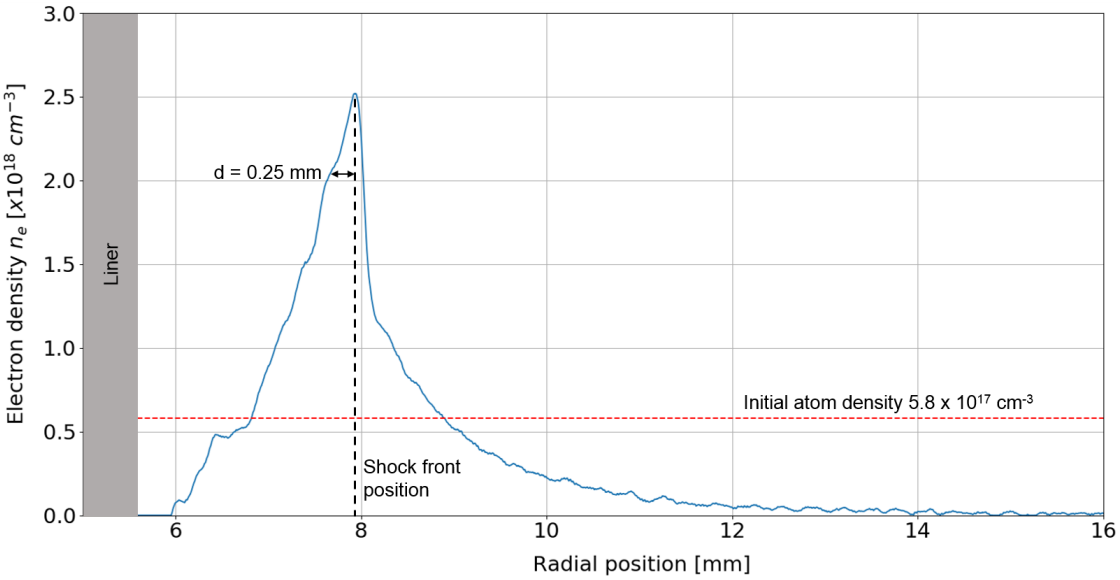


Figure 3.42: Inverse Abel transformation, of a horizontal profile taken from the hashed region in Fig 3.40.b, showing electron density as a function of radius. The initial atom density is indicated with the red dashed line.

Fig 3.43 shows a comparison between the integrated electron density and the optical self-emission intensity for experiment s1212_16. Horizontal profiles were taken from the uniform region of Fig 3.40.b and Fig 3.31e-f, averaged between $y = 6$ mm and $y = 8$ mm. As the self-emission images were captured 20 ns before and after the laser interferometry, they have been shifted by ± 0.2 mm (calculated by assuming a shock velocity of $v_s = 10$ km/s). The integrated electron density and self-emission intensity show very similar structures with a peak at roughly the same position followed by a gradual decrease towards the liner surface. Ahead of the shock front, both profiles are non-zero, indicating the presence of a precursor. Plotting the electron density, calculated via Abel inversion, indicates the position of the shock

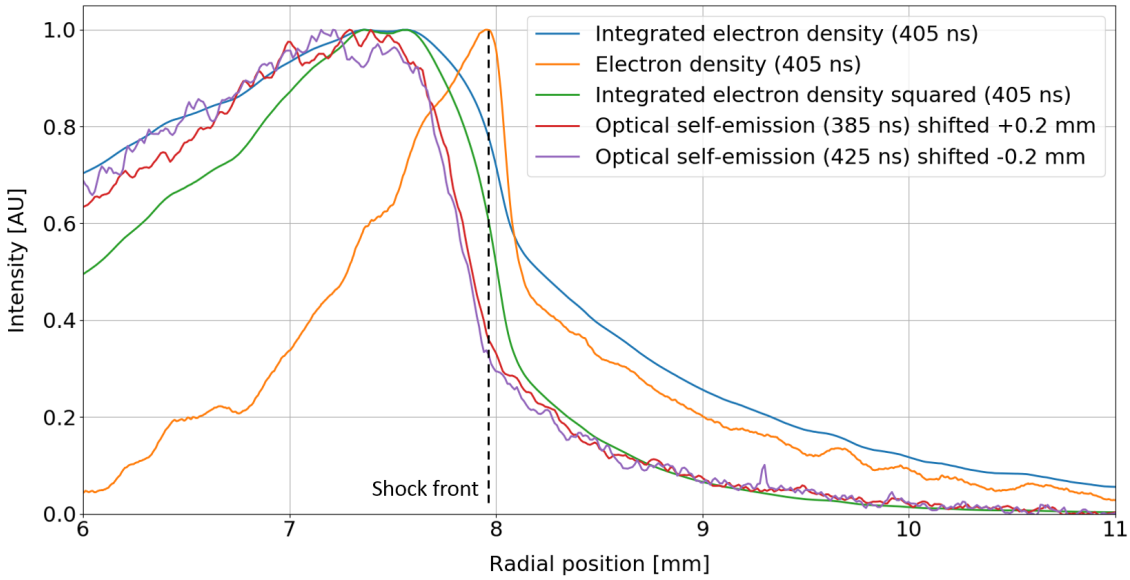


Figure 3.43: Profiles of integrated electron density from interferometry compared against profiles of optical self-emission intensity for experiment s1212_16. Self-emission profiles have been shifted by ±0.2 mm to coincide with the time the laser interferometry image was taken (assuming a shock velocity of $v_s = 10$ km/s). The electron density, determined by Abel inversion, is also plotted and indicates the shock front position. The square of the integrated electron density is also plotted, showing excellent agreement with the self-emission in the radiative precursor region.

front. This approximately coincides with the steep gradient in the self-emission, matching conclusions made in Section 3.4. The integrated electron density decays more gradually than the self-emission. However, the square of the integrated electron density shows very good agreement with the self-emission in the precursor region, the reason for this is not yet understood.

3.5.1 Post-shock material

Unlike experiments performed on the Orion laser facility, the post-shock region is not opaque to the interferometry probe beam. This made it possible to trace fringes directly through the shock front, allowing the electron density to be determined in the post-shock region.

The raw interferogram, shown in Fig 3.40.a, shows a decreasing fringe shift behind the shock front despite integrating through a larger region of post-shock material. This indicates

a rapid drop in electron density, confirmed by the Abel inversion shown in Fig 3.42. This suggests that the shock front is closely followed by a rarefaction and thus is similar to a blast wave with a thin shell of dense material followed by a hot low density gas, as described in Section 1.5.3.

The post-shock temperature and ionization were measured with an optical spectrometer, as described in Section 3.3.5. An optical fibre bundle was used to collect self-emission from fourteen collection volumes, with a diameter of $\sim$250 μm, spaced radially outwards from the liner surface over $\sim$8.1 mm, as shown in Fig 3.28. Fibres focused on the post-shock region were shown to also capture emission from the precursor region.

Optical spectra between $435 - 490$ nm was recorded on an Andor SR500 imaging spectrometer with a 300 lines per millimetre grating. Spectra recorded from experiment s0623_16 is shown in Fig 3.44. Fibres 1-5 are focused inside the post-shock material, as indicated in Fig 3.44.a, and show a similar peak intensity of $\sim$2500. Fibres 6-12 are focused to the precursor region and show a steady decay in intensity with distance from the shock front. Fibres 13 and 14 recorded negligible signal and so are not shown.

The same lines are observed in all recorded spectrum, indicating that singularly ionized Argon ions are also present in the precursor region. This analysis suggests that the temperature and ionization are constant throughout the entire precursor region. By contrast, laser interferometry shows a gradually decreasing electron density shown in Fig 3.42. This discrepancy is further investigated in Section 3.5.2.

The atomic transitions for the major lines have been identified and are labelled in Fig 3.44.b. All of these transitions occur within an Ar-II ion (singularly ionized). No lines from Ar-III (doubly ionized) transitions are observed, such as the line at 456.5 nm due to the ${}^1P_1^o \rightarrow {}^1P_1$ transition or the line at 468.8 nm due to the ${}^3D_2^o \rightarrow {}^3P_2$ transition. This allows the ionization in the post-shock region to be estimated to be $Z_{ps} = 1$. PrismSPECT simulations of Argon, shown in Fig 1.4, indicate that this requires a post-shock temperature of $T_{ps} = 2 - 3.5$ eV for singularly ionized atoms.

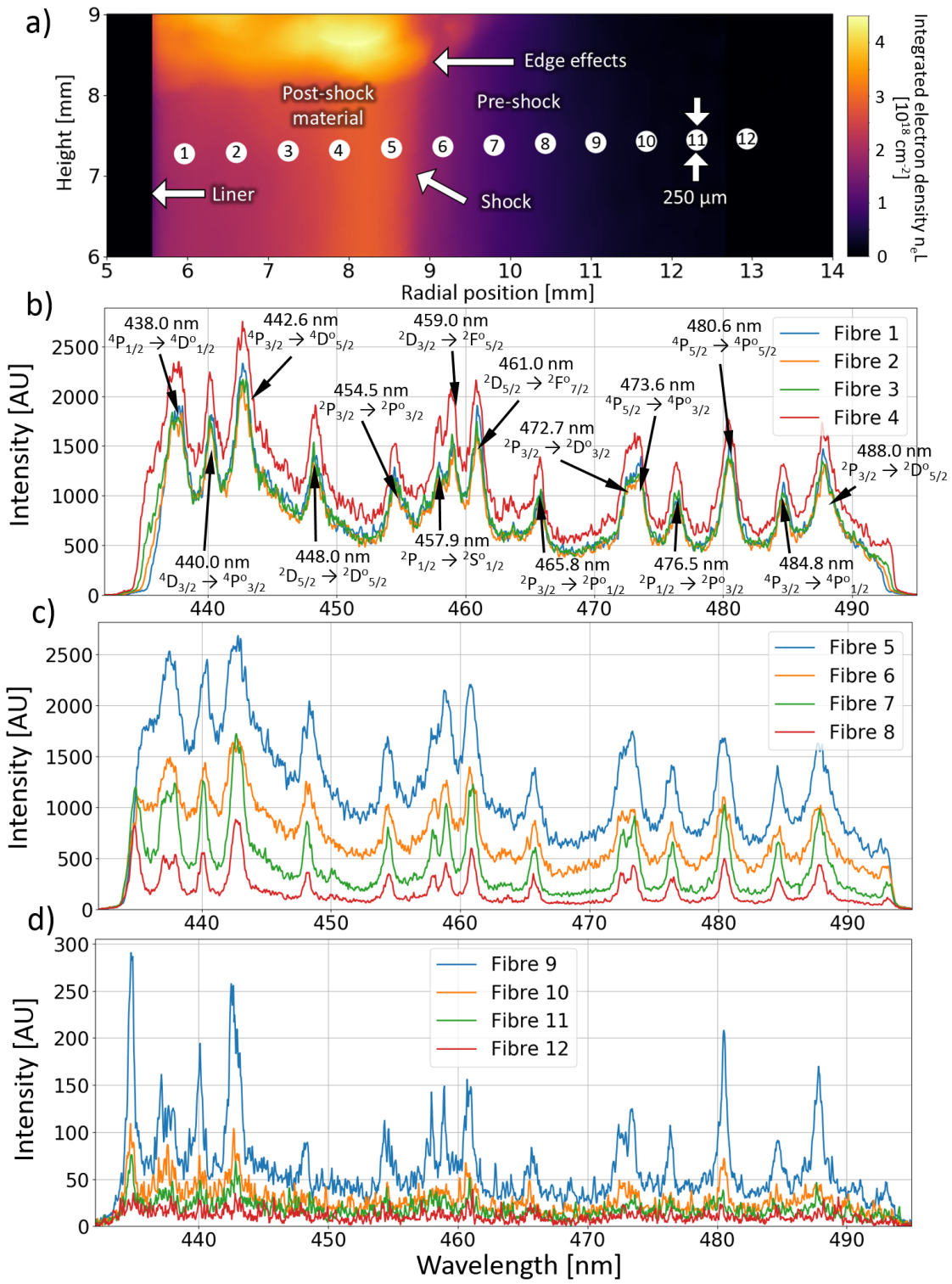


Figure 3.44: Spectra recorded from experiment s0623_16. a) Locations of fibre focal spots. b) Fibres 1-4 with atomic transitions of major peaks labelled. c) Fibres 5-8. d) Fibres 9-12.

To verify this estimate, the atomic physics code PrismSPECT, detailed in Section 1.4.1, was used to simulate the expected spectrum. Simulations were run for an Argon plasma at 0.04 mg/cm^3 with Detailed Configuration Accounting (DCA) and the Low Temperature Spectroscopy model. For simplicity the plasma was modelled with zero width and assumed to be in steady state. Although simulated with a non local thermodynamic equilibrium model (non LTE), this resulted in a similar spectra to that seen with an LTE model. This may not fully represent this system, but allowed for initial estimates to be made. The normalized spectrum calculated for a variety of temperatures are shown in Fig 3.45.a. The majority of lines are due to transitions in Ar-II ions, labelled in black. However, several lines due to transitions in Ar-III ions, labelled in red are present in spectra for plasma at 3 and 4 eV. This allows the shock temperature to be constrained to < 3 eV. PrismSPECT simulations of plasma between 1.5 and 2.5 eV yielded similar spectra, shown in Fig 3.45.b, with the same lines present, and thus the temperature may be estimated as $T_{ps} = 2.0 \pm 0.5$ eV and the ionization as $Z_{ps} = 0.8 \pm 0.3$.

However, these estimates are based on simulations which presume the plasma is in steady state with similar electron and ion temperatures, which implies local thermodynamic equilibrium (LTE). To determine if this is the case for the post-shock material the electron and ion mean free paths were estimated, using Eq. 1.17 and Eq. 1.18 respectively. Post-shock temperature and ionization estimates were taken from optical spectroscopy and electron density estimates from the peak in laser interferometry, $n_e = 2.5 \times 10^{18}$ cm^{-3}. This yielded mean free paths of $\lambda_e \sim 350$ nm and $\lambda_i \sim 470$ nm for the electrons and ions respectively. This is many orders of magnitude below the observed post-shock region, ~ 1 mm. Thus particles in this region are expected to quickly thermalize and so the region is expected to be in LTE with similar electron and ion temperatures.

The post shock temperature may also be estimated using the equation for the post-shock temperature Eq. 1.63, assuming a strong shock with negligible radiation. Using measurements of the post-shock ionization from spectroscopy, a shock velocity of $v_s = 10$ km/s and assuming

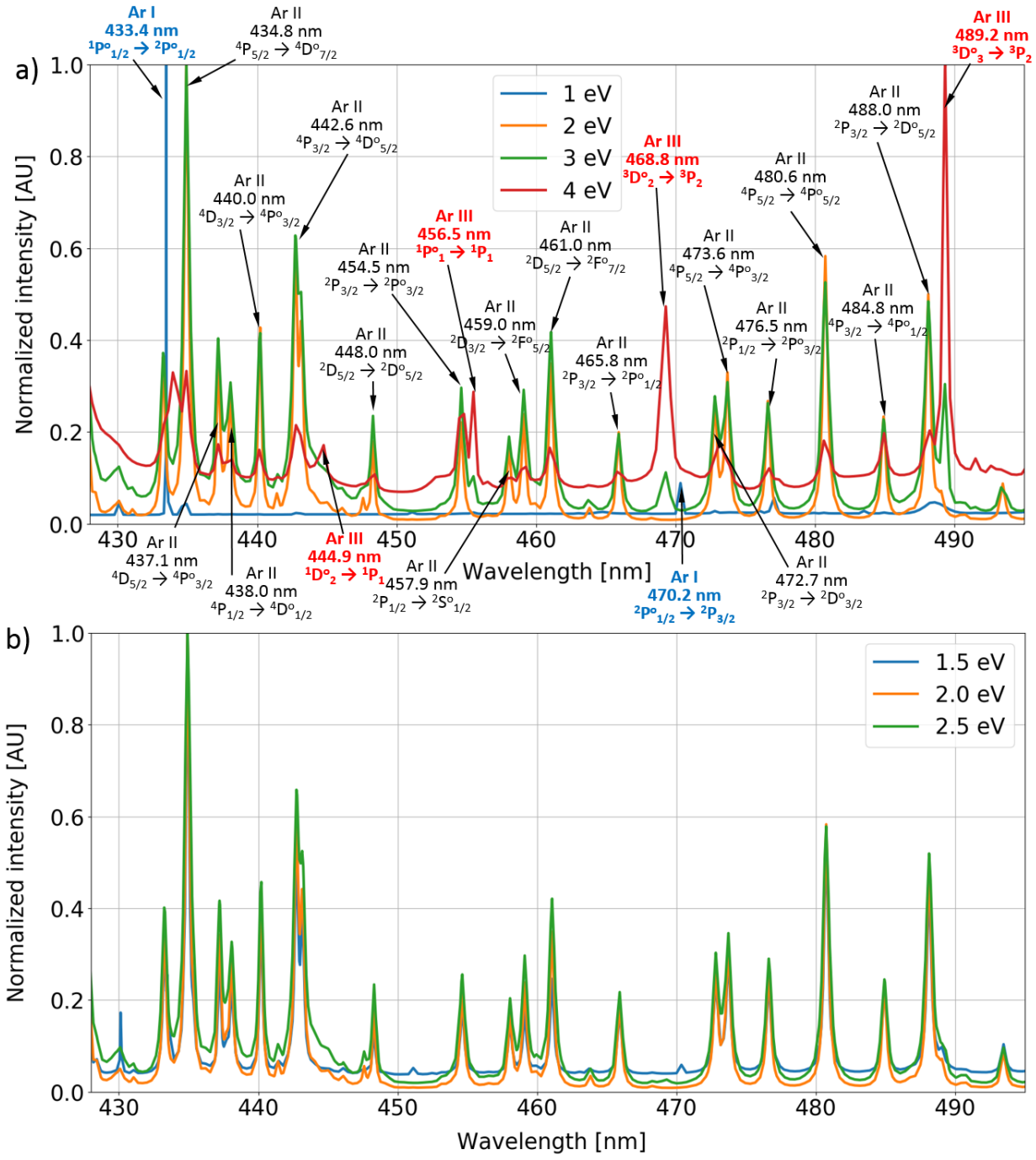


Figure 3.45: Spectra calculated for a PrismSPECT simulation of a zero width, steady state Argon plasma at 0.04 mg/cm^3 and at several different temperatures. a) $1-4$ eV. Ar-I (neutral atom) transitions are labelled in blue. Ar-II (singly ionized) transitions are labelled in black. Ar-III (doubly ionized) transitions are labelled in red. b) $1.5-2.5$ eV.

an adiabatic index of $\gamma = 5/3$ yields a post-shock temperature of $T_{ps} \sim 4.4$ eV. This is inconsistent with spectroscopy measurements, indicating that radiation plays a significant

role in this shock and that Eq. 1.63 is not valid for these conditions.

Improved estimates of the post-shock temperature were made using the radiative shock model developed in Section 1.6.4. Assuming an initial mass density of $\rho_0 = 0.04$ mg/cm^3 and shock velocity of $v_s = 10$ km/s therefore yields a post-shock temperature of $T_{ps} = 1.6$ eV and ionization of $Z_{ps} = 0.6$. This is similar to measurements made with spectroscopy which yielded a temperature of $T_{ps} = 2.0 \pm 0.5$ eV and ionization of $Z_{ps} = 0.8 \pm 0.3$. This model suggests that 37% of the kinetic energy of the incoming particles is dissipated as radiation. This model also predicts a post-shock mass density of $\rho_{ps} = 0.32$ mg/cm^3, representing a compression of $\Gamma = \times 8$ and post-shock ion density of $n_i = 4.8 \times 10^{18}$ cm^{-3}. Multiplying this by the predicted post-shock ionization, $Z_{ps} = 0.6$, yields a post-shock electron density of $n_e = 2.9 \times 10^{18}$ cm^{-3}. This is similar to the peak electron density observed in experiment s1212_16, shown in Fig 3.42.

The thickness of the post-shock region may then be estimated geometrically. Fig 3.42 suggests that the majority of the post-shock material is swept up into a thin cylindrical shell directly behind the shock front. The total amount of post-shock material, N_i, is given by:

$$N_i = n_{i0} h \pi \left(r_s^2 - r_L^2 \right) \tag{3.68}$$

where h is the height of the shock, r_s is the radius of the shock front and $r_L = 5.6$ mm is the liner outer radius. Assuming all of this material is swept up into a thin cylindrical shell, with a thickness d and ion density n_{i0}, Eq. 3.68 may be equated to:

$$\Gamma n_{i0} h \pi \left(r_s^2 - (r_s - d)^2 \right) = N_i \tag{3.69}$$

Therefore the post-shock thickness may be given as:

$$d = r_s - \sqrt{\frac{r_s^2(\gamma - 1) + r_L^2}{\gamma}} \tag{3.70}$$

At the time the interferometry image, shown in Fig 3.40.a, was taken $r_s = 7.95$ mm.

Assuming the post-shock compression predicted by the radiative shock model, $\Gamma = \times 8$, this therefore yields a post-shock thickness of $d = 0.25$ mm. This has been marked on the Abel inversion shown in Fig 3.42 but does not closely match the post-shock structure estimated by the Abel inversion.

3.5.2 The radiative precursor

Ionization is observed ahead of the shock front in both laser interferometry, shown in Fig 3.42, and in optical spectroscopy, shown in Fig 3.44, thus indicating the formation of a precursor. In the precursor region the ion density is expected to remain constant as subsonic flows are limited to the local sound speed, $c_s \sim 320$ m/s, and thus unable to expand significantly prior to the arrival of the shock. Therefore the average ionization in the precursor region, as a function of radius, can be determined by dividing the electron density, $n_e(r)$ (shown in Fig 3.42) by the initial atom density, $n_{i0} = 5.8 \times 10^{17}$ cm^{-3}. The result is shown in Fig 3.46.a. The same may not be done for the post-shock region, as in this region the mass density is expected to increase resulting in a non-constant n_i. The ionization decays gradually, over a distance of ~4 mm, with increasing distance from the shock front at $r \sim 8$ mm, with a peak ionization of $Z \sim 4$.

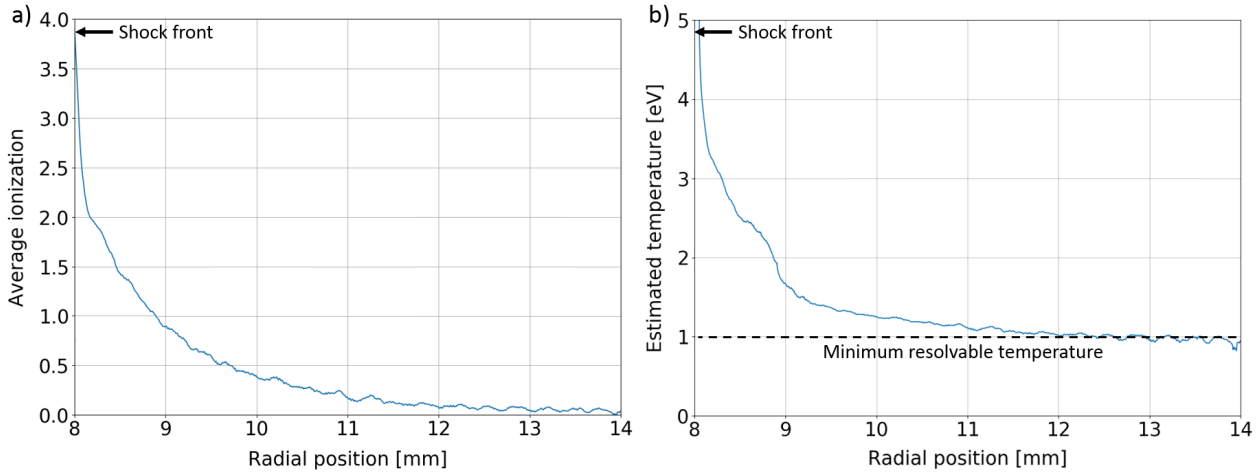


Figure 3.46: a) Average ionization as a function of radius in the precursor region. b) Approximate temperature as a function of radius in the precursor region. Temperatures below ~1 eV result in negligible ionization and so may not be resolved.

A rough estimate of the temperature in the precursor, as a function of radius, can be estimated using PrismSPECT simulations of an Argon plasma at multiple temperatures, shown in Fig 1.4.b. The ionization at each point was matched with the corresponding temperature yielding the plot shown in Fig 3.46.b. However, PrismSPECT simulations suggest that Argon has negligible ionization below a temperature of ∼1 eV and thus this sets the minimum temperature that may be determined with this method. The temperature plot follows a similar structure to the ionization plot, gradually decaying to the minimum temperature in ∼4 mm.

Optical spectroscopy, shown in Fig 3.44, observed the same lines present in spectrum recorded from the precursor region and post-shock region, extending out to $r \sim 13$ mm, albeit with lower intensity. This might indicate a constant ionization of $Z = 0.8 \pm 0.3$ and temperature of $T = 2.0 \pm 0.5$ eV at all regions in the precursor. However, this was found to not be the case. Regions close to the shock front, $r < 8.8$ mm, exhibited higher ionizations and temperatures. This indicates there is a significant amount of radiative cooling in the post-shock region, bringing the post-shock temperature below that of the shock front.

In addition, laser interferometry measured lower ionizations and temperatures with at $r > 9.7$ mm than the optical spectroscopy. These match observations made in [Burdiak et al., 2014] in which it was suggested that the precursor is not in LTE and photo-ionization results in a small fraction of ions dominating the emission spectrum. This is a situation also encountered in photo-ionised plasmas in astrophysics, where the optical spectra would suggest a hotter electron temperature than is actually the case.

To verify this, the ion collision times were calculated with Eq. 1.16 for different regions in the precursor. Electron densities were taken from Fig 3.42, ionizations from Fig 3.46.a and temperatures from Fig 3.46.b. This yielded collision times of $\tau_i \sim 0.3$ ns at $r = 9$ mm and $\tau_i \sim 60$ ns at $r = 11$ mm. As the shock propagates at ∼10 km/s it will take ∼100 ns to reach the plasma at $r = 9$ mm. This is several orders of magnitude longer than the collision time at this location and so this region may be approximated as being in LTE. However, it

will take the shock ∼300 ns to reach the plasma at $r = 11$ mm, which is not significantly longer than the collision time at this location. Therefore beyond $r > 11$ mm the plasma is expected to not be in thermal equilibrium, agreeing with conclusions made in [Burdiak et al., 2014], and the observed spectrum is likely dominated by a small fraction of ionized ions.

The precursor observed in these experiments is expected to have formed due to reabsorption of radiation emitted by the shock front. The shock velocity required to produce a radiative precursor may be estimated using Eq. 1.80. Using post-shock ionization predicted from spectroscopy, $Z_{ps} \sim 0.8$, and assuming $\gamma = 5/3$ and $\epsilon_0 = \epsilon_1 = \eta \sim 1$ yields a shock velocity of $v_s \sim 6$ km/s. This is below the shock velocity measured for these experiments, $v_s \sim 10$ km/s, and so a radiative precursor is expected to form. However, precursors ahead of the shock may also form due to particles reflected by the shock front or due to electron thermal conduction [Drake, 2006]. The following discussion follows a similar argument to that presented for counter-propagating radiative shock experiments performed on the Orion laser facility, in Section 2.4.3, albeit with different parameters.

To determine if electron or ion acceleration plays a role, the electron and ion mean free path were calculated using Equation 1.17 and Equation 1.18. Temperature and ionization estimates were taken from optical spectroscopy, $T_e \sim 2$ eV and $Z \sim 0.8$, and the electron density was approximated as the initial ion density multiplied by the ionization, yielding $n_e = 4.8 \times 10^{17}$ cm^{-3}. This yielded mean free paths of $\lambda_e \sim 0.96$ μm and $\lambda_i \sim 1.5$ μm for the electron and ions respectively, both of which are several of orders of magnitude smaller than the observed precursor. To fully discount this mechanism the mean free path was recalculated for ions travelling at the shock velocity of $v_s \sim 10$ km/s. Argon ions travelling at this velocity will have a kinetic energy equivalent to a temperature of ~ 21 eV. Using this temperature estimate yielded a larger ion mean free path of ∼60 μm, still significantly smaller than the observed precursor. Thus this mechanism may be ignored in this experiment.

To determine if thermal conduction was responsible for the formation of the precursor, the thermal diffusion was approximated as a Marshak wave where the conductivity, k_{th}, is given

by Eq. 2.37. The heat capacity at constant pressure, C_p, for Argon is $\sim 5.2 \times 10^6$ erg/g/K [Kramida et al., 2015], which results in a conductivity of $\sim 1.3 \times 10^6$ gcm/s^{3}K. The position of the thermal wave front, x_0, in a Marshak wave is given by Eq. 2.38, which indicates that the Marshak wave has propagated $\sim$0.5 mm after 215 ns (the time between the shock being launched and the interferometry image in this experiment). This is insufficient to account for the large precursor observed ahead of the shock front but may be resolvable by the interferometry diagnostic and may partially contribute to the precursor directly ahead of the shock front. However, this model does not take into account the motion of the shock front itself and thus is likely to be a significant overestimate. Therefore this precursor is indeed believed to be formed due to the reabsorption of radiation emitted by the shock front.

Experiments performed on the Orion laser facility observed that the radiative precursor width remained constant for the duration of the experiment, shown in Section 2.4.2. To test if this was also the case for these radiative shocks, laser interferometry was performed at different times on seven similar experiments with Argon gas-fills and an initial mass density between 0.0387 and 0.0396 mg/cm^3. The same analysis to that performed for experiment s1212_16 was used to produce radial plots of electron density for all seven experiments. Fig 3.47.a plots the peak electron density against time after current start for seven experiments with a similar gas fill. A weak general negative trend is visible indicating that the peak electron density decreases over time. This is not surprising as the energy density decreases as the radius of the shock increases and energy is lost via radiation. However, there is significant noise in the points and insufficient data to fit a model. This noise is likely party due to significant variation in the MAGPIE current between experiments, ranging from 0.87 to 1.20 MA.

The width of the radiative precursor was defined as the distance between the peak electron density and the initial ion density (equivalent to an ionization of $Z = 1$). This is plotted against time after current start in Fig 3.47.b. All points, except for experiment s0622_16, show a very similar radiative precursor width indicating that the radiative precursor remains

stable, with a width of 0.93 ± 0.06 mm, for more than 200 ns. Despite the wide variation in MAGPIE drive current between experiments the radiative precursor width only varies by an average of 6% (excluding experiment s0622_16). The reason for the outlier in experiment s0622_16 is currently unknown.

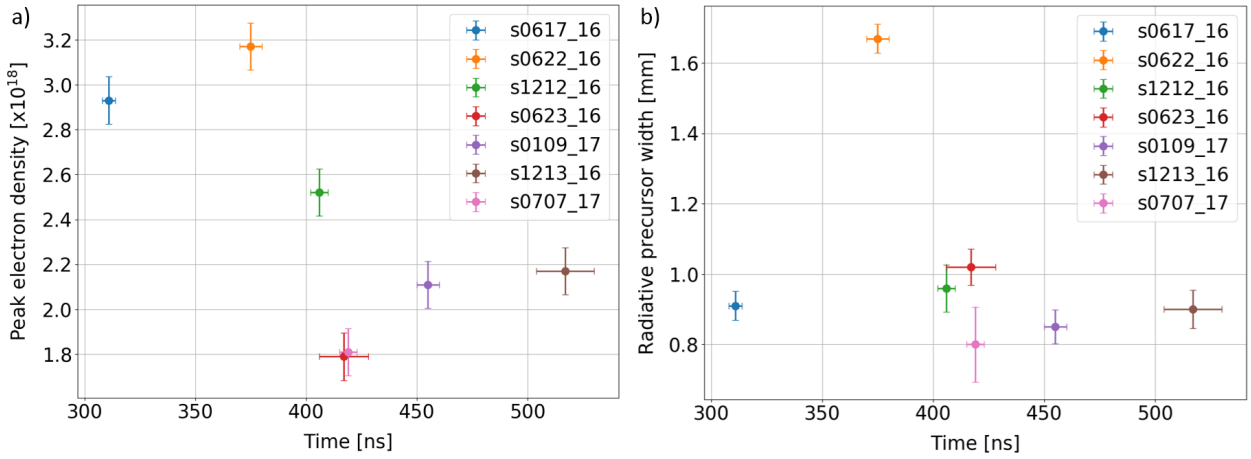


Figure 3.47: a) Peak electron density plotted against time after current start. b) Radiative precursor width plotted against time after current start.

In addition the peak electron density and radiative precursor width were plotted against the peak MAGPIE current for the same series of experiments, show in Fig 3.48. A weak general positive trend is visible in Fig 3.47.a indicating that the peak electron density increases with peak current. While the points in Fig 3.47.b do have a positive correlation, experiment s0622_16 is likely an outlier and the remaining points show a minor increase with peak current.

3.5.3 Edge shocks

Additional shocks were launched from the bottom and top of the liner, appearing as toroids travelling towards the centre of the liner, labelled in the self-emission images from experiment s1212_16 shown in Fig 3.49. The presence of these edge shocks highlights the importance of probing the experiment side-on. Probing the experiment end-on, parallel to the liner, does not indicate the origin of these edge shocks and they may be interrupted as cylindrical shocks launched ahead of the primary shock. The edge shocks launched from near the bottom of the

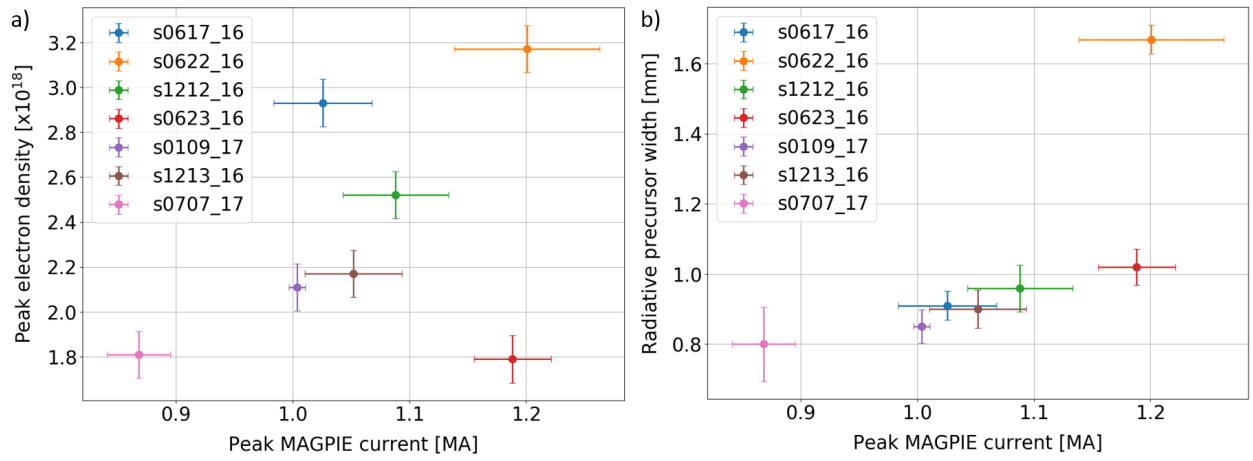


Figure 3.48: a) Peak electron density plotted against peak MAGPIE current. b) Radiative precursor width plotted against peak MAGPIE current.

liner appear to expand radially, forming a region of increased optical emission when colliding with the primary shocks.

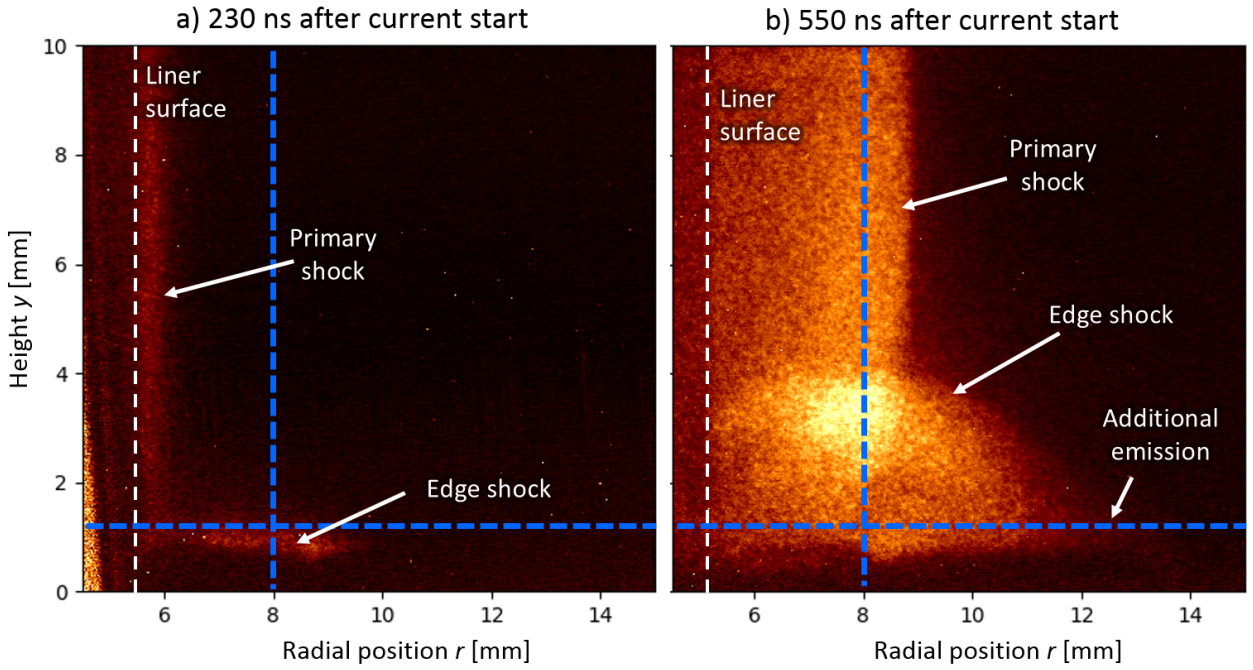


Figure 3.49: Self-emission images from experiment s1212_16 showing the edge shocks. a) Taken 230 ns after current start. b) Taken 550 ns after current start.

A similar analysis to that in Section 3.4 was performed to determine the expansion velocities. Horizontal and vertical profiles were taken through this edge shock at $y = 1.2$

mm and $r = 8$ mm, averaged over 200 μm, shown as blue lines in Fig 3.49. The resulting shock position as a function of time is plotted in Fig 3.50. Early in time the edge shock was relatively dim and so the shock front position could not be accurately determined in the vertical direction. Linear trendlines may be fit to these points to estimate the expansion velocity, found to be 8.3 ± 0.5 km/s horizontally and 9.2 ± 0.1 km/s vertically, comparable to the primary shock velocity of 9.0 ± 0.3 km/s.

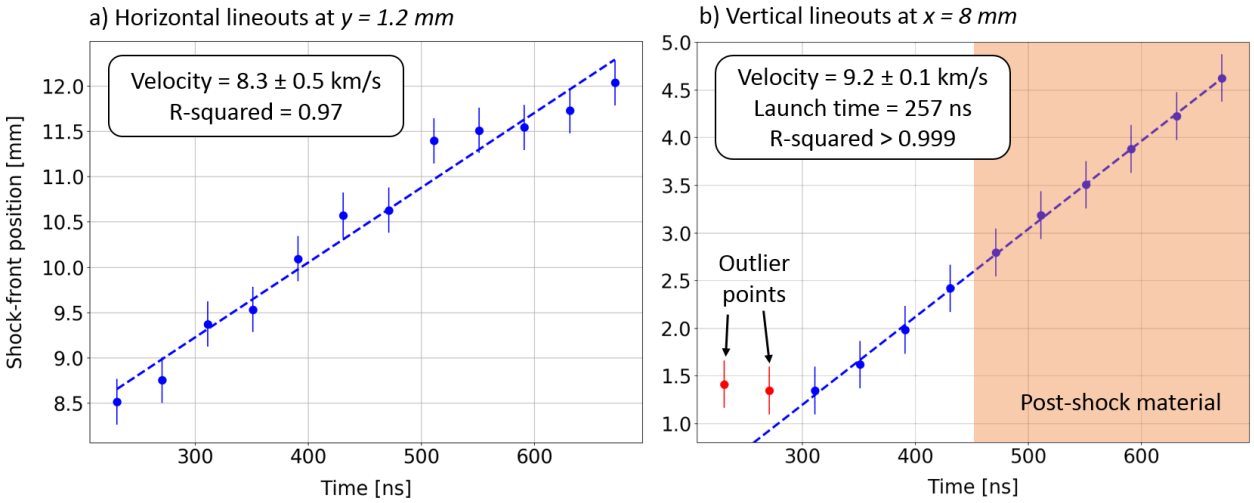


Figure 3.50: Edge shock position as a function of time from experiment s1212_16. a) Horizontal profiles at $y = 1.2$ mm and b) Vertical profiles $x = 8$ mm.

Additional emission just above the hardware (possibly plasma formation on the floor of th gas cell, labelled in Fig 3.49 right) made locating the shock front position in the horizontal profiles less reliable, resulting in increased errors and poorer fit to a linear trendline, with $R^2 \sim 0.97$. However, the shock was easily identified in the vertical profiles, even though in several of these images the edge shock was propagating through the post-shock material of the primary shock, as is the case in Fig 3.49.b. Despite this, no change in the shock velocity was observed and the shock position closely followed a linear trendline, with $R^2 > 0.99$.

By extrapolating the trendline for vertical profiles to the hardware surface, at $y = 0.8$ mm, the edge shock was found to form $\sim 194 \pm 7$ ns after current start. This is coincidental with the formation of the primary shock, at $\sim 181 \pm 10$ ns.

At its formation, the edge shock is already extended in the horizontal direction as seen

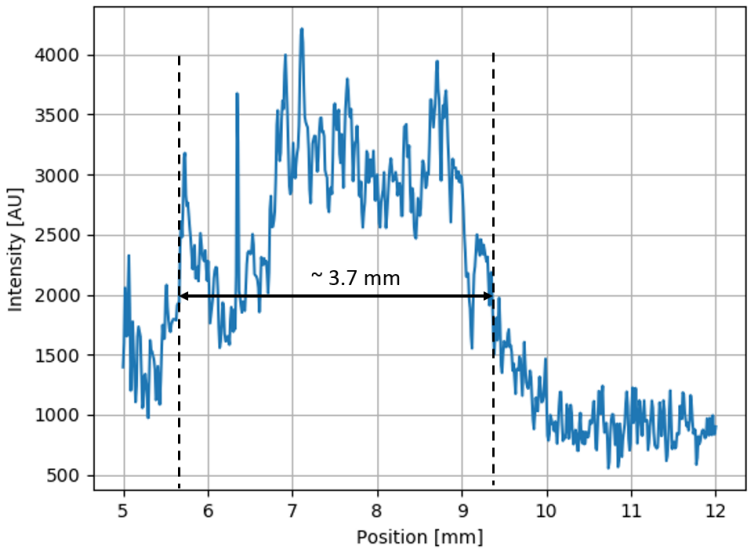


Figure 3.51: Horizontal profile through the approximate centre of the edge shock at $y = 0.9$ mm in Fig 3.49.a, with a width of 100 μm. The approximate full-width-half-maximum was visually estimated to be $\sim$3.7 mm.

in Fig 3.49.a, the earliest self-emission camera image, taken 230 ns after current start and just $\sim$30 ns after the primary shock is launched. A horizontal profile was taken through the approximate centre of this region, at $y = 0.9$ mm and averaged over 100 μm, and is shown in 3.51. A rough approximation of the width of this profile was visually estimated to be $\sim$3.7 mm.

These edge-shocks are also visible in the laser interferometry diagnostic, shown in Fig 3.52. As the shock front of the edge shocks is not perpendicular to the interferometry fringes it is non-trivial to interpret the raw interferogram in Fig 3.52.a. Processing the interferogram to produce a 2-D map of line integrated electron density ($n_e L$), shown in Fig 3.52.b, reveals a similar structure to that seen in the primary shock. The edge shock is also preceded by a similar sized precursor and proceeded by a layer of lower electron density. Enhanced electron density is observed where the edge shock collides with the primary shock.

Three horizontal profiles were taken through the primary shock, through the edge shock and through their collision point, at $y = 0.6, 4, 1.5$ mm respectively, and are shown in Fig 3.53.a. Assuming the edge shocks also evolve with cylindrical symmetry (which is seen to be

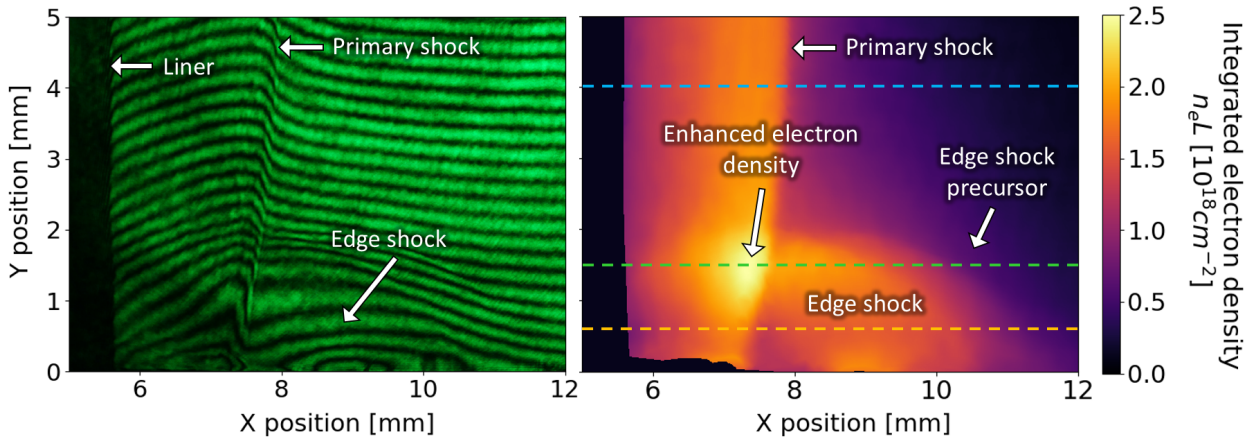


Figure 3.52: 532 nm interferometry from experiment s1212_16 with an Argon gas-fill initially at 0.04 mg/cm^3, taken 407 ns after current start. a) Raw interferogram. b) Map of integrated unbound electron density.

the case in similar experiments such as s0623_16 shown in Fig 3.30), an Abel inversion can be applied to these profiles. The resulting plots of electron density as a function of radius are shown in Fig 3.53.b.

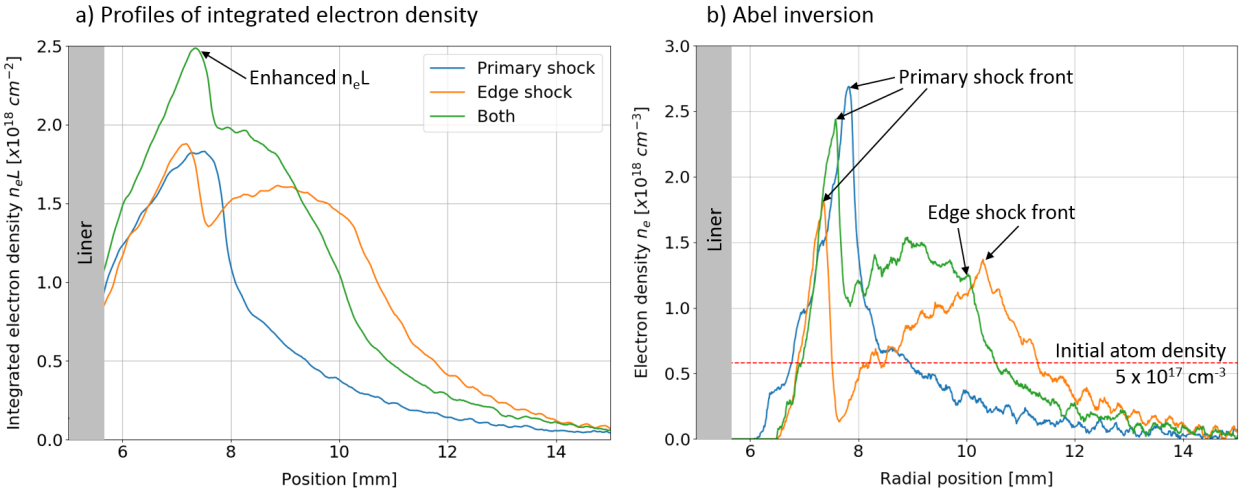


Figure 3.53: a) Profiles of integrated electron density through the primary and edge shock, as indicated in Fig 3.52. b) Abel inversions showing electron density as a function of radius.

In all three Abel inversions the primary shock is well defined between $r = 7 - 8$ mm and proceeded by a region of low density post-shock material. Profiles taken closer to the base of the liner have lower peak electron densities in the shock front and have not propagated as far.

The Abel inversion through the edge shock, shown with an orange line in Fig 3.53.b, has

a peak in electron density at $r = 7.4$ mm, which is the primary shock front, and a less well defined peak at $r = 10.3$ mm, which is the edge shock front position. Behind both shock fronts the electron density returns to zero, indicating a shock structure similar to a blast wave. Ahead of the edge shock a precursor is observed, with a similar structure and size to that observed in the Abel inversion through just the primary shock, shown in blue in Fig 3.53.b. However, behind the edge shock no radiative precursor from the primary shock is observed. If the edge shock is similar to a blast wave then this is expected, as the post-shock material is already highly ionized and of very low density so further heating results in negligible increases in electron density.

The Abel inversion through the primary and edge shocks interaction, green line in Fig 3.53.b, does not actually show a region of increased electron density, despite observations of increased $n_e L$ in Fig 3.53.a. Instead the electron density remains above 1×10^{18} cm^{-3} for over 2 mm ahead of the shock front as the profile runs parallel to the edge shock front. Integrating through this thick region of post-shock material makes it appear as if there is a region of enhanced emission and electron density in the side-on self-emission and laser interferometry diagnostics.

The primary shock and edge shock collide at an oblique angle and so the formation of a Mach stem may be expected. Section 1.5.3 suggests that a Mach Stem will form if the angle between the two shocks is over 74° (assuming an adiabatic index of $\gamma \sim 5/3$). However, no Mach stem is observed in Fig 3.52 despite an angle of ∼85° between the two shocks. This allows an upper-bound to be approximated for the local adiabatic index using Eq. 1.66. This yields a value of $\gamma < 1.5$

As the primary focus of this experiment was on the radially expanding cylindrically symmetric shock, several attempts were made to mitigate these edge shocks. However, the source of these is not understood. Initial experiment designs used clamps to compress rubber O-rings at the top and bottom of the liner and create a vacuum seal, detailed in Section 3.2.1, which may have resulted in imperfect contact. It is possible that electrical breakdown of the

gas between, or immediately adjacent to, the liner and the rest of the hardware occurred. Resistive heating of any electrical arcs would deposit significant amounts of energy capable of launching strong shocks. However, edge shocks are radially symmetric and no evidence of electrical tracking could be seen on the surface of the rubber O-rings.

The experimental setup was later simplified by replacing the rubber O-rings and clamps with a groove for the liner to sit in and coating the join with a layer of glue. This helped mitigate the edge shocks (particularly from the top of the liner) but did not completely remove them, as seen in experiment s1212_16 shown in Fig 3.49. An investigation into the effect of different glues has not yet been performed and would greatly help improve this experimental platform, allowing symmetric radially expanding shocks to be reliably produced.

Fortunately, the high impedance of the MAGPIE generator allows the liners to be extended without significantly affecting the current. Liners with a height of 20 mm were found to be long enough that a large portion of the primary shock remains unperturbed for over > 500 ns, allowing the primary shock to be studied in detail.

3.5.4 Variation with gas species

Experiments were performed with four different noble gas-fills (Neon, Argon, Krypton and Xenon) to study the effect of gas species on the formation of a shock and radiative precursor. To produce similar shock velocities and hydrodynamics the initial gas pressure in each experiment was varied to ensure a constant mass density of $\rho \sim 0.04$ mg/cm^3. The required fill pressure, P_0, was calculated using Eq. 2.23, assuming the gas-fill acted like an ideal gas. The desired fill pressures for gases used in these experiments are shown in Table 3.3. Experiments have not yet been performed using Helium, which is expected to not exhibit significant radiative effects, or Radon, which is highly radioactive and so is impractical to use at the MAGPIE facility.

Optical self-emission images, taken approximately the same time after current start, from experiments using four different gases are shown in Fig 3.54.a-d. These images have been

Gas	Atomic number	Atomic mass	Fill pressure
Neon	10	20.18	48.3 mbar
Argon	18	39.95	24.4 mbar
Krypton	36	83.80	11.6 mbar
Xenon	54	131.29	7.42 mbar

Table 3.3: Fill pressure required to reach a mass density of $\rho \sim 0.04$ mg/cm^3 for gases used in these experiments.

normalized for clarity but higher atomic number gases, at lower pressures, are significantly dimmer. The liner wall is visible on the left hand side of each image and the shock propagates to the right. Ahead of the shock front emission is visible, with light gases such as Neon showing very little emission and heavier gases such as Xenon showing increased emission. This suggests that heavier elements are experiencing enhanced radiative effects, as was seen in experiments performed on the Orion facility, detailed in Chapter 2.

Velocity and shock launch times were measured for these four experiments using the methods described in Section 3.4. Plots of shock front position as a function of time are shown in Fig 3.54.e. Similar shock velocities, between $10.0 - 11.0$ km/s, and launch times, between $121 - 209$ ns, are observed for all four experiments. The apparent decrease in shock launch time with increasing atomic number is comparable to variation seen in a collection of nine experiments in Argon ($135 - 234$ ns) and so is most likely due to variation in the MAGPIE drive current. Therefore by maintaining a constant initial mass density, shock hydrodynamics may be kept constant while radiative effects varied.

Laser interferometry was fielded on experiments with these four gas-fills to investigate how the radiative precursor varied. The raw interferometry images for these four experiments are shown in Fig 3.55.a-d. and the processed maps of integrated electron density, $n_e L$, in Fig 3.55.e-h. In all images the liner is visible on the left hand side and shocks propagate to the right. In several experiments, edge shocks were visible near the base of the liner. These images show that the radiative precursor extends significantly further in heavier gases such as Xenon than lighter gases such as Neon.

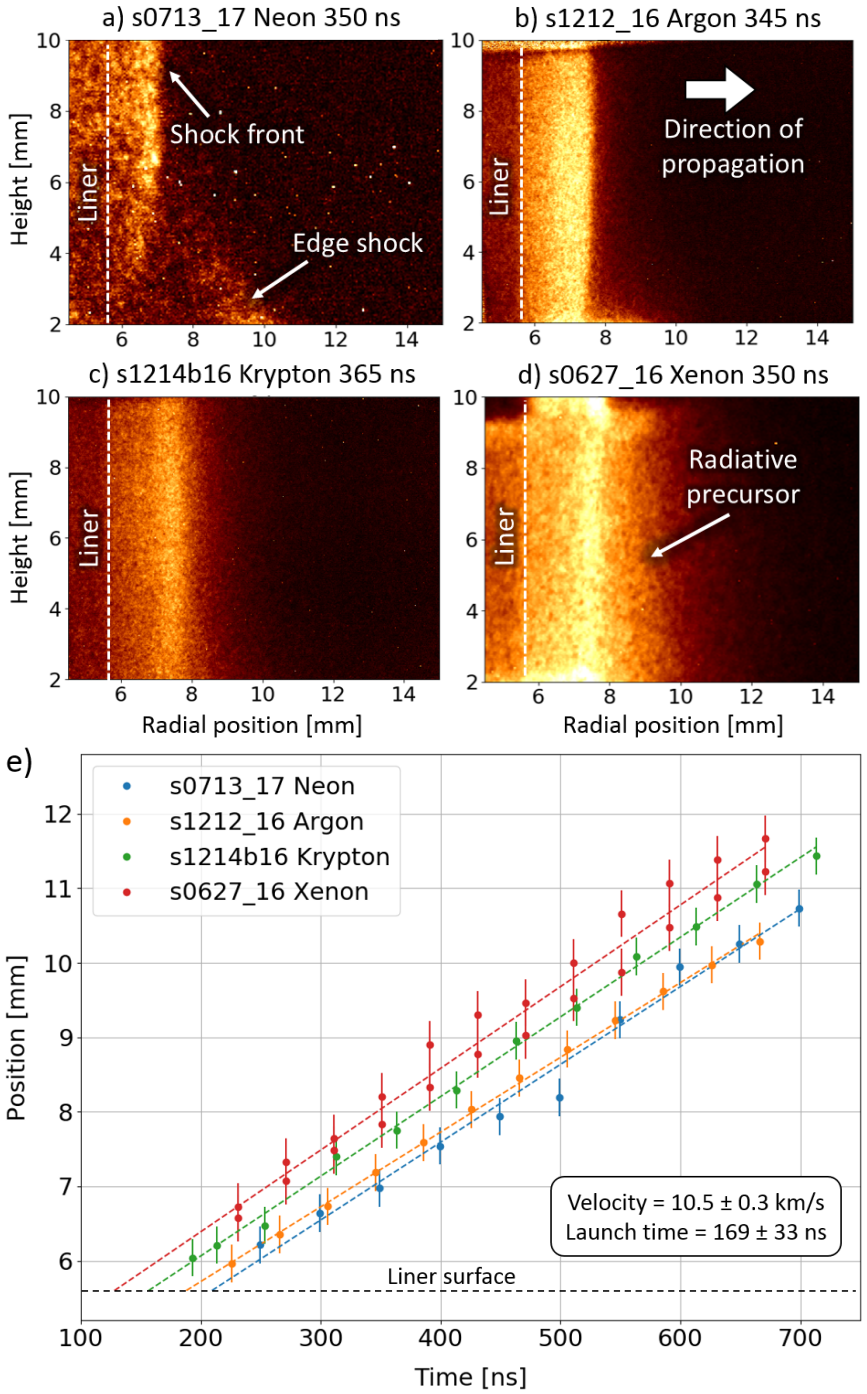


Figure 3.54: a-d) Self-emission recorded from experiments with four different gas species at approximately the same time after current start. e) Shock front position as a function of time for the same series of experiments.

To quantify this, profiles were taken from Fig 3.55.e-h, at a height of $y = 8$ mm, and Abel inverted to produce profiles of electron density as a function of radial position. These profiles

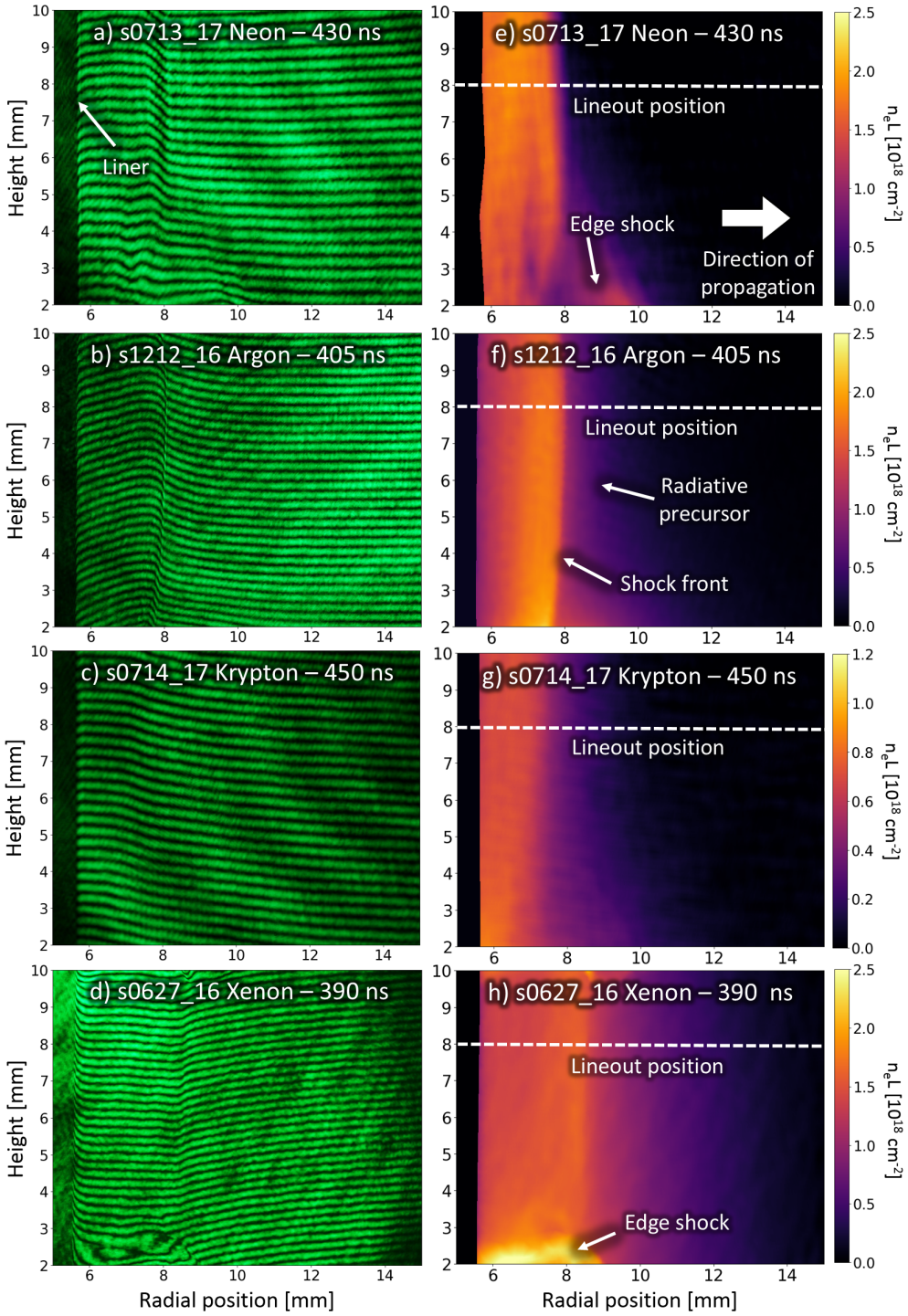


Figure 3.55: a-d) Interferograms from experiments with Neon, Argon, Krypton and Xenon gas-fills with the same initial mass density of 0.04 mg/cm^3. e-h) Results of processed interferograms showing maps of integrated electron density, n_eL.

have been offset to the reference frame of the shock front (defined as the peak in electron density) and are shown in Fig 3.56.a. Dotted lines indicate the initial atom density.

In the radiative precursor the ion density remains constant and so these profiles may be divided by the initial atom density to yield ionization as a function of radius, shown in Fig 3.56.b. This method may not be extended to determine ionization in the post-shock material as the post-shock compression is expected to change depending on the gas species.

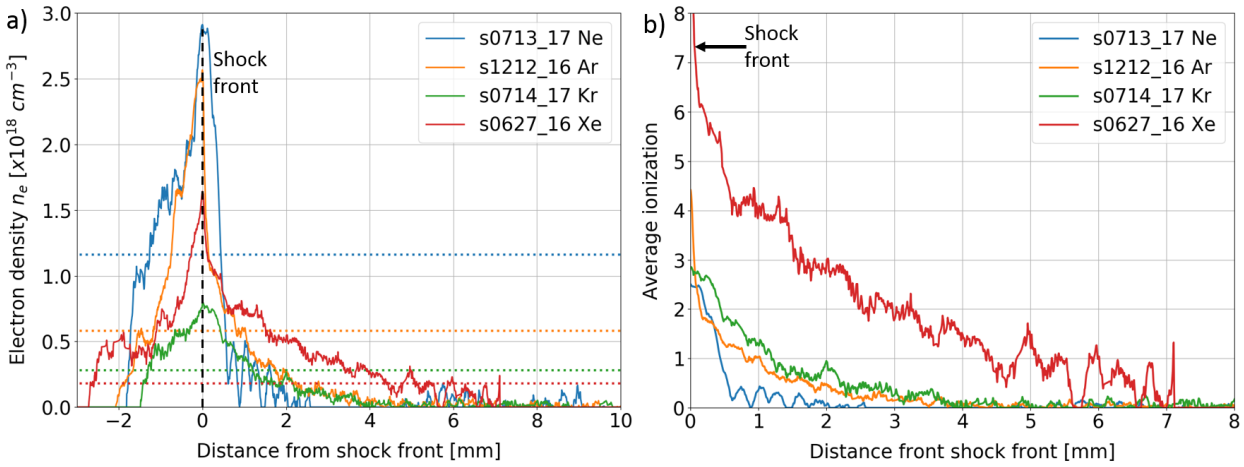


Figure 3.56: a) Abel inversion of profiles taken from 3.55.e-h showing electron density as a function of radial position. Dotted lines indicate initial atom density. b) Average ionization for different gas species.

Due to their lower ionization potential, heavier elements exhibit a larger radiative precursor width. The approximate radiative precursor width, defined as the distance between the shock front and where the ionization is $Z = 0.5$ (selected to be above the noise floor), is plotted in Fig 3.57. A standard error of ± 0.5 mm was visually selected for these points while a larger error of 1 mm was selected for Xenon due to the increased noise seen in Fig 3.56.b.

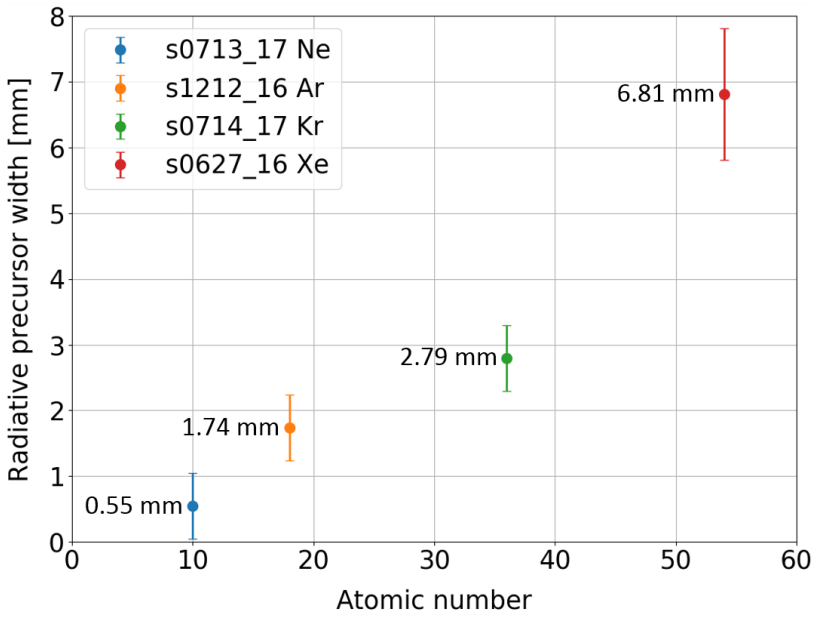


Figure 3.57: Radiative precursor width plotted against gas-fill atomic mass, defined as distance between the shock front and $Z = 0.5$. All four shots have similar initial mass densities of 0.5 mg/cm^3.

Chapter 4

Conclusions and future work

4.1 Summary

This Thesis has introduced two novel experimental configurations used to produce radiative shocks in low density gas-fills using high powered lasers and pulsed power generators, demonstrated on the Orion laser facility and MAGPIE generator. Experiments were performed in Neon, Argon, Krypton and Xenon gas-fills and radiative effects were found to increase with higher atomic number gases, with shocks exhibiting larger radiative precursors and increased radiative cooling. This experimental data is relevant for both inertial confinement fusion and astrophysical research, helps to characterise radiative shocks in Neon, Argon, Krypton and Xenon and allows for benchmarking of numerical simulations.

4.1.1 Counter-propagating shock experiments

Experiments described in Chapter 2 presented a new experimental configuration for producing counter-propagating radiative shocks. These experiments build upon previous work by introducing a larger gas cell, allowing the shocks to evolve in 3-D, and a second counter-propagating shock, allowing reverse shocks to be studied. X-ray backlighting (XRBL) and optical self-emission streak imaging were employed to study the shock hydrodynamics while

multi-frame and streak imaging interferometry were simultaneously used to study the radiative precursor. Experiments were conducted in Neon, Argon, Krypton and Xenon gas-fills with initial mass densities of $\rho_0 = 0.5$ or 1.6 mg/cm^3. Experiments were performed using the Orion laser facility, at AWE Aldermaston UK, which delivered ∼1.6 kJ of laser light (with a wavelength of 351 nm and pulse duration of 1 ns) to 600 μm diameter focal spots on plastic pistons on either side of a 4 mm long gas cell. Laser ablation of the pistons drove two counter-propagating radiative shocks into the gas fill, which propagated at ∼60 km/s.

Experiments primarily focused on two gas-fills, Neon at ∼0.5 mg/cm^3 and Xenon at ∼1.6 mg/cm^3. In both cases XRBL and self-emission streak imaging measured shock velocities to be constant over time, at $v_s = 60 \pm 10$ km/s, in Section 2.3.1 and Section 2.3.4. This constant velocity is expected to be due to the significantly more massive piston, on which the gas-fill had a negligible effect. Shocks were observed to evolve as semi-ellipsoids with an aspect ratio $A_r \sim 0.4$.

Comparing X-ray transmission through the post-shock and unshocked material indicated an average post-shock compressions of $\Gamma = \times 23 \pm 4$ for experiments conducted with a Neon gas-fill, measured in Section 2.3.2. This compression is significantly higher than the $\times 4$ limit for a strong shock and thus suggests significant energy is being radiated away, resulting in post-shock cooling. However, this analysis could not be repeated for experiments with a Xenon gas-fill, suggesting that the thickness of the post-shock Xenon is below the ∼40 μm resolution of the XRBL (corresponding with a compression of $\Gamma > \times 50$). This suggests that radiative shocks in Xenon are experiencing increased compression due to enhanced radiative cooling. After the shocks collided, in the centre of the gas cell, material stagnated forming a dense reverse shock structure which was found to expand at $v_{rs} = 32 \pm 14$ km/s, measured in Section 2.3.3. Estimates of X-ray attenuation, and 1-D hydrodynamic models, estimate a reverse shock compression of $\times 62 \pm 20$ for experiments with a Neon gas-fill.

Streaked and 2-D imaging of laser interferometry indicated the formation of a radiative precursor ahead of the shock front. The distance the radiative precursor extends remained

constant over the observed time and was found to extend a similar distance both directly in front of the shock and off the shock axis. The radiative precursor was estimated to extend ∼190 μm in a Neon gas-fill (measured in Section 2.4.2) and more than a factor of two further, ∼430 μm, in Xenon gas-fills (measured in Section 2.4.4). This increased radiative precursor size in Xenon is expected to be due to increased emission from the post-shock material and the lower ionization potential of Xenon. To achieve a better understanding of how the gas-fill effects the radiative precursor, experiments were conducted with Neon, Argon, Krypton and Xenon all initially filled to an initial mass density of $\rho_0 \sim 0.5$ mg/cm^3, in Section 2.4.5. This ensures that shock hydrodynamics, such as the shock velocity remained constant. However the precursor was observed to extend significantly further in higher atomic number gases, such as Krypton and Xenon, as a result of increased emission and the lower ionization potentials.

Radiative hydrodynamic simulations were performed with the 1-D code HELIOS, as described in Section 2.5.1, with a Neon gas-fill and initial mass density of $\rho_0 = 0.5$ mg/cm^3. These simulations qualitatively reproduced the evolution of the radiative shocks but significantly overestimated the shock velocity to be $v_s \sim 125$ km/s. Shocks exhibited strong radiative effects, with post-shock radiative cooling achieving an average post-shock compression of $\Gamma \sim \times 20$, similar to experimentally determined values. These simulations also predicted the formation of a radiative precursor, but its structure did not match that observed in experiments. In addition, these simulations predicted the radiative precursor would extend for ∼2000 μm, approximately ten times further than observed in experiments. By significantly reducing the laser intensity, to ∼20% of that used in experiments, similar shock velocities of $v_s \sim 60$ km/s were reproduced. However, in these simulations the average post-shock compression was significantly smaller than estimates from experiments, at $\times 12$, while the radiative precursor width was still overestimated to be ∼1000 μm.

2-D radiative hydrodynamic simulations were performed with the codes NYM and PETRA, as discussed in Section 2.5.2. Simulations were run for both gas fills: Neon and Xenon with initial mass densities of $\rho_0 = 0.5$ and $\rho_0 = 1.6$ mg/cm^3 respectively. In general, these

simulations resembled experimental results more closely than HELIOS simulations. Radiative precursors predicted by these 2-D simulations matched the structure of those observed in experiments. However, these simulations overestimated the post-shock velocity (to be $v_s \sim 105$ km/s for Neon and $v_s \sim 82$ km/s for Xenon), the post-shock compression ($\Gamma \sim \times 30$ for Neon) and the radiative precursor width ($\sim$360 for Neon and $\sim$1470 for Xenon).

Previous radiative shock experiments described in the literature, discussed in Section 1.7.1, have primarily focused on driving single radiative shocks in Xenon gas-fills [Drake et al., 2011] or low density foams [Keiter et al., 2002] with mass densities ranging from $\rho_0 = 0.2$ to 33 mg/cm^3 [Dizière et al., 2011, Bozier et al., 1986]. Shock velocities of $v_s = 50 - 80$ km/s are typically achieved and post-shock temperatures of $T_{ps} \sim 15 - 30$ eV are estimated [Fleury et al., 2002, Keiter et al., 2002, Singh et al., 2017]. The majority of these experiments are also conducted with narrow shock tubes, resulting in quasi-planar shocks and the formation of 'wall shocks' [Doss et al., 2010]. Experiments presented in Chapter 2 add unique results to this body of literature. While experiments were performed with similar mass densities of $\rho_0 = 0.5$ or 1.6 mg/cm^3, a variety of different noble gas fills were used to examine how radiative effects change with atomic species. Similar shock velocities of $v_s = 60 \pm 10$ km/s were achieved and XRBL was used to estimate a post-shock compression of $\Gamma > \times 20$, agreeing with estimates for previous experiments [Drake et al., 2011].

4.1.2 Radially expanding shock experiments

Experiments described in Chapter 3 presented a new pulsed power experimental configuration for studying radiative shocks. These experiments build upon previous work, discussed in Section 1.7.2, which suffered from limited diagnostic access. In addition radiative effects occurred on spacial scales larger than the experiment, limiting studies of the radiative precursor and making it impossible to determine electron densities with interferometry diagnostics. To solve these problems the 'inverse liner z-pinch' experimental configuration was designed to produce radially expanding radiative shocks. Experiments were conducted

on the MAGPIE pulsed power facility, at Imperial College London in the UK. A current of ∼1 MA was passed through a 100 μm thick liner, with an interior diameter of 11 mm, and returned through a central cathode. This drove cylindrically expanding radiative shocks into a surrounding Neon, Argon, Krypton or Xenon gas-fill, with an initial mass density of $\rho_0 \sim 0.04$ mg/cm^3. Shocks propagated at a constant velocity of $v_s \sim 10$ km/s for over 500 ns, measured in Section 3.4. These experiments were diagnosed with a combination of multiframe self-emission imagining, laser interferometry, optical spectroscopy and magnetic probes.

Experiments initially focused on Argon gas-fills with an initial mass density of $\rho_0 \sim 0.04$ mg/cm^3. Shock velocities ranging from $6.9-13.8$ km/s were achieved and a positive correlation was found with the peak MAGPIE current in Section 3.4. Shock launch times were found to also vary significantly between $135 - 179$ ns after current start, but no correlation was found with the MAGPIE current. Models of a snowplough explosion, performed in Section 3.4.4, indicate that the constant shock velocity is most likely a result of ablation of a small part of the liner and not due to magnetic fields advected in the shock, confirming results from Section 3.4.3.

Laser interferometry revealed that shocks exhibited a structure similar to a blast wave and optical spectroscopy determined a post-shock temperature of $T_{ps} = 2.0 \pm 0.5$ eV and ionization of $Z_{ps} = 0.8 \pm 0.3$, measured in Section 3.5.1. This closely matched predictions made by the radiative shock model developed in 1.6.4. The formation of a radiative precursor is observed, extending ∼4 mm ahead of the shock front with a peak ionization of $Z \sim 4$, measured in Section 3.5. Interferometry and optical spectroscopy diagnostics disagreed on ionization and temperature in the radiative precursor region indicating that this region is not in LTE and photo-ionization results in a small fraction of ionized ions dominating the emission spectrum, matching conclusions by Burdiak et al. [Burdiak et al., 2014].

In addition, experiments were conducted with Neon, Argon, Krypton and Xenon all initially filled to an initial mass density of $\rho_0 \sim 0.04$ mg/cm^3. This ensures that shock hydrodynamics, such as the shock velocity, remained constant, while radiative effects could be

varied. The precursor was observed to extend significantly further in higher atomic number gases, such as Krypton and Xenon, as a result of increased emission and the lower ionization potentials, confirming results from Chapter 2.

Previous radiative shock experiments have been conducted on the MAGPIE facility using radial foils as discussed in Section 1.7.2. These experiments typically used lower density gas fills, with a mass density of $\rho_0 = 0.004 - 0.008$ mg/cm^3 and foils with a thickness of $1 - 15$ μm. Ablation of the foil drove shocks at a constant velocity of $v_s \sim 30$ km/s, several times faster than that observed in these experiments. Previous experiments also saw increased radiative effects with heavy gases [Skidmore, 2013]. However, the formation of post-shock instabilities, such as the thermal-cooling instability, was also observed which are not present in these experiments.

These experiments built on the work performed on radially converging shocks by Burdiak et al. (detailed in Section 1.7.2). While converging shock experiments observed multiple shocks, driven by different mechanisms, experiments performed for this thesis launched a single shock. These shocks were reported to have been launched due to the magnetic pressure exceeding the material yield strength of the liner or due to the melting of the liner. However, these mechanisms were found to not be present in these experiments. Stainless steel liners present much higher material yield strengths which were not exceeded and the larger diameter liners resulted in lower current densities that were insufficient to melt the liner, as described in Section 3.4.2.

Key shock parameters measured in these experiments and previous work are summarised in Table 4.1. The shock launch times in these experiments were comparable to the magnetic pressure loading driven shocks seen in previous experiments for both 6 mm diameter Aluminium and 10 mm diameter Copper liners. However, shock velocities observed in these experiments were slower than those observed in converging shock experiments, e.g. shocks launched from 6 mm diameter Aluminium liners propagated with a velocity of $v_s \sim 20$ km/s, possibly due to the increased mass density. However, converging shocks from the larger

	These experiments Expanding shocks	**Previous experiments Converging shocks**
Liner material	Stainless steel (AISI 321)	Aluminium (AL 6061)
Liner inner-diameter [mm]	11	5.8
Liner outer-diameter [mm]	11.2	6
Liner wall thickness [μm]	100	90
Liner length [mm]	16/20	14
Gas species	Argon	Argon
Gas fill pressure P_0 [mbar]	24	7
Gas fill mass density ρ_0 [mg/cm^3]	0.04	0.01
Shock velocities v_s [km/s]	$6.9 - 13.8$	$14 - 20$
Shock launch time [ns]	$135 - 179$	150

Table 4.1: Comparison of key shock parameters measured in these experiments on radially expanding shocks and previous work on radially converging shocks detailed in Section 1.7.2.

diameter, 10 mm, Copper liners yielded shock velocities of $v_s \sim 14$ km/s, similar to that found in these experiments.

A significant limitation of the previous experiments on radially converging shocks was the experimental size, limited to the diameter of the liner. This prevented absolute measurements of the electron density as fringes could not be traced to a position of zero phase shift. The result was that only relative changes in electron density were known. The radially expanding geometry, introduced in this Thesis removes this problem by using a large gas cell, allowing the radiative precursor to develop over several millimetres. Publications on the radially converging shocks correctly assumed that there was a sizeable offset in absolute electron density [Burdiak et al., 2015]. This is evident when plotting average ionization from both experiments together, offset so that the shock fronts coincide, shown in Fig 4.1. A significantly larger radiative precursor is seen in this work, comparable to the diameter of the imploding liner (6 mm), with higher peak ionizations.

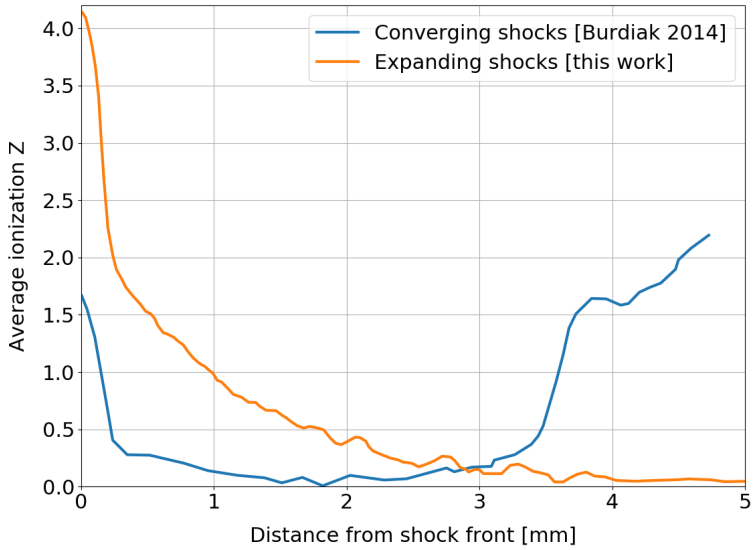


Figure 4.1: Average ionization in the radiative precursor from converging shock experiments [Burdiak et al., 2015] and this work.

4.2 Future work

4.2.1 Post-shock structure in laser driven experiments

Counter-propagating radiative shock experiments, described in Chapter 2, observed dense structures in the post-shock region. Dark spikes were observed in XRBL images from experiments with light gases, such as Neon, but not observed in heavy gases, such as Xenon, as shown in Fig 4.2.a. These dark spikes have a width of ∼100 μm and are believed to be piston material poking through into the layer of post-shock Neon. However, these effects are not observed in 2-D radiative hydrodynamic simulations with Neon gas-fill. The reason for this is not yet understood but may be due to the growth of perturbations in the piston material. In contrast, simulations indicate that perturbations should be present in Xenon gas-fill experiments, leading to mixing between the piston material and post-shock Xenon. At the tip of the shock small, ∼30 μm, spike shaped perturbations are present, seen in Fig 4.2.b. This is bellow the XRBL resolution of 80 μm and thus is unlikely to be visible with this diagnostic. However, to the sides of the shock much larger, reaching ∼200 μm after

30 ns, perturbations were observed, as seen in Fig 4.2.c. These should be visible in XRBL images but are not observed in experiments. These perturbations appears to have a degree of vorticity and may have formed due to the sheer between the shock and ambient gas, indicating that these are possibly Kelvin-Helmholtz instabilities.

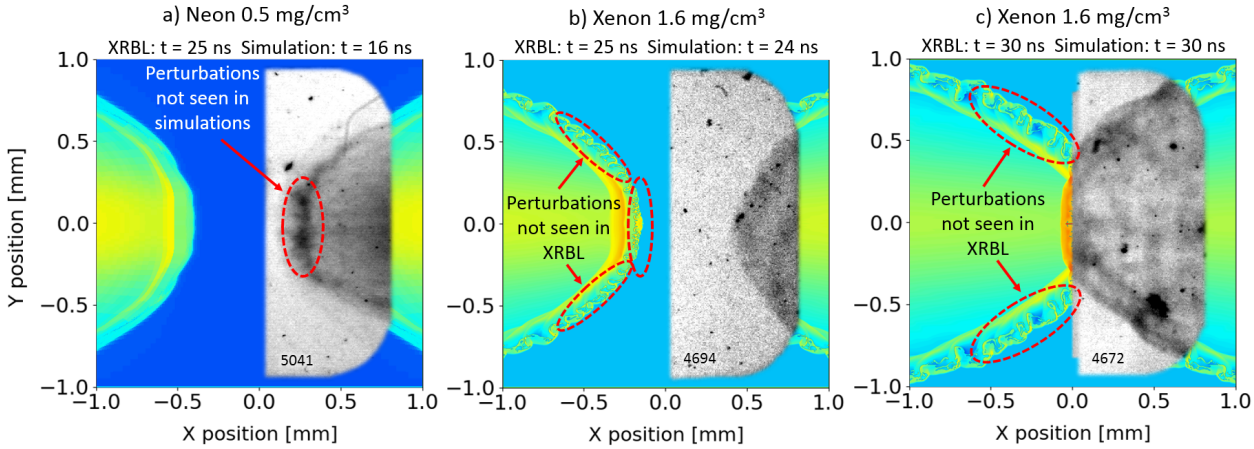


Figure 4.2: XRBL images shown with 2-D simulation predicted densities. a) Post-shock instabilities are observed in XRBL images but not simulations for Neon gas-fills with an initial mass density of 0.5 mg/cm^3. b-c) Post-shock instabilities are observed in simulations but not XRBL images for Xenon gas-fills with an initial mass density of 1.6 mg/cm^3.

To understand this discrepancy between simulation and experimental results, future experiments aim to be performed on the Shenguang II laser facility in Shanghai China [Lin et al., 1999]. This Nd:glass laser facility consists of eight long pulse beams, each capable of delivering up to 750 J with a wavelength of 1053 nm and pulse duration of 1 ns. Frequency tripling to a wavelength of 351 nm reduces the beam energy to ∼400 J. This facility also features a 1 kJ short pulse beam with a wavelength 1053 nm and pulse duration of $1 - 10$ ps [Xu et al., 2008].

These experiments aim to initially repeat experiments conducted on the Orion laser facility but with a higher resolution XRBL diagnostic. Higher spatial resolution can be achieved by placing larger sheets of image plate further from the gas cell target. Higher temporal resolution (thus reducing effects from motion blurring) can be achieved using the Shenguang II facility's short pulse beam. In addition, by inserting a 'step wedge' into the target the

X-ray source intensity can be characterised for each experiment, allowing the mass density in the post-shock region to be accurately determined.

One possibility for future experiments will be to produce a single radiative shock in a longer gas cell. Having the shock propagate further will allow the thickness of the post-shock material to increase, so that it's structure may be more easily probed, and allow post-shock instabilities longer to develop. This would thus allow the growth rate of these instabilities to be estimated, aiding in their identification. An additional possibility would be to field a spectrometer to determine the temperature in both the post-shock and radiative precursor regions, which would allow estimates from simulations to be confirmed.

4.2.2 Magnetized radially expanding radiative shocks

Experiments on the inverse liner Z-pinch, described in Chapter 3, were conducted with metal and plastic gas cell lids. Experiments with a metal lid observed electrical breakdown between the top of the liner and the gas cell lid, confirmed by self-emission images as shown in Fig 4.3.a. This breakdown could have resulted in current returning to ground through the sides of the gas cell, generating a toroidal magnetic field and pre-magnetize the gas-fill, as described in Fig 4.3.b.

In order to prevent electrical breakdown, a 5 mm thick laser cut acrylic insulating lid was used in later experiments. Inspection of the lid after experiments indicated that no significant electrical breakdown occurred and different magnetic fields were observed by the magnetic probe, as shown in Fig 4.4. For experiments with a plastic lid the measured magnetic field is initially negative before reversing after 250 ns, coinciding with the approximate time the shock is launched. However, for experiments with the metal lid this feature is absent and instead the magnetic field remains positive at all times, reaching significantly higher magnetic fields of $\sim$5 T. This change in lid material had no detectable effect on the evolution of the shock.

To confirm the generation of a toroidal magnetic field in experiments with a metal lid,

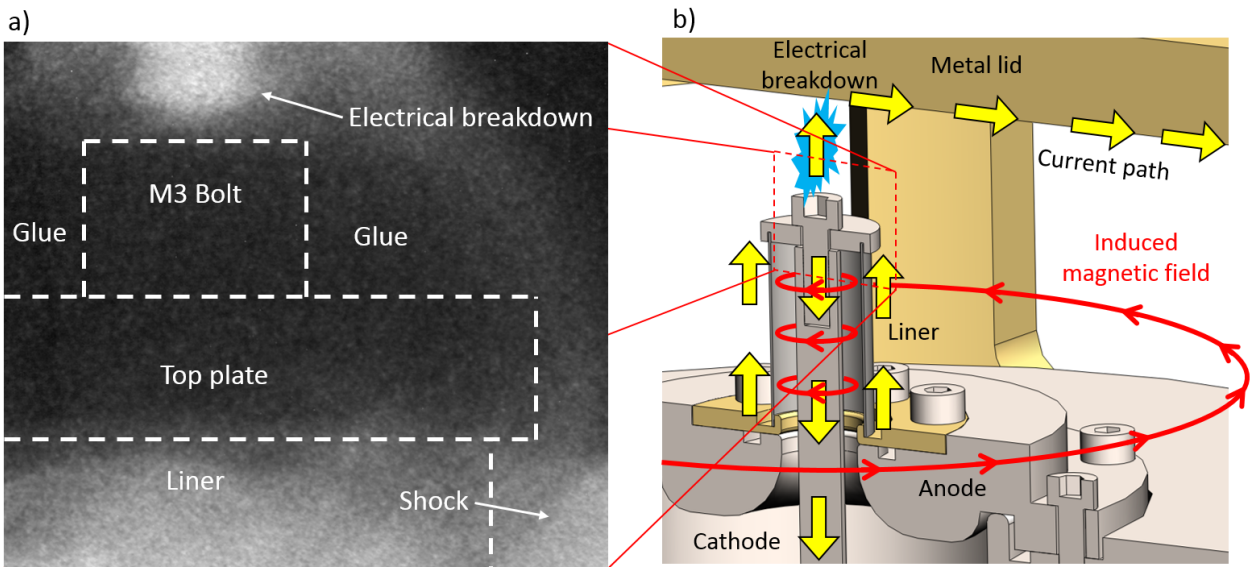


Figure 4.3: a) Self-emission image, from experiment s0109_17, of the top of the liner showing optical emission from electrical breakdown. b) 3D CAD model of the liner indication how the pre-magnetization of the gas-fill may occur.

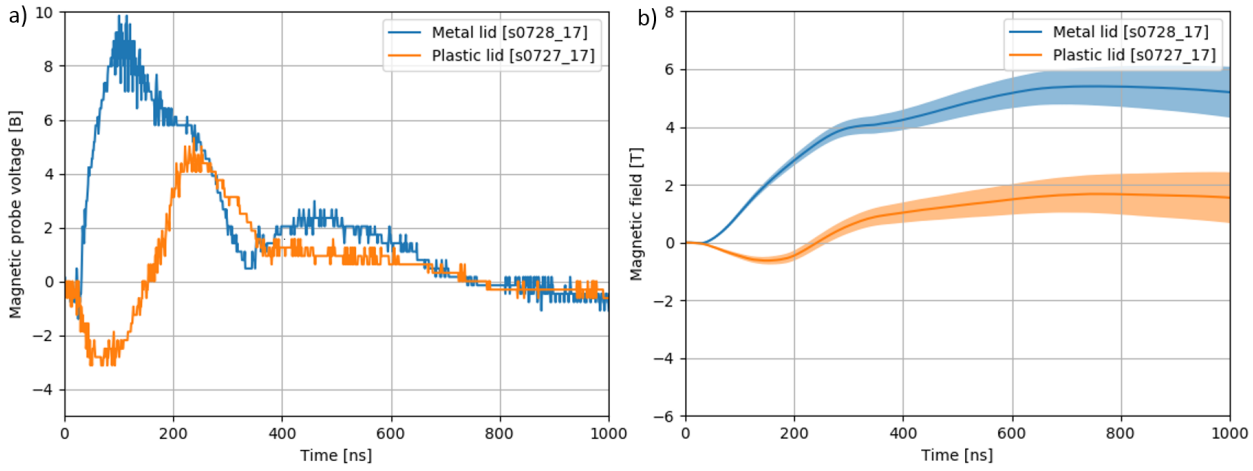


Figure 4.4: Magnetic probe signals from an experiment with a metal gas cell lid, experiencing electrical breakdown, and a experiment with a plastic lid. a) Raw voltages recorded by magnetic probes. b) The signal was integrated to yield the magnetic field, the shaded region indicates the standard error.

and further understand the difference in magnetic probe signals in Fig 4.4, more detailed measurements of the magnetic field are required. Faraday polarimetry offers a non-intrusive method of obtaining a 2-D image of the magnetic field [Swadling et al., 2014]. Future experiments will use this diagnostic to further investigate the magnetic field in this experiment. In addition, the generation of a toroidal magnetic field opens up an interesting expansion to

these experiments and a method of pre-magnetizing the gas-fill with the MAGPIE current. By connecting the top of the liner to the metal gas cell lid with a known resistance, a portion of the MAGPIE current may be discharged through the metal lid. This will generate a controllable magnetic field, a portion of which may be frozen into the plasma.

4.2.3 Seeding perturbation in radially expanding radiative shocks

The uniformity and reproducibility of the radiative shocks produced with the inverse liner Z-pinch, described in Chapter 3, make it suitable for the study of perturbed radiative shocks and radiative instabilities. A diagram of the process to create perturbed shocks is shown in Fig 4.5. Controllable perturbations may be seeded into the shock by carving grooves on the surface of the liner. This drives modulated radiative shocks with peaks in the shock front position correlating with thinner regions of the liner. The spacing and depth of these grooves allows the wavelength and amplitude of perturbations in the radiative shock to be controlled. The delay between the peak and trough of the resulting radiative shock is approximated as the difference in sound crossing time. The speed of sound in stainless steel is ∼5.8 km/s [Engineering ToolBox, 2014] and thus the delay in traversing 50 μm is ∼8.6 ns. Assuming the radiative shocks proceed to propagate at ∼10 km/s, the amplitude of the perturbation is expected to be $\delta \sim 86$ μm.

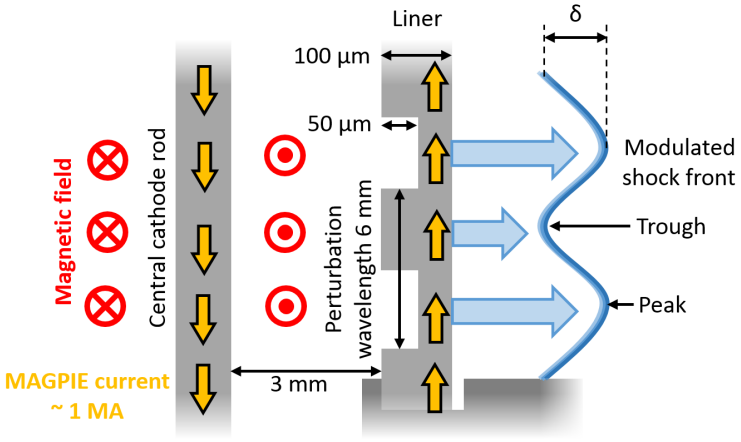


Figure 4.5: Process to create perturbed shocks on the inverse liner Z-pinch platform.

Preliminary experiments have been conducted on the MAGPIE facility which verify this method. Toroidal grooves were carved into the inner surface of the liner as described in Fig 4.6. Three 3 mm wide grooves were carved to a depth of 50 μm (half the liner wall thickness), separated by 3 mm, thus crudely approximating a sinusoidal wave with a wavelength of 6 mm. This was achieved by rotating the liner on a miniature lathe and using a stationary cutting tool with a 60° blade. Some of the liners were slightly tapered and ~30 μm wider at one end. In these cases groove depths were measured relative to the local liner surface, resulting in a consistent wall thickness at the grooves.

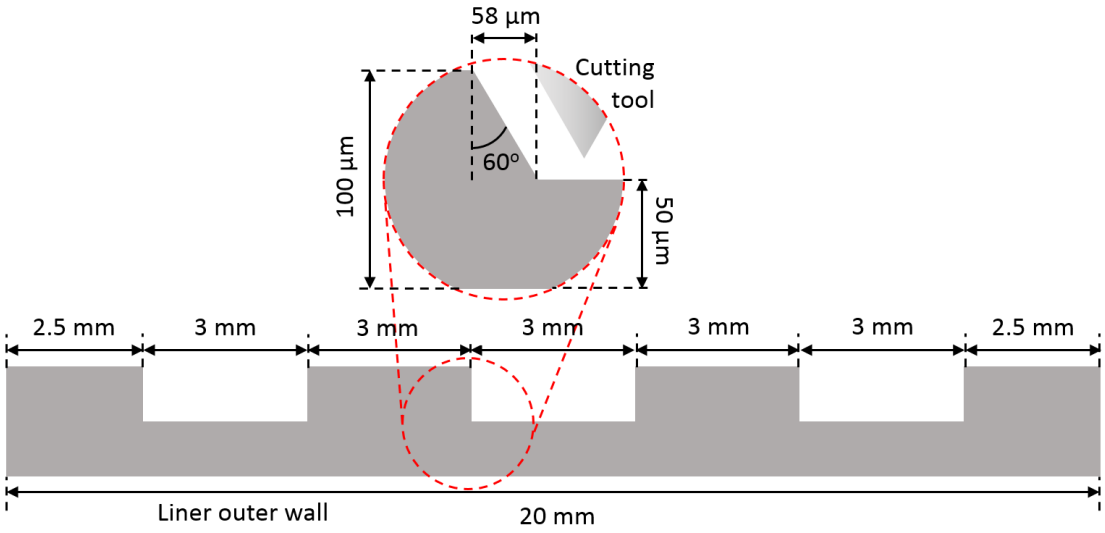


Figure 4.6: Details of grooves cut onto the inside surface of the liner. Not to scale.

Optical self-emission images (captured with the fast multiframe camera described in Section 3.3.3) are shown in Fig 4.7 for experiment s0209_17. The liner is on the right hand side and the shock propagates to the left. The shock is modulated with a wavelength of 6 mm, with peaks corresponding with the location of the grooves in the liner as expected. However, the width of the troughs is significantly smaller than that of the peaks. This could be due to material from the peaks falling into the troughs, which correlates with the increased self-emission intensity observed in the troughs.

The velocity of both the peaks and troughs was determined by measuring the shock front position as described in Section 3.4. profiles were taken through the peak and trough, at

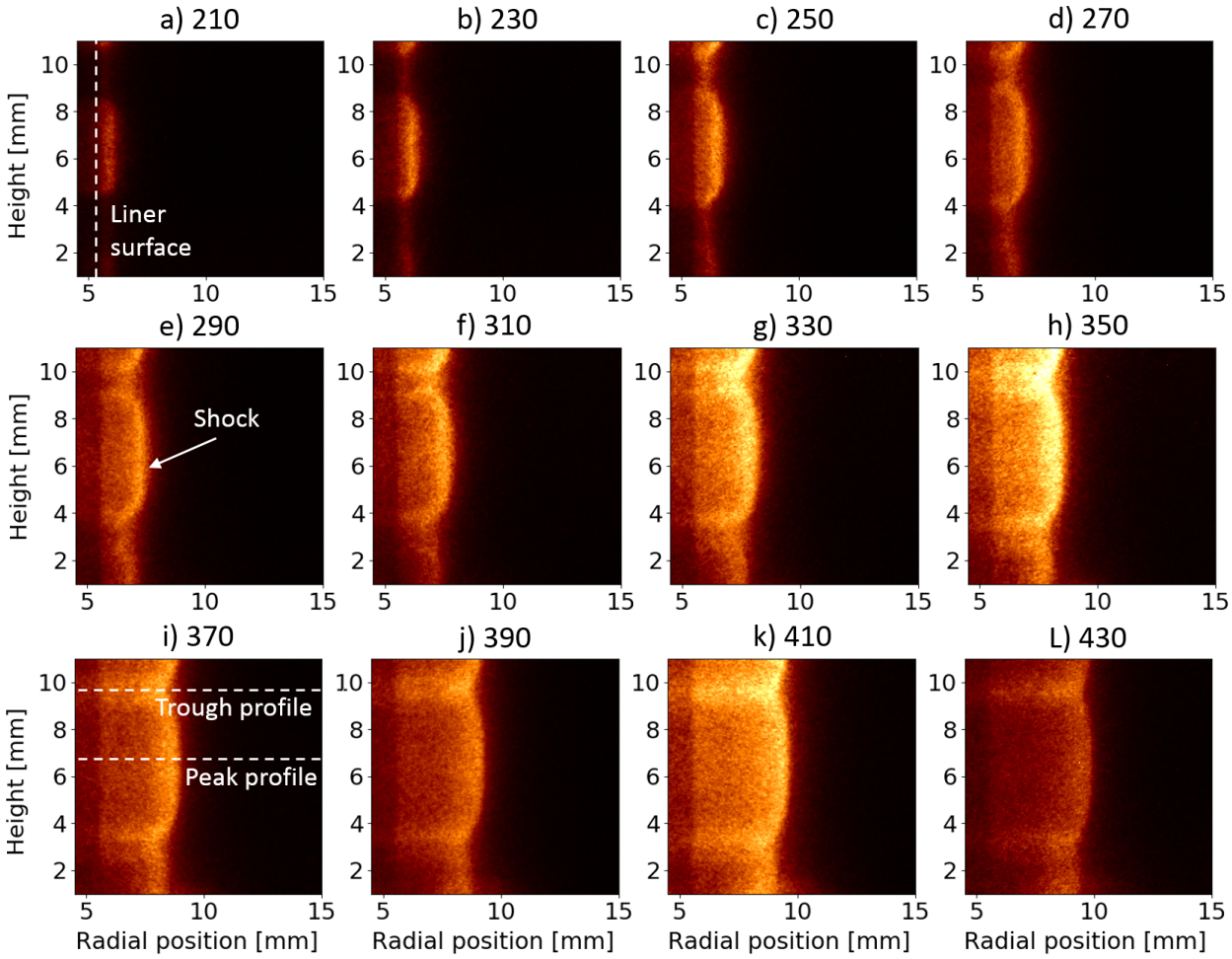


Figure 4.7: Optical self-emission images from the perturbed shock experiment s0209_17.

a height of 4.5 mm and 6.5 mm respectively. The shock front positions as a function of time are shown in Fig 4.7 for two identical experiments: s0208_17 and s0209_17. In both experiments, the shock front positions closely follow linear trendlines with similar gradients, indicating speeds of $v_s = 16.6 \pm 0.5$ km/s for experiment s0208_17 and $v_s = 17.5 \pm 0.4$ km/s for experiment s0209_17. These velocities are significantly faster than velocities observed in non-perturbed shocks of $6.9 - 13.8$ km/s and may be due to the reduced total liner mass. The perturbation amplitude (distance between the peak and trough) was measured to be constant at $\delta = 155 \pm 47$ μm for experiment s0208_17 and $\delta = 144 \pm 46$ μm for experiment s0209_17.

Extrapolating these trendlines to the liner surface at 5.6 mm yielded launch times of

$t_L = 124 \pm 8$ and 135 ± 7 ns for the peak and trough in experiment s0208_17 and $t_L = 177 \pm 1$ and 186 ± 2 ns for the peak and trough in experiment s0209_17 (comparable to launch times for experiments with liners without grooves). For experiment s0209_17 the difference in launch time between the peak and trough is 9 ± 2 ns. This closely agrees with the estimate of ~8.6 ns from the sounds crossing time (errors in launch times for experiment s0208_17 were too large to define a meaningful difference in launch time).

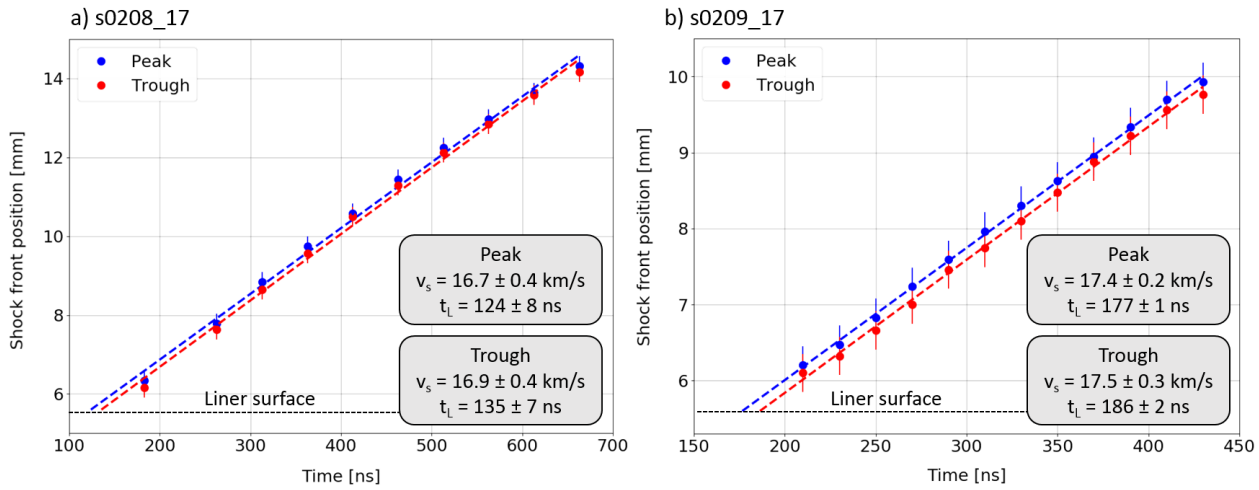


Figure 4.8: Position of the shock front at the peaks and toughs of the perturbed shock as a function of time. Profile position show in shown in Fig 4.7.i. a) Experiment s0208_17. b) Experiment s0209_17.

Fig 4.9 shows pictures of two liners before and after an experiment. The thin-walled regions of the liner, where the grooves were carved, have completely disintegrated leaving behind a series of rings. Due to the thinner liner wall thickness the current density is expected to approximately double. Following the analysis in Section 3.4.2, this would yield a four-fold increase in the action integral in these regions achieving a value of $J \sim 7$ A^2s/m^4. However, this is significantly smaller than the action integral predicted to melt the liner, of $J \sim 32$ A^2s/m^4. In addition, self-emission imaging, shown in Fig 4.7 shows no signs of movement in the liner.

Laser interferometry performed on this experiment shows the modulated shock in higher resolution, shown in the raw interferogram in Fig 4.10.a and the processed map of line



Figure 4.9: a) Picture of a liners before an experiment. b) Picture of a liner after an experiment. The thin-walled regions of the liner have completely disintegrated leaving a series of rings.

integrated electron density, $n_e L$, in Fig 4.10.b. As with the non-modulated shocks produced with this experimental platform, a radiative precursor proceeds the shock.

Horizontal profiles were taken through the peaks and troughs, at a height of 6.6 mm and 9.6 mm respectively and are shown in Fig 4.10.c. Higher values of integrated electron density, $n_e L$, were observed in the troughs, consistent with enhanced self-emission observed in Fig 4.7. Applying an Abel inversion, as described in Section 2.2.3, produces the profiles of electron density as a function of radius, shown in Fig 4.10.d. The shock front is located at the maxima in electron density at 10.65 mm and 10.95 mm for the peak and trough respectively, indicating a perturbation amplitude of $\delta \sim 300$ μm. Peak electron densities of $n_e = 4 - 5 \times 10^{18}$ cm^{-3} were observed in these experiments, approximately double that which was observed in experiments without perturbations, $n_e \sim 2.5 \times 10^{18}$ cm^{-3} measured in Section 3.5.

Following the successful demonstration of this experimental platform for generating perturbed radiative shocks, future experiments aim to use this platform for studying radiative instabilities. One such instability of interest is the Vishniac overstability, described in Fig 4.11.a-b. This instability can occur in blast waves with an effective adiabatic index of $\gamma < 1.2$, which corresponds to a post-shock compression of $\Gamma > \times 11$ [Vishniac, 1983, Grun et al., 1991]. This instability is caused by a misalignment between the ram pressure, which acts opposite the direction of propagation, and the thermal pressure, which acts perpendicular to the shock

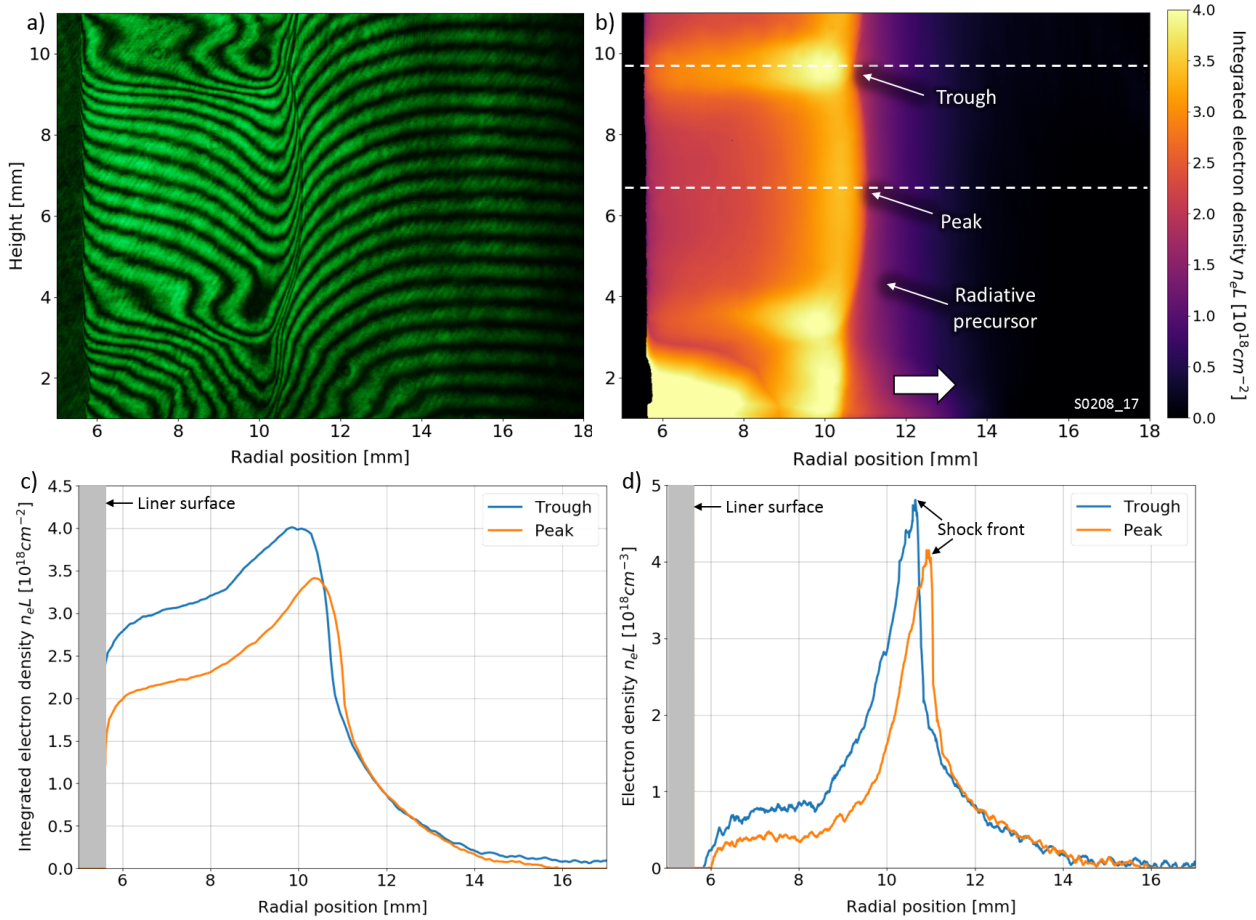


Figure 4.10: a) Laser interferometry from experiment s0208_17, taken 480 ns after current start. b) Processed map of integrated electron density, n_eL. c) Horizontal profiles of integrated electron density. d) Abel inversions showing profiles of electron density as a function of radius.

front. This causes material to flow from the peaks of the blast wave to the troughs. Material then accumulates in the troughs causing these to become peaks of increased amplitude, and vice versa. The process then reverses, oscillating and growing in amplitude over time until the perturbation amplitude is comparable to the shock thickness, at which point the shock begins to fragment. This process is believed to be present in supernova remnants and be partially responsible for the observed filamentation structure, e.g. seen in the Crab Nebula shown in Fig 1.1.a.

This instability was reproduced in the laboratory by Grun et al. [Grun et al., 1991] using laser produced blast waves in a low density gas-fill. Blast waves produced in Nitrogen,

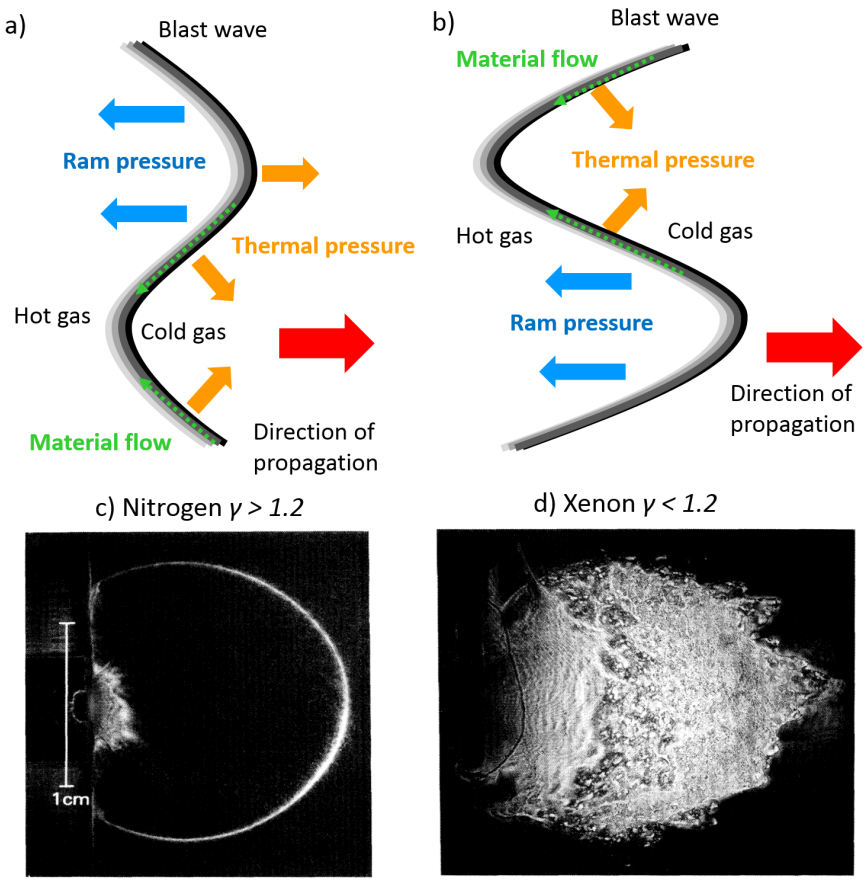


Figure 4.11: Description of the Vishniac overstability in a blast wave. a) Ram pressure acts opposite the direction of propagation while thermal pressure acts perpendicular to the shock front. This misalignment of pressures forces materials into the troughs. b) When the effective adiabatic index of $\gamma < 1.2$ the troughs grow to become peaks of increased amplitude and the process reverses. c-d) Schlieren imaging from laser blast waves produced in Nitrogen, with $\gamma > 1.2$, and Xenon, with $\gamma < 1.2$, reproduced from [Grun et al., 1991]

with $\gamma > 1.2$, observed no signs of instabilities as shown in 4.11.c. However, blast waves produced in Xenon, with $\gamma < 1.2$, yielded a turbulent and fragmented blast wave indicating the formation of a Vishniac overstability as shown in 4.11.d. In these experiments the initial perturbations were not seeded and so were set by variation in the beam intensity and target surface. However, using the inverse liner Z-pinch experimental platform, specific perturbations could be seeded into the radiative shocks allowing this instability to be studied.

Theory suggests that the Vishniac overstability grows faster for smaller wavelength perturbations, with $\Gamma_{vish} \propto \sqrt{\lambda_p}$ where λ_p is the perturbation wavelength. Therefore inverse

liner Z-pinch experiments were conducted with perturbation wavelengths of 4 mm and 2 mm. However, in both cases the resulting radiative shocks were not modulated and indistinguishable from those produced with a smooth liner. In addition, an experiment with grooves carved on the liners outside surface, with a wavelength of 4 mm, also failed to produce a modulated shock. The reason for this is not yet understood, but may be due to the peaks expanding before the troughs are launched. Therefore shallower grooves may be able to mitigate this problem by reducing the time between shock launched and therefore the amount the peaks have expanded before the troughs are launched. Future experiments hope to further explore this method of producing controllable perturbed radiative shocks.

Licenses to reuse figures

A list of figures from external sources is provided in the following Table. Written permission has been obtained for all items and these permissions are shown on the subsequent pages.

Figures	Source and copyright holder
Fig 1.1.a	[NASA and ESA, 2005] Creative Commons CC-BY license
Fig 1.1.b	[J. Morse/STScI and ESA, 1995] Public domain
Fig 1.2.a	Physics of Plasmas [Edwards et al., 2011]
Fig 1.2.b	Physics of Plasmas [Pak et al., 2013]
Fig 1.3	Lawrence Livermore National Laboratory [LLNL, 2010] (Creative Commons CC-BY-NC-SA license)
Fig 1.7, 3.4	Imperial College London [Burdiak, 2012]
Fig 1.12	High Energy Density Physics [Hansen et al., 2014]
Fig 1.17.b	Physical Review Letters [Bozier et al., 1986]
Fig 1.18	Physical Review Letters [Keiter et al., 2002]
Fig 1.19.a	Laser and Particle Beams [Fleury et al., 2002]
Fig 1.19.b	Physical Review Letters [Bouquet et al., 2004]
Fig 1.20	Laser and Particle Beams [González et al., 2006]
Fig 1.21	Physics of Plasmas [Koenig et al., 2006]
Fig 1.22, 2.1.b	High Energy Density Physics [Drake et al., 2011]
Fig 1.23	Astrophysics and Space Science [Dizière et al., 2011]
Fig 1.24.a	High Energy Density Physics [Falize et al., 2012]
Fig 1.24.b	Nature Communications [Cross et al., 2016] (Creative Commons CC-BY license)
Fig 1.25	High Energy Density Physics [Singh et al., 2017]
Fig 1.26.b	Plasma Physics and Controlled Fusion [Lebedev et al., 2005]
Fig 1.26.d	Physics of Plasma [Suzuki-Vidal et al., 2012] (Creative Commons CC-BY license)
Fig 1.27, 1.28, 1.29	Journal of Plasma Physics [Burdiak et al., 2015]
Fig 2.2, 2.3, 2.4.a	Plasma Physics and Controlled Fusion [Hopps et al., 2015]
Fig 2.7, 2.8	High Power Laser Science and Engineering [Spindloe et al., 2017] (Creative Commons CC-BY license)
Fig 2.13	Review of Scientific Instruments [Workman and Kyrala, 2001]
Fig 3.10.a	Imperial College London [Skidmore, 2013]
Fig 4.11.c-d	Physical Review Letters [Grun et al., 1991]

AIP PUBLISHING LICENSE
TERMS AND CONDITIONS

Apr 06, 2018

This Agreement between Thomas Clayson ("You") and AIP Publishing ("AIP Publishing") consists of your license details and the terms and conditions provided by AIP Publishing and Copyright Clearance Center.

License Number	4322990828533
License date	Apr 06, 2018
Licensed Content Publisher	AIP Publishing
Licensed Content Publication	Physics of Plasmas
Licensed Content Title	Radiative shocks produced from spherical cryogenic implosions at the National Ignition Facility
Licensed Content Author	A. Pak, L. Divol, G. Gregori, et al
Licensed Content Date	May 1, 2013
Licensed Content Volume	20
Licensed Content Issue	5
Type of Use	Thesis/Dissertation
Requestor type	Student
Format	Print and electronic
Portion	Figure/Table
Number of figures/tables	1
Title of your thesis / dissertation	Experimental study of radiative shocks in noble gases on the Orion laser and the MAGPIE pulsed-power facility
Expected completion date	Apr 2018
Estimated size (number of pages)	290
Requestor Location	Thomas Clayson Imperial College London Exhibition Road London, London SW7 2AZ United Kingdom Attn: Thomas Clayson
Billing Type	Invoice
Billing Address	Thomas Clayson Imperial College London Exhibition Road London, United Kingdom SW7 2AZ Attn: Thomas Clayson
Total	0.00 USD
Terms and Conditions	

AIP Publishing -- Terms and Conditions: Permissions Uses

AIP Publishing hereby grants to you the non-exclusive right and license to use and/or distribute the Material according to the use specified in your order, on a one-time basis, for the specified term, with a maximum distribution equal to the number that you have ordered. Any links or other content accompanying the Material are not the subject of this license.

AIP PUBLISHING LICENSE
TERMS AND CONDITIONS

Apr 06, 2018

This Agreement between Thomas Clayson ("You") and AIP Publishing ("AIP Publishing") consists of your license details and the terms and conditions provided by AIP Publishing and Copyright Clearance Center.

License Number	4322990902373
License date	Apr 06, 2018
Licensed Content Publisher	AIP Publishing
Licensed Content Publication	Physics of Plasmas
Licensed Content Title	The experimental plan for cryogenic layered target implosions on the National Ignition Facility—The inertial confinement approach to fusion
Licensed Content Author	M. J. Edwards, J. D. Lindl, B. K. Spears, et al
Licensed Content Date	May 1, 2011
Licensed Content Volume	18
Licensed Content Issue	5
Type of Use	Thesis/Dissertation
Requestor type	Student
Format	Print and electronic
Portion	Figure/Table
Number of figures/tables	1
Title of your thesis / dissertation	Experimental study of radiative shocks in noble gases on the Orion laser and the MAGPIE pulsed-power facility
Expected completion date	Apr 2018
Estimated size (number of pages)	290
Requestor Location	Thomas Clayson Imperial College London Exhibition Road London, London SW7 2AZ United Kingdom Attn: Thomas Clayson
Billing Type	Invoice
Billing Address	Thomas Clayson Imperial College London Exhibition Road London, United Kingdom SW7 2AZ Attn: Thomas Clayson
Total	0.00 USD

Terms and Conditions

AIP Publishing -- Terms and Conditions: Permissions Uses

AIP Publishing hereby grants to you the non-exclusive right and license to use and/or distribute the Material according to the use specified in your order, on a one-time basis, for the specified term, with a maximum distribution equal to the number that you have ordered. Any links or other content accompanying the Material are not the subject of this license.

ELSEVIER LICENSE
TERMS AND CONDITIONS

Apr 06, 2018

This Agreement between Thomas Clayson ("You") and Elsevier ("Elsevier") consists of your license details and the terms and conditions provided by Elsevier and Copyright Clearance Center.

License Number	4322991131217
License date	Apr 06, 2018
Licensed Content Publisher	Elsevier
Licensed Content Publication	High Energy Density Physics
Licensed Content Title	Numerical simulations of Mach stem formation via intersecting bow shocks
Licensed Content Author	E.C. Hansen,A. Frank,P. Hartigan,K. Yirak
Licensed Content Date	Dec 1, 2015
Licensed Content Volume	17
Licensed Content Issue	n/a
Licensed Content Pages	5
Start Page	135
End Page	139
Type of Use	reuse in a thesis/dissertation
Intended publisher of new work	other
Portion	figures/tables/illustrations
Number of figures/tables/illustrations	1
Format	both print and electronic
Are you the author of this Elsevier article?	No
Will you be translating?	No
Original figure numbers	Figure 1
Title of your thesis/dissertation	Experimental study of radiative shocks in noble gases on the Orion laser and the MAGPIE pulsed-power facility
Expected completion date	Apr 2018
Estimated size (number of pages)	290
Requestor Location	Thomas Clayson Imperial College London Exhibition Road London, London SW7 2AZ United Kingdom Attn: Thomas Clayson
Publisher Tax ID	GB 494 6272 12
Total	0.00 USD
Terms and Conditions	

INTRODUCTION

American Physical Society
Reuse and Permissions License

05-Apr-2018

This license agreement between the American Physical Society ("APS") and Thomas Clayson ("You") consists of your license details and the terms and conditions provided by the American Physical Society and SciPris.

Licensed Content Information

License Number:	**RNP/18/APR/003025**
License date:	05-Apr-2018
DOI:	10.1103/PhysRevLett.57.1304
Title:	Experimental Observation of a Radiative Wave Generated in Xenon by a Laser-Driven Supercritical Shock
Author:	J. C. Bozier et al.
Publication:	Physical Review Letters
Publisher:	American Physical Society
Cost:	USD $ 0.00

Request Details

Does your reuse require significant modifications: No

Specify intended distribution locations:	UK & Commonwealth (excluding Canada)
Reuse Category:	Reuse in a thesis/dissertation
Requestor Type:	Student
Items for Reuse:	Figures/Tables
Number of Figure/Tables:	1
Figure/Tables Details:	Figure 2.b
Format for Reuse:	Print and Electronic
Total number of print copies:	Up to 1000

Information about New Publication:

University/Publisher:	Imperial College London
Title of dissertation/thesis:	Experimental study of radiative shocks in noble gases on the Orion laser and the MAGPIE pulsed-power facility
Author(s):	Thomas Clayson
Expected completion date:	Apr. 2018

License Requestor Information

Name:	Thomas Clayson
Affiliation:	Individual
Email Id:	thomasalbertclayson@gmail.com
Country:	United Kingdom

CAMBRIDGE UNIVERSITY PRESS LICENSE
TERMS AND CONDITIONS

Apr 05, 2018

This Agreement between Thomas Clayson ("You") and Cambridge University Press ("Cambridge University Press") consists of your license details and the terms and conditions provided by Cambridge University Press and Copyright Clearance Center.

License Number	4322610075695
License date	Apr 05, 2018
Licensed Content Publisher	Cambridge University Press
Licensed Content Publication	Laser and Particle Beams
Licensed Content Title	A laser experiment for studying radiative shocks in astrophysics
Licensed Content Author	X. FLEURY, S. BOUQUET, C. STEHLÉ, M. KOENIG, D. BATANI, A. BENUZZI-MOUNAIX, J.-P. CHIÈZE, N. GRANDJOUAN, J. GRENIER, T. HALL, E. HENRY, J.-P. LAFON, S. LEYGNAC, V. MALKA, B. MARCHET, H. MERDJI, C. MICHAUT, F. THAIS
Licensed Content Date	Nov 13, 2002
Licensed Content Volume	20
Licensed Content Issue	2
Start page	263
End page	268
Type of Use	Dissertation/Thesis
Requestor type	Author
Portion	Text extract
Number of pages requested	1
Author of this Cambridge University Press article	No
Author / editor of the new work	Yes
Order reference number	
Territory for reuse	World
Title of your thesis / dissertation	Experimental study of radiative shocks in noble gases on the Orion laser and the MAGPIE pulsed-power facility
Expected completion date	Apr 2018
Estimated size(pages)	290
Requestor Location	Thomas Clayson Imperial College London Exhibition Road London, London SW7 2AZ United Kingdom Attn: Thomas Clayson
Publisher Tax ID	GB823847609
Billing Type	Invoice
Billing Address	Thomas Clayson Imperial College London Exhibition Road

American Physical Society
Reuse and Permissions License

05-Apr-2018

This license agreement between the American Physical Society ("APS") and Thomas Clayson ("You") consists of your license details and the terms and conditions provided by the American Physical Society and SciPris.

Licensed Content Information

License Number:	**RNP/18/APR/003024**
License date:	05-Apr-2018
DOI:	10.1103/PhysRevLett.89.165003
Title:	Observation of a Hydrodynamically Driven, Radiative-Precursor Shock
Author:	P. A. Keiter et al.
Publication:	Physical Review Letters
Publisher:	American Physical Society
Cost:	USD $ 0.00

Request Details

Does your reuse require significant modifications: No

Specify intended distribution locations:	UK & Commonwealth (excluding Canada)
Reuse Category:	Reuse in a thesis/dissertation
Requestor Type:	Student
Items for Reuse:	Figures/Tables
Number of Figure/Tables:	2
Figure/Tables Details:	Figure 1, Figure 2.a
Format for Reuse:	Electronic and Print
Total number of print copies:	Up to 1000

Information about New Publication:

University/Publisher:	Imperial College London
Title of dissertation/thesis:	Experimental study of radiative shocks in noble gases on the Orion laser and the MAGPIE pulsed-power facility
Author(s):	Thomas Clayson
Expected completion date:	Apr. 2018

License Requestor Information

Name:	Thomas Clayson
Affiliation:	Individual
Email Id:	thomasalbertclayson@gmail.com
Country:	United Kingdom

American Physical Society
Reuse and Permissions License

05-Apr-2018

This license agreement between the American Physical Society ("APS") and Thomas Clayson ("You") consists of your license details and the terms and conditions provided by the American Physical Society and SciPris.

Licensed Content Information

License Number:	**RNP/18/APR/003027**
License date:	05-Apr-2018
DOI:	10.1103/PhysRevLett.92.225001
Title:	Observation of Laser Driven Supercritical Radiative Shock Precursors
Author:	S. Bouquet et al.
Publication:	Physical Review Letters
Publisher:	American Physical Society
Cost:	USD $ 0.00

Request Details

Does your reuse require significant modifications: No

Specify intended distribution locations:	UK & Commonwealth (excluding Canada)
Reuse Category:	Reuse in a thesis/dissertation
Requestor Type:	Student
Items for Reuse:	Figures/Tables
Number of Figure/Tables:	1
Figure/Tables Details:	Figure 4
Format for Reuse:	Print and Electronic
Total number of print copies:	Up to 1000

Information about New Publication:

University/Publisher:	Imperial College London
Title of dissertation/thesis:	Experimental study of radiative shocks in noble gases on the Orion laser and the MAGPIE pulsed-power facility
Author(s):	Thomas Clayson
Expected completion date:	Apr. 2018

License Requestor Information

Name:	Thomas Clayson
Affiliation:	Individual
Email Id:	thomasalbertclayson@gmail.com
Country:	United Kingdom

CAMBRIDGE UNIVERSITY PRESS LICENSE TERMS AND CONDITIONS

Apr 06, 2018

This Agreement between Thomas Clayson ("You") and Cambridge University Press ("Cambridge University Press") consists of your license details and the terms and conditions provided by Cambridge University Press and Copyright Clearance Center.

License Number	4322950476457
License date	Apr 06, 2018
Licensed Content Publisher	Cambridge University Press
Licensed Content Publication	Laser and Particle Beams
Licensed Content Title	Astrophysical radiative shocks: From modeling to laboratory experiments
Licensed Content Author	MATTHIAS GONZÁLEZ, CHANTAL STEHLÉ, EDOUARD AUDIT, MICHEL BUSQUET, BEDRICH RUS, FRÉDÉRIC THAIS, OUALI ACEF, PATRICE BARROSO, ABRAHAM BAR-SHALOM, DANIEL BAUDUIN, MICHAELA KOZLOVÀ, THIBAUT LERY, ALI MADOURI, TOMAS MOCEK, JIRI POLAN
Licensed Content Date	Nov 28, 2006
Licensed Content Volume	24
Licensed Content Issue	4
Start page	535
End page	540
Type of Use	Dissertation/Thesis
Requestor type	Author
Portion	Text extract
Number of pages requested	1
Author of this Cambridge University Press article	No
Author / editor of the new work	Yes
Order reference number	
Territory for reuse	World
Title of your thesis / dissertation	Experimental study of radiative shocks in noble gases on the Orion laser and the MAGPIE pulsed-power facility
Expected completion date	Apr 2018
Estimated size(pages)	290
Requestor Location	Thomas Clayson Imperial College London Exhibition Road London, London SW7 2AZ United Kingdom Attn: Thomas Clayson
Publisher Tax ID	GB823847609
Billing Type	Invoice
Billing Address	Thomas Clayson Imperial College London Exhibition Road

AIP PUBLISHING LICENSE
TERMS AND CONDITIONS

Apr 06, 2018

This Agreement between Thomas Clayson ("You") and AIP Publishing ("AIP Publishing") consists of your license details and the terms and conditions provided by AIP Publishing and Copyright Clearance Center.

License Number	4322950658683
License date	Apr 06, 2018
Licensed Content Publisher	AIP Publishing
Licensed Content Publication	Physics of Plasmas
Licensed Content Title	Radiative shocks: An opportunity to study laboratory astrophysics
Licensed Content Author	M. Koenig, T. Vinci, A. Benuzzi-Mounaix, et al
Licensed Content Date	May 1, 2006
Licensed Content Volume	13
Licensed Content Issue	5
Type of Use	Thesis/Dissertation
Requestor type	Student
Format	Print and electronic
Portion	Figure/Table
Number of figures/tables	2
Title of your thesis / dissertation	Experimental study of radiative shocks in noble gases on the Orion laser and the MAGPIE pulsed-power facility
Expected completion date	Apr 2018
Estimated size (number of pages)	290
Requestor Location	Thomas Clayson Imperial College London Exhibition Road London, London SW7 2AZ United Kingdom Attn: Thomas Clayson
Billing Type	Invoice
Billing Address	Thomas Clayson Imperial College London Exhibition Road London, United Kingdom SW7 2AZ Attn: Thomas Clayson
Total	0.00 USD

Terms and Conditions

AIP Publishing -- Terms and Conditions: Permissions Uses

AIP Publishing hereby grants to you the non-exclusive right and license to use and/or distribute the Material according to the use specified in your order, on a one-time basis, for the specified term, with a maximum distribution equal to the number that you have ordered. Any links or other content accompanying the Material are not the subject of this license.

1. You agree to include the following copyright and permission notice with the reproduction of the Material:"Reprinted from [FULL CITATION], with the permission of AIP Publishing." For

ELSEVIER LICENSE
TERMS AND CONDITIONS

Apr 06, 2018

This Agreement between Thomas Clayson ("You") and Elsevier ("Elsevier") consists of your license details and the terms and conditions provided by Elsevier and Copyright Clearance Center.

License Number	4322950805883
License date	Apr 06, 2018
Licensed Content Publisher	Elsevier
Licensed Content Publication	High Energy Density Physics
Licensed Content Title	Radiative effects in radiative shocks in shock tubes
Licensed Content Author	R.P. Drake,F.W. Doss,R.G. McClarren,M.L. Adams,N. Amato,D. Bingham,C.C. Chou,C. DiStefano,K. Fidkowski,B. Fryxell,T.I. Gombosi,M.J. Grosskopf,J.P. Holloway,B. van der Holst,C.M. Huntington,S. Karni,C.M. Krauland,C.C. Kuranz,E. Larsen,B. van Leer et al.
Licensed Content Date	Sep 1, 2011
Licensed Content Volume	7
Licensed Content Issue	3
Licensed Content Pages	11
Start Page	130
End Page	140
Type of Use	reuse in a thesis/dissertation
Intended publisher of new work	other
Portion	figures/tables/illustrations
Number of figures/tables/illustrations	2
Format	both print and electronic
Are you the author of this Elsevier article?	No
Will you be translating?	No
Original figure numbers	Figure 2 and Figure 3
Title of your thesis/dissertation	Experimental study of radiative shocks in noble gases on the Orion laser and the MAGPIE pulsed-power facility
Expected completion date	Apr 2018
Estimated size (number of pages)	290
Requestor Location	Thomas Clayson Imperial College London Exhibition Road London, London SW7 2AZ United Kingdom Attn: Thomas Clayson
Publisher Tax ID	GB 494 6272 12
Total	0.00 USD
Terms and Conditions	

SPRINGER NATURE LICENSE
TERMS AND CONDITIONS

Apr 06, 2018

This Agreement between Thomas Clayson ("You") and Springer Nature ("Springer Nature") consists of your license details and the terms and conditions provided by Springer Nature and Copyright Clearance Center.

License Number	4322950972075
License date	Apr 06, 2018
Licensed Content Publisher	Springer Nature
Licensed Content Publication	Astrophysics and Space Sciences
Licensed Content Title	Highly radiative shock experiments driven by GEKKO XII
Licensed Content Author	A. Dizière, C. Michaut, M. Koenig et al
Licensed Content Date	Jan 1, 2011
Licensed Content Volume	336
Licensed Content Issue	1
Type of Use	Thesis/Dissertation
Requestor type	academic/university or research institute
Format	print and electronic
Portion	figures/tables/illustrations
Number of figures/tables/illustrations	2
Will you be translating?	no
Circulation/distribution	<501
Author of this Springer Nature content	no
Title	Experimental study of radiative shocks in noble gases on the Orion laser and the MAGPIE pulsed-power facility
Instructor name	n/a
Institution name	n/a
Expected presentation date	Apr 2018
Portions	Figure 1 Figure 4.g
Requestor Location	Thomas Clayson Imperial College London Exhibition Road London, London SW7 2AZ United Kingdom Attn: Thomas Clayson
Billing Type	Invoice
Billing Address	Thomas Clayson Imperial College London Exhibition Road London, United Kingdom SW7 2AZ Attn: Thomas Clayson
Total	0.00 USD
Terms and Conditions	

ELSEVIER LICENSE
TERMS AND CONDITIONS

Apr 06, 2018

This Agreement between Thomas Clayson ("You") and Elsevier ("Elsevier") consists of your license details and the terms and conditions provided by Elsevier and Copyright Clearance Center.

License Number	4322951081357
License date	Apr 06, 2018
Licensed Content Publisher	Elsevier
Licensed Content Publication	High Energy Density Physics
Licensed Content Title	High-energy density laboratory astrophysics studies of accretion shocks in magnetic cataclysmic variables
Licensed Content Author	É. Falize,A. Ravasio,B. Loupias,A. Dizière,C.D. Gregory,C. Michaut,C. Busschaert,C. Cavet,M. Koenig
Licensed Content Date	Mar 1, 2012
Licensed Content Volume	8
Licensed Content Issue	1
Licensed Content Pages	4
Start Page	1
End Page	4
Type of Use	reuse in a thesis/dissertation
Intended publisher of new work	other
Portion	figures/tables/illustrations
Number of figures/tables/illustrations	1
Format	both print and electronic
Are you the author of this Elsevier article?	No
Will you be translating?	No
Original figure numbers	Figure 2
Title of your thesis/dissertation	Experimental study of radiative shocks in noble gases on the Orion laser and the MAGPIE pulsed-power facility
Expected completion date	Apr 2018
Estimated size (number of pages)	290
Requestor Location	Thomas Clayson Imperial College London Exhibition Road London, London SW7 2AZ United Kingdom Attn: Thomas Clayson
Publisher Tax ID	GB 494 6272 12
Total	0.00 USD
Terms and Conditions	

INTRODUCTION

ELSEVIER LICENSE
TERMS AND CONDITIONS

Apr 06, 2018

This Agreement between Thomas Clayson ("You") and Elsevier ("Elsevier") consists of your license details and the terms and conditions provided by Elsevier and Copyright Clearance Center.

License Number	4322951418844
License date	Apr 06, 2018
Licensed Content Publisher	Elsevier
Licensed Content Publication	High Energy Density Physics
Licensed Content Title	Experimental study of the interaction of two laser-driven radiative shocks at the PALS laser
Licensed Content Author	R.L. Singh,C. Stehlé,F. Suzuki-Vidal,M. Kozlova,J. Larour,U. Chaulagain,T. Clayson,R. Rodriguez,J.M. Gil,J. Nejdl,M. Krus,J. Dostal,R. Dudzak,P. Barroso,O. Acef,M. Cotelo,P. Velarde
Licensed Content Date	Jun 1, 2017
Licensed Content Volume	23
Licensed Content Issue	n/a
Licensed Content Pages	11
Start Page	20
End Page	30
Type of Use	reuse in a thesis/dissertation
Intended publisher of new work	other
Portion	figures/tables/illustrations
Number of figures/tables/illustrations	2
Format	both print and electronic
Are you the author of this Elsevier article?	No
Will you be translating?	No
Original figure numbers	Figure 5 Figure 7
Title of your thesis/dissertation	Experimental study of radiative shocks in noble gases on the Orion laser and the MAGPIE pulsed-power facility
Expected completion date	Apr 2018
Estimated size (number of pages)	290
Requestor Location	Thomas Clayson Imperial College London Exhibition Road London, London SW7 2AZ United Kingdom Attn: Thomas Clayson
Publisher Tax ID	GB 494 6272 12
Total	0.00 USD
Terms and Conditions	

Copyright Clearance Center

Confirmation Number: 11709526
Order Date: 04/06/2018

Customer Information

Customer: Thomas Clayson
Account Number: 3001270428
Organization: Thomas Clayson
Email: thomasalbertclayson@gmail.com
Phone: +44 7517026424
Payment Method: Invoice

This is not an invoice

Order Details

Plasma Physics and Controlled Fusion

Billing Status: **N/A**

Order detail ID: 71107524
ISSN: 0741-3335
Publication Type: Journal
Volume:
Issue:
Start page:
Publisher: IOP Publishing
Author/Editor: Institute of Physics (Great Britain)

Permission Status: **Granted**
Permission type: Republish or display content
Type of use: Thesis/Dissertation
Order License Id: 4322960394958

Requestor type	Academic institution
Format	Print, Electronic
Portion	image/photo
Number of images/photos requested	1
The requesting person/organization	Thomas Clayson
Title or numeric reference of the portion(s)	Figure 1.b
Title of the article or chapter the portion is from	Production of radiatively cooled hypersonic plasma jets and links to astrophysical jets
Editor of portion(s)	N/A
Author of portion(s)	S. V. Lebedev et al.
Volume of serial or monograph	N/A
Page range of portion	B467
Publication date of portion	2005
Rights for	Main product
Duration of use	Life of current and all future editions
Creation of copies for the disabled	no
With minor editing privileges	yes
For distribution to	Worldwide
In the following language(s)	Original language of publication
With incidental promotional use	no
Lifetime unit quantity of new product	Up to 499
Title	

	Experimental study of radiative shocks in noble gases on the Orion laser and the MAGPIE pulsed-power facility
Instructor name	n/a
Institution name	n/a
Expected presentation date	Apr 2018
Attachment	

Note: This item was invoiced separately through our **RightsLink service.** More info **$ 0.00**

Total order items: 1 **Order Total: $0.00**

About Us | Privacy Policy | Terms & Conditions | Pay an Invoice

Copyright 2018 Copyright Clearance Center

CAMBRIDGE UNIVERSITY PRESS LICENSE
TERMS AND CONDITIONS

Apr 06, 2018

This Agreement between Thomas Clayson ("You") and Cambridge University Press ("Cambridge University Press") consists of your license details and the terms and conditions provided by Cambridge University Press and Copyright Clearance Center.

License Number	4322980856834
License date	Apr 06, 2018
Licensed Content Publisher	Cambridge University Press
Licensed Content Publication	Journal of Plasma Physics
Licensed Content Title	Cylindrical liner Z-pinch experiments for fusion research and high-energy-density physics
Licensed Content Author	G. C. Burdiak, S. V. Lebedev, F. Suzuki-Vidal, G. F. Swadling, S. N. Bland, N. Niasse, L. Suttle, M. Bennet, J. Hare, M. Weinwurm, R. Rodriguez, J. Gil, G. Espinosa
Licensed Content Date	Mar 31, 2015
Licensed Content Volume	81
Licensed Content Issue	3
Start page	365810301
End page	undefined
Type of Use	Dissertation/Thesis
Requestor type	Author
Portion	Text extract
Number of pages requested	3
Author of this Cambridge University Press article	No
Author / editor of the new work	Yes
Order reference number	
Territory for reuse	World
Title of your thesis / dissertation	Experimental study of radiative shocks in noble gases on the Orion laser and the MAGPIE pulsed-power facility
Expected completion date	Apr 2018
Estimated size(pages)	290
Requestor Location	Thomas Clayson Imperial College London Exhibition Road London, London SW7 2AZ United Kingdom Attn: Thomas Clayson
Publisher Tax ID	GB823847609
Billing Type	Invoice
Billing Address	Thomas Clayson Imperial College London Exhibition Road

Copyright Clearance Center

Note: Copyright.com supplies permissions but not the copyrighted content itself.

1 PAYMENT 2 REVIEW 3 CONFIRMATION

Step 3: Order Confirmation

Thank you for your order! A confirmation for your order will be sent to your account email address. If you have questions about your order, you can call us 24 hrs/day, M-F at +1.855.239.3415 Toll Free, or write to us at info@copyright.com. This is not an invoice.

Confirmation Number: 11709542
Order Date: 04/06/2018

If you paid by credit card, your order will be finalized and your card will be charged within 24 hours. If you choose to be invoiced, you can change or cancel your order until the invoice is generated.

Payment Information

Thomas Clayson
thomasalbertclayson@gmail.com
+44 7517026424
Payment Method: n/a

Order Details

Plasma Physics and Controlled Fusion

Order detail ID: 71107559
Order License Id: 4322981295665

ISSN: 0741-3335
Publication Type: Journal
Volume:
Issue:
Start page:
Publisher: IOP Publishing
Author/Editor: Institute of Physics (Great Britain)

Permission Status: Granted

Permission type: Republish or display content
Type of use: Thesis/Dissertation

Requestor type	Academic institution
Format	Print, Electronic
Portion	image/photo
Number of images/photos requested	4
The requesting person/organization	Thomas Clayson
Title or numeric reference of the portion(s)	Figure 1, Figure 3, Figure 13, Figure 31
Title of the article or chapter the portion is from	Comprehensive description of the Orion laser facility
Editor of portion(s)	N/A
Author of portion(s)	N. Hopps et al.
Volume of serial or monograph	N/A

AIP PUBLISHING LICENSE
TERMS AND CONDITIONS

Apr 06, 2018

This Agreement between Thomas Clayson ("You") and AIP Publishing ("AIP Publishing") consists of your license details and the terms and conditions provided by AIP Publishing and Copyright Clearance Center.

License Number	4322990147908
License date	Apr 06, 2018
Licensed Content Publisher	AIP Publishing
Licensed Content Publication	Review of Scientific Instruments
Licensed Content Title	X-ray yield scaling studies performed on the OMEGA laser
Licensed Content Author	J. Workman, G. A. Kyrala
Licensed Content Date	Jan 1, 2001
Licensed Content Volume	72
Licensed Content Issue	1
Type of Use	Thesis/Dissertation
Requestor type	Student
Format	Print and electronic
Portion	Figure/Table
Number of figures/tables	1
Title of your thesis / dissertation	Experimental study of radiative shocks in noble gases on the Orion laser and the MAGPIE pulsed-power facility
Expected completion date	Apr 2018
Estimated size (number of pages)	290
Requestor Location	Thomas Clayson Imperial College London Exhibition Road London, London SW7 2AZ United Kingdom Attn: Thomas Clayson
Billing Type	Invoice
Billing Address	Thomas Clayson Imperial College London Exhibition Road London, United Kingdom SW7 2AZ Attn: Thomas Clayson
Total	0.00 USD

Terms and Conditions

AIP Publishing -- Terms and Conditions: Permissions Uses

AIP Publishing hereby grants to you the non-exclusive right and license to use and/or distribute the Material according to the use specified in your order, on a one-time basis, for the specified term, with a maximum distribution equal to the number that you have ordered. Any links or other content accompanying the Material are not the subject of this license.

1. You agree to include the following copyright and permission notice with the reproduction of the Material:"Reprinted from [FULL CITATION], with the permission of AIP Publishing." For

Copyright Clearance Center RightsLink®

Home | Account Info | Help

IEEE Requesting permission to reuse content from an IEEE publication

Title: Images of unstable Taylor-Sedov blast waves propagating through a uniform gas
Author: C. Manka
Publication: Plasma Science, IEEE Transactions on
Publisher: IEEE
Date: Feb. 1996
Copyright © 1996, IEEE

Logged in as:
Thomas Clayson
Account #:
3001270428
LOGOUT

Thesis / Dissertation Reuse

The IEEE does not require individuals working on a thesis to obtain a formal reuse license, however, you may print out this statement to be used as a permission grant:

Requirements to be followed when using any portion (e.g., figure, graph, table, or textual material) of an IEEE copyrighted paper in a thesis:

1) In the case of textual material (e.g., using short quotes or referring to the work within these papers) users must give full credit to the original source (author, paper, publication) followed by the IEEE copyright line © 2011 IEEE.
2) In the case of illustrations or tabular material, we require that the copyright line © [Year of original publication] IEEE appear prominently with each reprinted figure and/or table.
3) If a substantial portion of the original paper is to be used, and if you are not the senior author, also obtain the senior author's approval.

Requirements to be followed when using an entire IEEE copyrighted paper in a thesis:

1) The following IEEE copyright/ credit notice should be placed prominently in the references: © [year of original publication] IEEE. Reprinted, with permission, from [author names, paper title, IEEE publication title, and month/year of publication]
2) Only the accepted version of an IEEE copyrighted paper can be used when posting the paper or your thesis on-line.
3) In placing the thesis on the author's university website, please display the following message in a prominent place on the website: In reference to IEEE copyrighted material which is used with permission in this thesis, the IEEE does not endorse any of [university/educational entity's name goes here]'s products or services. Internal or personal use of this material is permitted. If interested in reprinting/republishing IEEE copyrighted material for advertising or promotional purposes or for creating new collective works for resale or redistribution, please go to http://www.ieee.org/publications_standards/publications/rights/rights_link.html to learn how to obtain a License from RightsLink.

If applicable, University Microfilms and/or ProQuest Library, or the Archives of Canada may supply single copies of the dissertation.

BACK CLOSE WINDOW

Copyright © 2018 Copyright Clearance Center, Inc. All Rights Reserved. Privacy statement. Terms and Conditions.
Comments? We would like to hear from you. E-mail us at customercare@copyright.com

American Physical Society
Reuse and Permissions License

06-Apr-2018

This license agreement between the American Physical Society ("APS") and Thomas Clayson ("You") consists of your license details and the terms and conditions provided by the American Physical Society and SciPris.

Licensed Content Information

License Number:	**RNP/18/APR/003067**
License date:	06-Apr-2018
DOI:	10.1103/PhysRevLett.66.2738
Title:	Instability of Taylor-Sedov blast waves propagating through a uniform gas
Author:	J. Grun et al.
Publication:	Physical Review Letters
Publisher:	American Physical Society
Cost:	USD $ 0.00

Request Details

Does your reuse require significant modifications: No

Specify intended distribution locations:	Worldwide
Reuse Category:	Reuse in a thesis/dissertation
Requestor Type:	Student
Items for Reuse:	Figures/Tables
Number of Figure/Tables:	1
Figure/Tables Details:	Figure 2
Format for Reuse:	Print and Electronic
Total number of print copies:	Up to 1000

Information about New Publication:

University/Publisher:	Imperial College London
Title of dissertation/thesis:	Experimental study of radiative shocks in noble gases on the Orion laser and the MAGPIE pulsed-power facility
Author(s):	Thomas Clayson
Expected completion date:	Apr. 2018

License Requestor Information

Name:	Thomas Clayson
Affiliation:	Individual
Email Id:	thomasalbertclayson@gmail.com
Country:	United Kingdom

Bibliography

[ASM Aerospace Specification Metals Inc., 2017] ASM Aerospace Specification Metals Inc. (2017). http://asm.matweb.com/search/SpecificMaterial.asp?bassnum=mq321a. Accessed: 2018-03-01.

[Bouquet et al., 2004] Bouquet, S., Stehlé, C., Koenig, M., Chièze, J. P., Benuzzi-Mounaix, A., Batani, D., Leygnac, S., Fleury, X., Merdji, H., Michaut, C., Thais, F., Grandjouan, N., Hall, T., Henry, E., Malka, V., and Lafon, J. P. J. (2004). Observation of laser driven supercritical radiative shock precursors. *Physical Review Letters*, 92(22).

[Bouquet et al., 2000] Bouquet, S., Teyssier, R., and Chieze, J. P. (2000). Analytical Study and Structure of a Stationary Radiative Shock. *The Astrophysical Journal Supplement Series*, 127.

[Bozier et al., 1986] Bozier, J. C., Thiell, G., Le Breton, J. P., Azra, S., Decroisette, M., and Schirmann, D. (1986). Experimental Observation of a Radiative Wave Generated in Xenon by a Laser-Driven Supercritical Shock. *Physics Review Letters*, 57(11).

[Burdiak, 2012] Burdiak, G. C. (2012). *Cylindrical Liner Z-pinches as Drivers for Converging Strong Shock Experiments*. PhD thesis, Imperial College London.

[Burdiak et al., 2017] Burdiak, G. C., Lebedev, S. V., Bland, S. N., Clayson, T., Hare, J., Suttle, L., Suzuki-Vidal, F., Garcia, D. C., Chittenden, J. P., Bott-Suzuki, S., Ciardi, A., Frank, A., and Lane, T. S. (2017). The structure of bow shocks formed by the interaction

of pulsed-power driven magnetised plasma flows with conducting obstacles. *Physics of Plasmas*, 24(072713).

[Burdiak et al., 2013] Burdiak, G. C., Lebedev, S. V., Hall, G. N., Harvey-Thompson, A. J., Suzuki-Vidal, F., Swadling, G. F., Khoory, E., Pickworth, L., Bland, S. N., De Grouchy, P., and Skidmore, J. (2013). Determination of the inductance of imploding wire array Z-pinches using measurements of load voltage. *Physics of Plasmas*, 20(3).

[Burdiak et al., 2014] Burdiak, G. C., Lebedev, S. V., Harvey-Thompson, A. J., Swadling, G. F., Suzuki-Vidal, F., Hall, G. N., Khoory, E., Pickworth, L., Bland, S. N., De Grouchy, P., Skidmore, J., Suttle, L., Bennett, M., Niasse, N. P. L., Williams, R. J. R., Blesener, K., Atoyan, L., Cahill, A., Hoyt, C., Potter, W., Rosenberg, E., Schrafel, P., and Kusse, B. (2014). Radiative precursors driven by converging blast waves in noble gases. *Physics of Plasmas*, 21(033302).

[Burdiak et al., 2015] Burdiak, G. C., Lebedev, S. V., Suzuki-Vidal, F., Swadling, G. F., Bland, S. N., Niasse, N., Suttle, L., Bennet, M., Hare, J., Weinwurm, M., Rodriguez, R., Gil, J., and Espinosa, G. (2015). Cylindrical liner Z-pinch experiments for fusion research and high-energy-density physics. *Journal of Plasma Physics*, 81(3).

[Chaulagain et al., 2015] Chaulagain, U., Stehlé, C., Larour, J., Kozlová, M., Suzuki-Vidal, F., Barroso, P., Cotelo, M., Velarde, P., Rodriguez, R., Gil, J. M., Ciardi, A., Acef, O., Nejdl, J., de Sá, L., Singh, R. L., Ibgui, L., and Champion, N. (2015). Structure of a laser-driven radiative shock. *High Energy Density Physics*, 17.

[Chemezova et al., 1998] Chemezova, L. I., Mesyats, G. A., Sedoi, V. S., Semin, B. N., and Valevich, V. V. (1998). The Integral of Specific Current Aaction and the Specific Energy Input Under Fast Electrical Explosion. *IEEE: Proceedings of the XVIII International Symposium on Discharges and Electrical Insulation in Vacuum, Eidhoven.*

[Clayson et al., 2017] Clayson, T., Suzuki-Vidal, F., Lebedev, S. V., Swadling, G., Stehle, C., Burdiak, G. C., Foster, J. M., Skidmore, J., Graham, P., Gumbrell, E., Patankar, S., Spindloe, C., Chaulagain, U., M., K., Larour, J., Singh, R. L., Rodriguez, R., Gil, J. M., Espinosa, G., P., V., and Danson, C. (2017). Counter-propagating radiative shock experiments on the Orion laser and the formation of radiative precursors. *High Energy Density Physics*, 23.

[Cross et al., 2016] Cross, J. E., Gregori, G., Foster, J. M., Graham, P., Bonnet-Bidaud, J. M., Busschaert, C., Charpentier, N., Danson, C. N., Doyle, H. W., Drake, R. P., Fyrth, J., Gumbrell, E. T., Koenig, M., Krauland, C., Kuranz, C. C., Loupias, B., Michaut, C., Mouchet, M., Patankar, S., Skidmore, J., Spindloe, C., Tubman, E. R., Woolsey, N., Yurchak, R., and Falize, É. (2016). Laboratory analogue of a supersonic accretion column in a binary star system. *Nature Communications*, 7(11899).

[Cuneo et al., 1997] Cuneo, M. E., Menge, P. R., Hanson, D. L., Fowler, W. E., Bernard, M. A., Ziska, G. R., Filuk, A. B., Pointon, T. D., Vesey, R. A., Welch, D. R., Bailey, J. E., Desjarlais, M. P., Lockner, T. R., Mehlhorn, T. A., Slutz, S. A., and Stark, M. A. (1997). Results of vacuum cleaning techniques on the performance of lif field-threshold ion sources on extraction applied-B ion diodes at 1-10 TW. *IEEE Transactions on Plasma Science*, 25(2).

[Dizière et al., 2011] Dizière, A., Michaut, C., Koenig, M., Gregory, C. D., Ravasio, A., Sakawa, Y., Kuramitsu, Y., Morita, T., Ide, T., Tanji, H., Takabe, H., Barroso, P., and Boudenne, J. M. (2011). Highly radiative shock experiments driven by GEKKO XII. *Astrophysics and Space Science*, 336(1).

[Doss et al., 2010] Doss, F. W., Drake, R. P., and Kuranz, C. C. (2010). Repeatability in radiative shock tube experiments. *High Energy Density Physics*, 6(2).

[Drake, 2005] Drake, R. P. (2005). Radiative Shocks in the Laboratory. *Astrophysics and Space Science*, 298(1-2).

[Drake, 2006] Drake, R. P. (2006). *High Energy Density Physics: Fundamentals, Inertial Fusion, and Experimental Astrophysics*. Springer, Berlin.

[Drake et al., 2011] Drake, R. P., Doss, F. W., McClarren, R. G., Adams, M. L., Amato, N., Bingham, D., Chou, C. C., DiStefano, C., Fidkowski, K., Fryxell, B., Gombosi, T. I., Grosskopf, M. J., Holloway, J. P., van der Holst, B., Huntington, C. M., Karni, S., Krauland, C. M., Kuranz, C. C., Larsen, E., van Leer, B., Mallick, B., Marion, D., Martin, W., Morel, J. E., Myra, E. S., Nair, V., Powell, K. G., Rauchwerger, L., Roe, P., Rutter, E., Sokolov, I. V., Stout, Q., Torralva, B. R., Toth, G., Thornton, K., and Visco, A. J. (2011). Radiative effects in radiative shocks in shock tubes. *High Energy Density Physics*, 7(3).

[Edwards et al., 2011] Edwards, M. J., Lindl, J. D., Spears, B. K., Weber, S. V., Atherton, L. J., Bleuel, D. L., Bradley, D. K., Callahan, D. A., Cerjan, C. J., Clark, D., Collins, G. W., Fair, J. E., Fortner, R. J., Glenzer, S. H., Haan, S. W., Hammel, B. A., Hamza, A. V., Hatchett, S. P., Izumi, N., Jacoby, B., Jones, O. S., Koch, J. A., Kozioziemski, B. J., Landen, O. L., Lerche, R., MacGowan, B. J., MacKinnon, A. J., Mapoles, E. R., Marinak, M. M., Moran, M., Moses, E. I., Munro, D. H., Schneider, D. H., Sepke, S. M., Shaughnessy, D. A., Springer, P. T., Tommasini, R., Bernstein, L., Stoeffl, W., Betti, R., Boehly, T. R., Sangster, T. C., Glebov, V. Y., McKenty, P. W., Regan, S. P., Edgell, D. H., Knauer, J. P., Stoeckl, C., Harding, D. R., Batha, S., Grim, G., Herrmann, H. W., Kyrala, G., Wilke, M., Wilson, D. C., Frenje, J., Petrasso, R., Moreno, K., Huang, H., Chen, K. C., Giraldez, E., Kilkenny, J. D., Mauldin, M., Hein, N., Hoppe, M., Nikroo, A., and Leeper, R. J. (2011). The experimental plan for cryogenic layered target implosions on the National Ignition Facility - The inertial confinement approach to fusion. *Physics of Plasmas*, 18(5).

[Engineering ToolBox, 2014] Engineering ToolBox (2014). `https://www.engineeringtoolbox.com/sound-speed-solids-d_713.html`. Accessed: 2018-03-

21.

[Engineers Edge LLC, 2017] Engineers Edge LLC (2017). https://www.engineersedge.com/materials/specific_heat_capacity_of_metals_13259.htm. Accessed: 2017-10-26.

[Everson et al., 2009] Everson, E. T., Pribyl, P., Constantin, C. G., Zylstra, A., Schaeffer, D., Kugland, N. L., and Niemann, C. (2009). Design, construction, and calibration of a three-axis, high-frequency magnetic probe (B-dot probe) as a diagnostic for exploding plasmas. *Review of Scientific Instruments*, 80(113505).

[Falize et al., 2012] Falize, É., Ravasio, A., Loupias, B., Dizière, A., Gregory, C. D., Michaut, C., Busschaert, C., Cavet, C., and Koenig, M. (2012). High-energy density laboratory astrophysics studies of accretion shocks in magnetic cataclysmic variables. *High Energy Density Physics*, 8(1).

[Fein et al., 2014] Fein, J. R., Peebles, J. L., Keiter, P. A., Holloway, J. P., Klein, S. R., Kuranz, C. C., Manuel, M. J. E., and Drake, R. P. (2014). Investigation of the hard x-ray background in backlit pinhole imagers. *Review of Scientific Instruments*, 85(11).

[Fiksel et al., 2012] Fiksel, G., Marshall, F. J., Mileham, C., and Stoeckl, C. (2012). Note: Spatial resolution of Fuji BAS-TR and BAS-SR imaging plates. *Review of Scientific Instruments*, 83(086103).

[Fleury et al., 2002] Fleury, X., Bouquet, S., Stehlé, C., Koenig, M., Batani, D., Chièze, J., Grandjouan, N., Grenier, J., Hall, T., Henry, E., Lafon, J., Leygnac, S., Malka, V., Marchet, B., Merdji, H., Michaut, C., and Thais, F. (2002). Alaser experiment for studying radiative shocks in astrophysics. *Laser and Particle Beams*, 20(2).

[Foster et al., 2005] Foster, J. M., Wilde, B. H., Rosen, P. a., Williams, R. J. R., Blue, B. E., Coker, R. F., Drake, R. P., Frank, A., Keiter, P. A., Khokhlov, A. M., Knauer, J. P., and

Perry, T. S. (2005). High-Energy-Density Laboratory Astrophysics Studies of Jets and Bow Shocks. *The Astrophysical Journal*, 634(1).

[Go-Araldite, 2017] Go-Araldite (2017). `http://www.go-araldite.com/products/epoxy-adhesives/araldite-instant-24ml-syringe`. Accessed: 2017-09-14.

[Gomez et al., 2014] Gomez, M. R., Slutz, S. A., Sefkow, A. B., Sinars, D. B., Hahn, K. D., Hansen, S. B., Harding, E. C., Knapp, P. F., Schmit, P. F., Jennings, C. A., Awe, T. J., Geissel, M., Rovang, D. C., Chandler, G. A., Cooper, G. W., Cuneo, M. E., Harvey-Thompson, A. J., Herrmann, M. C., Hess, M. H., Johns, O., Lamppa, D. C., Martin, M. R., McBride, R. D., Peterson, K. J., Porter, J. L., Robertson, G. K., Rochau, G. A., Ruiz, C. L., Savage, M. E., Smith, I. C., Stygar, W. A., and Vesey, R. A. (2014). Experimental demonstration of fusion-relevant conditions in magnetized liner inertial fusion. *Physical Review Letters*, 113(155003).

[Gonzalez et al., 2002] Gonzalez, A., Li, H., Mitch, M., Tolk, N., and Duggan, D. (2002). Energy response of an imaging plate exposed to standard beta sources. *Applied Radiation and Isotopes*, 57(6).

[González et al., 2006] González, M., Stehlé, C., Audit, E., Busquet, M., Rus, B., Thais, F., Acef, O., Barroso, P., Bar-Shalom, A., Bauduin, D., Kozlovà, M., Lery, T., Madouri, A., Mocek, T., and Polan, J. (2006). Astrophysical radiative shocks: From modeling to laboratory experiments. *Laser and Particle Beams*, 24:535–540.

[Grun et al., 1991] Grun, J., Stamper, J., Manka, C., Resnick, J., Burris, R., Crawford, J., and Ripin, B. (1991). Images of unstable Taylor-Sedov blast waves propagating through a uniform gas. *Physical Review Letters*, 66(21).

[Hansen et al., 2014] Hansen, E. C., Frank, A., Hartigan, P., and Yirak, K. (2014). Numerical Simulations of Mach Stem Formation via Intersecting Bow Shocks. *High Energy Density Physics*, 17.

[Hansen et al., 2007] Hansen, J. F., Robey, H. F., Klein, R. I., and Miles, A. R. (2007). Experiment on the mass-stripping of an interstellar cloud in a high Mach number post-shock flow. *Physics of Plasmas*, 14(056505).

[Hare, 2017] Hare, J. D. (2017). *High Energy Density Magnetic Reconnection Experiments in Colliding Carbon Plasma Flows*. PhD thesis, Imperial College London.

[Hare et al., 2017a] Hare, J. D., Lebedev, S. V., Suttle, L. G., Loureiro, N. F., Ciardi, A., Burdiak, G. C., Chittenden, J. P., Clayson, T., Eardley, S. J., Garcia, C., Halliday, J. W., Niasse, N., Robinson, T., Smith, R. A., Stuart, N., Suzuki-Vidal, F., Swadling, G. F., Ma, J., and Wu, J. (2017a). Formation and structure of a current sheet in pulsed-power driven magnetic reconnection experiments. *Physics of Plasmas*, 24(102703).

[Hare et al., 2017b] Hare, J. D., Suttle, L., Lebedev, S. V., Loureiro, N. F., Ciardi, A., Burdiak, G. C., Chittenden, J. P., Clayson, T., Garcia, C., Niasse, N., Robinson, T., Smith, R. A., Stuart, N., Suzuki-Vidal, F., Swadling, G. F., Ma, J., Wu, J., and Yang, Q. (2017b). Anomalous Heating and Plasmoid Formation in a Driven Magnetic Reconnection Experiment. *Physical Review Letters*, 118(085001).

[Hare et al., 2018] Hare, J. D., Suttle, L. G., Lebedev, S. V., Loureiro, N. F., Ciardi, A., Chittenden, J. P., Clayson, T., Eardley, S. J., Garcia, C., Halliday, J. W. D., Robinson, T., Smith, R. A., Stuart, N., Suzuki-Vidal, F., and Tubman, E. R. (2018). An Experimental Platform for Pulsed-Power Driven Magnetic Reconnection. *Physical Review Letters*, 25(055703).

[Hartigan, 1989] Hartigan, P. (1989). The visibility of the Mach disk and the bow shock of a stellar jet. *The Astrophysical Journal*, 339:987–999.

[Hartigan, 2005] Hartigan, P. (2005). Laboratory Experiments of Stellar Jets from the Perspective of an Observer. *Astrophysics and Space Science*, 298.

[Henke et al., 1993] Henke, B. L., Gullikson, E. M., and Davis, J. C. (1993). X-ray interactions: photoabsorption, scattering, transmission, and reflection at E=50-30000 eV, Z=1-92. *Atomic Data and Nuclear Data Tables*, 54(2).

[Hohenberger et al., 2010] Hohenberger, M., Symes, D., Lazarus, J., Doyle, H., Carley, R., Moore, A. S., Gumbrell, E., Notley, M., Clarke, R., Dunne, M., and Smith, R. (2010). Observation of a Velocity Domain Cooling Instability in a Radiative Shock. *Physical Review Letters*, 105(205003).

[Hopps et al., 2015] Hopps, N., Oades, K., Andrew, J., Brown, C., Cooper, G., Danson, C., Daykin, S., Duffield, S., Edwards, R., Egan, D., Elsmere, S., Gales, S., Girling, M., Gumbrell, E., Harvey, E., Hillier, D., Hoarty, D., Horsfield, C., James, S., Leatherland, A., Masoero, S., Meadowcroft, A., Norman, M., Parker, S., Rothman, S., Rubery, M., Treadwell, P., Winter, D., and Bett, T. (2015). Comprehensive description of the Orion laser facility. *Plasma Physics and Controlled Fusion*, 57(064002).

[J. Morse/STScI and ESA, 1995] J. Morse/STScI, N. and ESA (1995). `https://www.spacetelescope.org/images/opo9524g/`. Accessed: 2018-03-20.

[Keiter et al., 2002] Keiter, P. A., Drake, R. P., Perry, T. S., Robey, H. F., Remington, B. A., Iglesias, C. A., Wallace, R. J., and Knauer, J. (2002). Observation of a hydrodynamically driven, radiative-precursor shock. *Physical Review Letters*, 89(16).

[Key et al., 1998] Key, M., Cable, M., Cowan, T., Estabrook, K., Hammel, B., Hatchett, S., Henry, E., Hinkel, D., Kilkenny, J., Koch, J., Kruer, W., Langdon, A., Lasinski, B., Lee, R., Macgowan, B., MacKinnon, A., Moody, J., Moran, M., Offenberger, A., Pennington, D., Perry, M., Phillips, T., Sangster, T., Singh, M., Stoyer, M., Tabak, M., Tietbohl, G., Tsukamoto, M., Wharton, K., and Wilks, S. (1998). Hot electron production and heating by hot electrons in fast ignitor research. *Physics of Plasmas*, 5(5).

[Knoepfel, 2000] Knoepfel, H. E. (2000). *Magnetic fields*. John Wiley Sons, Inc.

[Koenig et al., 2006] Koenig, M., Vinci, T., Benuzzi-Mounaix, A., Ozaki, N., Ravasio, A., Rabec Le Glohaec, M., Boireau, L., Michaut, C., Bouquet, S., Atzeni, S., Schiavi, A., Peyrusse, O., and Batani, D. (2006). Radiative shocks: An opportunity to study laboratory astrophysics. *Physics of Plasmas*, 13(056504).

[Kramida et al., 2015] Kramida, A., Yu. Ralchenko, Reader, J., and and NIST ASD Team (2015). NIST Atomic Spectra Database (ver. 5.3), [Online]. Available: `http://physics.nist.gov/asd` [2016, October 20]. National Institute of Standards and Technology, Gaithersburg, MD.

[Krauland et al., 2013] Krauland, C. M., Drake, R. P., Kuranz, C. C., Sweeney, R., Grosskopf, M., Klein, S., Gillespie, R., Keiter, P. A., Loupias, B., and Falize, E. (2013). Radiative reverse shock laser experiments relevant to accretion processes in cataclysmic variables. *Physics of Plasmas*, 20(056502).

[Krauland et al., 2012] Krauland, C. M., Jarrott, L. C., Drake, R. P., Keiter, P. A., Kuranz, C. C., Westover, B., Sawada, H., Kaczala, D. N., and Bonofiglo, P. (2012). An evaluation of high energy bremsstrahlung background in point-projection x-ray radiography experiments. *Review of Scientific Instruments*, 83(10).

[Kuphaldt, 2017] Kuphaldt, T. R. (2017). Lessons in Electric Circuits. `https://www.allaboutcircuits.com/textbook`. Accessed: 2017-10-26.

[Landen et al., 2001] Landen, O. L., Farley, D. R., Glendinning, S. G., Logory, L. M., Bell, P. M., Koch, J. a., Lee, F. D., Bradley, D. K., Kalantar, D. H., Back, C. a., and Turner, R. E. (2001). X-ray backlighting for the National Ignition Facility (invited). *Review of Scientific Instruments*, 72(627).

[Lebedev et al., 1998] Lebedev, S. V., Aliaga-Rossel, R., Chittenden, J. P., Mitchell, I. H., Dangor, A. E., Haines, M. G., and Worley, J. F. (1998). Coronal plasma behavior of the Z pinch produced from carbon and cryogenic deuterium fibers. *Physics of Plasmas*, 5(9).

[Lebedev et al., 2005] Lebedev, S. V., Ciardi, A., Ampleford, D. J., Bland, S. N., Bott, S. C., Chittenden, J. P., Hall, G. N., Rapley, J., Jennings, C., Sherlock, M., Frank, A., and Blackman, E. G. (2005). Production of radiatively cooled hypersonic plasma jets and links to astrophysical jets. *Plasma Physics and Controlled Fusion*, 47(12B).

[Lebedev et al., 2014] Lebedev, S. V., Suttle, L., Swadling, G. F., Bennett, M., Bland, S. N., Burdiak, G. C., Burgess, D., Chittenden, J. P., Ciardi, A., Clemens, A., de Grouchy, P., Hall, G. N., Hare, J. D., Kalmoni, N., Niasse, N., Patankar, S., Sheng, L., Smith, R. A., Suzuki-Vidal, F., Yuan, J., Frank, A., Blackman, E. G., and Drake, R. P. (2014). The formation of reverse shocks in magnetized high energy density supersonic plasma flows. *Physics of Plasmas*, 21(056305).

[Lin et al., 1999] Lin, Z., Deng, X., Fan, D., Wang, S., Chen, S., Zhu, J., Qian, L., Shen, X., Xu, F., Zhu, J., Ma, W., Xie, X., Zheng, Y., Zhang, W., Chen, Q., Ling, M., Huang, H., and Zhang, J. (1999). SG-II laser elementary research and precision SG-II program. *Fusion Engineering and Design*, 44(1-4).

[LLNL, 2010] LLNL (2010). `https://lasers.llnl.gov/science/understanding-the-universe/plasma-physics`. Accessed: 2018-03-19.

[MacFarlane et al., 2006] MacFarlane, J. J., Golovkin, I. E., and Woodruff, P. R. (2006). HELIOS-CR - A 1-D radiation-magnetohydrodynamics code with inline atomic kinetics modeling. *Journal of Quantitative Spectroscopy and Radiative Transfer*, 99(1-3).

[Matthews et al., 1983] Matthews, D. L., Campbell, E. M., Ceglio, N. M., Hermes, G., Kauffman, R., Koppel, L., Lee, R., Manes, K., Rupert, V., Slivinsky, V. W., Turner, R., and Ze, F. (1983). Characterization of laserproduced plasma xray sources for use in xray radiography. *Journal of Applied Physics*, 54(8).

[McKee, 1974] McKee, C. F. (1974). X-Ray Emission from an Inward-Propagating Shock in Young Supernova Remnants. *The Astrophysical Journal*, 188.

[Meerson, 1996] Meerson, B. (1996). Nonlinear dynamics of radiative condensations in optically thin plasmas. *Reviews of Modern Physics*, 68(1).

[Michaut et al., 2007] Michaut, C., Vinci, T., Boireau, L., Koenig, M., Bouquet, S., Benuzzi-Mounaix, A., Osaki, N., Herpe, G., Falize, E., Loupias, B., and Atzeni, S. (2007). Theoretical and Experimental Studies of Radiative Shocks. *Astrophysics and Space Science*, 307(1-3).

[Mitchell et al., 1996] Mitchell, I. H., Bayley, J. M., Chittenden, J. P., Worley, J. F., Dangor, a. E., Haines, M. G., and Choi, P. (1996). A high impedance mega-ampere generator for fiber z-pinch experiments. *Review of Scientific Instruments*, 67(4).

[NASA and ESA, 2005] NASA and ESA (2005). `https://en.wikipedia.org/wiki/Crab_Nebula#/media/File:Crab_Nebula.jpg`. Accessed: 2018-03-20.

[Orlando et al., 2013] Orlando, S., Bonito, R., Argiroffi, C., Reale, F., Peres, G., Miceli, M., Matsakos, T., Stehlé, C., Ibgui, L., de Sa, L., Chièze, J. P., and Lanz, T. (2013). Radiative accretion shocks along nonuniform stellar magnetic fields in classical T Tauri stars. *Astronomy & Astrophysics*, 559.

[Pak et al., 2013] Pak, A., Divol, L., Gregori, G., Weber, S., Atherton, J., Bennedetti, R., Bradley, D. K., Callahan, D., Casey, D. T., Dewald, E., Döppner, T., Edwards, M. J., Frenje, J. A., Glenn, S., Grim, G. P., Hicks, D., Hsing, W. W., Izumi, N., Jones, O. S., Johnson, M. G., Khan, S. F., Kilkenny, J. D., Kline, J. L., Kyrala, G. A., Lindl, J., Landen, O. L., Le Pape, S., Ma, T., Macphee, A., Macgowan, B. J., Mackinnon, A. J., Masse, L., Meezan, N. B., Moody, J. D., Olson, R. E., Ralph, J. E., Robey, H. F., Park, H. S., Remington, B. A., Ross, J. S., Tommasini, R., Town, R. P. J., Smalyuk, V., Glenzer, S. H., and Moses, E. I. (2013). Radiative shocks produced from spherical cryogenic implosions at the National Ignition Facility. *Physics of Plasmas*, 20(056315).

[Park et al., 2006] Park, H. S., Chambers, D. M., Chung, H. K., Clarke, R. J., Eagleton, R., Giraldez, E., Goldsack, T., Heathcote, R., Izumi, N., Key, M. H., King, J. a., Koch,

J. a., Landen, O. L., Nikroo, A., Patel, P. K., Price, D. F., Remington, B. a., Robey, H. F., Snavely, R. a., Steinman, D. a., Stephens, R. B., Stoeckl, C., Storm, M., Tabak, M., Theobald, W., Town, R. P. J., Wickersham, J. E., and Zhang, B. B. (2006). High-energy K \alpha radiography using high-intensity, short-pulse lasers. *Physics of Plasmas*, 13(056309).

[Park et al., 2012] Park, H. S., Ryutov, D. D., Ross, J. S., Kugland, N. L., Glenzer, S. H., Plechaty, C., Pollaine, S. M., Remington, B. a., Spitkovsky, A., Gargate, L., Gregori, G., Bell, A., Murphy, C., Sakawa, Y., Kuramitsu, Y., Morita, T., Takabe, H., Froula, D. H., Fiksel, G., Miniati, F., Koenig, M., Ravasio, A., Pelka, A., Liang, E., Woolsey, N., Kuranz, C. C., Drake, R. P., and Grosskopf, M. J. (2012). Studying astrophysical collisionless shocks with counterstreaming plasmas from high power lasers. *High Energy Density Physics*, 8(1).

[Phillion and Hailey, 1986] Phillion, D. W. and Hailey, C. J. (1986). Brightness and duration of x-ray line sources irradiated with intense 0.53-um laser light at 60 and 120 ps pulse width. *Physical Review A*, 34(6).

[Reighard et al., 2006] Reighard, A. B., Drake, R. P., Dannenberg, K. K., Kremer, D. J., Grosskopf, M., Harding, E. C., Leibrandt, D. R., Glendinning, S. G., Perry, T. S., Remington, B. A., Greenough, J., Knauer, J., Boehly, T., Bouquet, S., Boireau, L., Koenig, M., and Vinci, T. (2006). Observation of collapsing radiative shocks in laboratory experiments. *Physics of Plasmas*, 13(082901).

[Reipurth et al., 1997] Reipurth, B., Bally, J., and Devine, D. (1997). Giant Herbig-Haro Flows. *The Astronomical Journal*, 114(6).

[Remington et al., 2006] Remington, B. A., Drake, R. P., and Ryutov, D. D. (2006). Experimental astrophysics with high power lasers and Z pinches. *Reviews of Modern Physics*, 78(3).

[Roberts et al., 1980] Roberts, P. D., Rose, S. J., Thompson, P. C., and Wright, R. J. (1980). The stability of multiple-shell ICF targets. *Journal of Physics D: Applied Physics*, 13(11).

[Rosen et al., 2009] Rosen, P. A., Foster, J. M., Wilde, B. H., Hartigan, P., Blue, B. E., Hansen, J. F., Sorce, C., Williams, R. J. R., Coker, R., and Frank, A. (2009). Laboratory experiments to study supersonic astrophysical flows interacting with clumpy environments. *Astrophysics and Space Science*, 322(1-4).

[Ryutov, 2015] Ryutov, D. D. (2015). Characterizing the Plasmas of Z-Pinches. *IEEE Transactions on Plasma Science*, 43(8).

[Ryutov et al., 1999] Ryutov, D. D., Drake, R. P., Kane, J., Liang, E., Remington, B. A., and Wood-Vasey, W. M. (1999). SIMILARITY CRITERIA FOR THE LABORATORY SIMULATION OF SUPERNOVA HYDRODYNAMICS. *The Astrophysical Journal*, 518.

[Sinars et al., 2003] Sinars, D. B., Cuneo, M. E., Bennett, G. R., Wenger, D. F., Ruggles, L. E., Vargas, M. F., Porter, J. L., Adams, R. G., Johnson, D. W., Keller, K. L., Rambo, P. K., Rovang, D. C., Seamen, H., Simpson, W. W., Smith, I. C., and Speas, S. C. (2003). Monochromatic x-ray backlighting of wire-array z -pinch plasmas using spherically bent quartz crystals. *Review of Scientific Instruments*, 74(3).

[Singh et al., 2017] Singh, R., Stehlé, C., Suzuki-Vidal, F., Kozlova, M., Larour, J., Chaulagain, U., Clayson, T., Rodriguez, R., Gil, J., Nejdl, J., Krus, M., Dostal, J., Dudzak, R., Barroso, P., Acef, O., Cotelo, M., and Velarde, P. (2017). Experimental study of the interaction of two laser-driven radiative shocks at the PALS laser. *High Energy Density Physics*, 23.

[Skidmore, 2013] Skidmore, J. W. (2013). *Experimental study of pulsed power driven radiative shockwaves in noble gases*. PhD thesis, Imperial College London.

[Slutz et al., 2010] Slutz, S. A., Herrmann, M. C., Vesey, R. A., Sefkow, A. B., Sinars, D. B., Rovang, D. C., and Peterson, K. J. (2010). Pulsed-power-driven cylindrical liner implosions of laser preheated fuel magnetized with an axial field. *Physics of Plasmas*, 17(056303).

[Spindloe et al., 2017] Spindloe, C., Wyatt, D., Astbury, S., Swadling, G. F., Clayson, T., Stehlé, C., Foster, J. M., Gumbrell, E., Charles, R., Danson, C. N., Brummitt, P., and Suzuki-Vidal, F. (2017). Design and fabrication of gas cell targets for laboratory astrophysics experiments on the Orion high-power laser facility. *High Power Laser Science and Engineering*, 5.

[Stehlé et al., 2010] Stehlé, C., González, M., Kozlova, M., Rus, B., Mocek, T., Acef, O., Colombier, J. P., Lanz, T., Champion, N., Jakubczak, K., Polan, J., Barroso, P., Bauduin, D., Audit, E., Dostal, J., and Stupka, M. (2010). Experimental study of radiative shocks at PALS facility. *Laser and Particle Beams*, 28(2).

[Stehlé et al., 2012] Stehlé, C., Kozlová, M., Larour, J., Nejdl, J., Champion, N., Barroso, P., Suzuki-Vidal, F., Acef, O., Delattre, P.-A., Dostál, J., Krus, M., and Chièze, J.-P. (2012). New probing techniques of radiative shocks. *Optics Communications*, 285(1).

[Suttle et al., 2016] Suttle, L. G., Hare, J. D., Lebedev, S. V., Swadling, G. F., Burdiak, G. C., Ciardi, A., Chittenden, J. P., Loureiro, N. F., Niasse, N., Suzuki-Vidal, F., Wu, J., Yang, Q., Clayson, T., Frank, A., Robinson, T. S., Smith, R. A., and Stuart, N. (2016). Structure of a Magnetic Flux Annihilation Layer Formed by the Collision of Supersonic, Magnetized Plasma Flows. *Physical Review Letters*, 116(225001).

[Suzuki-Vidal, 2009] Suzuki-Vidal, F. (2009). *Experimental Study of Radiatively Cooled Magnetically Driven Plasma Jets*. PhD thesis, Imperial College London.

[Suzuki-Vidal et al., 2012] Suzuki-Vidal, F., Bocchi, M., Lebedev, S. V., Swadling, G. F., Burdiak, G., Bland, S. N., De Grouchy, P., Hall, G. N., Harvey-Thompson, a. J., Khoory, E., Patankar, S., Pickworth, L., Skidmore, J., Smith, R., Chittenden, J. P., Krishnan, M., Madden, R. E., Wilson-Elliot, K., Ciardi, a., and Frank, a. (2012). Interaction of a supersonic, radiatively cooled plasma jet with an ambient medium. *Physics of Plasmas*, 19(2).

[Suzuki-Vidal et al., 2017] Suzuki-Vidal, F., Clayson, T., Stehlé, C., Swadling, G. F., Foster, J. M., Skidmore, J., Graham, P., Burdiak, G. C., Lebedev, S. V., Chaulagain, U., Singh, R. L., Gumbrell, E. T., Patankar, S., Spindloe, C., Larour, J., Kozlova, M., Rodriguez, R., Gil, J. M., Espinosa, G., Velarde, P., and Danson, C. (2017). Counterpropagating Radiative Shock Experiments on the Orion Laser. *Physical Review Letters*, 119(055001).

[Suzuki-Vidal et al., 2010] Suzuki-Vidal, F., Lebedev, S. V., Bland, S. N., Hall, G. N., Swadling, G., Harvey-Thompson, A. J., Chittenden, J. P., Marocchino, A., Ciardi, A., Frank, A., Blackman, E. G., and Bott, S. C. (2010). Generation of episodic magnetically driven plasma jets in a radial foil Z-pinch. *Physics of Plasmas*, 17(112708).

[Suzuki-Vidal et al., 2015] Suzuki-Vidal, F., Lebedev, S. V., Ciardi, A., Pickworth, L. A., Rodriguez, R., Gil, J. M., Espinosa, G., Hartigan, P., Swadling, G. F., Skidmore, J., Hall, G. N., Bennett, M., Bland, S. N., Burdiak, G., De Grouchy, P., Music, J., Suttle, L., Hansen, E., and Frank, A. (2015). Bow shock fragmentation driven by a thermal instability in laboratory astrophysics experiments. *Astrophysical Journal*, 815(96).

[Swadling, 2011] Swadling, G. (2011). *An experimental investigation of the azimuthal structures formed during the ablation phase of wire array z-pinches*. PhD thesis.

[Swadling et al., 2014] Swadling, G. F., Lebedev, S. V., Hall, G. N., Patankar, S., Stewart, N. H., Smith, R. a., Harvey-Thompson, a. J., Burdiak, G. C., de Grouchy, P., Skidmore, J., Suttle, L., Suzuki-Vidal, F., Bland, S. N., Kwek, K. H., Pickworth, L., Bennett, M., Hare, J. D., Rozmus, W., and Yuan, J. (2014). Diagnosing collisions of magnetized, high energy density plasma flows using a combination of collective Thomson scattering, Faraday rotation, and interferometry. *Review of Scientific Instruments*, 85(11).

[Swadling et al., 2016] Swadling, G. F., Lebedev, S. V., Hall, G. N., Suzuki-Vidal, F., Burdiak, G. C., Pickworth, L., De Grouchy, P., Skidmore, J., Khoory, E., Suttle, L., Bennett, M., Hare, J. D., Clayson, T., Bland, S. N., Smith, R. A., Stuart, N. H., Patankar, S.,

Robinson, T. S., Harvey-Thompson, A. J., Rozmus, W., Yuan, J., and Sheng, L. (2016). Experimental investigations of ablation stream interaction dynamics in tungsten wire arrays: Interpenetration, magnetic field advection, and ion deflection. *Physics of Plasmas*, 23(5).

[Swadling et al., 2013] Swadling, G. F., Lebedev, S. V., Niasse, N., Chittenden, J. P., Hall, G. N., Suzuki-Vidal, F., Burdiak, G., Harvey-Thompson, A. J., Bland, S. N., De Grouchy, P., Khoory, E., Pickworth, L., Skidmore, J., and Suttle, L. (2013). Oblique shock structures formed during the ablation phase of aluminium wire array z-pinches. *Physics of Plasmas*, 20(022705).

[Vishniac, 1983] Vishniac, E. T. (1983). The dynamic and gravitational instabilities of spherical shocks. *The Astrophysical Journal*, 274.

[Warner, 1995] Warner, B. (1995). *Cataclysmic Variable Stars*. Cambridge University Press, UK.

[Weinwurm et al., 2013] Weinwurm, M., Bland, S. N., and Chittenden, J. P. (2013). Metal liner-driven quasi-isentropic compression of deuterium. *Physics of Plasmas*, 20(092701).

[Workman and Kyrala, 2001] Workman, J. and Kyrala, G. A. (2001). X-ray yield scaling studies performed on the OMEGA laser. *Review of Scientific Instruments*, 72(1).

[Xu et al., 2008] Xu, G., Wang, T., Li, Z., Dai, Y., Lin, Z., Gu, Y., and Zhu, J. (2008). 1 kJ Petawatt Laser System for SG-II-U Program. *The Review of Laser Engineering*, 36(APLS).

[Youngs, 1984] Youngs, D. L. (1984). Numerical simulation of turbulent mixing by Rayleigh-Taylor instability. *Physica D: Nonlinear Phenomena*, 12(1-3).

[Zel'dovich and Raizer, 2002] Zel'dovich, Y. B. and Raizer, Y. P. (2002). *Physics of Shock Waves and High-Temperature Hydrodynamic Phenomena*. Dover Publications.